Experimental study on the estimation of discontinuity characteristics and mechanical properties of jointed rock masses

October, 1999

Kiyoshi Kishida

Experimental study on the estimation of discontinuity characteristics and mechanical properties of jointed rock masses

October, 1999

Kiyoshi Kishida

Acknowledgment

The present research work was carried out at the Department of Civil Engineering, Faculty of Engineering, Kyoto University. The work of this thesis could not been accomplished without many supports and helps of professors, colleagues, students and friends, to whom I should like to express my gratitude.

Sincerest thanks go to my supervisor, Professor Toshihisa Adachi, Department of Civil Engineering, Kyoto University, for his invaluable help, guidance, encouragement and a great deal of tolerance during all these years.

I should also like to express my sincere gratitude to Professor Chikaosa Tanimoto, Department of Global Architecture, Osaka University for taking a chance, and providing technical comments and moral support throughout this research.

I wish to express sincere gratitude to Professor Yuzo Ohnishi, Department of Civil Engineering Systems, Kyoto University, and Professor Yuzuru Ashida, Department of Earth Resources Engineering, Kyoto University for giving me their constant encouragement and valuable suggestions during all these years, Professors Takeshi Tamura and Fusao Oka, Department of Civil Engineering, Kyoto University, for giving their witty suggestions and encouragement.

Special thanks are due to Associate Professors Kazuyoshi Tateyama, Makoto Kimura, and Mamoru Mimura at Kyoto University for their many helps, valuable suggestions, and constant encouragement from my student days.

Many laboratory tests were carried out in Construction Engineering Laboratory, Department of Civil Engineering, Kyoto University. I am deeply great thanks to many students and graduated students at Construction Engineering Laboratory, especially, Mrs. Hiroshi Morioka, Hiroyuki Tanaka, Satoshi Matsusaki, Takayuki Umezawa, Taku Ando, Yuichi Odawara, Daisuke Tomizu, Naoki Ando, Keisuke Nakanishi, Koji Tabata, and Kiyoshi Fujisaki, Shinichiro Nakashima, and Hiroshi Fujii for their many helps. I wish their happiness and success.

Special thanks are due to Kansai Electric Power Co. Ltd. for taking a chance to carry out the field measurements.

I wish also to express special thanks to Mr.Jun Kawakami, Mr. Michito Shimo, Dr. Tomoyuki Aoki and Dr. Masahiro Iwano of Taisei Corporation for their helping during my stay in Yokohama.

Many thanks to all my friends, team mates of my basketball clubs for their helping from my middle high school days.

Finally, I would like to thank my wife, Chiemi, my parents and my grandparents for their many many supports and great patience.

Contents

List of tables, photos and figures

Chapter 1

Introduction

1.1 Background

In Japan, which is a small island country, there is an increasing need for the effective use of underground space, as it is indispensable for human life. As the population explodes in urban areas, subways, water, gas, and electric supply pipelines as well as underground rivers are being constructed under areas where structures are closely clustered together. Thus, careful attention must be paid to the influence of these existing structures when constructing underground structures. In mountain districts, which have highways of superior quality, large-faced tunnels will be constructed. And, with the lack of electric power and oil, underground caverns must be built for powerhouses and oil storage. Recently, underground space is also often being used for storing industrial waste and radioactive waste materials. Therefore, the efficient construction of underground space and the effective use of it are very important factors to keep in mind, since the creation of an affluent society for the 21st century is desirable.

Based on the above background information, we civil engineers insist that methods for both the design and the construction of underground structures, considering high quality and economics, be developed and created.

A question then arises of just how such high-quality and economical underground structures can be constructed. Consideration must be given to what important problems exist in constructing underground structures. When these problems are faced, they must be matched against the joints and/or the discontinuities in rock masses. It is inevitable that joints and/or discontinuities will be encountered in rock masses when underground structures are being constructed. Thus, the subject of the construction of underground structures in a jointed rock mass is taken up in this thesis.

The mechanical and the hydromechanical behaviors of a jointed rock mass are strongly affected by rock joints and/or discontinuities. In order to grasp the mechanical behavior of a jointed rock mass, an estimation of the mechanical behavior of the rock joints must be carried out. In other words, it is important to grasp the discontinuity characteristics and the mechanical properties. In this thesis, field measurements such as a joint survey, a seismic exploration, and borehole jacking tests are carried out and both the distribution and the mechanical properties of the jointed rock mass are discussed. In addition, fundamental laboratory tests, such as direct shear tests and seismic propagating experiments, are carried out on rock joints, and the knowledge obtained through the laboratory tests is applied to discussions on the results of the field

measurements. Therefore, the distribution and the mechanical properties of the jointed rock mass can be estimated in further detail.

The purpose of this thesis is to grasp the distribution and the mechanical properties of a jointed rock mass through field measurements. The conclusion of this thesis hopes to contribute to the design and the construction of underground structures in jointed rock masses.

1.2 Review of background literature

In order to understand and to quantify the influence that discontinuities have on rock mass behavior, it is necessary to quantitatively measure and represent the relevant characteristics of the discontinuities. The suggested methods for the quantitative description of discontinuities in rock masses prepared by ISRM' (1978) provide a good, but general, introduction to the qualitative aspects of discontinuity measurement. The suggested methods are limited, however, by the fact that they do not incorporate data processing techniques, developed in the 1980s, for the elimination of sampling bias and the quantification of discontinuity characteristics. The two broad sampling strategies that can be adopted involve either the logging of borehole cores and borehole walls or the examination of exposed rock faces.

The recovery, examination, and testing of high quality drill cores obtained by diamond drilling have been used for many years to probe rock conditions at great depths. Hoek and Brown (1980) and Brady and Brown (1985) described the principal types of drill rigs, core barrels, and drill bits that have been used in diamond drilling. The primary purpose here is to identify the various rock types and their mineral compositions, and to build up a three-dimensional picture of mine geology. Borehole cores can, however, also provide relatively undisturbed samples of rock materials containing discontinuities from deep within a rock close to the area of a proposed excavation or potential instability, making it a valuable source of information for the geotechnical design. The Geological Society (1970) and Rosengren (1970) presented valuable guidelines for the logging of rock cores for engineering purposes. In addition, the mechanical and hydromechanical tests were conducted on recovered rock material and on the walls of boreholes (Snow, 1970). The borehole image processor, described earlier than the observation of recovered rock cores, provides data on the absolute orientation of discontinuities photographed in a borehole wall. A variety of additional techniques were developed for determining the absolute orientation of drill cores in different situations, including soft rock and hard rock, as reviewed by Goodman (1976) and Hoek and Bray (1977). Murai, et al. (1988), Kamewada, et al. (1990), and Tanimoto, et al. (1992) carried out inspections using remote visual techniques. Rock quality designation (*RQD*), devised by Deere (1964), was defined as the percentage length of a given length of a core consisting of

intact, sound pieces that are longer than the threshold value of 0.1 m. *RQD* is one index which can present the quality of a rock mass.

Taking measurements at exposed rock faces, either above or below the ground, provides the advantage of utilizing a relatively large area of rock, which enables the direct measurement of discontinuity orientation, size, and other large-scale geometrical features. The geological relations between the various discontinuity groups can be also clearly obtained. One disadvantage of this approach, however, is that the rock face is often at a distance from the zone of interest and may suffer from blasting damage or degradation by weathering and vegetation cover. Until recently, measurements at exposed faces were taken in an arbitrary and subjective manner, and were derived from geological mapping techniques. This yielded an insufficient amount of quantitative data of value for engineering designs. Lately, however, more rigorous statistical sampling and data processing methods have been adopted. The most widely used of these methods are scanline and window sampling techniques. These techniques were described and discussed by many authors, namely, Fookes and Denness (1969), Attewell and Farmer (1976), Baecher and Lanney (1978), Kikuchi, et al. (1978), ISRM (1978), and Priest and Hudson (1981). The relative simplicity of the measurement process at exposed face and the statistical rigor of these techniques make them ideally suited to the determination of the discontinuity orientation and other large-scale geometrical properties of rock structures. Rouleau and Gale (1985) and then Kulatilahe, et al. (1990) presented instructive case studies on the use of these techniques in conjunction with borehole sampling for the characterization, modeling, and verification of discontinuity orientation, spacing, frequency, and size for a granite rock mass in Stripa, Sweden.

Before sampling and conducting the preliminary processing of the discontinuity data in a jointed rock mass, the characteristics of discontinuities, namely, orientation, groups and sets, frequency, size, and spacing, must be determined. One of the most important characteristics of discontinuities is their orientation. One of the simplest forms of the graphical representation of orientation is a rose diagram (Attewell and Farmer, 1976; Cawsey, 1977). The results of a rose diagram are plotted wedges which have a radial extent that is proportional to the frequency in each class interval. This frequency can be expressed as a raw number, a proportion, or a percentage of the total sampling size. The disadvantage of rose diagrams, however, is that they contain no information on dip angles. This disadvantage can be overcome to some extent by selecting data from the more significant class intervals and then plotting a histogram of the dip angles. The difficulties involved with representing three-dimensional orientation data in two dimensions on a sheet of paper can be overcome by adopting a technique known as a stereographic or hemispherical projection (Duncan, 1981; Goodman, 1976; Kalkani and von Frese, 1979; Phillips, 1971; Priest, 1985). A fracture plane is uniquely represented by a line normal to the plane, called a pole. A pole is represented by a unit-length vector, conventionally down-dipping for geologic structures. In turn, a vector is represented by its intersection point on a unit-radius lower hemisphere. Orientation densities on the hemispherical surface are calculated by counting points within circular-shaped counting cells. Points and contours on the

hemispherical surface are projected onto the equatorial plane by the equal-area spherical projection, which preserves relative areas between the hemisphere and the projection.

Hemispherical projection methods were introduced earlier as graphical approaches to the analysis of orientation data. Clusters, or sets of preferred orientation, can be identified. Bailey (1975), Shaneley and Mahtab (1976), Mahtab and Yegulalp (1982), and Bridges (1990), among others, presented an analysis of clusters for orientation data. Many authors have applied the Chi-square goodness-of-fit test to the Poisson, binomial, or similar models to distinguish the real from the chance clustering of points on a spherical surface. Flinn (1958) and Kamb (1959) were among the earliest contributors in the geological field. Stauffer (1966) compared several alternative approaches with Poisson's model. Mahtab, et al. (1972) incorporated it into a computer program that has frequently been quoted. Recent reviews of this approach are provided by Mahtab and Yegulalp (1982) and Fisher, et al. (1987), among others. In particular, Mahtab and Yegulalp (1982) modified the approach by Shanley and Mahtab (1982) which presented a rigorous and less subjective approach to the analysis of clusters in orientation data. This has some common elements with the technique used in the present thesis. However, many authors have commented that the technique may not identify sets within complex distributions of orientations, or where clusters overlap. Visual recognition of clustering, namely, taking advantage of the human ability to recognize patterns, has been advocated as an alternative method in these circumstances (e.g., Einstein and Baecher, 1983; Bridges, 1990). More fundamental limitations on Poisson's test have been discussed in recent years. Ohnishi and Nakagawa (1993) described a comparison of Poisson's distribution and Bingham's distribution to the analysis of clusters, and showed that Bingham's distribution has an advantage in the real distribution.

Using orientation data and the results of an orientation analysis, a discussion on the mechanical and the hydromechanical behaviors of a jointed rock mass can be effectively carried out. In discussing both mechanical and hydromechanical behaviors of a jointed rock mass, the model must be made and the numerical analysis must be applied based on the statistical data. The two broad models involve either the equivalent continuum model or the discontinuous model in consideration of the numerical methods. The crack tensor theory (Oda, 1982, 1985a, and 1985b), the damage theory (Kyoya, et al., 1985; Kawamoto, et al., 1988.), the equivalent volumetric damage method (Kaneko, et al., 1985 and 1990), and the parallel plate model (Snow, 1965) all involve equivalent continuum models and analyses. On the other hand, the joint element method of the finite element method (*FEM*) (Goodman, et al., 1968; Zienkiewucz, et al., 1970; Heuze and Barbour, 1982; Desai, et al., 1984), the linkage element of *FEM* (Ngo and Scodelis, 1967), the rigid body spring model (*RBSM*) (Kawai and Toi, 1977; Kawamoto, et al., 1982), the distinct element method (*DEM*) (Cundall, 1971 and 1987; Lorig, et al., 1986), the discontinuous deformation analysis (*DDA*) (Shi and Goodman, 1985; Shi, 1990), and the fracture network model (Long, et al., 1985; Dershowitz, et al., 1989) all involve discontinuous models and analyses.

As for testing and modeling the rock joints, some research works have already been presented. When considering the mechanical behavior of the rock joints, the characterization properties have been generally observed and determined for both normal and shear directions of the joints, respectively.

Stephansson and Jing (1995) proposed two types of empirical models for the behavior of the normal stress - normal displacement of rock joints. One type is a hyperbolic function proposed by Goodman (1976) and then Bandis (1980), respectively, and the other is a logarithmic function proposed by Brown and Scholz (1986). These three models are widely applied to either mated or unmated rock joints. However, the irreversible damage of the asperities during deformation is not considered in these models. On the other hand, the normal stiffness by Yoshinaka and Yamabe (1986) is an exponential function.

In investigating the shear behavior of rock joints, joint samples can be sheared under either a constant normal stress or a constant normal stiffness. The former represents the pure behavior of an unconfined joint, while the latter represents a joint confined by the surrounding rock. Under a normal stiffness constraint, an apparent peak shear stress may occur only when normal stiffness K_n is equal to 0, which is equivalent to an initial normal stress condition. Stephansson and Jing (1995) explained that the true stiffness of a rock mass is of a finite value ranging from very low, near a free surface, to very high, when confined at a great depth. Representative research works on direct shear under a constant normal stress include Barton (1976) and Bandis, et al. (1981), while representative research works on direct shear under a constant normal stiffness include Obert, et al. (1976), Leichniz (1985), Skinas, et al. (1990), and Wibiwo, et al. (1992).

In the shear strength of rock joints, two types of models were proposed. Patton (1966) proposed the shear strength of rock joints in consideration of regular unevenness whose average angle is *i*. In Patton's model, the shear strength is controlled by the friction of the contact face and the asperity angle under a lower normal stress condition. On the other hand, under a higher normal stress condition, the shear strength is affected by the low friction including the cohesion. Patton proposed the property of shear strength using a bi-linear model. Based on Patton's model, Ladanyi and Archambault (1970) described the shear strength. They believed that the dilation occurred because of the asperities and the progressive failure of the asperities. In consideration of the residual component of the friction angle, the material strength upon shearing the asperities, and the dilatancy angles at the peak shear strength, Barton (1971) presented the shear behavior of rock joints. After carrying out many direct shear tests on rock joints, Barton (1973) proposed an empirical equation. In this equation, in particular, Barton introduced two parameters, namely, the joint wall compressive strength (*JCS*) and the joint roughness coefficient (*JRC*). Barton and Choubey (1977) presented the representative shapes of joint surface roughness and their *JRC* values so as to estimate *JRC*. However, it is important to remember that *JRC* is determined by a back analysis after performing the direct shear tests. Barton and Bandis (1980 and 1990), Bandis (1990), and Barton (1990) investigated the scale effect of *JRC* and *JCS*.

Barton's *JRC* (Barton, 1973; Barton and Choubey, 1977) is too famous to estimate the joint surface roughness quantitatively. However, there is no method for determining *JRC* except for a back analysis. Tse and Cruden (1979) proposed eight parameters, which determined the uneven function along one scan line of a rock joint. In particular, two parameters, namely, Z_2 and *SF*, were used to describe the relation of *JRC* using Barton and Choubey representative roughness models (1977). And, Swan (1983) and then Swan and Zongqi (1985) discussed the relationship between the mechanical properties and the unevenness of joint surfaces by applying the tribology method.

Geophysical tomography is an imaging technique for underground structures using certain physical parameters. The word "geotomography" was first used in 1979 (Dines and Lylte, 1979). The pioneers of geophysical tomography were Bois, et al. (1971) who presented the original principle of the reconstruction of a velocity distribution. In the 1980s, doing research on geotomography became popular. Pino and Nur (1985) proposed a reconstruction method for velocity distributions in consideration of not only traveltime but also the arriving direction of seismic waves. And, Pihl, et al. (1985) tried a three-dimensional analysis. Ishii (1986) and Matsuoka (1986) described it as an inversion of the theoretical and numerical points of view. On the other hand, Rokugawa (1986) and Ohtomo (1986) described it as geotomography. In particular, Ohtomo (1986) presented the theoretical background of geotomography, carried out numerical simulations using certain types of numerical models, and showed the capacity of geotomography. Sassa (1990) showed the need for applying geotomography to rock engineering, and presented applied samples of geotomography to jointed rock masses. In particular, Sassa not only proposed seismic velocity geotomography, but also seismic attenuation geotomography.

1.3 Content of this thesis

The purpose of the present research work is to observe the joint distribution of a jointed rock mass and to determine the mechanical properties of the mass's rock joints through field measurements and laboratory tests. The outline of each chapter is described as follows:

1) In Chapter 2, joint investigations in the field, such as a borehole wall survey and joint mapping, are carried out. In particular, the borehole wall survey using the borehole scanner system (*BSS*) is performed and joint orientation, apertures, and locations are determined through the observed data. Based on joint data, an analysis is carried out, and the characterization of joint distributions are clarified.
2) In Chapter 3, a measurement system for natural joint surface roughness is set up using a non-contact laser scan micrometer. Applying a spectral analysis, the determination method for natural joint surface roughness is established. In applying it to certain

spectral analyses, namely, the fast Fourier transform (*FFT*) and the maximum entropy method (*MEM*), the validity of the established method is confirmed.

3) In Chapter 4, direct shear tests are carried out on rock joints and the shear behavior of the rock joints is discussed. When discussing the shear behavior of rock joints, the influence of joint surface roughness, normal confining conditions, and the material strength are considered. Applying the roughness parameter described in Chapter 3, the validity of the parameter is confirmed and the constitutive models for the shear behavior of the rock joints are built in consideration of joint surface roughness, material strength, and normal confining conditions.
4) In Chapter 5, seismic propagating experiments are carried out using rock specimens which include natural and artificial joints. Changes in propagating seismic waves (velocity and amplitude) through several types of rock joints are investigated, and the influence of the rock joints on the seismic waves is clarified. The knowledge gained in this chapter is applied to a discussion on the results of geotomography.
5) In Chapter 6, the development of seismic geotomography and its application to a jointed rock mass are carried out. First of all, an algorithm for the geotomographic analysis is developed and then confirmed through a numerical simulation. In particular, both seismic velocity and seismic attenuation geotomographic techniques are developed. The capacity of the geotomographic technique is confirmed through numerical simulations in consideration of the locations of both source and receiver points and the size and the location of the lower velocity zone. Based on the numerical simulations, the geotomographic technique is applied to the field data. When discussing the results of the field data, the knowledge in Chapter 5 is applied and a new concept of rock classification is proposed.
6) In Chapter 7, borehole loading tests are conducted and the mechanical properties of a jointed rock mass are discussed. In particular, the main point aims at a permanent deformation of the load - displacement relation, and the physical meaning of a permanent deformation is considered. On the other hand, based on the laboratory modeling tests, the joint stiffness is determined through the load - displacement curves in consideration of joint distributions in the loading point.

Figure 1.1 shows the flow of the research work. In the present thesis, several types of field measurements and laboratory experiments are conducted. In the construction and the design of rock structures in jointed rock masses, joint distributions and joint properties must be known. Since the mechanical behavior of a jointed rock mass is very complex, it is thought that certain field measurements and laboratory experiments must be applied.

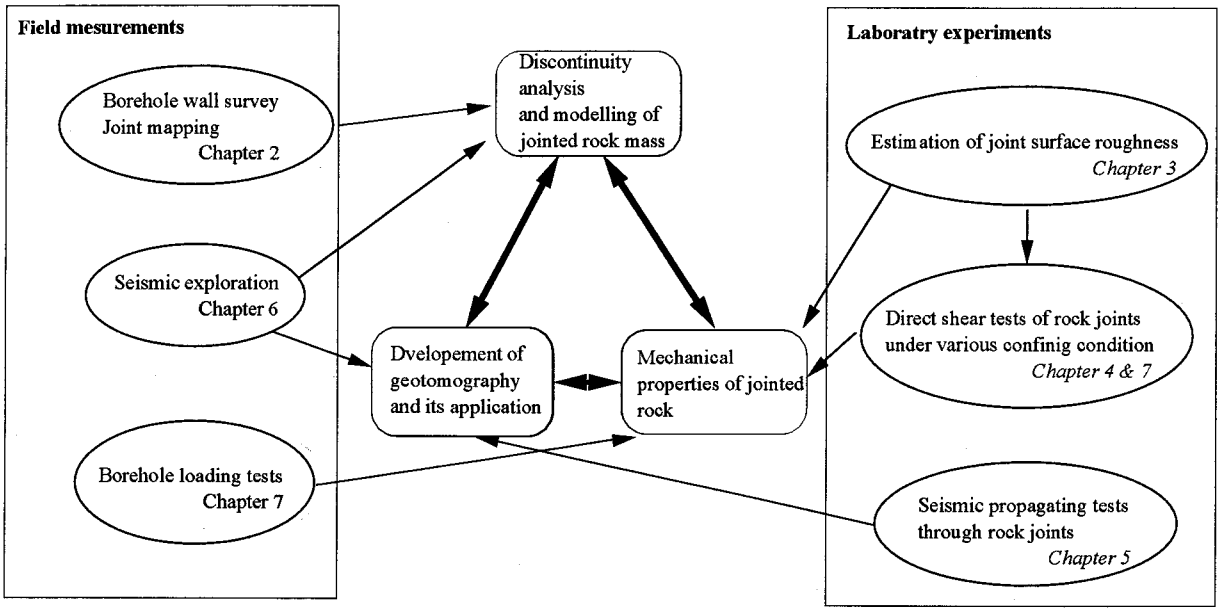

Figure 1.1 Schematic view of content of the research

REFERENCES

Attewell, P. B. and Farmer, I. W. (1976) : *Principles of Engineering Geology*, Chapman & Hall, London.

Baecher, G. B. and Lanney, N. A. (1978) : Trace length biases in joint surveys, *Proceedings of 19th U. S. Symposium on Rock Mechanics*, Vol. 1, pp. 56 - 65.

Bailey, A. I. (1975) : A method of analyzing polymodal distributions in orientation data, *Journal of Mathematical Geology*, Vol. 7, pp. 285 - 293.

Bandis, S. C. (1980) : *Experimental studies of scale effects on shear strength and deformation of rock joints*, Ph. D. thesis, University of Leeds, UK.

Bandis, S. C. (1990) : Mechanical properties of rock joints, *Rock Joints*, Barton & Stephansson (eds.), Balkema, pp. 125 - 140.

Bandis, S. C., Lumsden, A. C. and Barton, N. (1981) : Fundamentals of rock joint deformation, *International Journal of Rock Mechanics and Mining Science and Geomechanics Abstracts*, Vol. 20, No. 6, pp. 249 - 268.

Barton, N. (1971) : A relationship between joint roughness and joint shear strength, *Proceedings of International Symposium on Rock Mechanics*, ISRM, pp. 1 - 8.

Barton, N. (1973) : Review of a new shear strength criterion for rock joints, *Engineering Geology*, Vol. 7, pp. 287 - 332.

Barton, N. (1976) : Rock Mechanics Review: The shear strength of rock and rock joints, *International Journal of Rock Mechanics and Mining Science and Geomechanics Abstracts*, Vol. 13, pp. 255 - 279.

Barton, N. (1990) : Scale effects or sampling bias ?, *Scale Effect in Rock Masses*, Pinto da Cunha (ed.), Balkema, pp. 31 - 35.

Barton, N. and Bandis, S. C. (1980) : Some effects of scale on the shear strength of joints, *International Journal of Rock Mechanics and Mining Science and Geomechanics Abstracts*, Vol. 17, pp. 69 - 73.

Barton, N. and Bandis, S. C. (1990) : Review of predictive capabilities of JRC - JCS model in engineering practice, *Rock Joints*, Barton & Stephansson (eds.), Balkema, pp. 603 - 610.

Barton, N. and Choubey, V. (1977) : The shear strength of rock joints in theory and practice, *Rock Mechanics*, Vol. 10, pp. 1 - 65.

Bois, P., La Porte, M., Lavergne, M. and Thomas, G. (1971) : Essai de détermination automatique des vitesses sismiques par mesures entre puits, *Geophysical Prospecting*, Vol. 19, pp. 42 - 83.

Brady, B. H. G. and Brown, E. T. (1985) : *Rock Mechanics for Underground Mining*, George Allen & Unwin, London.

Bridges, M. C. (1990) : Identification and characterization of sets of fractures and faults in rock, *Proceedings of International Symposium on Rock Joints*, Loen, Norway, N. Barton and O. Stephansson (eds), Balkema, pp.19 - 26.

Brown, S. R. and Scholz, C. H. (1988) : Normal joints in rock: mechanical, hydraulic and seismic behaviour and properties under normal stress, First Jaeger Memorial Lecture, *29th U. S. Symposium on Rock Mechanics.*

Cawsey, D. C. (1977) : The measurement of fracture patterns in the Chalk of Southern England, *Engineering Geology*, Vol. 11, pp. 210 - 215.

Cundall, P. A. (1971) : A computer model for simulating progressive, large-scale movements in blocky rock systems, *Proceeding of the ISRM International Symposium*, Nancy, pp. 129 - 136.

Cundall, P. A. (1987) : Distinct element models of rock and rock structure, *Analytical and computational methods in engineering rock mechanics*, E. T. Brown (ed), Allen & Unwin, pp. 129 - 163.

Deere, D. U. (1964) : Technical description of rock cores for engineering purposes, *Rock Mechanics and Rock Engineering*, Vol. 1, pp. 17 - 22.

Dershowitz, W., et al. (1989) : Fracture flow code cross-verification plan, *Stripa Project TR*, 88-02, p. 64.

Desai, C. S., Zaman, M. M., Lightner, J. G. and Siriwardane, H. J. : Thin-layer element for interfaces, and joints, *International Journal of Numerical and Analytical Methods in Geomechanics*, Vol. 8, No. 1, pp. 19 - 43.

Dines, K. A. and Lylte, R. J. (1979) : Computerized geophysical tomography, *Proceedings of IEEE*, Vol. 67, pp. 1065 - 1073.

Duncan, A. C. (1981) : A review of Cartesian coordinate construction from a sphere, for generation of two-dimensional geological net projections, Computers and Geosciences, Vol. 7, No. 4, pp. 367 - 385.

Einstein, H. H. and Baecher, G. B. (1983) : Probabilistic and statistical methods in engineering geology, specific methods and examples, part 1: exploration, *Rock Mechanics and Rock Engineering*, Vol. 16, pp. 39 - 72.

Fisher, N. I., Lewis, T. E. and Embleton, B. J. J. (1987) : Statistical Analysis of Spherical Data, *Cambridge University Press.*

Flinn, D. (1958) : On tests of significance of preferred orientation in three-dimensional fabric diagrams, *Journal of Geology*, Vol. 66, pp. 526 - 539.

Fookes, P. G. and Denness, B. (1969) : Observational studies on fissure patterns in Cretaceous sediments of South-East England, *Geotechnique*, Vol. 19, No. 4, pp. 453 - 477.

Geological Society (1970) : The logging of rock cores for engineering purposes, Geological Society Engineering Group Working Party Report, *Quarterly Journal of Engineering Geology*, Vol. 3, pp. 1 - 24.

Goodman, R. E. (1976) : *Methods of Geological Engineering in Discontinuous Rocks*, West Publishing Company, St. Paul, pp. 112 - 121.

Goodman, R. E., Taylor, R. L. and Brekke, T. L. (1968) : A model for the mechanics of jointed rocks, *Proceedings of American Society of Civil Engineer*, SM4, Vol. 98, pp. 399 - 422.

Heuze, F. E. and Barbour, T. G. (1982) : New model for rock joints and interfaces, *Proceedings of American Society of Civil Engineer*, GT5, Vol. 108, pp. 757 - 776.

Hoek, E. and Bray, J. W. (1977) : *Rock Slope Engineering*, 2nd ed. Institution of Mining and Metallurgy, London.

Hoek, E. and Brown, E. T. (1980) : *Underground Excavations in Rock*, Institution of Mining and Metallurgy, London.

Ishii, Y. (1986) : Inversion - it's theoretical concepts and background, *BUTURI-TANSA (Geophysical Exploration)*, Vol. 39, No. 6, pp. 3 - 13. (in Japanese)

ISRM Commission on Standardization of Laboratory and Field Tests (1978) : Suggested Methods for the Quantitative Description of Discontinuities in Rock Masses, *International Journal of Rock Mechanics and Mining Sciences & Geomechanics Abstracts*, Vol. 15, No. 6, pp. 319 - 368.

Kalkani, E. C. and von Frese, R. R. B. (1979) : An efficient construction of equal area fabric diagrams, *Computer and Geosciences*, Vol. 5, No. 3/4, pp. 301 - 311.

Kamb, W. B. (1959) : Ice petrofabric observations from Blue Glacier, Washington, in relation to theory and experiment, *Journal of Geophysical Research*, Vol. 64, pp. 1891 - 1909.

Kamewada, S., Gi, H. S., Taniguchi, S. and Yoneda, H. (1990) : Application of borehole image processing system to survey of tunnel, *Proceedings of the International Symposium on Rock Joints, Loen, Norway*, N. Barton & O. Stephansson (eds), Balkema, pp. 51 - 58.

Kawai, T. and Toi, Y. (1977) : A new element in discrete analysis of plane strain problems, *Journal of Seisan Kenkyu*, Institute of Industrial Science, University of Tokyo, Vol. 29, No. 4, pp. 204 - 207.

Kawamoto, T., Ichikawa, Y. and Hirano, T. (1982) : Limit analysis of seismic ground motion by a rigid body-spring model, *Proceeding of 4th International Conference on Numerical Methods in Geomechanics*, pp. 383 - 391.

Kawamoto, T., Ichikawa, Y. and Kyoya, T. (1988) : Deformation and fracturing behaviour of discontinuous rock mass and damage mechanics theory, *International Journal of Numerical and Analytical Methods in Geomechanics*, Vol. 12, No. 1, pp. 1 - 30.

Kimuchi, K., Saito, K., Inoue, D. and Kanaori, Y. (1978) : Quantitative estimation and analysis of property of joint distribution in a basement rock, *Proceedings of the 10th Symposium on Rock Mechanics*, Committee on Rock Mechanics J.S.C.E., pp. 11 - 15 (in Japanese).

Kulatilahe, P. H. S., Wathugala, D. N. and Stephansson, O. (1990) : Three dimensional stochastic joint geometry modelling including a verification: a case study, *Proceedings of the International Symposium on Rock Joints, Loen, Norway*, N. Barton & O. Stephansson (eds), Balkema, pp. 67 - 74.

Kyoya., T., Ichikawa, Y. and Kawamoto, T. (1985) : An application of damage tensor for estimating mechanical properties of rock mass, *Proceedings of the Japan Society of Civil Engineers*, No. 358/III-3, pp. 27 - 35. (in Japanese)

Ladanyi, B. and Archambault, G. (1970) : Simulation of shear behaviour of jointed rock masses, *Proceedings of 11th U.S. Symposium on Rock Mechanics*, pp. 105 - 125.

Leichniz, W. (1985) : Mechanical properties of rock joints, *International Journal of Rock Mechanics and Mining Science and Geomechanics Abstracts*, Vol. 22, No. 5, pp. 313 - 321.

Long, J. S. C., Gilmour, P. and Witherspoon, P. A. (1985) : A model for steady fluid flow in random three-dimensional networks of disc-shaped fractures, *Water Resources Research*, Vol. 21, No. 8, pp. 1105 - 1115.

Lorig, L. J., Brady, B. H. G. and Cundall, P. A. (1986) : Hybrid distinct element-boundary element analysis of jointed rock, International Journal of Rock Mechanics and Mining Science & Geomechanics Abstracts, Vol. 23, No. 4, pp. 303 - 312.

Mahtab, M. A., Bolstad, D. D., Alldredge, J. R. and Shanley, R. J. (1972) : Analysis of fracture orientations for input to structural models of discontinuous rock, *Report of Investigations 7669 U. S. Dept. of the Interior, Bureau of Mines.*

Mahtab, M. A. and Yegulalp, T. M. (1982) : A rejection criterion for definition of clusters in orientation data, *In Issues in Rock Mechanics, Proceedings of the 22nd Symposium on Rock Mechanics*, Berkeley, R. E. Goodman and F. E. Heuze (eds), American Institute of Mining Metallurgy and Petroleum, Engineers, New York, pp. 116 - 123.

Matsuoka, T. (1986) : Numerical analysis in inversion theory - application of least squares methods, *BUTURI-TANSA (Geophysical Exploration)*, Vol. 39, No. 6, pp. 14 - 30. (in Japanese)

Murai, S., et al. (1988) : Development of Borehole Scanner for underground geological survey, *Proc. of 16th Congress of Int'l Society for Photogrammetry & Remote Sensing*, Vol. 27, Part B7, Commission VII, pp. 391 - 395.

Nago, D. and Scodelis, A. C. (1967) : Finite element analysis of reinforced concrete beames, *ACI Journal*, pp. 152 - 163.

Obert, L., Brady, B. T. and Schmechel, F. W. (1976) : The effect of normal stiffness on the shear resistance of rock, *Rock Mechanics and Rock Engineering*, Vol. 8, pp. 57 - 72.

Oda, M. (1982) : Fabric tensor for discontinuous geological materials, *Soil and Foundations*, Vol. 22, pp. 96 - 108.

Oda, M. (1985a) : Permeability tensor for discontinuous rock masses, *Géotechnique*, Vol. 35, pp. 483 - 495.

Oda, M. (1985b) : A theory for coupled stress and fluid flow analysis in jointed rock masses, *Research Report of Department of Foundation Engineering and Construction Engineering, Saitama University*, Vol. 15, pp. 1 - 22.

Ohnishi, Y. and Nakagawa, S. (1993) : A method for grouping and probabilistic modelling of joint orientations, *Proceedings of the Japan Society of Civil Engineers*, No. 463/III-22, pp. 173 - 176. (in Japanese)

Ohtomo, H. (1986) : Present technical situation of geophysical tomography, *BUTURI-TANSA (Geophysical Exploration)*, Vol. 39, No. 6, pp. 58 - 71. (in Japanese)

Patton, F. D. (1966) : Multiple modes of shear failure in rock, *Proceedings of 1st International Congress of ISRM*, Vol. 1, I pp. 509 - 513.

Phillips, F. C. (1971) : *The Use of Stereographic Projection in Structural Geology*, 3rd edition, Edward Arbold, London.

Pihl, J., Gustavsson, M., Ivansson, S. and Morén, P. (1985) : Tomographic analysis of crosshole seismic measurements, *Proceedings of Symposium on In Situ Experiment in Granite Associated with the Disposal of Radioactive Waste.*

Pino, E. D. and Nur, A. (1985) : Seismic wave polarization applied to geophysical tomography, *Exp. Asbtr., 55th SEG Annual Meeting*, pp. 620 - 622.

Priest, S. D. (1985) : *Hemispherical Projection Methods in Rock Mechanics*, George Allen and Unwin, London.

Priest, S. D. and Hudson, J. A. (1981) : Estimation of discontinuity spacing and trace length using scanline surveys, *International Journal of Rock Mechanics and Mining Science and Geomechanics Abstracts*, Vol. 18, pp. 183 - 197.

Rokugawa, S. (1986) : Geotomography - Theoretical Background -, *BUTURI-TANSA (Geophysical Exploration)*, Vol. 39, No. 6, pp. 51 - 57. (in Japanese)

Rosengren, K. J. (1970) : Diamond drilling for structural purposes at Mount Isa, *Industrial Diamond Review*, Vol. 30, No. 359, pp. 388 - 395.

Rouleau, A. and Gale, J. E. (1985) : Statistical characterization of the fracture system in the Stripa Granite, Sweden, *International Journal of Rock Mechanics and Mining Science and Geomechanics Abstracts*, Vol. 22, No. 6, pp. 353 - 367.

Sassa, K. (1990) : Applications of Geotomography to Rock Engineering, *Proceedings of SEGJ International Symposium on Geotomography*, SEGJ, pp. 21 - 28.

Shaneley, R. J. and Mahtab, M. A. (1976) : Delineation and analysis of clusters in orientation data, *Journal of Mathematical Geology*, Vol. 8, No. 3, pp. 9 - 23.

Shi, G. H. (1990) : Forward and backward discontinuous deformation analysis, *Proceedings of International Symposium on Rock Joints*, Loen, Norway, N. Barton and O. Stephansson (eds), Balkema, pp. 731 - 743.

Shi, G. H. and Goodman, R. E. (1985) : Two dimensional discontinuous deformation analysis, *International Journal of Numerical and Analytical Methods in Geomechanics*, Vol. 9, pp. 541 - 556.

Skinas, C. A., Bandis, S. C. and Demiris, C. A. (1990) : Experimental investigations and modelling of rock joint behaviour under constant stiffness, *Rock Joints*, Barton & Stephansson (eds.), Balkema, pp. 301 - 308.

Snow, D. T. (1965) : A parallel plate model of fractured permeable media, *Ph. D. Thesis of University of California, Berkeley.*

Stauffer, M. R. (1966) : An empirical-statistical study of three-dimensional fabric diagrams as used in structural analysis, *Canadian Journal of Earth Sciences*, Vol. 3, pp. 473 - 498.

Stephansson, O. and Jing, L. (1995) : Testing and modeling of rock joints, *Mechanics of Jointed and Faulted Rock*, Rossmanith (ed.), Balkema, pp. 37 - 47.

Swan, G. (1983) : Determination of stiffness and other joint properties from roughness measurements, *Rock Mechanics and Rock Engineering*, Vol. 16, pp. 16 - 38.

Swan. G. and Zongqi, S. (1985) : Prediction of shear behaviour of joints using profiles, *Rock Mechanics and Rock Engineering*, Vol. 18, pp. 183 - 212.

Tanimoto, C., Murai, S., Matsumoto, T., Kishida, K. and Ando, T. (1992) : Immediate image and its analysis of fractured/jointed rock mass through the borehole scanner, *Fractured and Jointed Rock Masses*, Myer, Tsang, Cook & Goodman (eds), Balkema, published in 1995, pp. 219 - 228.

Tse, R. and Cruden, D. M. (1979) : Estimating joint roughness coefficients, *International Journal of Rock Mechanics and Mining Science and Geomechanics Abstracts*, Vol. 16, pp. 303 - 307.

Wibowo, J. T., Amadei, B., Sture, S., Robertson, A. B. and Price, R. (1995) : Shear response of a rock joint under different boundary conditions: An experimental study, *Fractured and Jointed Rock Masses*, Myer, Cook, Goodman & Tsang (eds.), Balkema, pp. 425 - 430.

Yoshinaka, R. and Yamabe, T. (1986) : Joint stiffness and the deformation behaviour of discontinuous rock, *International Journal of Rock Mechanics and Mining Science and Geomechanics Abstracts*, Vol. 23, No. 1, pp. 19 - 28.

Zienkiewicz, O. C., Best, B., Dullage, C., and Stagg, K. G. (1970) : Analysis of nonlinear problem in rock mechanics with paticular reference to jointed rock systems, Proceedings of 2nd ISRM International Congress, Beograd, Vol. 3, pp. 501 - 509.

Chapter 2

Joint Survey and Joint Analysis

2.1 Introduction

In the design and the construction of rock structures, such as underground caverns, tunnels, and the foundations of dams and bridges, it is very important to grasp the geological conditions and the history of the geology. In the case of a jointed rock mass, it is necessary to grasp not only the geology but also the character and the distribution of the rock joints. This is because both the character and the distribution of the rock joints strongly affect the mechanical behavior and the hydromechanical behavior of the rock mass. However, neither type of rock mass behavior can be explained merely by clarifying the character of the intact rock.

In this chapter, an outline of the geology of an objective area will be described. A survey and an analysis of the rock joints will then be shown, using the borehole scanner system (*BSS*), and a mechanical model for the jointed rock mass will be determined.

2.2 Geology of the objective area

The underground opening of a hydroelectric powerhouse, in the central part of Honshu Island, Japan, is situated 70 *m* beneath the top of a mountain on the right-hand bank of the Kiso River. The river flows through a steep valley. As for the geology, this site is located in the northern part of the Late Cretaceous Cauldron Movement area. The surface of the mountain consists of Cenozoic Neogene Pliocene sediment and Quaternary Diluvium sediment.

The geological classification in this area is an igneous rock group in the Mino zone. The volcanic rock in this Mino zone, from the Mesozoic and Paleozoic Eras, consists of Nouhi-rhyolite and granite. Nouhi-rhyolite can be divided into six volcanic movement stages. **Table 2.1** shows the relationship between the six volcanic movement stages and the geological ages. The objective area is located at the southern edge of the Nouhi-rhyolite area and consists of Fujimidai-welded tuff which was classified by Stage Ia (Editional Committee of CHUBU II, 1988).

The basement rock is made up of granite porphyry, rhyolite, and slate. These types of rock contain many joints which dip at steep angles and have comparatively high joint frequencies and wide apertures. Slate comprised the basement rock before the occurrence of any volcanic activity,

Table 2.1 Volcanic movement stages of Nouhi-rhyolite and geologic times

Stage	Geologic time (Ma)
Ia	100 (?) ~ 90
Ib	100 (?) ~ 90
II	90 ~ 64
III	65 ~ 45
IV	45 ~ 35(?)
V	35 (?) ~ 25 (?)

and it is distributed unsystematically, which caused a volcanic collapse. It contains many irregular joints from hydrothermal metamorphism.

Figure 2.1 shows a topographical map of the objective area. This figure is described by the use of the digital data of contour lines on the map. In creating the digital data of contour lines, certain types of mesh-size data were applied to change the original data.

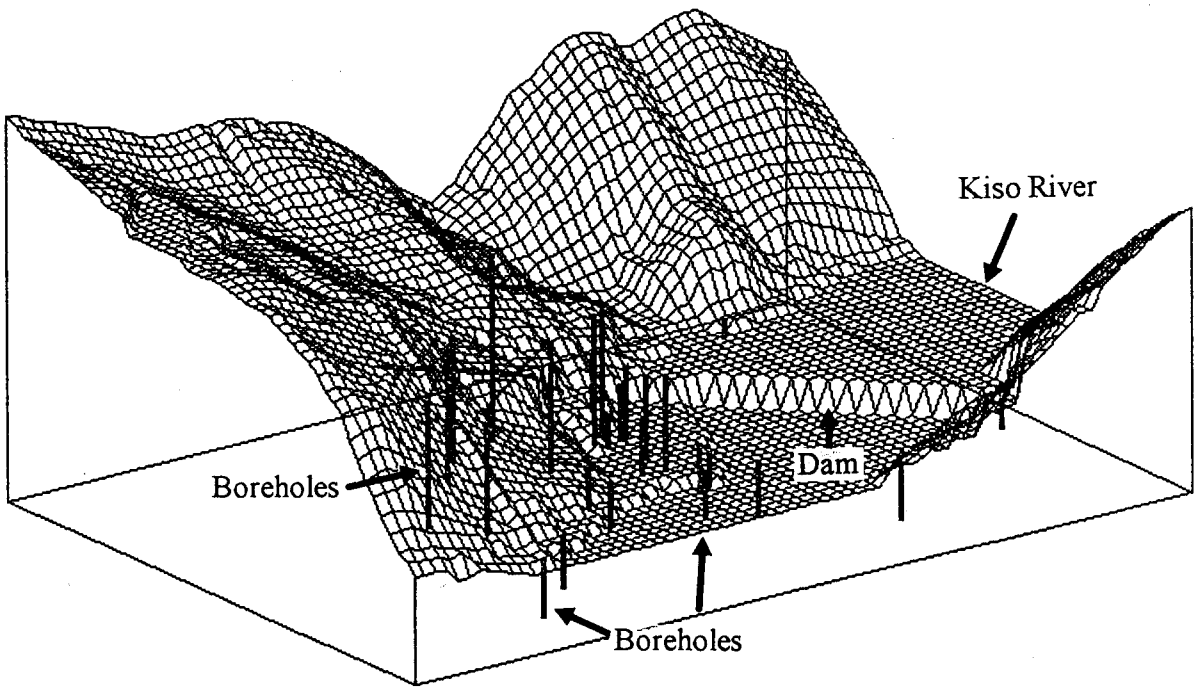

Figure 2.1 Topographical map of the objective area

2.3 Borehole scanner system (*BSS*)

All-round appraisals in the form of geological surveys were conducted prior to construction and they play an increasingly important role. Up to now, such surveys have consisted of collecting recovered core samples through boring. Although such methods allow investigators to look at the samples first hand, the accumulated core samples require extensive storage space and lengthy inspection time. And, such methods do not provide information on the sizes and the apertures of the cavities and the fissures or on the movable filling materials, which are all of vital importance to any site investigation.

To improve site investigations, the borehole scanner system (*BSS*) was invented as a system that can respond to today's needs for advanced geological surveys prior to construction.

2.3.1 Problems with *BTV* and the need for *BSS*

Up to the present time, the conventional method for investigating the geology and the fractures in rock has been to bore through the surface and to lower a *TV* camera (*BTV*) into the borehole to examine the borehole wall. However, the use of *BTV* is limited primarily because the *TV* camera must be rotated approximately 40 degrees for each shot at the same level of depth in order to obtain a full view of the wall. This results in excessive observation time as each photograph taken by *BTV* must be manually rearranged into a mosaic. In addition, the image quality is not uniform due to shading and illumination effects. Consequently, there has been a strong demand for the development of a new system that would improve the observation speed and provide continuous images of good quality.

Based on the same scanning concept as the remote sensing technique used for satellites, *BSS* has been developed to obtain immediate digital imagery of the full inner wall of a borehole (Murai, et al., 1988).

2.3.2 *BSS* units

BSS is composed of three units, namely, the scanner, the control, and the cable, as shown in **Photo 2.1**. The scanner consists of a light, a rotating mirror, an optical electronic converter with *R-G-B* channels, a compass, a data transmitter, and an amplifier. The scanner is carefully lowered into a borehole, 66-86 *mm* in diameter, and the mirror is quickly rotated 360 degrees around the borehole wall to collect the reflected light through the observational window, as shown in **Figure 2.2**. Data obtained by the scanner are transmitted to the surface control unit and then recorded on a video tape and a digital magnetic tape for reproduction on a monitor system for data processing.

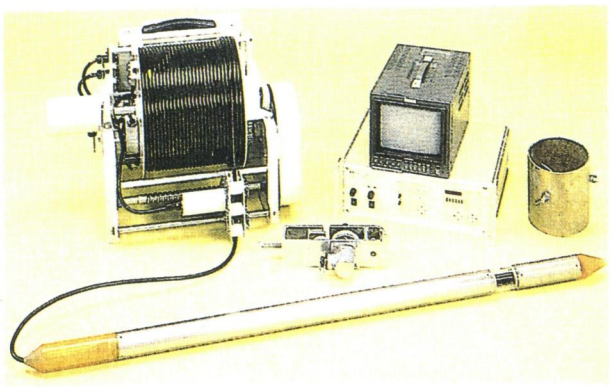

Photo 2.1 *BSS* (Borehole Scanner System)

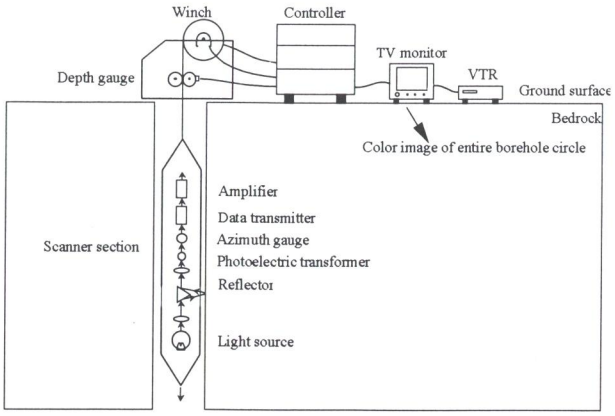

Figure 2.2 Set-up of the *BSS*

2.3.3 Performance of *BSS*

BSS is unique because of its real-time performance. As of yet, no similar system has been developed.

a) Continuous image through a rotating scanner

The scanner is lowered into the borehole while the reflector revolves at 3000 rpm. Concurrently, the reflector collects reflected light from the borehole wall as it makes its revolutions. The collected data are digitized and then sent to the controller on the surface to produce a continuous image.

Thus, *BSS* provides the first probe to realize a 360-degree continuous panoramic image of a borehole wall in real time. Its approach allows geological engineers to obtain a simultaneous grasp of the entire borehole surface at a glance, and since it provides a continuous image, geological appraisals and the quick measurement of fractures can now be completed with greatly improved efficiency. Moreover, since data are recorded on standard video tapes, it is now possible to leave the on-site observations to a professional operator and to allow engineering geologists the chance to conduct appraisals, measurements, and other analytical work at a time which is convenient for them.

b) Observation speed

Since *BSS* scans the borehole at a maximum speed of 120 *cm/min*, 72 *m* can be logged in an hour. This is thirty times faster than with *BTV*. The shorter operating time provides an increased data volume at a lower cost. The observation area is displayed at the site in real time, as a panoramic image on a monitor; therefore, the collection of data with *BSS* is also ideal for grouting and other operations where a quick grasp of the geological situation prior to moving on to other operations is crucial.

c) Image quality

BSS provides full-scale and continuous color images of the inner wall of a borehole, over 360 degrees in real time, which can be monitored on the surface. The image quality is uniform due to a constant angle of illumination. The image quality is high, even in turbid water, since it is a short distance between the rotating mirror and the inner wall and a resolution of 0.1 *mm* on the surface of the wall is provided.

The high 0.1 *mm* resolution permits the observation of fractures and fissures which have a width of 0.1 *mm* or more. The clear color images provide non-stop information on the direction and the inclination of fractures and fissures. This means that although the measuring is done without attention, *BSS* can be used to evaluate the fine image of fissures.

d) Recording method

A video tape recorder (*VTR*) and digital recordings are available. Since the *VTR* system utilizes commercially available video tapes, it is possible for geological analyses and evaluations to be conducted by geologists away from the site. The analyses can be done through continuously scanned images to be viewed in a scrolling manner.

Table 2.2 shows a comparison in performance between *BSS* and the *BTV* system. To summarize, *BSS* provides significant advantages in that continuous color images of the entire borehole wall can be obtained in digital form, while *BTV* produces only partial images in analog form. In addition, the speed of data acquisition with *BSS* is much higher (72 *m* per hour) than with *BTV* (1-2 *m* per hour), and a digital image analysis can be effectively applied to extract useful information on rock characteristics with higher resolution.

BSS is a direct, immediate, and clearly visual observation method used for obtaining details of the geology, the forming minerals, the joint orientation, the fracture system, the water content, the apertures, and the thermal variations along a given borehole. The figures listed in **Table 2.2** are based on past achievements. According to the principle of *BSS*, specifications related to resolution, observation speed, and borehole size can be changed without any significant difficulties.

2.3.4 Uses of *BSS*

BSS has been used in the following applications (Tanimoto, et al., 1992):

i) Geological surveys : joint mapping and orientation, thickness of formations, pre-existing cavities and particle-size distribution in dam foundations, tunnels, and underground openings

ii) Grouting effect : penetration of grouting material and contact in dam foundation and underground openings

Table 2.2 Comparison in perfomance between *BSS* and *BTV*

Item	Borehole scanner	Borehole TV
Filming method	Continuous 360° display	Intermittent 40° display
Display	Continuous color display	Partial color display
Observation speed	72 *m/h*	1 ~ 2 *m/h*
Analysis efficiency	10 ~ 50 *m/day*	1 ~ 2 *m/day*
Recording method	VTR and Digital	VTR
Resolution	0.1 *mm*	0.1 *mm*
Max. Observation depth	200 m	200 m
Borehole diameter requirement	66 ~ 86 *mm*	66 ~ 86 *mm*

iii) Water table and permeability : investigation of water tables, highly permeable layers, hydrothermal alternations, etc., at dam sites

iv) Loosening of rock masses : openings of apertures in dams, slopes, and tunnel sites

v) Rock tests and classifications : load bearing tests and the determination of rock classes at dam and tunnel sites

vi) Concrete structures : crack observation, backfilling and cavities behind concrete linings, and quality control of roller compacted dam (*RCD*) at dam and tunnel sites

2.3.5 Borehole survey using *BSS*

Figure 2.3 shows the location of five boreholes (*A*, *B*, *C*, *D*, and *E*, which are common name of boreholes in this thesis) and the geology of the cross section along Boreholes *A*, *B*, and *C* in the objective area. All five boreholes were 70 *m* in depth and were prepared for the investigation by a borehole survey and other field measurements, as shown in the following chapters.

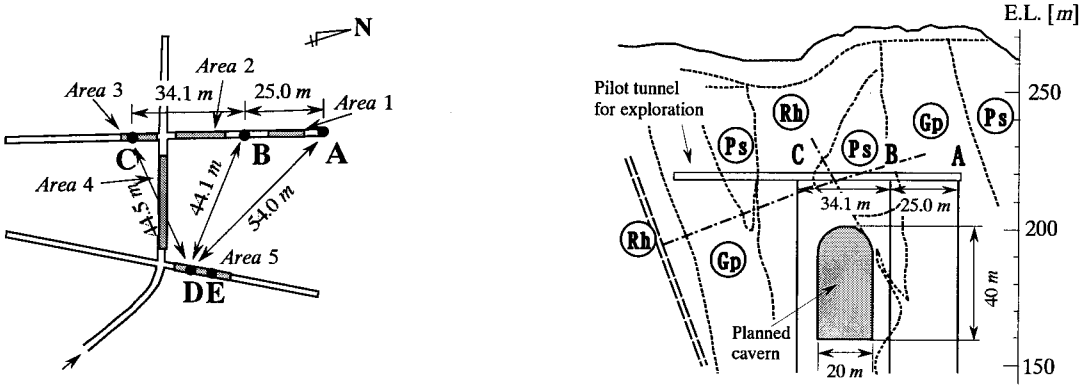

(a) Plane section
(*A*, *B*, *C*, *D*, & *E* : boreholes,
Area : joint mapping area)

(b) Profile (in *A*-*C* section)
(Ps : slate, Gp : granite porphyry, Rh : rhyolite,
A, *B*, & *C* : boreholes)

Figure 2.3 Location of boreholes and geology map

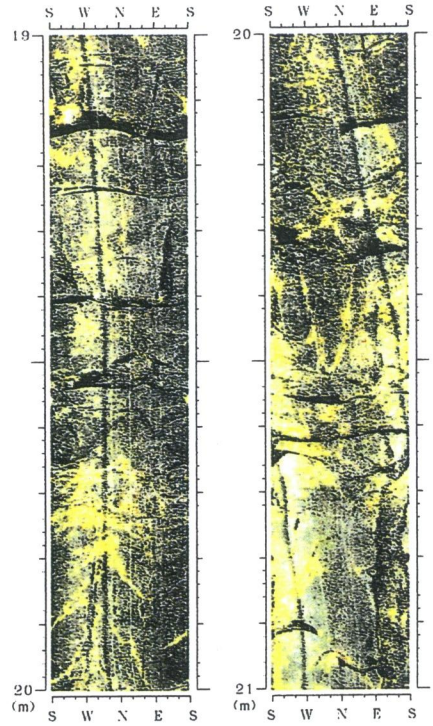

Photo 2.2 360 degrees continuous image through *BSS*
(Slate at the depth of 19 ~ 21 m below G. L.)

One of the results of the *BSS* survey is shown in **Photo 2.2**.

2.4 Measurement of the discontinuity characteristics

The *ISRM* Commission on the Standardization of Laboratory and Field Tests (1978) described and defined ten parameters which show the character of discontinuities and/or joints, namely, orientation, spacing, persistence, roughness, wall strength, apertures, filling, seepage, the number of sets, and block size. Orientation, roughness, apertures, and the existence of filling materials can be obtained from the *BSS* survey. In this section, the acquisition and the results of the orientation and the apertures from the *BSS* images are described.

2.4.1 Extraction of joint profiles

Image processing techniques are used to extract joint profiles from the *BSS* images as developed by Thapa (Thapa, 1994; Thapa, et al., 1995). The entire profile extraction process is done in four steps on a monochrome transform of the *BSS* images. The first step involves thresholding of original image $f(x,y)$ between two thresholds, T_1 and T_2, to produce binary image $g(x,y)$ such that

$$g(x,y) = \begin{cases} 255 \text{ if } T_1 < f(x,y) \leq T_2 \\ 0 \quad \text{otherwise} \end{cases} \tag{2-1}$$

In **Equation 2-1**, the coordinates (x,y) refer to the row and the column number of each pixel of the unrolled borehole wall image. Thresholds T_1 and T_2 are chosen so that in binary image $g(x,y)$, all pixels falling inside the joint aperture are white, while all pixels outside the aperture on the rock wall are black. To accomplish this segmentation, the selection of T_1 and T_2 has to be made so as to cover only the dark range of pixel intensities in the aperture region between opposing joint walls. T_1 and T_2 can be determined from a histogram of image intensities or by probing the image with a mouse on a screen display of the image. The value of T_1 can usually be set at zero. After obtaining binary image $g(x,y)$, the pixels on the roughness profile are isolated by detecting the discontinuity which separates the rock wall from the joint aperture region. No differential operators are needed to detect the discontinuity of the binary image. Instead, the roughness profile pixels are isolated owing to the fact that only pixels on the profile and pixels in the aperture region will have at least one white adjacent pixel in the binary image. The pixels on the profile and those in the aperture region can be further distinguished by the fact that the profile pixels in the binary image will be black, while the pixels in the aperture region will be white. Only the pixels on the rock wall qualify as points on the roughness profile. These rules are applied to binary image $g(x,y)$ to produce another binary image, $h(x,y)$, in which pixels on the roughness profile have an intensity of zero, while all other pixels have intensities of 255.

The next step involves a pixel connectivity routine to produce an *ASCII* file listing of consecutive roughness profile pixel image coordinates. The connectivity routine begins with the first pixel on the profile and searches for the next pixel on the profile until no further connected pixels can be found. The center pixel in the 3 x 3 pixel box in **Figure 2.4** is a pixel on the roughness profile, while the adjacent pixels are candidate consecutive profile points. The numbers

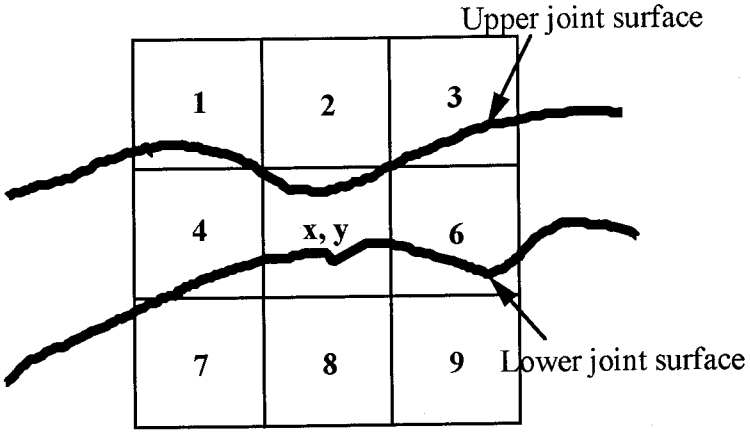

The search sequence for the upper profile is 2, 3, 6, 8, 9.
The search sequence for the lower profile is 8, 9, 6, 2, 3.

Figure 2.4 Pixel connectivity search sequences (Thapa, et al., 1995)

in the adjacent cells identify the cells. The search sequence for the upper profile is 2, 3, 6, 8, 9, while the search sequence for the lower profile is 8, 9, 6, 3, 2. The first adjacent pixel has an intensity of zero and is identified as the next profile point. That point then becomes the center pixel in **Figure 2.4** and the search is repeated.

The final step in the profile extraction procedure is a transformation of coordinates. The *ASCII* file produced by the connectivity routine contains profile points in the image (x,y) coordinates. A utility program is used to substitute the borehole coordinates of azimuth and depth for the image coordinates through a comparison with the original *BSS* images.

2.4.2 Measurement of the joint orientation

Techniques for extracting joint profiles were described in the previous section. These techniques can determine the joint surface roughness from the borehole survey (Thapa, 1994). On the other hand, one of the most important characteristics of joints is their orientation. A joint's orientation represents two parameters, namely, dip direction and dip angle. This section describes the determination of both dip direction and dip angle form the borehole survey.

Smoothing the extracted data from the joint profiles, a joint represents the sine curve in a 360-degree expansion, as shown in **Figure 2.5**. Then, the joint surface closely resembles that which is expressed in **Equation 2-2** as follows:

$$y = A\sin\left\{\frac{2}{l}(x - B)\right\} + C \qquad (2\text{-}2)$$

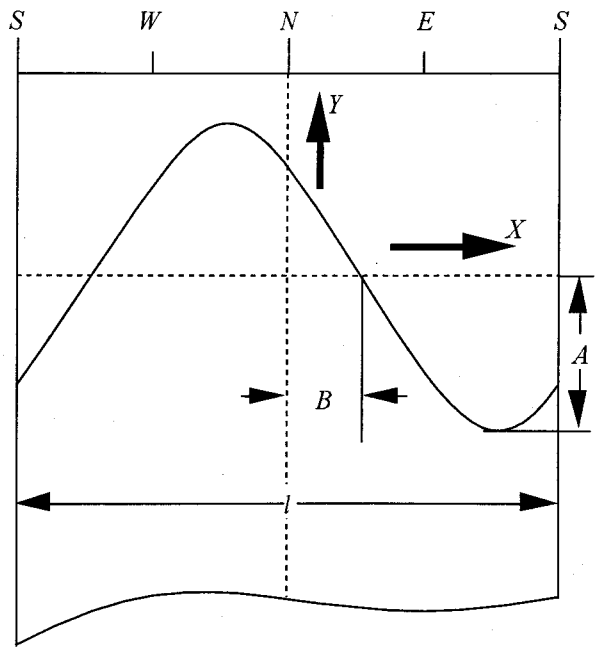

Joint appearing as a sine curve

Figure 2.5 Determination of joint orientation

where l : periphery of the borehole
A : amplitude of the sine curve ($A \geq 0$)
B : initial phase of the sine curve ($-\frac{2}{l} \leq B < \frac{2}{l}$)
C : depth (the distance from a datum line).

From this equation, the amplitude and the initial phase are determined. Then, both dip direction α ($0^\circ \leq \alpha < 360^\circ$) and dip angle β ($0^\circ \leq \beta < 90^\circ$) are calculated using **Equations 2-3** and **2-4** as follows:

$$\alpha = \begin{cases} (2\pi + \frac{2\pi B}{l}) \cdot \frac{360}{2\pi} & (-\frac{l}{2} \leq B < 0) \\ \frac{2\pi B}{l} \cdot \frac{360}{2\pi} & (0 < B < \frac{l}{2}) \end{cases} \tag{2-3}$$

$$\beta = \left\{ \tan^{-1}\left(\frac{2A}{d}\right) \right\} \cdot \frac{360}{2\pi} \quad . \tag{2-4}$$

2.4.3 Measurement of a joint aperture

In the next step, a joint aperture is calculated. **Figure 2.6** shows a joint on the vertical borehole. In this figure, joints and/or discontinuities comprise two smooth opposing joint walls with the same orientation. The true aperture of the joint is shown by vector $\vec{n}$ connecting the lower profile point o to its opposing point a. However, in the *BSS* profiles, vector $\vec{n}$ cannot be found since point a does not lie on the curve defined by the intersection of the borehole and the upper joint wall. Since the true aperture cannot be found, one of two alternative approaches may be taken to estimate $\vec{n}$. One approach involves the correction of an apparent aperture vector, such as $\vec{b}$, which is vertically parallel to the borehole axis, namely,

$$\|\vec{n}\| = \|\vec{b}\| \cos\theta \quad . \tag{2-5}$$

In this approach, θ is equal to dip angle β. This approach can easily estimate the true aperture after determining the dip direction and the dip angle.

The apparent aperture approach assumes that the upper joint wall is a smooth plane between points b and a, as shown **Figure 2.6**. This assumption contradicts the entire exercise of measuring roughness and apertures where deviations from a mean plane are being sought. The other approach to aperture measurement (Thapa, 1994) uses vector $\vec{n}_d$ to estimate $\vec{n}$. Point p on vector $\vec{n}_d$ is chosen so that error vector $\vec{e}$ is minimum along one or more segments of the profile.

This second approach, based on error minimization, was used to obtain the apertures for a joint shown in **Figure 2.7**. This may be the advantage of discussing an anisotropy analysis of joints.

In this thesis, apertures are used to estimate the average results from the second approach, and they use the analysis and the discussion which follow.

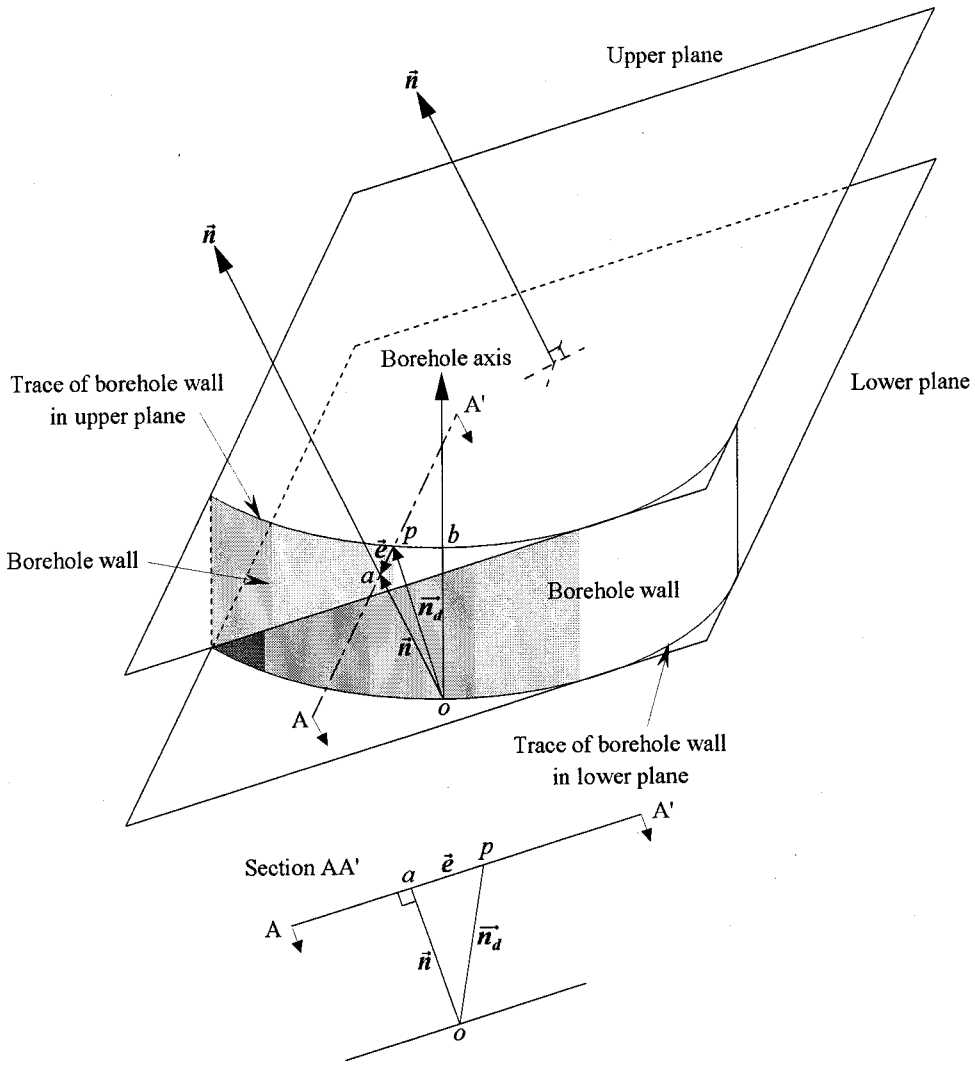

Figure 2.6 Aperture measurement error (Thapa, et al., 1995)

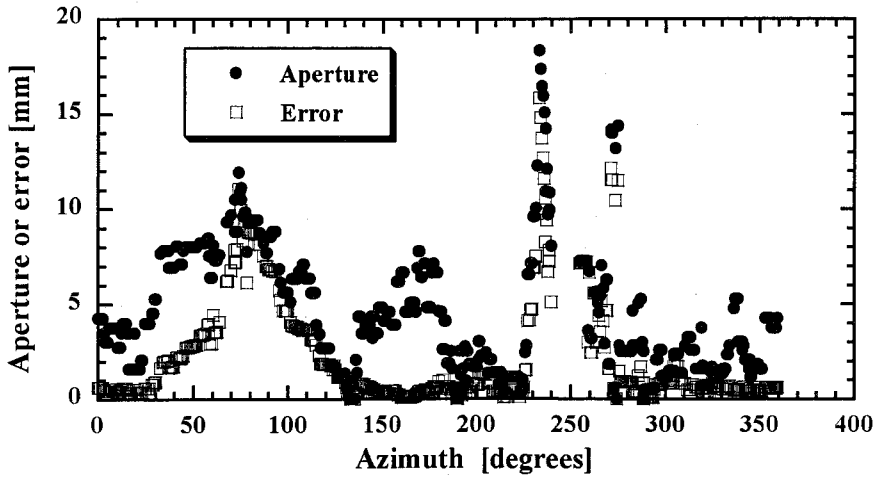

Figure 2.7 Aperture measurement errors for a joint

2.5 Comparison of the *BSS* analysis with the observation of core samples

Using an rock quality designation (*RQD*) parameter, the *BSS* analysis is compared with the borehole log and the core samples from a photo, and the correlation and the difference among the results are then discussed. *RQD* was devised by Deere (1964) and is defined as the percentage length of a given length of core consisting of intact rock. On the other hand, the photo of the core samples was taken from the recovered core samples in the core box. Since the photo shows a picture image of the results of *BSS*, the *BSS* image is compared with the photo of the core samples for the condition of the joints.

The length of the core samples used in calculating *RQD* is measured at the center scanline of the core samples (*ISRM*, 1978). In the case of the photo of the core samples, however, the length of the scanline is measured at the core sample surface since the photo presents just one side of the core samples. **Figure 2.8** shows the distribution of *RQD* determined by many kinds of tools through boreholes. In comparing *RQD*, it is confirmed through each method that *RQD* decreases in *BSS*. The difference in *RQD* between *BSS* and the photo is less than that between the borehole log and the photo. In comparing *RQD* at Boreholes *B* with *C*, where rhyolite can be found in most parts, it is discovered through every method that each *RQD* is equal. **Figures 2.9**(a), (b), and (c) show the relationship between *RQD* through the borehole log and *RQD* through the *BSS* image. From these figures, a tendency for *RQD* through *BSS* to be larger than that through the borehole log can be confirmed. This is because when core samples are extracted, commotion and loss occur, and these incidents contribute to the smaller value of *RQD* determined from the borehole log. Thus, joints must be found under different conditions. As compared to the photo of core samples with the detailed *BSS* image, each joint which can be found is in a one-to-one relation between the photo and the *BSS* image. As for the results, it is understood that joints which can only be found through the *BSS* image consist of only a small percentage of the total number of joints. The results are shown in **Table 2.3**. From this table, the difference in *RQD* is thought to have been caused by many joints being represented by only one photo image of the core samples. The main differences in *RQD* between the *BSS* image and the photo are described as follows:

i) Joints whose apertures are very close cannot be extracted.

ii) New joints are formed in the process of recovering core samples.

The latter causes the release of in-situ stress and/or vibrations in the making of boreholes and in the handing of core samples. These joints cannot be found naturally in rock masses. The need to create new joints can be prevented by improving the borehole drilling method and by taking care in the handing of the core samples.

The former expresses the fact that joints cannot be extracted from a picture image, since apertures are very close and picture images are not clear. These problems cause the need for field investigations and require research on the capacity of the scanning system and the techniques of

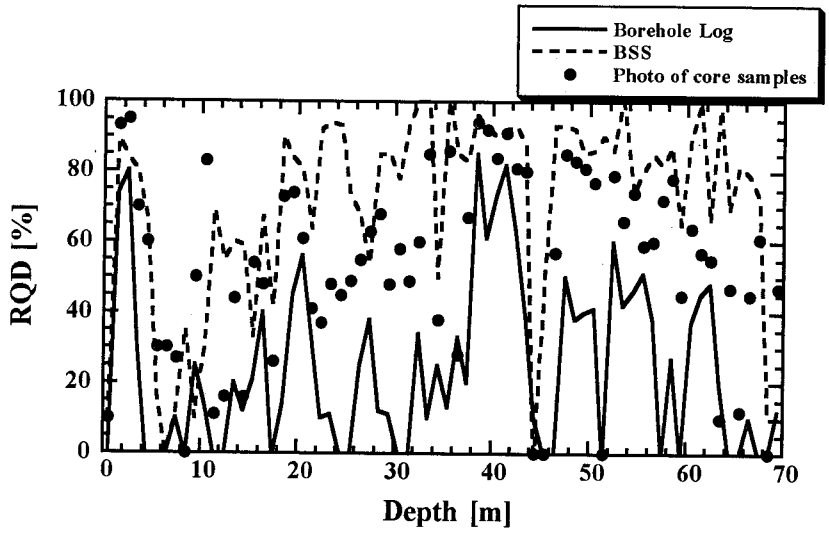

(a) Borehole *A*

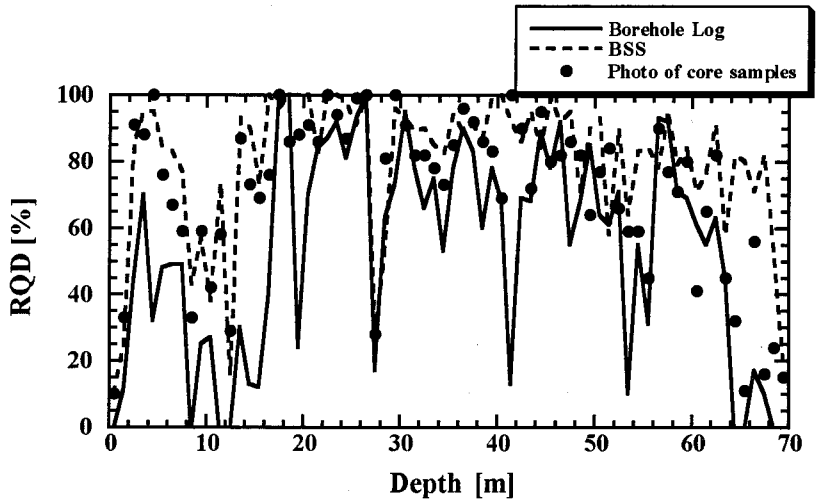

(b) Borehole *B*

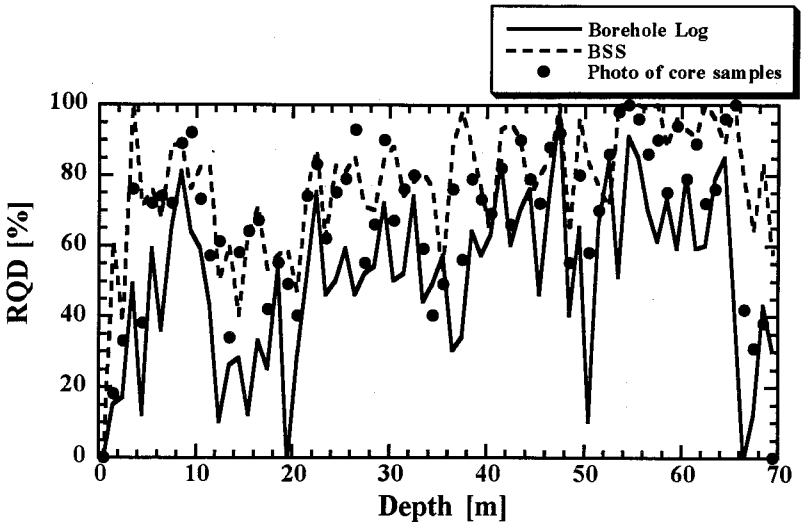

(c) Borehole *C*

Figure 2.8 The distribution of *RQD* determined by many kinds of tools through boreholes

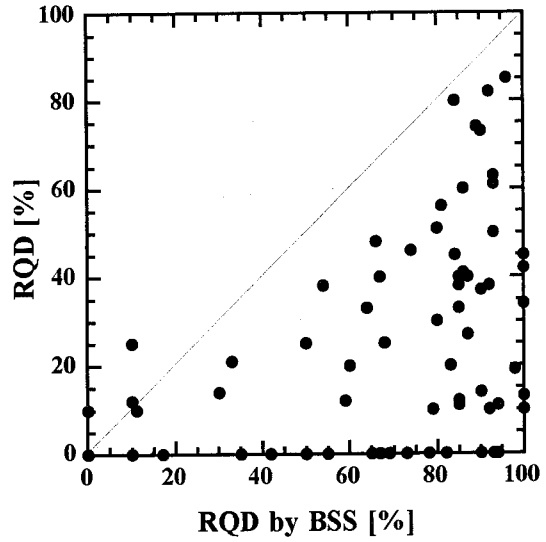

(a) Borehole *A*

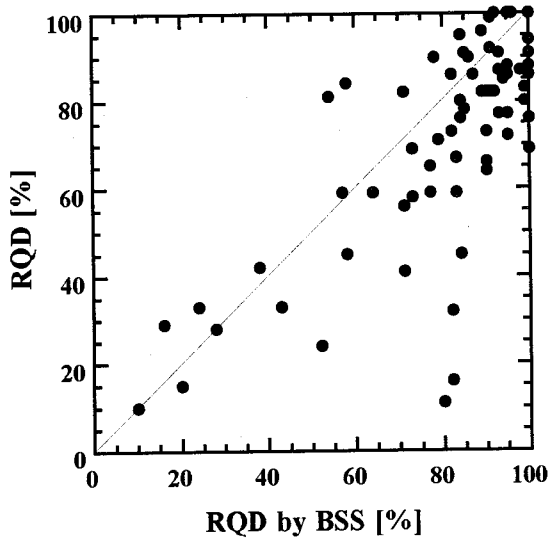

(b) Borehole *B*

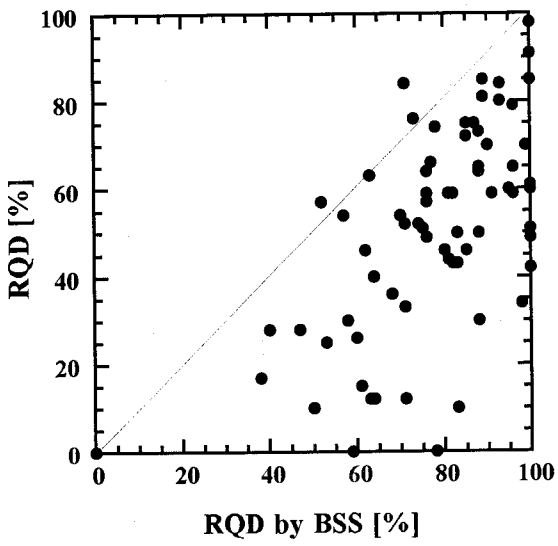

(c) Borehole *C*

Figure 2.9 The relationship between *RQD* through the borehole log and *RQD* through the *BSS* image

Table 2.3 The difference in the number of joints based on the measuring method

	Borehole *A*	Borehole *B*	Borehole *C*
Common number of joints through both the photo and *BSS*	395	354	413
The number of joints through only photo	184	120	155
The number of joints through only *BSS*	18	9	30

investigations and require research on the capacity of the scanning system and the techniques of the image analysis. As for the capacity of the scanning system, *BSS* is advantageous and can supply higher quality images than other borehole scanning methods, as stated above (Murai, et al., 1988; Tanimoto, et al., 1992). Thapa (1994) developed an image analysis which could be used comfortably and produce high-quality results without the influence of artificial errors. Therefore, it is thought that *BSS* images can sufficiently estimate in-situ joint conditions.

Considering the above-mentioned circumstances and the ability to grasp jointed rock masses, especially the estimation of parameter *RQD*, *BSS* images have more advantages than the investigation of core samples and other methods.

2.6 Bias errors in the joint survey

The joint frequency of observations at boreholes and/or rock surfaces represents the difference in the relation between the survey direction and the joint orientation. This is called a bias error, and Terzaghi explained that the impossibility of making adequate observations was an effect of the angle of intersection in observations of joint orientation (1965). In other words, the joint set, which presents a nearly uniform angle of the observed direction, can be more difficult to measure than other joint sets. Since the field measurements are carried out under many restrictions related to geometry, economics and so on, however, it is impossible to prevent bias errors. In order to reduce bias errors in the observed direction, the method, which is an improvement of Terzaghi's method, can be applied to the observation data on boreholes.

In the first step of this method, the weight value, W_i, is defined as follows:

i) θ_i formed where the normal line of the joint plane and the borehole intersect with each other.

ii) $w_i = \dfrac{1}{\cos \theta_i}$ is calculated of each joint.

iii) The weight value (0 ~ 1) of each joint is defined in **Equation 2-6** as follows:

$$W_i = \frac{w_i}{\sum w_i} \quad . \tag{2-6}$$

In this way, weight value W_i is used in the analysis of the joint orientations. The angle, θ_i, is defined by both the orientation of joints or joint sets and the scanning direction. When making the contoured lower hemisphere projection, the dip and the dip direction of the joints are plotted in the lower hemisphere and the plot points are afforded the weight values of the joints. In making the contoured lower hemisphere projection with the weight value, it can be described in consideration of the effect of bias errors of the orientation.

Next, the regular joint model shown in **Figure 2.10**(a) is considered. In the case of **Figure 2.10**(a), only one scanline can be determined for which a true joint frequency can be measured. That is, for measuring this scanline, the interval of the joints is equal to the so-called spacing of the joints (Grossmann, 1993). The relationship between joint frequency and angle θ_i, which consists of two lines, namely, the measuring scanline in the field and the scanline determined from the true joint frequency in the rock masses, can be described by the staircase function, as shown in **Figure 2.10**(b). This function closely resembles **Equation 2-7** as follows:

$$n = n_0 \cos \theta_i \tag{2-7}$$

where n is the joint frequency from the field measurements and n_0 is the true joint frequency in the rock masses. Therefore, the true joint frequency is given by **Equation 2-8**. By multiplying the measured joint frequency, n, by $1 / \cos \theta_i$, bias errors for the measuring direction can be reduced, namely,

$$n_0 = \frac{n}{\cos \theta_i} \quad . \tag{2-8}$$

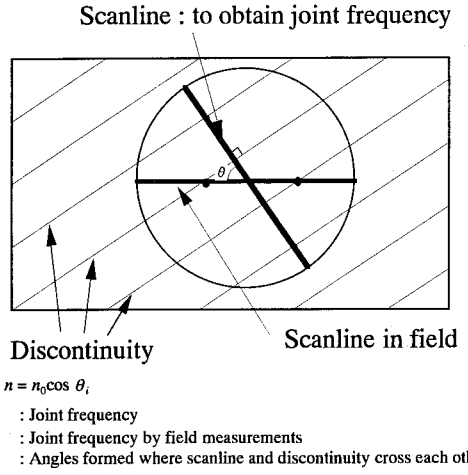

(a) Relationship between discontinuity set and scanline in a regular joint model

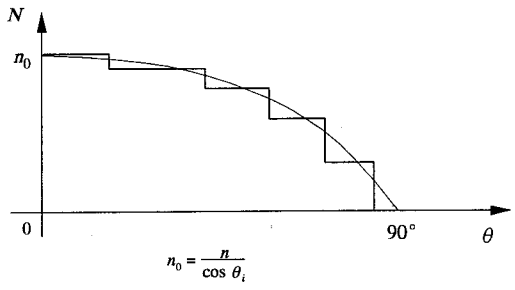

(b) Weight function to revise the survey error

Figure 2.10 The concept of errors in joint surveys and its revise function

Using the above method, it is possible to determine the true joint frequency by measuring the right scanline against a joint set.

2.7 Identifying joint sets

A graphical approach to the analysis of orientation data can easily be done by plotting the points which represent the normals on each discontinuity plane of the lower hemisphere. The preferred orientation, clusters, and joint sets can be identified with the human eye. If the preferred orientation and joint sets can be determined, a discontinuity model of the jointed rock mass can be made. A discontinuity numerical simulation, such as the distinct element method (*DEM*) (Cundall, 1971a, 1971b) or the discontinuous deformation analysis (*DDA*) (Shi, 1985), etc., can be carried out. In general, the orientation limits for each joint set can be specified either in terms of a range in trend and plunge angles, as an angular range from an axis near the center of the clusters, or by a manual delineation of a range of orientations. This method is advantageous in that it allows an individual's expertise and familiarity with a particular site to play a part in the identification of the clusters (Priest, 1993). In advocating this subjective approach, Bridges (1990) emphasized the value of human capabilities in pattern recognition where there are complex and overlapping clusters of discontinuity orientation. With such advantageous measuring systems as *BSS* and *BTV*, however, it is thought that as the amount of joint data increases, dealing with this data using the human eye becomes distracting, difficult, and complex.

An accurate and less individual approach to the analysis of clusters in orientation data was then presented by Shanley and Mahtab (1976) and later modified by Mahtab and Yegulalp (1982). In this section, a brief account of the approach to the analysis of joint data described in this research work will be presented. The Mahtab and Yegulalp algorithm is based upon the assumption that a discontinuity set will exhibit a significantly greater degree of clustering than a totally random distribution of orientations. The probabilities associated with random events can be expressed in terms of Poisson's process. The probability, $P(t,v)$, of exactly t events occurring at an interval $[0,v]$ is given by **Equation 2-9** as follows:

$$P(t,v) = \frac{e^{-\lambda v}(\lambda v)^t}{t!} \qquad (2\text{-}9)$$

where t : an integer (0, 1, 2, ••••••)

λ : the event frequency per unit dimension (time, distance, angle, etc.).

The interval of v, shown in **Equation 2-9**, can be prescribed for a range of orientations for discontinuity normals in the case of the analysis of orientation data. The range can be determined

in terms of a cone angle, ψ, whose axis can be specified as dip direction/dip (α/β). Such a cone angle contains a proportion, c, on the hemisphere given by **Equation 2-10**, namely,

$$c = 1 - \cos(\psi) \quad . \tag{2-10}$$

If the sample range of all orientations on the hemisphere is considered to be a constant unit size, interval v is equal to c. Therefore, if the total sample number of discontinuity normals is n, the event frequency, λ, is equal to n. Substituting c and n for v and λ in **Equation 2-9** gives **Equation 2-11**, namely,

$$P(t,c) = \frac{e^{-nc}(nc)^t}{t!} \quad . \tag{2-11}$$

In actuality, the poles which represent the inside of a counter circle have been counted. This circle can be defined by the cross section of a cone whose apex is located at the center point of the sphere and the surface of the hemisphere projects the discontinuity normals. From cone angle ψ, 1% of the surface area of the hemisphere will be a counter circle. In calculating the poles, sampling cells on the hemisphere which show the isotropic constant area can then be made as well as possible. Nodal points are at the center of the cells. The density distribution for each nodal point can be calculated through Poisson's distribution.

In the next step, a grouping discontinuity is carried out. The probability, $P(>t,c)$, of more than t randomly orientated discontinuity normals occurring with cone angle ψ is given by the following simple summation:

$$P(>t,c) = 1 - \sum_{j=1}^{t} \frac{e^{-nc}(nc)^j}{j!} \leq s \tag{2-12}$$

where j is an integer pointer.

For the analysis of orientation data, a critical value of t, that is, a critical frequency t_{crit}, can be defined as the smallest value of t for which $P(>t,c) \leq s$, where s is a limiting probability. Shanley and Mahtab (1976) took s to be 0.05, that is, the certification of Poisson's distribution. On the other hand, Mahtab and Yegulalp (1982) took the limiting probability of $s = c$. For example, in the case of a cluster analysis of 162 discontinuity normals and a cone angle of $\psi = 10$ (degrees), c is taken as 0.0152 from **Equation 2-10**. Inputting this value into **Equation 2-12** yields a value of 6. On the other hand, in the case of $s = 0.05$, t_{crit} is 5 (Priest, 1993). For each nodal point, the discussion to enclose the adjoining points which specify more than t_{crit} can be determined by the clusters or the sets.

The probability distribution, such as Fisher's distribution or Bingham's distribution, etc., can then be estimated for each discontinuity set, and the statistical parameters (the resultant vector $\vec{R}$, population parameter k, and deviation angle Ω) can be calculated with it, respectively. Resultant vector $\vec{R}$ presents the average normal vector of the discontinuity sets. As the unevenness of the normal vector of discontinuity sets decreases, the population parameter increases. Deviation angle Ω presents the degree of unevenness for the discontinuity sets.

In this research work, a test with a 95% Poisson distribution method is carried out for the orientation data obtained from five boreholes, as shown in **Figure 2.3**. The results of the cluster analysis are shown in **Figure 2.11** and **Table 2.4**. In **Table 2.4**, the statistical parameters applied in Fisher's distribution (Fisher, 1953) are also shown. **Equations 2-13 ~ 2-15** give each statistical parameter as follows:

$$\vec{R} = \frac{\sum \vec{r}}{M} \tag{2-13}$$

$$k = \frac{M-1}{M - \left|\vec{R}\right|} \tag{2-14}$$

$$\Omega = \arcsin \sqrt{\frac{2-(\frac{1}{M})}{k}} \tag{2-15}$$

where M is the number of samples in the discontinuity sets. In comparing the data from the boreholes with the data from the adit wall observation, the results of the analyzed measurement data taken from the exposed rock surfaces at five parts of the adit, as shown in **Figure 2.3**, are also presented.

From **Table 2.4**, it is clear that the orientations of the major joint sets resemble Boreholes A, B, and C which are located in the inner part of the adit. And, the same tendency can be found for Boreholes D and E which are located near the entrance of the adit. From the analytical results of all the boreholes, a major joint set, whose dip is less than 30 degrees and whose dip direction is around 250 degrees, can be commonly found and is presented as a continuous and dominant joint set. From a geological point of view, it is thought that this set formed because of the common late Cretaceous Cauldron Movement.

In addition, a comparison of the joint mapping data results at the adit wall (**Figures 2.11**(f) ~ (j)) and the results of the discontinuity data from the borehole survey are carried out. As for joint mapping at the adit wall, the total station (Jeck Co.) was used. More than three points on the discontinuity surface of the adit wall are measured, and the dip angle and the dip direction are analyzed. Based on the results, the vertical discontinuity and the relative vertical discontinuity are found. In each borehole, however, the apparent frequency of joints that have dip angles of more than 70 degrees is very small. Although an analysis of the discontinuities is applied to reduce bias errors for the measuring direction, bias errors for measuring cannot be removed. Two joint sets whose dip angles are more than 70 degrees are confirmed in the analysis of the joint

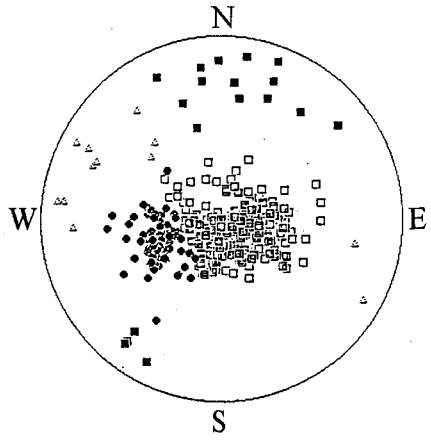

(a) Borehole *A*

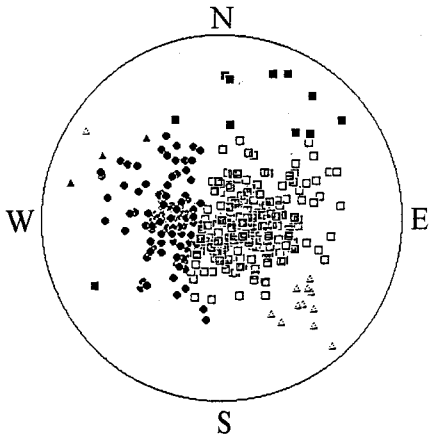

(b) Borehole *B*

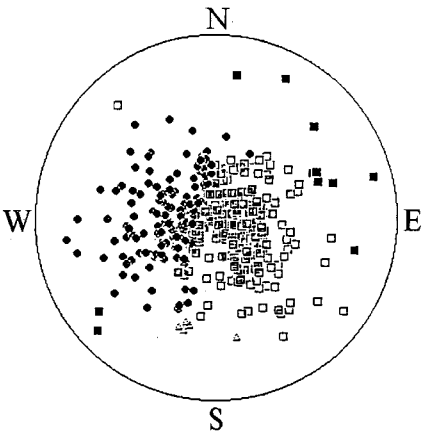

(c) Borehole *C*

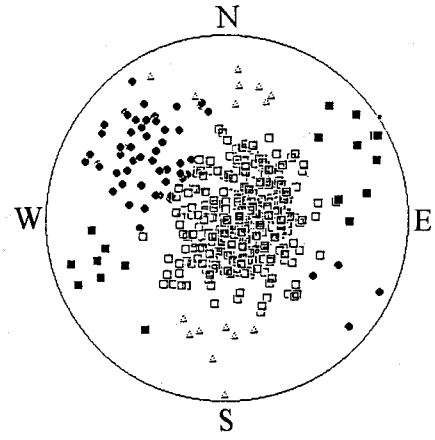

(d) Borehole *D*

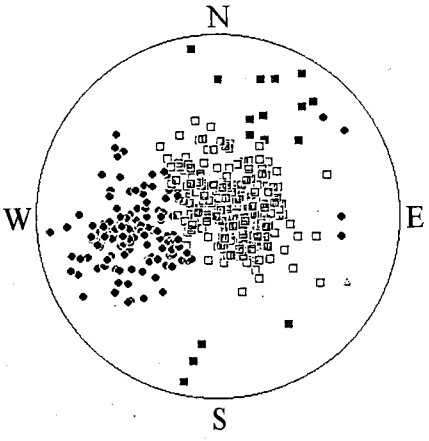

(d) Borehole *E*

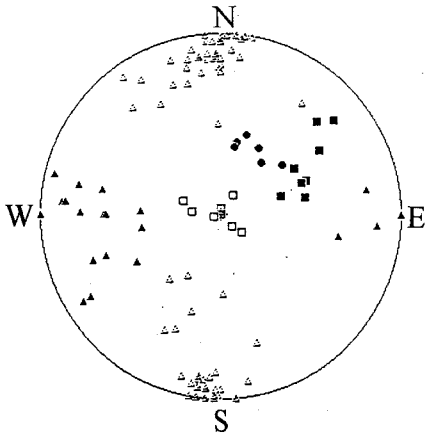

(f) *Area* 1

Figure 2.11 Lower hemisphere projection of discontinuity normals labelled by set

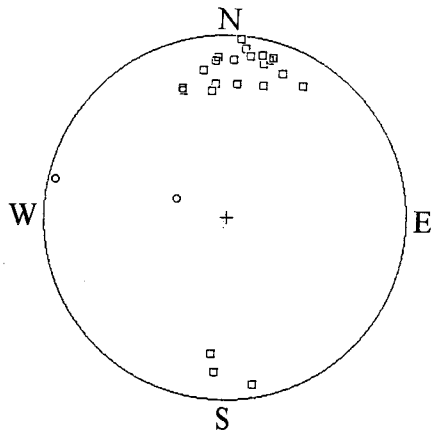

(g) *Area* 2

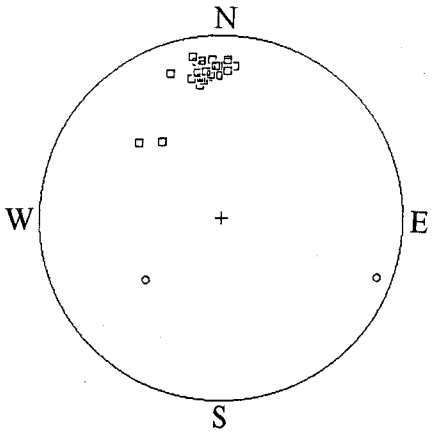

(h) *Area* 3

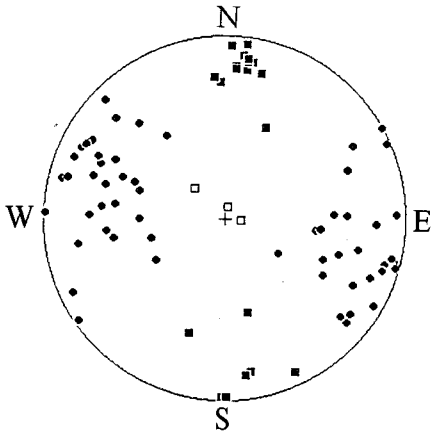

(i) *Area* 4

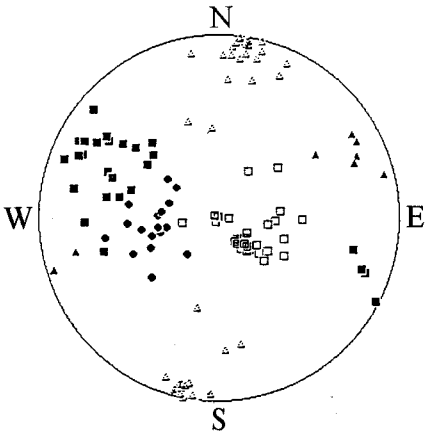

(j) *Area* 5

Figure 2.11 Lower hemisphere projection of discontinuity normals labelled by set

mapping data. When measuring the discontinuity in the field, therefore, it is thought that linear measurements should be taken independently in three directions in consideration of both geometry and economies.

From the analysis of the borehole data, two major joint sets in this field can be confirmed as follows:

i) The dip direction is around 250 degrees, such as $N20^{o}W$, and the dip angle is less than 30 degrees to the west (set No. 1 in **Table 2.4**)

ii) The dip direction is *N-S* and the dip angle is in the range of 40 to 60 degrees to the east (set No. 2 in **Table 2.4**).

Table 2.4 Dip direction and dip, k, Ω , and *R.I.* of the joint sets

Borehole	Joint set	The number of joints	Dip direction	Dip	k	Ω	*R.I.*	%
A	1 □	312	250	24	13.6	22.5	72.7	77.4
	2 ●	61	332	45	27.7	15.5	12.5	15.1
	3 ■	18	102	81	10.4	25.27	8.57	4.47
	4 △	12	32	80	14.2	21.1	6.21	2.98
B	1 □	218	237	32	9.67	26.9	55.3	61.1
	2 ●	113	322	40	11.8	24.2	30.7	31.7
	3 ■	11	112	75	8.7	27.2	6.47	3.08
	4 △	12	227	70	34.1	13.4	5.73	3.36
	5 ▲	3	33	73	19.7	15.1	1.79	0.84
C	1 □	262	120	30	10.7	25.6	58.1	59.7
	2 ●	161	46	38	9.37	27.4	35.9	36.7
	3 ■	11	125	79	4.05	42.1	4.71	2.51
	4 △	5	79	64	51	10.2	1.26	1.14
D	1 □	393	249	30	8.79	28.5	67.3	80.9
	2 ●	57	47	64	9.94	26.4	16.8	11.7
	3 ■	19	328	89	13.7	21.9	8.94	3.91
	4 △	17	86	88	10.8	24.7	6.97	3.50
E	1 □	324	247	27	11.3	24.8	60.3	67.9
	2 ●	136	330	57	12.1	23.9	32.6	28.5
	3 ■	16	272	88	2.24	66.1	6.79	3.35
	4 △	1	207	77	-	-	0.31	0.21
Area 1	1 □	8	81	15	28.1	14.5	-	7.27
	2 ●	6	116	45	49.8	10.5	-	5.45
	3 ■	8	146	59	24.7	15.4	-	7.27
	4 △	68	85	90	20.5	18.1	-	61.8
	5 ▲	20	331	79	80.1	29.1	-	18.2
Area 2	1 □	24	93	83	30.6	14.5	-	100
Area 3	1 □	24	82	77	41.1	12.5	-	100
Area 4	1 □	3	83	17	20.5	14.8	-	3.37
	2 ●	63	38	82	5.37	37.3	-	70.8
	3 ■	23	271	87	8.92	27.6	-	25.8
Area 5	1 □	31	231	29	16.2	20.2	-	25.8
	2 ●	18	334	43	21.7	17.1	-	10.8
	3 ■	26	31	75	16.9	19.7	-	21.7
	4 △	37	97	87	13.4	22.4	-	30.8
	5 ▲	8	154	83	40.1	12.1	-	6.67

On the other hand, from the results of the joint mapping data shown in **Table 2.4**, two other major joint sets (set Nos. 3 and No. 4) can be found as follows:

i) The dip direction is *E-W* and the dip angle is more than 70 degrees.

ii) The dip direction is *N-S* and the dip angle is more than 70 degrees.

2.8 Suggestion of the relative importance (*R.I.*) of discontinuity sets

After carrying out a discontinuous numerical simulation, such as *DEM*, the elements can then be determined with a large number of joint sets. In this case, however, the large number of joints can easily be affected by the results of the numerical simulation and the influence of the joints. The joints are few in number, but are strongly controlled by the mechanical behavior and the hydromechanical behavior. They cannot be considered in the numerical simulation. As mentioned above, if the joint sets in only one direction are measured, the results of the discontinuity analysis will contain bias errors and only the numerical simulation will be affected by it. On the other hand, it is more difficult to determine joints and joint sets, which are few in number but are strongly controlled by both the mechanical behavior and the hydromechanical behavior, than those which are great in number. Thus, a parameter can be described which presents the degree of relative importance of the analyzed joint sets.

In jointed rock masses, both mechanical and hydromechanical behaviors can be affected by discontinuities. These factors are thought to be the number of joints, such as joint frequency and/or spacing, area, the apertures, joint surface roughness, and so on. Then, so as to determine which joint set takes the influence from those behaviors, it is suggested that the parameter, the relative importance (*R.I.*) of a joint set, be used in consideration of the number, the area, and the apertures of the joints, respectively.

$$R.I. = \frac{\frac{n}{n_T} + \frac{A_s}{A_{sT}} + \frac{i_v}{i_{vT}}}{3} \times 100\ (\%) \qquad (2\text{-}16)$$

where $R.I.$: relative importance of the selected joint set
n : joint frequency of the selected joint set
n_T : joint frequency of the rock mass
A_S : total joint area of the selected joint set
A_{ST} : total joint area of the rock mass
i_v : total void of the selected joint set
i_{vT} : total void of the rock mass.

In joint mapping at an adit and a ground surface, A_S and A_{ST} are used for the trace length in place of the area. And, i_v and i_{vT} can be substituted for the sum of the apertures. When the area, the trace length, and the apertures cannot be measured, **Equation 2-16** can be changed to the following:

$$R.I. = \frac{\frac{n}{n_T} + \frac{A_s}{A_{sT}}}{2} \times 100\ (\%) \qquad (2\text{-}17)$$

$$R.I. = \frac{\frac{n}{n_T} + \frac{i_v}{i_{vT}}}{2} \times 100\,(\%) \qquad (2\text{-}18)$$

As for joint sets measured from the borehole survey, *R.I.* is calculated in this research work using weight value W_i and the apertures as follows:

$$R.I. = \frac{\frac{\sum W_i}{1} + \frac{i_v}{i_{vT}}}{2} \times 100\,(\%) \qquad (2\text{-}19)$$

R.I. in this field is calculated, as shown in **Table 2.4**, and the percentage of discontinuities in each joint set against the total number of joints can also be described. In comparing *R.I.* with the percentage at Borehole *C* in **Table 2.4**, a definite difference cannot be found. However, at other boreholes, *R.I.* is smaller than the percentage for joint set Nos. 1 and 2. In particular, it is found that the *R.I.* of joint set No.1 at Borehole *D* is 20 points smaller than the percentage, while the *R.I.* of joint set Nos. 3 and 4, which have few joints, such as the smaller percentage, clearly presents the larger value. If the numerical simulation of the discontinuous model is performed in consideration of only joint set Nos. 1 and 2, the selected joint sets are strongly controlled by the results, and it is impossible to consider the influence of the joints and the joint sets which are few in number. It is believed that if a joint set consists of a few joints which represent a large area and wide apertures, they are influenced by the mechanical behavior.

A case is then presented in which two joint sets are taken from analyzing the orientation data. If both sets present the same number of joints and the same population parameters, their estimations are equivalent and they are applied to the numerical simulation equally. However, if they present different values for *R.I.*, it is possible to apply the joint sets to the numerical simulation in consideration of the difference in *R.I.* and to perform a numerical simulation that conforms to the in-situ conditions. *R.I.* is based on the concept that joints (contained in a large area) and apertures are strongly affected by mechanical and hydromechanical behaviors and this is appropriate. Since it is necessary to estimate the mechanical and the hydromechanical properties for each joint, they must be investigated. In this research work, however, more than 300 joints can be found in each borehole, and it is impossible to estimate both types of properties in each joint and apply them to the numerical simulation. It is thought that *R.I.* effectively represents the in-situ joint conditions, from a mechanical point of view, since it is able to estimate joint sets in consideration of not only the number of joints, but also the area and the apertures.

2.9 Discontinuity modeling

2.9.1 Extraction of the region of homogeneous joint distribution through the accumulated aperture

In making a discontinuity model for a jointed rock mass, the changes in joints and joint sets for each region of an objective area must be considered. Then, after investigating where the same tendency of a joint orientation and joint sets can be presented, a discontinuity model which shows a homogeneous joint distribution must be made for each region. Kikuchi et al. (1987) described how to extract the region of homogeneous joint distribution using orientation data through the scanline sampling observation on a ground surface.

After the region of homogeneous joint distribution, found through the borehole survey, is classified, the concept of the accumulated aperture is introduced and its validity for discontinuity modeling is confirmed.

a) The concept of an accumulated aperture

An accumulated aperture is defined to accumulate aperture observed joints along a borehole, and it is presented to function as the depth of the borehole. By increasing the gradient of the curve in order to relate the accumulated aperture with the location in the borehole, it is seen that many joints densely exist or that joints whose apertures are wide can be found (Nakata, et al., 1991).

b) Standardization of the accumulated aperture

In order to extract the range of homogeneous joint distribution through the accumulated aperture, the standardization of it will be performed as follows:

i) Describe the function, $F(x)$, which represents changes in the accumulated aperture along a borehole.

ii) Link both starting and end points at $F(x)$ by a straight line, $f(x)$. $f(x)$ means that the joint distribution is uniform for the joint distribution.

iii) Extract the region of homogeneous joint distribution by comparing $F(x)$ and $f(x)$.

The gradient of the curve represents the difference between $F(x)$ and $f(x)$ and can be identified where a region is homogeneous or inhomogeneous. In other words, a region in which the gradient is positive can relatively indicate the concentration of wide aperture joints. On the other hand, the concentration of close aperture joints can be considered for a region in which the gradient is negative. The concept of this method is shown in **Figure 2.12**.

Figures 2.13 ~ 17 show the standardization of the accumulated aperture and the extraction of the homogeneous joint distribution for each borehole, respectively. Based on these systems, the boreholes can be divided into regions of homogeneous joint distribution, except around the 62

m point in Borehole *B*. These regions are called *a*, *b*, *c*, *d*,,,,, in order from the upper side of each borehole. Comparing these figures, a tendency for the gradient of the standardization of the accumulated aperture to show a large value for depths of 10 *m* to 20 *m* in each borehole can be confirmed. Regarding this tendency, joints which have a large aperture are thought to exist in a concentrated manner and this region is a weak part of the jointed rock mass. As for making a standardization for the accumulated aperture, it becomes possible not only to extract the region of homogeneous joint distribution, but also to estimate the weak part of the jointed rock mass.

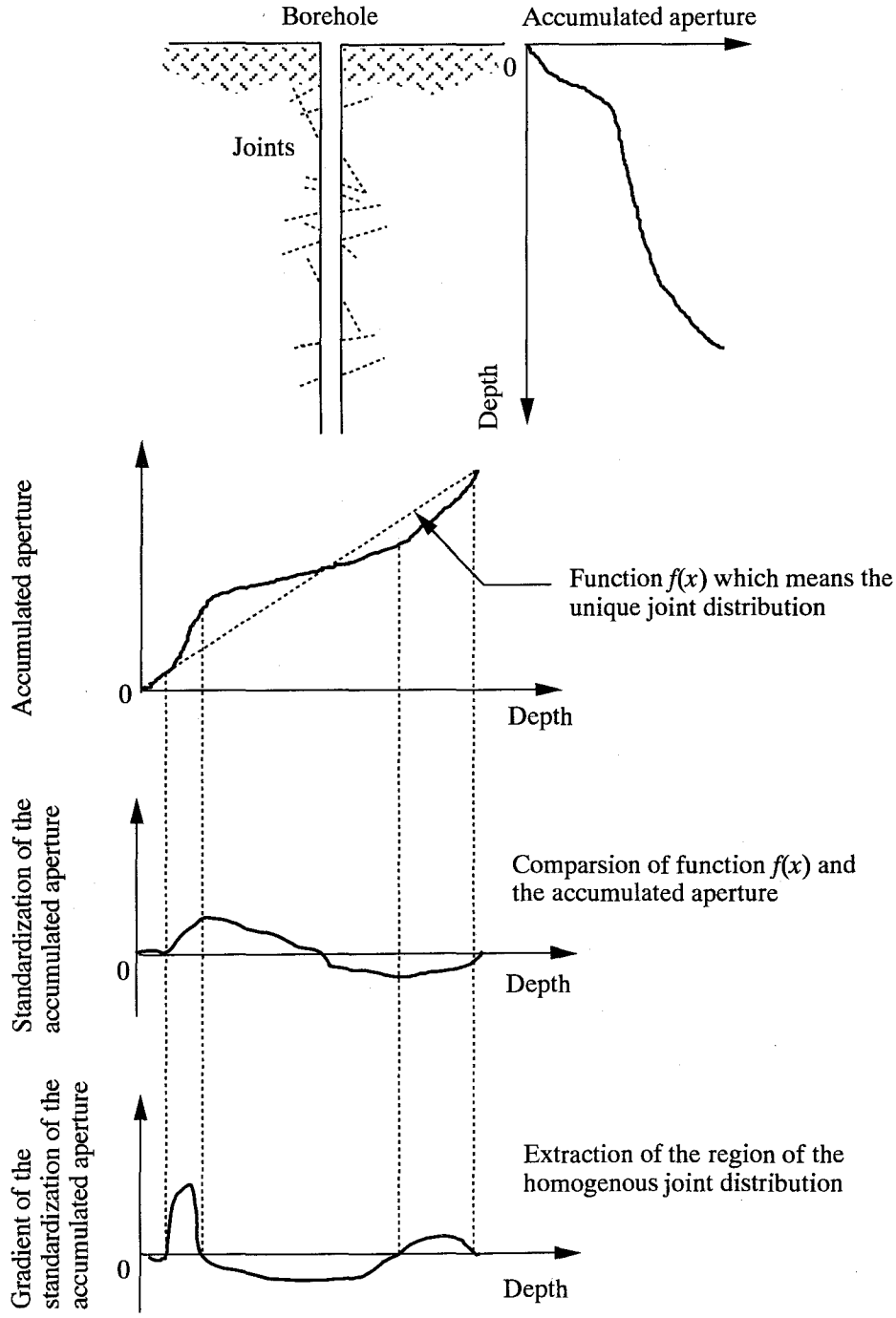

Figure 2.12 The concept of the accumulated aperture and its standardization

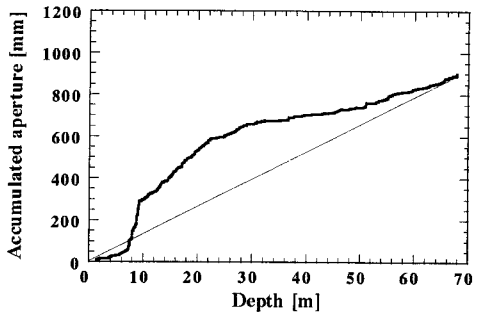

(a) Accumulated aperture along borehole *A*

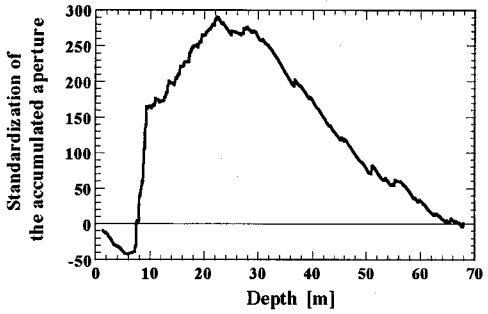

(b) Standardization of the accumulated aperture

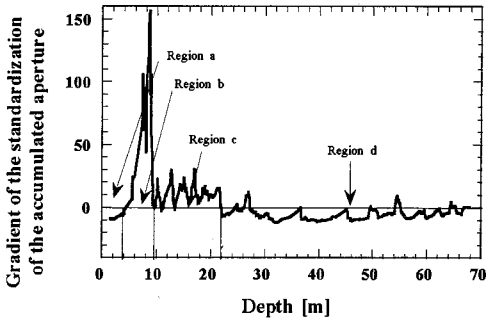

(c) Gradient of the standardization of the accumulated aperture

Figure 2.13 The extraction of the region of homogenous joint distribution in borehole *A*

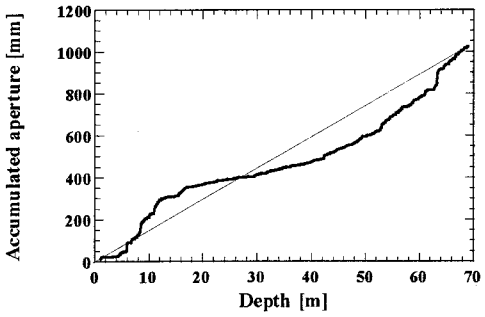

(a) Accumulated aperture along borehole *B*

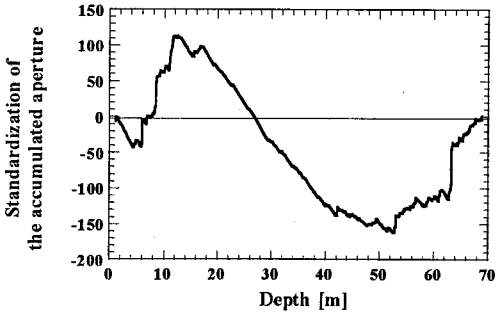

(b) Standardization of the accumulated aperture

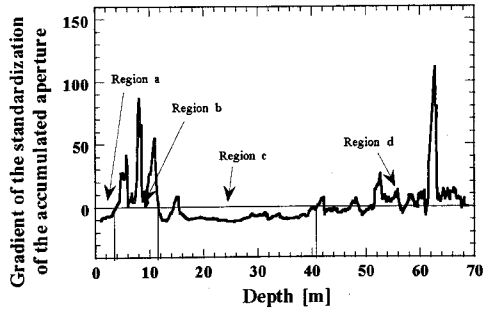

(c) Gradient of the standardization of the accumulated aperture

Figure 2.14 The extraction of the region of homogenous joint distribution in borehole *B*

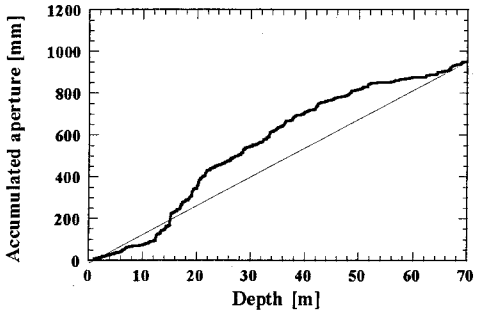

(a) Accumulated aperture along borehole *C*

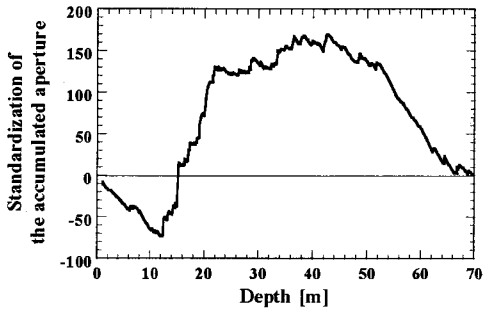

(b) Standardization of the accumulated aperture

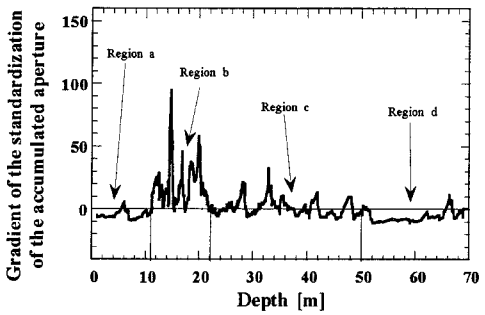

(c) Gradient of the standardization of the accumulated aperture

Figure 2.15 The extraction of the region of homogenous joint distribution in borehole *C*

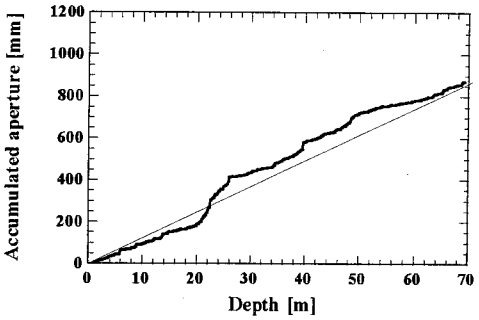

(a) Accumulated aperture along borehole *D*

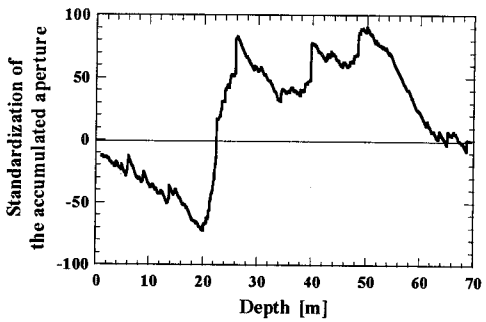

(b) Standardization of the accumulated aperture

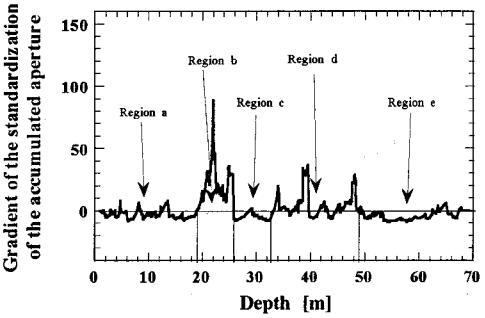

(c) Gradient of the standardization of the accumulated aperture

Figure 2.16 The extraction of the region of homogenous joint distribution in borehole *D*

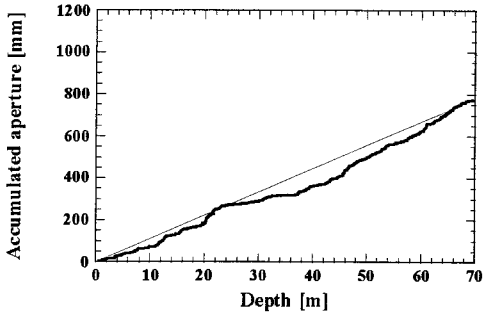

(a) Accumulated aperture along borehole *E*

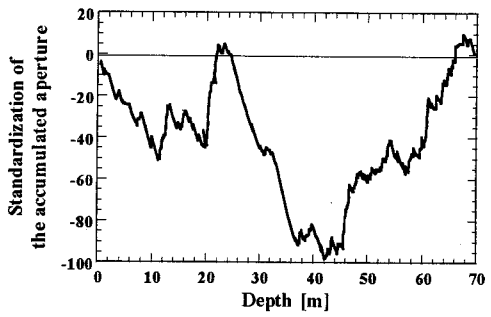

(b) Standardization of the accumulated aperture

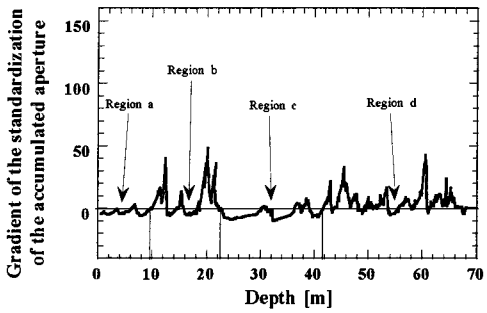

(c) Gradient of the standardization of the accumulated aperture

Figure 2.17 The extraction of the region of homogenous joint distribution in borehole *E*

2.9.2 Discussion of the analysis of orientation data for each region of homogeneous joint distribution

In this section, an orientation analysis is conducted for each region of the homogeneous joint distribution and the results are discussed. The order of the analysis is described as follows:

i) In order to reduce bias errors caused by the investigation direction, weight value W_i mentioned in the above section is estimated.

ii) A lower hemisphere projection of the discontinuity normal is made.

iii) The joint sets are analyzed using weight value W_i.

iv) The number of joints, *R.I.*, and the population parameter in each joint set are estimated.

From **Figure 2.13**, Borehole *A* is divided into four regions. Then, an orientation analysis is conducted in these regions. **Figures 2.18**(a) ~ (d) and **Table 2.5** show the results. At Borehole *A* in Region *c*, between a depth of 10 *m* and 20 *m* where many joints whose apertures are wide can be found, the dip angles of these joints are estimated to be small in the orientation analysis, as shown in **Figure 2.13**. Then, it is thought that some geological interaction is at work in this region in a horizontal direction. And, in the region of the homogeneous joint distribution, such as

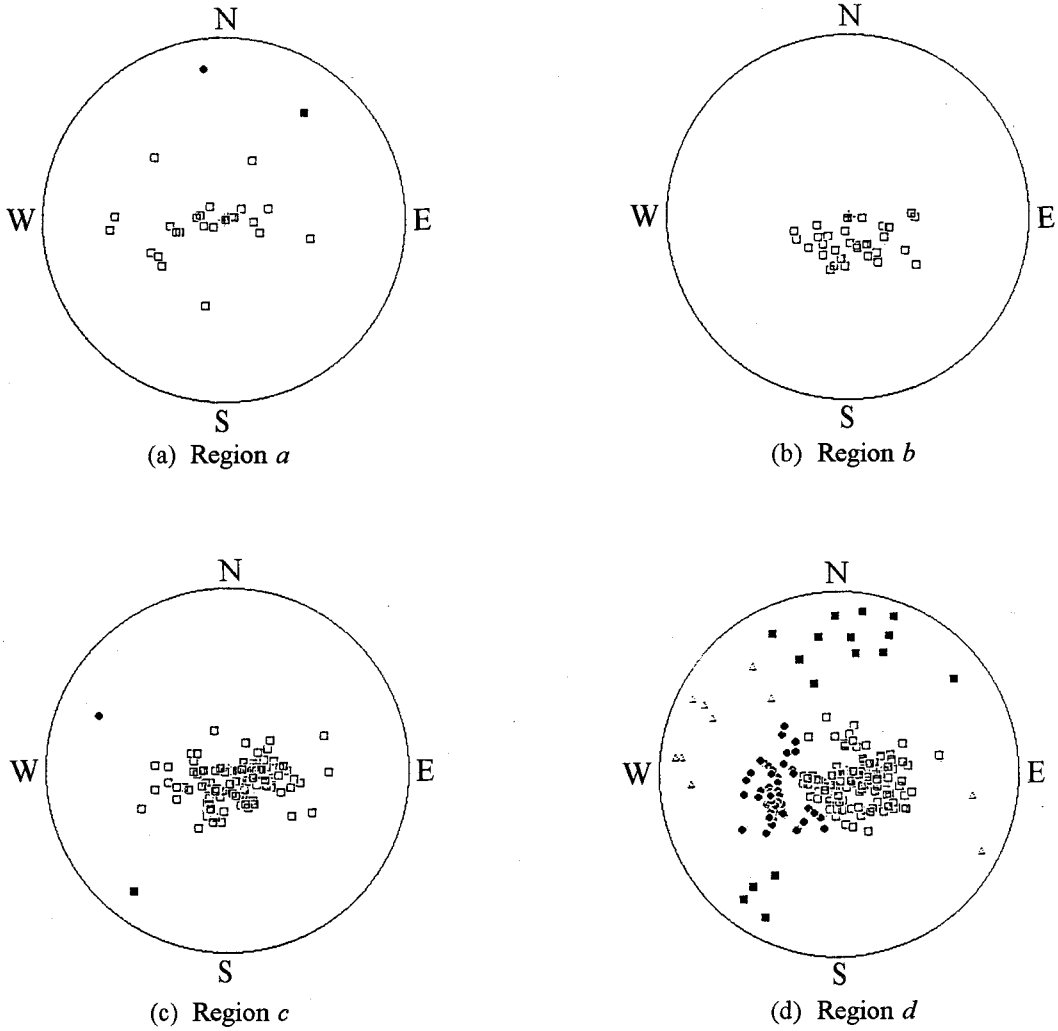

Figure 2.11 Lower hemisphere projection of discontinuity normals labelled by set

Table 2.5 Discontinuity analysis in borehole *A* for each region

Region	Joint set	The number of joints	Dip direction	Dip	*k*	*Ω*	*R.I.*	%
a	1 □	23	290	34	6.24	33.6	86.1	92.0
	2 ●	1	82	80	-	-	6.3	4.0
	3 ■	1	127	73	-	-	7.7	4.0
b	1 □	31	264	28	13.63	22.1	100	100
c	1 □	119	256	23	11.91	24.1	96.2	98.3
	2 ●	1	23	76	-	-	1.5	0.85
	3 ■	1	308	81	-	-	2.3	0.85
d	1 □	183	266	28	8.59	28.76	72.5	81.0
	2 ●	17	318	41	9.95	25.78	6.7	7.52
	3 ■	16	101	82	9.7	26.07	12.1	7.08
	4 △	10	30	82	14.2	20.85	8.8	4.42

Region *d* in Borehole *A*, more joints whose dip angles are steep can be found than in other regions, as shown in **Figure 2.18**(d).

Considering the above-mentioned circumstances, the characters of joint distribution are different for each region along the borehole and it is impossible to grasp the joint character from the orientation analysis based on the uniform borehole data. Thus, it is necessary to analyze the orientation data and grasp the joint character of each region along the borehole individually. When the borehole is divided into regions, the concept of the accumulated aperture is effective and convenient. Based on this concept, it is possible to find a region in consideration of the joint frequency and aperture. It is necessary to grasp the character of the orientation in each region. And, when making the discontinuity models, the joint character must be applied to each region.

2.10 Joint frequency map through the borehole survey

2.10.1 Semi-continuity model for a jointed rock mass

As mentioned earlier in this chapter, the extraction of joints and/or discontinuities and their analyses are described. And, with the analyzed orientation data and determined joint sets, information is prepared on how to perform the discontinuity mechanical and hydromechanical analyses. In this section, a joint frequency map, which belongs to the semi-continuity model of a jointed rock mass, is proposed through the joint data at the boreholes. Then, the distribution characters of the joints and/or discontinuities at unknown areas between boreholes are estimated.

Sakurai, et al. (1987) described the model of a ground and identified three types, namely, the continuity model, the discontinuity model, and the semi-continuity model. In particular, in the case of a weathered and/or a fractured jointed rock mass, not only major joint sets but also many joints which do not belong to joint sets can be found and the mechanical behavior seems to combine the continuity model and the discontinuity model. Sakurai, et al. (1987) defined this ground as a semi-continuity model. In considering this type of ground, the discontinuity model cannot be applied since it is impossible for it to deal with all joints in an objective area after estimating their mechanical and hydromechanical properties. The continuity model, which is considered along with the influence of the discontinuities, is then applied to this ground effectively.

The joint frequency map presented in this thesis is thought to belong to the semi-continuity model. By estimating the joint frequency in each element of the joint frequency map and clarifying the relationship between the mechanical parameter and the joint frequency, it is possible to apply the continuity analysis to the jointed rock mass in consideration of the influence of discontinuities.

2.10.2 Concept of a joint frequency map

The concept of joint frequency (n) has been applied as one of the major parameters for determining the mechanical behavior of a jointed rock, which is defined by the number of joints per unit length [$1/m$] (in the case of a one-dimensional survey), by the total length of joints per unit area [m/m^2] (in the case of a two-dimensional survey), or by the total area of joint planes per unit volume [m^2/m^3] (in the case of a three-dimensional survey), as shown in **Figure 2.19** (Tanimoto et al., 1994). The unit of joint frequency (n) becomes [$1/m$] in any representation. **Figure 2.20** shows the results of joint frequency for two different types of representation. The 3-D representation shows higher values than the 1-D case for the same points.

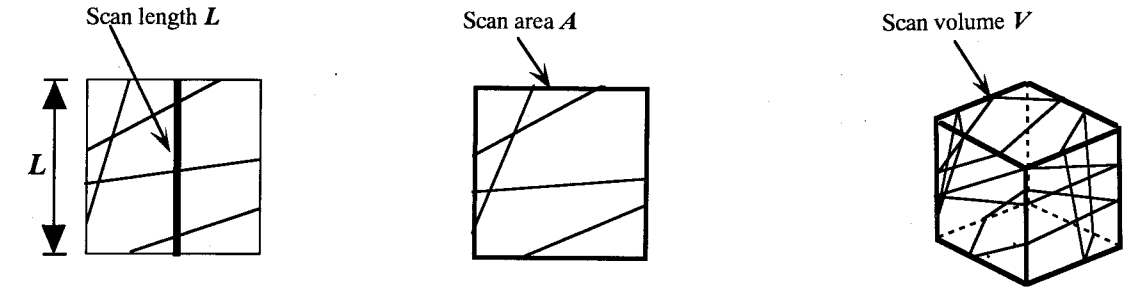

(a) 1-D scanning (b) 2-D scanning (c) 3-D scanning

Figure 2.19 Definition of joint frequency (n)

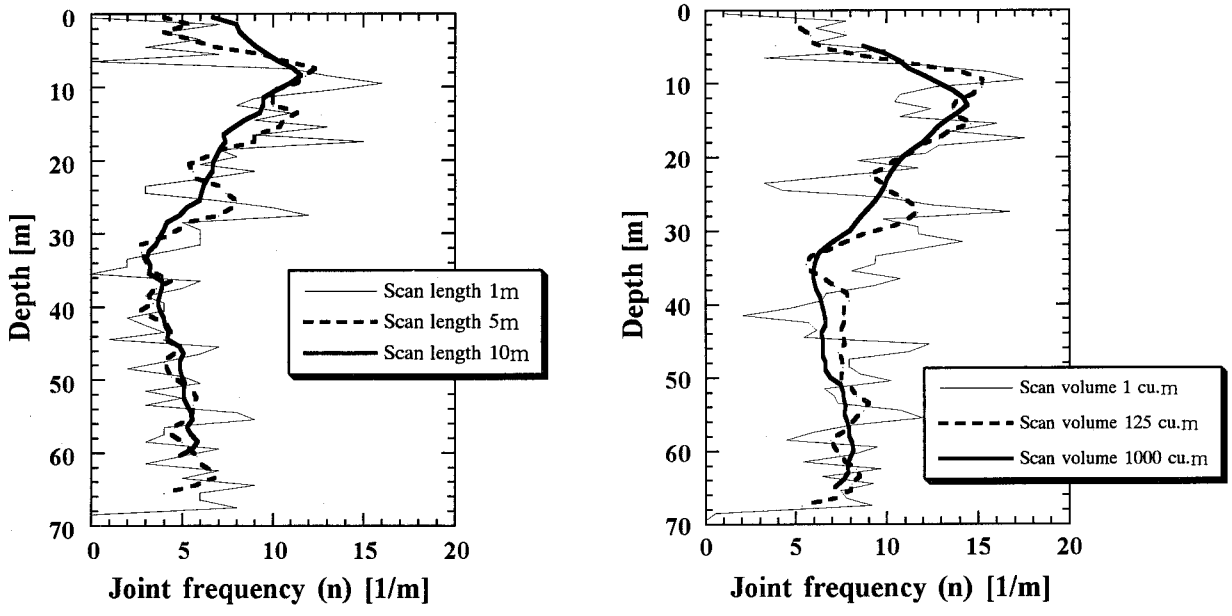

(a) 1-D scanning (b) 3-D scanning

Figure 2.20 Comparison of joint frequency (n) between 1-D and 3-D scanning

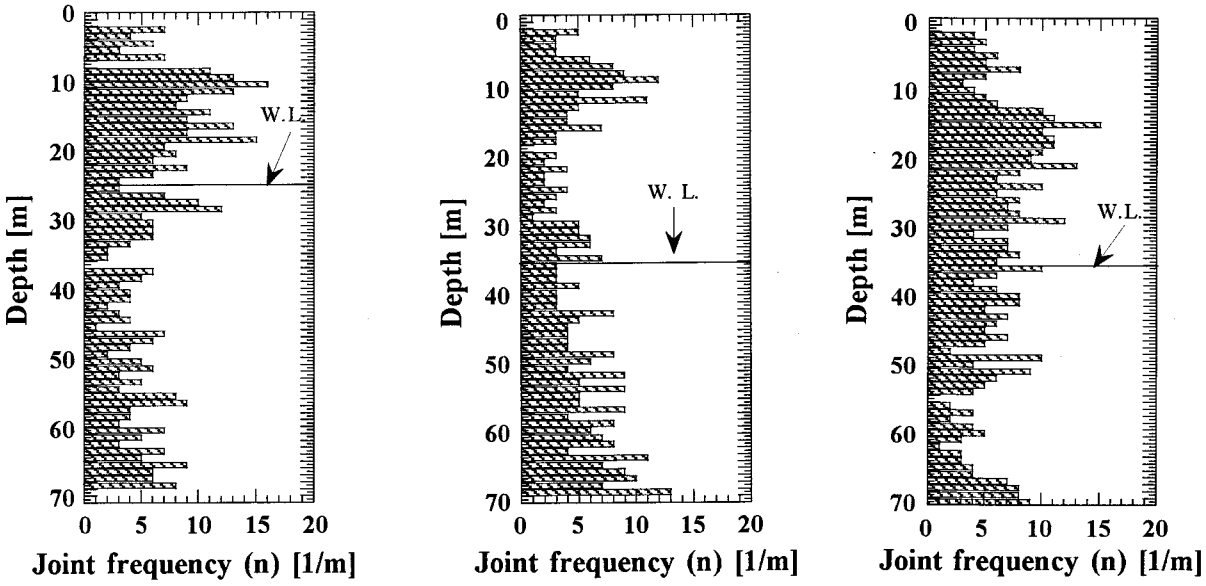

(a) Borehole *A* (b) Borehole *B* (c) Borehole *C*

Figure 2.21 Distribution of joint frequency along borehole (by 1-*D* survey)

Three boreholes (*A*, *B*, and *C*), each 70 *m* in length, respectively, are given. They are shown in **Figure 2.3**. **Figure 2.21** shows the distributions of joint frequency through the 1-*D* analysis based on the *BSS* survey.

Assuming that the joints extend planely and continuously between the boreholes, the joint distribution is interpolated in an unknown area. Then, by applying the concept of two-dimensional joint frequency, the joint frequency map between boreholes is described. This concept is shown in **Figure 2.22**. In making the joint frequency map, the following two problems exist:

i) If a joint is picked up in both boreholes, the estimate of the joint frequency will be duplicated.

ii) The suitability of an assumption whose joints extend planely and continuously between boreholes is doubted.

The way to solve these problems will be described in a latter section.

2.10.3 Avoiding duplication

The method for duplicating one joint at both sides of a borehole has been improved. One joint, which is measured at the borehole on the left-hand side, is applied to a weight of 1 at the borehole on the left-hand side and a weight of 0 at the borehole on the right-hand side, as shown in **Figure 2.23**. The weight decreases from 1 to 0 proportionally to the horizontal distance from the observed borehole. **Equations 2-20** and **2-21** describe the left- and right- side weights, respectively.

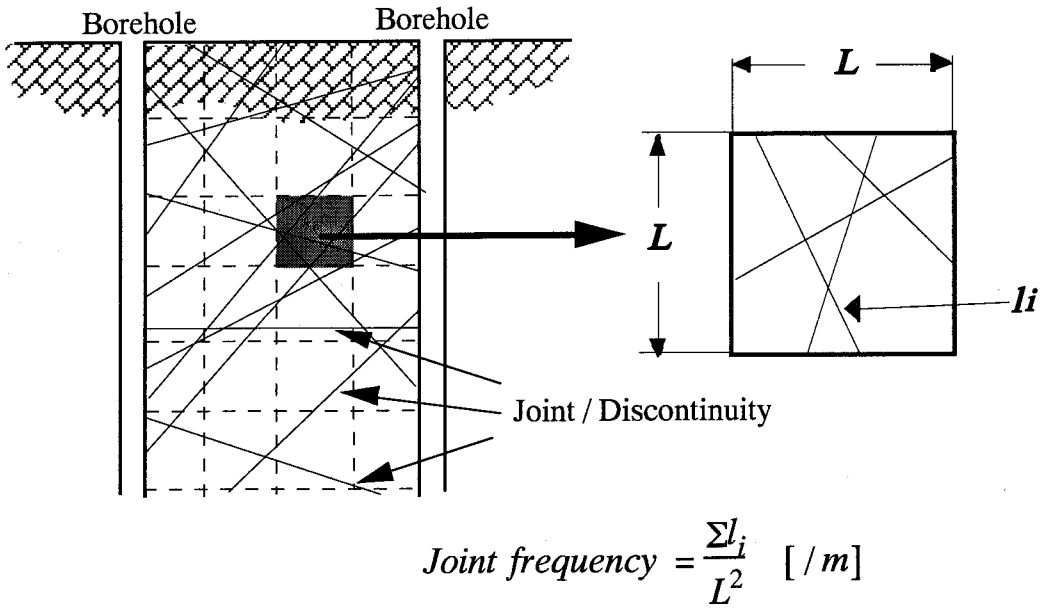

Figure 2.22 The concept of a joint frequency map (Tanimoto, et. al., 1994)

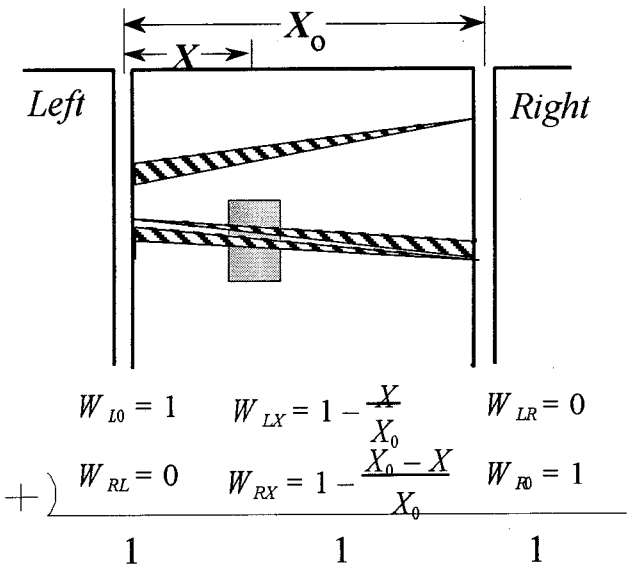

Figure 2.23 Weight set up in consideration of distance (Tanimoto, et. al., 1994)

$$W_{Lx} = 1 - \frac{x}{X_0} \tag{2-20}$$

$$W_{Rx} = 1 - \frac{X_0 - x}{X_0} \tag{2-21}$$

where W_{Lx} and W_{Rx} are the left- and the right- side weight values which are applied to joints obtained at both boreholes, respectively, X_0 is the distance between the boreholes, and x is the horizontal distance from the borehole on the left-hand side to the target point. Even if one joint is measured at both boreholes, it is prevented from yielding a duplicated estimation because of the relation of $W_{Lx} + W_{Rx} = 1$.

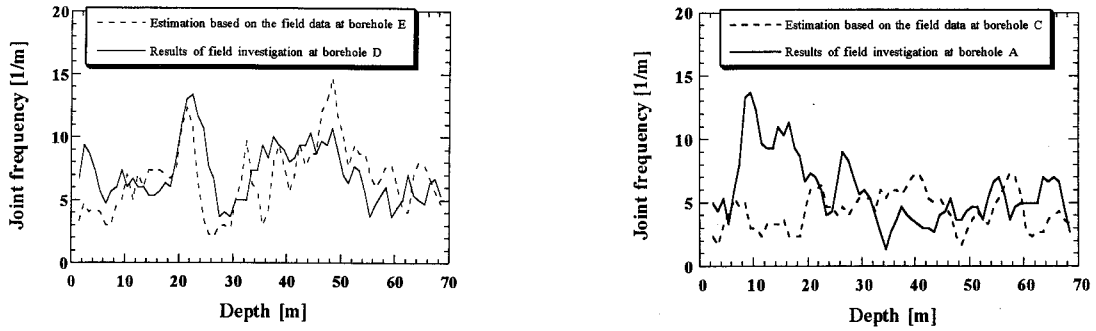

(a) 4.09 *m* distance between boreholes (b) 59.07 *m* distance between boreholes

Figure 2.24 Investigation v.s. estimation of joint frequency

In addition, **Figures 2.24**(a) and (b) show a comparison of the joint frequency, which is assumed from the other borehole data, with the observed joint frequency. In **Figure 2.24**(a), the distance between boreholes is 4.09 *m*, which shows a good correlation between both kinds of joint frequencies. It is suitable to apply the weight in consideration of the distance from the observed borehole to the objective location. In **Figure 2.24**(b), however, the distance between boreholes is 59.07 *m*, which results in an irregular correlation. The influence of the length between boreholes or between a borehole and an objective location and the three-dimensional expansion of joints needs to be considered.

2.10.4 Consideration of the extension of joints

Discontinuities and/or joints have some extended areas in the field. In past research work, Tanimoto, et al. (1994) assumed that a discontinuity existed with unlimited expanding. Based on this assumption, therefore, they calculated the joint frequency and made a joint frequency map in the objective area. However, this assumption cannot present the real conditions of a jointed rock mass due to the lack of consideration to the extension and the continuity of the joints. In order to give some consideration to the real field conditions, therefore, an assumption which presents the real conditions in the field must be defined and a joint frequency map msut be made.

In considering the extension of joints and the area of discontinuity at an unknown field, an assumption is needed. To apply the assumption, the validity of it must first be contemplated. In the author's research work, the expansion of joints is considered from a geological point of view. The orientation of some faults agrees with one of the distinguished joint sets in this field. Based on this tendency, it is thought that the joints are created by the movement of the faults and the hydrothermal metamorphism and that they exist along a major fault orientation. Therefore, joints in this field appear along some major orientation of sets, while joints in a joint set show an extension and an area. Although each joint represents an area, joints have continuously existed

along the joint set orientation. Thus, the distribution of joints is assumed to be collinear, intermittent, and periodic, like the Veneziano model (Dershowitze & Einstein, 1988).

In order to apply the concept of the Veneziano model, the period of the joints must be determined. Kinashi et al. (1995) described the relationship between an aperture and the trace length. They showed the tendency for the trace length to be longer as the aperture grows longer. The continuity of the joints, considering the aperture, is thus suggested as follows:

i) The aperture is transformed to the threshold, t, whose range is between 0 and 1.

ii) The periodical function, $f(x)$, is established.

iii) The joints are assumed to exist in the range of $t > f(x)$.

The function, which transforms the aperture to the threshold, is described as a convex curve against the positive direction, as shown in **Figure 2.25**, and the periodical function is described as a convex curve against the negative direction, as shown in **Figure 2.26**. From the results investigated through the *BSS* survey, it is confirmed that there are many joints whose apertures are very narrow and dense. One example of the relationship between an aperture and the number of joints is shown in **Figure 2.27**. One can see that most joints have an aperture of less than 3 *mm*. With a small aperture range between 0 *mm* and 10 *mm*, the difference in the distribution of the histogram in **Figure 2.27** is evident. In particular, the distribution of the histogram changes greatly in an aperture range of 0 *mm* to 3 *mm*. Based on the concept that the extension of the joints is closely related to the joint aperture, the influence of a joint aperture in applying a function must be considered when determining the extension of the joints. In actuality, when considering the extension of the joints, a function must be determined through the trace length. However, it is impossible to obtain the results of the trace length from the borehole wall survey. In this research work, therefore, the shape of the function is determined in **Figure 2.25** based on the distributive property of joints shown in **Figure 2.27**.

At first, the aperture transforms threshold t using one function, as shown in **Figure 2.25**. The threshold, whose range is between 0 and 1, is obtained by **Equation 2-22**, namely,

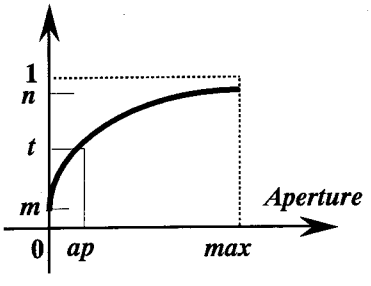

Figure 2.25 The function is determined by threshold t

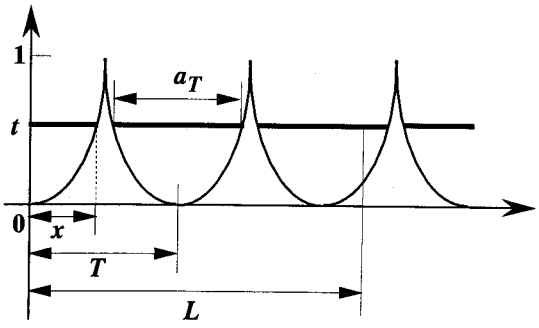

Figure 2.26 The shape of the function represents the period of the joints

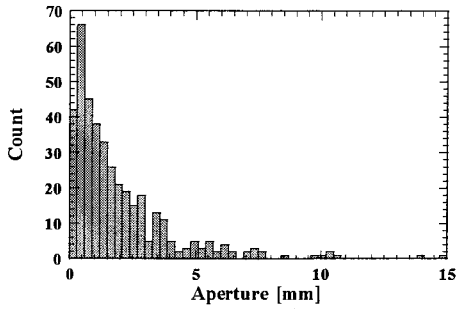

Figure 2.27 Histogram of the joint aperture

$$t = \frac{m_2 - m_1}{max^{m_3}} ap^{m_3} + m_1 \tag{2-22}$$

where *ap* is the aperture, *t* is the threshold, *max* is the maximum aperture, and m_1, m_2, and m_3 are constants ($0 \le m_1 < m_2 \le 1$, $0 < m_2 < 1$). In this research work, an investigation is conducted using $m_1 = 0.05$, $m_2 = 0.95$, $m_3 = 1/3$, and $max = 10$. Therefore, joints whose apertures are more than 10 *mm* are transformed into apertures of 10 *mm*.

Secondly, function *f(x)*, which represents the periodic appearance of joints shown in **Figure 2.26**, is defined in **Equation 2-23** as

$$f(x) = \left(\frac{T}{2}\right)^{-q} x^q \quad (1 \le q) \tag{2-23}$$

where q is a constant and T is the period. In **Figure 2.26**, therefore, it is thought that a joint existed in the range of $t > f(x)$ and its extension is equal to the trace length, a_T. a_T can be represented by period T, threshold t, and constant parameter q in function *f(x)*. Then, x is calculated and satisfies the relation $t = f(x)$ as follows:

$$x = \frac{T}{2} t^{-q} \tag{2-24}$$

A part of discontinuous trace length a_T is represented by **Equation 2-25** using threshold t, namely,

$$a_T = 2x = Tt^{-q} \tag{2-25}$$

where a_T consists of threshold t and repeats cycle L/T (L is the trace length if the joints are continuous in one mesh.) in one mesh. The total trace length of the joints in one mesh is represented by **Equation 2-26**, namely,

$$\sum a_T = \frac{L}{T} a_T = Lt^{-q} \tag{2-26}$$

The above-mentioned method is described for calculating the joint frequency in a case in which calculated trace length a_T is within one mesh and the period appeared joint is L/T. Since joints appear with great continuity, however, trace length a_T is longer than the size of the sampling mesh. In such a case, a_T depends on the T/L number of meshes. Thus, in order to estimate trace length a_T in each mesh, a_T is divided by T/L. Ultimately, it comes down to **Equation 2-26**. Since period T is eliminated, the total trace length is independent of T and the joint frequency can be calculated without the influence of the repeated period of the joints.

2.10.5 Joint frequency map

Considering the above, trace length L' exists in the unit area of the joint frequency map and is illustrated by taking the weight for the distance between the boreholes and the threshold for the aperture by **Equation 2-27**. The joint frequency in each mesh, n, is then estimated by **Equation 2-28**, namely,

$$L' = W\sum a_T = WL\left(\frac{m_2 - m_1}{max^{m_3}} ap^{m_3} - m_1\right)^{-q} \tag{2-27}$$

$$n = \frac{\sum L'}{S} \tag{2-28}$$

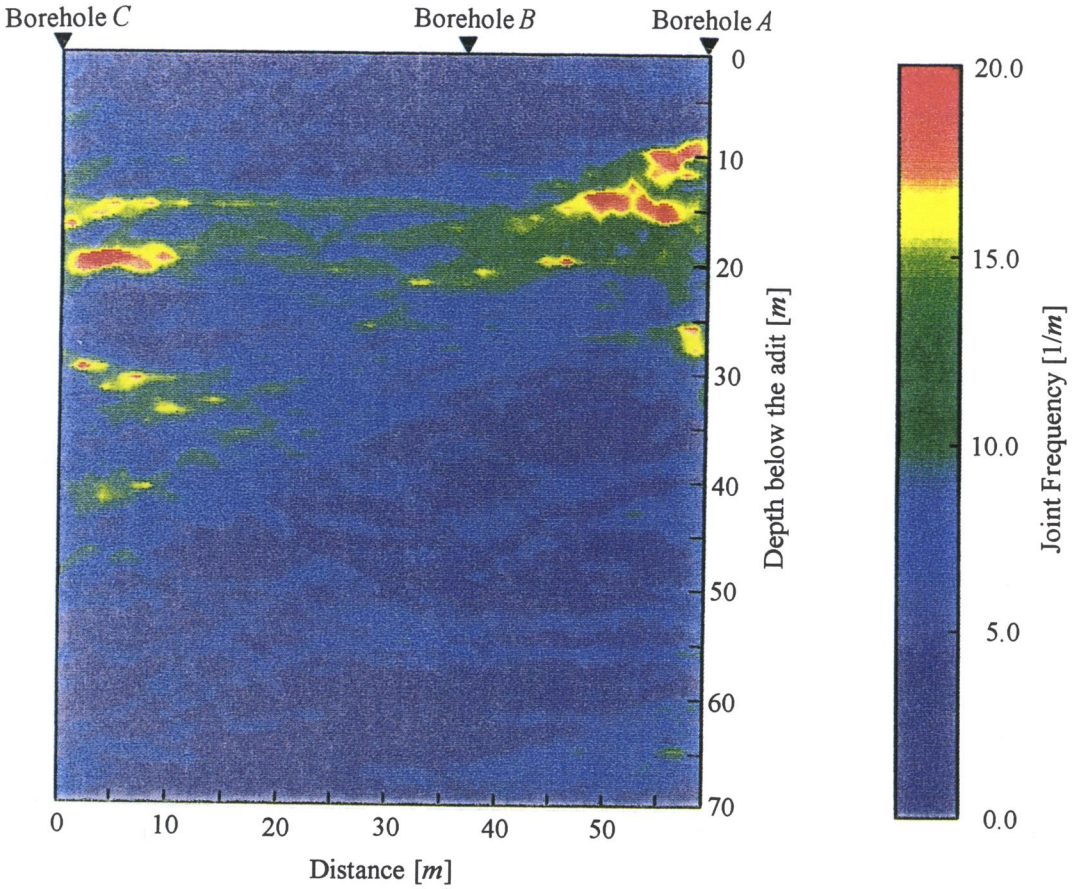

Figure 2.28 Joint frequency map in *A*-*C* section

where L' is the trace length in consideration of the continuity, W is a weight (W_{Lx} or W_{Rx}), S is an area of mesh, and n is the joint frequency. The joint frequency map between Boreholes A and C is shown in **Figure 2.28**.

2.11 Conclusion

In this chapter, a geological survey and a joint investigation have been carried out and the joint data have been analyzed. To addition, the joint aperture, the joint frequency, and the orientation of the joints, such as the dip and the dip direction, have been estimated and a discontinuity model of a jointed rock mass and a semi-continuity model have been made based on the joint frequency.

In the investigation of the discontinuities and/or joints, borehole wall sensing was performed by *BSS* and the character of the discontinuities was grasped in detail. *BSS* was confirmed to have an advantage regarding images and analyses over other investigating methods. In particular, in comparing the number of joints and *RQD* obtained from the *BSS* images with those obtained through the investigation of recovered core samples, the values were found to be different for the same borehole. Since the core samples were broken, it is thought that the *BSS* images presented a more practical picture of the in-situ rock mass than the core samples. From the *BSS* images, the orientation, the aperture, and the joint surface roughness have been estimated.

Based on the orientation data, an orientation analysis has been carried out and joint sets have been extracted. Using the extracted results, it is possible to perform a discontinuity simulation, such as *DEM*, to represent the joint orientation. However, the extraction of joint sets only considered the number of joints, and it is thought that merely knowing the number of joints is not sufficient for estimating the mechanical and the hydromechanical properties of a jointed rock mass. In this research, therefore, *R.I.*, which presents the relative importance of the joint set, has been proposed. This parameter has been thought to be influenced by the number of joints, the extension (an area), and the apertures. Based on the idea that a joint, which consists of a wide aperture and covers a large area, strongly affects both the mechanical and the hydromechanical behaviors more than others, *R.I.* has been able to estimate both properties in detail. In particular, it has been confirmed that a joint set presents a large number of *R.I.*, although it has shown more small numbers of joints than other joint sets. It is thought that not enough consideration has been given to the extension of joints since only the borehole survey data has been analyzed in this thesis. However, the apertures of most joints in a joint set have been found to be wide, although the number of joints has been few. The joint analysis has estimated the intensive orientation, only giving consideration to the same number of joints as usual. However, *R.I.* has supplemented the joint analysis with some factors, such as the apertures and the extension of joints, and joint sets

have been obtained in consideration of both mechanical and hydromechanical properties. As for the above-mentioned reasons, it is thought that *R.I.* has presented essential information on jointed rock masses.

As for the semi-continuity model for the jointed rock mass, a joint frequency map has been proposed. While making the joint frequency map, the composition of the geology and a comparison of the orientation of major faults with that of the joints have been considered. The model has been created in consideration of the geological structure. As for the extension of joints, consideration for the index of the joint apertures has been given. This consideration was based on the concept that joints with wide apertures present high continuity. The joint frequency map can be applied to certain numerical models, and this discussion will be described in the following chapters.

REFERENCES

Bridges, M. C. (1990) : Identification and characterization of sets of fractures and faults in rock, *Proceedings of International Symposium on Rock Joints*, Loen, Norway, N. Barton and O. Stephansson (eds), Balkema, pp.19 - 26.

Cundall, P. A. (1971a) : The measurement and analysis of acceleration in rock slopes, *Ph. D. Dissertation, University of London, Imperial College of Science and Technology.*

Cundall, P. A. (1971b) : A computer model for simulating progressive large scale movements in blocky rock systems, *Proc. of Symp. on Rock Fracture*, ISRM, Nancy, paper II-8.

Deere, D. U. (1964) : Technical description of rock cores for engineering purpose, *Rock Mechanics and Rock Engineering*, Vol. 1, pp. 17 - 22.

Dershowitze, W. S. and Einstein, H. H. (1988) : Characterizing Rock Joint Geometry with Joint System Models, *Rock Mechanics & Rock Engineering*, Vol. 21, pp. 21 - 51.

Editional Committee of CHUBU II (1988) : Regional Geology of Japan Part 5 CHUBU II

Fisher, R. (1953) : Dispersion on a sphere, *Proceedings of the Royal Society of London*, Vol. A217, pp. 295 - 305.

Grossmann, N. F. (1993) : New Developments in the In-situ Determination of Rock Mass Parameters, *A Short Course on Dam Foundations in Rock Masses, 1993 ISRM International Symposium EUROCK '93*, LNEC, pp. 47 - 79.

ISRM Commission on Standaraization of Laboratory and Field Tests (1978) : Suggested Methods for the Quantitative Description of Discontinuities in Rock Masses, *International Journal of Rock Mechanics and Mining Sciences & Geomechanics Abstracts*, Vol. 15, No. 6, pp. 319 - 368.

Kikuchi, K., Kobayasi, T., Mito, Y. and Izumiya, Y. (1987) : Division of the wide site into the region of homogeneous joint distribution character, *Proceedings of the 19th Symposium on Rock Mechanics*, Committee on Rock Mechanics J.S.C.E., pp. 96 - 100 (in Japanese).

Kinashi, H., Shirahata, H., Nagahisa, K., Tamano, I. and Tanaka, T. (1995) : Estimation of Joint Characteristics Based on Joint Survey and Application of DEM, *Proceedings of the 26th Symposium of Rock Mechanics*, Committee of Rock Mechanics J.S.C.E., pp. 431 - 435. (in Japanese)

Mahtab, M. A. and Yegulalp, T. M. (1982) : A rejection criterion for definition of clusters in orientation data, *In Issues in Rock Mechanics, Proceedings of the 22nd Symposium on Rock Mechanics*, Berkeley, R. E. Goodman and F. E. Heuze (eds), American Institute of Mining Metallurgy and Petroleum Engineers, New York, pp. 116 - 123.

Murai, S., et al. (1988) : Development of Borehole Scanner for underground geological survey, *Proc. of 16th Congress of Int'l Society for Photogrammetry & Remote Sensing*, Vol. 27, Part B7, Commission VII, pp. 391 - 395.

Nakata, M., Kose, Y., Sasaki, K. and Fukuma, T. (1991) : Examination of loose zone in rock around underground openings, , *Proceedings of the 23rd Symposium on Rock Mechanics*, Committee on Rock Mechanics J.S.C.E., pp. 16 - 20 (in Japanese).

Priest, S. D. (1993) : Discontinuity Analysis for Rock Engineering, Chapman & Hall, pp. 76 - 79.

Sakurai, S., Deeswasmongkol, N. and Shinji, M. (1987) : Estimation of the Stability of Cut Slopes by Means of Displacement Measurements during Slope Excavation, *Proceedings of the 7th Japan Symposium on Rock Mechanics*, ISRM- Japan, pp. 307 - 312. (in Japanese)

Shanley, R. J. and Mahtab, M. A. (1976) : Delineation and analysis of clusters in orientation data, *Journal of Mathematical Geology*, Vol. 8, No. 3, pp. 9 - 23.

Shi, G. H. (1985) : Discontinuous deformation analysis : a new approach to the statics and dynamics of block systems, *Ph. D. Dissertation, University of California at Berkeley.*

Tanimoto, C., Murai, S., Matsumoto, T., Kishida, K. and Ando, T. (1992) : Immediate image and its analysis of fractured/jointed rock mass through the borehole scanner, *Fractured and Jointed Rock Masses*, Myer, Tsang, Cook & Goodman (eds), Balkema, published in 1995, pp. 219 - 228.

Tanimoto, C., Kishida, K., Yoshizu, Y. and Kunii, K. (1994) : Seismic attenuation geotomographic technique in designing a large underground cavern, *Proc. of the 1994 ISRM International Symposium*, Van Sint Jan (ed), Vol. 1, pp. 195 - 206.

Terzaghi, R. D. (1965) : Source of error in joint surveys, Geotechnique, Vol. 15, pp. 287 - 304.

Thapa, B. B. (1994) : Analysis of in-situ rock joint strength using digital borehole scanner images, *Ph.D. Thesis, University of California at Berkeley.*

Thape, B.B., Goodman, R.E., Tanimoto, C., Kishida, K. (1995) : Analysis of in-situ joint strength anisotropy and aperture, *Proc. of the 26th Symposium of Rock Mechanics*, Committee of Rock Mechanics J.S.C.E., pp. 549 - 553.

Chapter 3

Quantitative Determination of Rock Joint Surface Roughness

3.1 Introduction

Many joints can be easily found in rock masses and they are strongly controlled by the deformation, the strength, and the permeability of the rock masses. Therefore, it becomes necessary to quantitatively grasp the joint distribution, the mechanical properties, and the hydromechanical properties of the joints.

In general, it is the mechanical properties of rock joints that are thought to identify the compressive behavior and the shear behavior. Goodman et al. (1968) defined two parameters, namely, the normal stiffness, k_n, and the shear stiffness, k_s, in order to represent the normal behavior and the shear behavior of rock joints, respectively. They assumed an equivalent stiffness spring model in both normal and shear directions, such as the joint element, and then applied it to a numerical simulation using *FEM*, etc. In considering the so-called `loosing zone`, which appears around openings in jointed rock masses after excavations, both normal and shear behaviors, in particular, the shear behavior of rock joints must be considered.

The shear behavior of rock joints is closely related to the filling materials and the joint surface roughness. Barton (1973) described some factors of the mechanical behavior of jointed rock masses, specifically the shear behavior, and presented four factors, namely, the magnitude of effective normal stress across the joints, the mode of failure which is controlled by the orientation of the joints with respect to the loading direction and by the spacing of the joints in relation to the loaded dimensions, the roughness of the joint surfaces, and the type of joints. After considering these factors, Barton (1973) suggested an empirical non-linear equation for the peak shear strength using the results of shear tests on many kinds of rock joints. Before Barton`s equation, Patton (1966) and Goldstein et al. (1966) had generally presented the shear strength of irregular rock surfaces and broken rock under low normal stress by

$$\tau_p = \sigma_n \tan\left(\phi_b + i\right) \quad . \tag{3-1}$$

Under high normal stress, it was assumed that the Coulomb relationship, shown in **Equation 3-2**, would be valid since most of the irregularities had been sheared off, namely,

$$\tau_p = \sigma_n \tan\phi \quad . \tag{3-2}$$

On the other hand, Barton's empirical equation was represented by the peak shear strength of the rock joints in consideration of the joint surface roughness and the joint wall compressive strength. In this equation, the influence of both the joint surface roughness and the strength of the material is shown in parameters *JRC* and *JCS*, respectively. *JRC* (Joint Roughness Coefficient), in the range of 0 to 20, was identified by smooth to rough joint surface roughness, and Barton and Choubey (1977) introduced twenty representative shapes of joint surface roughness. *JCS* (Joint Wall Compressive Strength) was estimated by Schmidt's hammer test, and its value is equal to 1/4 σ_C. If the *JRC* value could easily be determined by the roughness profile data, the in-situ shear strength of rock joints could then be estimated quickly and conveniently. In this way, the empirical equation developed by Barton is more effective than the Coulomb relationship in estimating the shear strength of rock joints. The shear strength of rock joints is closely related to the joint surface roughness, and it is important to grasp this relationship. Therefore, *JRC* is thought to be an effective parameter for representing the joint surface roughness.

After determining the *JRC* value, however, the empirical equation could not estimate the shear strength. In fact, Barton (1973) and Barton and Choubey (1977) estimated the *JRC* value based on the results of the shear tests which were performed. The peak shear strength, the effective normal stress, and the *JCS* value were already known after the shear tests were performed. The *JRC* value was then estimated by back analyzing the empirical equation using those parameters. Concerning this point, it seems that the *JRC* value is not exact enough to represent the roughness in detail, and it contains the influence of all other factors except for the roughness. In particular, when discussing the relationship between the shear behavior and the roughness from the results of laboratory shear tests, the quantitative determination of the joint surface roughness must be made with high precision.

Under these circumstances, the measurement and the quantitative determination of the joint surface roughness are discussed in this chapter. First of all, a spectral analysis of the representative shapes of roughness which was introduced by Barton and Choubey (1977) is presented, and parameter M_S is suggested for determining the joint surface roughness. Next, a measurement system for the joint surface roughness in specimens developed by Tanimoto and Kishida (1995) is described, and M_S is calculated from the roughness profiling data. Finally, another quantitative determination of roughness is described in consideration of the shear behavior in order to discuss the relationship between shear behavior and roughness, as shown in the following chapter.

3.2 Quantitative determination of two-dimensional joint surface roughness

3.2.1 Estimation of joint surface roughness using Barton's *JRC*

Many researchers have published studies on the relationship between shear properties and joint surface roughness. In particular, the empirical equation for shear strength, using the *JRC* described by Barton (1973), has been used for reference.

Barton conducted joint direct shear tests on specimens which represented high uniaxial compressive strength. Based on the results, Barton presented the following empirical equation for the peak shear strength:

$$\tau_p = \sigma_n \tan\left\{ JRC \cdot \log_{10}\left(\frac{JCS}{\sigma_n}\right) + \phi_b \right\} \tag{3-3}$$

where τ_p : peak shear strength of the rock joint
σ_n : effective normal stress
JRC : joint roughness coefficient
JCS : effective joint wall compressive strength (saturated)
ϕ_b : basic friction angle (wet, residual, drained).

The joint surface roughness coefficient (*JRC*) for a particular joint has been defined as follows:

$$JRC = \frac{\tan^{-1}\left(\frac{\tau_p}{\sigma_n}\right) - \phi_b}{\log_{10}\left(\frac{\sigma_c}{\sigma_n}\right)} \tag{3-4}$$

where σ_C is the rock's compressive strength which is replaced by *JCS* for weathered joints.

The remarkable point in **Equation 3-3** is the introduction of parameter *JRC*, which represents joint surface roughness, into the equation for shear strength and to describe the representative shape of *JRC* (Barton and Choubey, 1977). **Figure 3.1** shows the representative shape of *JRC*. From **Figure 3.1**, *JRC* is found to be in the range of 0 to 20. As the *JRC* value increases, the shape of the joint surface roughness becomes complicated and rough. In fact, the *JRC* of an in-situ rock joint can be determined not only by the back analysis in **Equation 3-3**, after performing the shear tests, but also by a comparison of the in-situ rock joints and shapes, as shown in **Figure 3.1**. If the quantitative determination of the joint surface roughness can be estimated or can determine the *JRC* value before performing the shear tests, the peak shear strength in the field can then be determined quickly and easily. From this point of view, Barton's empirical equation (**Equation 3-3**) is very effective for estimating the peak shear strength in the field. When the peak shear strength is estimated before performing the shear tests, using **Equation 3-3**, however, many problems such as the following arise:

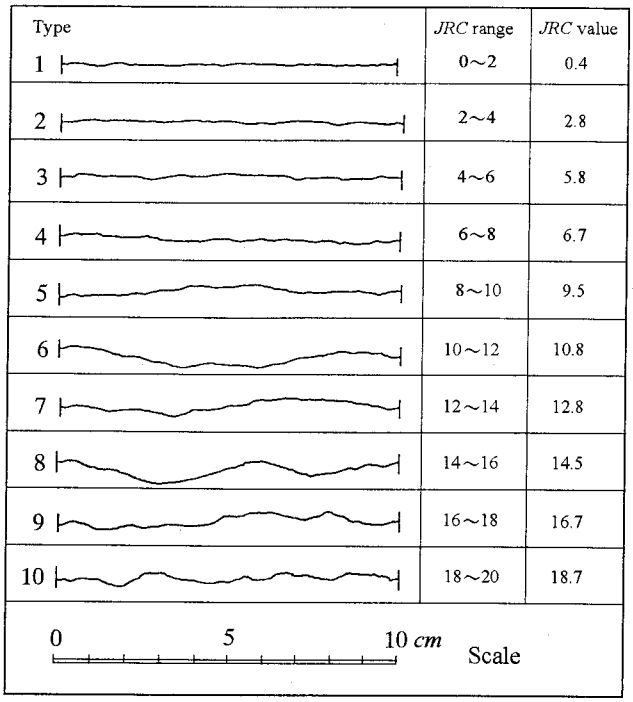

Figure 3.1 Typical roughness profile for the *JRC* range, as shown by Barton and Choubey (1977)

1) How is the *JRC* value determined?
2) If the determined *JRC* value is compared with the representative shape (**Figure 3.1**) with the human eye, will the human eye become distracted and cause errors in the estimation of the peak shear strength?
3) Can *JRC* itself truly represent the joint surface roughness?

Thus, a method which can determine the *JRC* value accurately has to be shown or another reliable quantitative determination for joint surface roughness must be introduced.

It is important that the *JRC* value be determined quantitatively since the relationship between *JRC* and the peak shear strength was clarified through the results of many laboratory direct shear tests (Barton, 1973; Barton and Choubey, 1977). Determining the *JRC* value quantitatively is one of the more effective methods for estimating the peak shear strength. In this section, therefore, the quantitative determination of two-dimensional roughness is firstly carried out, as shown in **Figure 3.1**.

3.2.2 Spectral analysis

In order to portray the image of **Figure 3.1** onto a personal computer using the image scanner system (NEC, PC-IN502) and to record the shape of the roughness of the scattered digital data, the author carries out a quantitative determination based on these data. The interval of the measurements is defined by 2048 points along a 10-*cm* measuring line. By assuming the roughness data on the wave, the determination has been applied to a spectral analysis. In a spectral analysis, the function defined in the time-displacement domain is transformed into one

defined in a frequency-amplitude or a frequency-phase domain by a Fourier transform. Then, in the frequency-amplitude domain, the wave character can be clarified by the properties of the frequency. In this research work, the power spectrum of the roughness data is calculated and the property of roughness is discussed in the frequency-amplitude domain. Since the roughness data assumes waves, the frequency of 1 *Hz* is said to be equal to a wave whose length is 1 *mm*. Therefore, the unit of frequency, *Hz*, is equivalent to 1/*mm*.

In general, a Fourier series, such as the trigonometric series expansion of a periodic function in which one period is in the range of [-*T*/2, *T*/2] is shown in **Equation 3-5** as follows:

$$\begin{aligned} x(t) \sim \frac{a_0}{2} &+ a_1\cos\frac{2\pi t}{T} + a_2\cos\frac{4\pi t}{T} + \cdots + a_n\cos\frac{2n\pi t}{T} + \cdots \\ &+ b_1\sin\frac{2\pi t}{T} + b_2\sin\frac{4\pi t}{T} + \cdots + b_n\sin\frac{2n\pi t}{T} + \cdots \\ = \frac{a_0}{2} &+ \sum_{n=1}^{\infty}\left(a_n\cos\frac{2n\pi t}{T} + b_n\sin\frac{2n\pi t}{T}\right) \end{aligned} \tag{3-5}$$

where coefficients a_n and b_n are

$$\begin{aligned} a_n &= \frac{2}{T}\int_{-T/2}^{T/2} x(t)\cos\frac{2n\pi t}{T}dt \\ b_n &= \frac{2}{T}\int_{-T/2}^{T/2} x(t)\sin\frac{2n\pi t}{T}dt \end{aligned} \tag{3-6}$$

Applying the Euler theory to **Equations 3-5** and **3-6**, a complex Fourier expansion can be described by **Equations 3-7** and **3-8** as follows:

$$x(t) = \sum_{n=1}^{\infty} A_n e^{i2\pi nt/T} + \sum_{n=1}^{\infty} B_n e^{-i2\pi nt/T} \tag{3-7}$$

$$\begin{aligned} A_n &= \frac{a_n - ib_n}{2} = \frac{1}{T}\int_{-T/2}^{T/2} x(t)e^{-i2\pi nt/T}dt \\ B_n &= \frac{a_n + ib_n}{2} = \frac{1}{T}\int_{-T/2}^{T/2} x(t)e^{i2\pi nt/T}dt \end{aligned} \tag{3-8}$$

When n is defined in the range of $-\infty$ to ∞, **Equations 3-7** and **3-8** are presented as follows:

$$x(t) = \sum_{n=-\infty}^{\infty} C_n e^{i2\pi nt/T} \tag{3-9}$$

$$C_n = \frac{1}{T}\int_{-T/2}^{T/2} x(t)e^{-i2\pi nt/T}dt \tag{3-10}$$

If T is a finite number, T/n is then equal to a period of n-th harmonics and its reciprocal becomes frequency f_n, namely,

$$f_n = \frac{n}{T} \tag{3-11}$$

$$\delta f = \frac{1}{T} \tag{3-12}$$

where δf is the difference between side-by-side frequencies. Substituting **Equations 3-11** and **3-12** for **Equations 3-9** and **3-10** and calculating a limit of T, **Equations 3-9** and **3-10** are represented by **Equations 3-13** and **3-14**, namely,

$$x(t) = \int_{-\infty}^{\infty} X(f) e^{i2\pi ft} df \tag{3-13}$$

$$X(f) = \int_{-\infty}^{\infty} x(t) e^{-i2\pi ft} dt \quad . \tag{3-14}$$

Equations 3-13 and **3-14** are generally called Fourier integrals or Fourier transforms.

In this thesis, the joint surface roughness is estimated based on the property of spectrum after being analyzed by a Fourier transform. In this section, two kinds of Fourier transforms, namely, the fast Fourier transform (*FFT*) and the maximum entropy method (*MEM*), are applied to the analysis of the joint surface roughness. The influence of the determination of the joint surface roughness caused by the difference in Fourier transform methods is discussed.

a) Fast Fourier transform (FFT)

A fast Fourier transform is applied to a Fourier transform since it is faster than other methods. The Blackman-Tukey method (1958) was originally applied to the spectral analysis of random data. However, it requires much time to calculate. Based on the need to calculate faster and the fact that starting in the 1960s, the advantage of electronics made it possible to correct high-quality and large-size data, Cooley and Tukey (1965) developed the fast Fourier transform (*FFT*). However, *FFT* has not been the estimation method for spectra. It has been the algorithm for calculating Fourier coefficients faster from random data. The reduction in calculating time has been excellent. The power spectra of *JRC* 0-2, 8-10, and 18-20, from **Figure 3.1**, are shown in **Figure 3.2** using *FFT*, respectively. Other roughness are estimated with the same analysis.

In general, when calculating a power spectrum with *FFT*, truncation errors must be considered since random data are limited in number. In the case of *FFT*, it is usually to smooth spectrum applied some kinds of window function. In this thesis, the smoothing power spectrum for a given random sample of data is calculated by applying Parzen's lag window (Ohsaki, 1976a). The band range to a smooth spectrum, *band* [*Hz*], is defined as follows:

$$band = \frac{280}{151 \cdot u} \tag{3-15}$$

where u (*sec* or *mm*) is the limited range. Based on **Equation 3-15**, the limited range, u, is calculated. Then, Parzen's lag window, $W(\tau)$, is determined and the spectrum is smoothed. In the

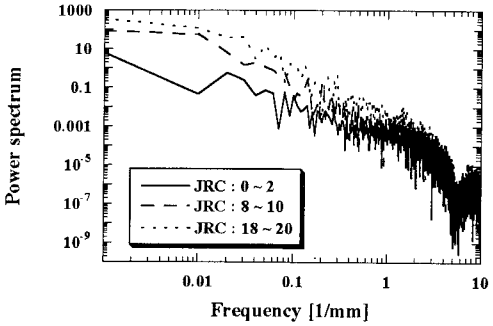

Figure 3.2 Power spectrum ~ Frequency relation by *FFT* method for representative *JRC* ranges

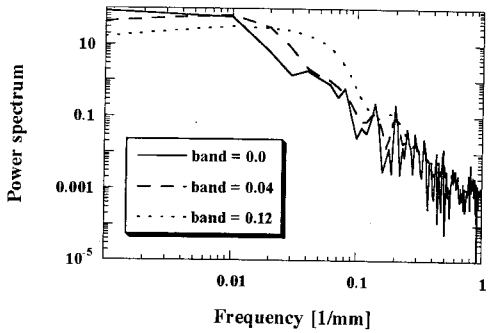

Figure 3.3 Power spectrum ~ Frequency relation for filtering with various band ranges : band (in the case of *JRC* 8 - 10)

case of *band* = 0.0, therefore, smoothing is not performed. **Figure 3.3** shows the power spectra of the *JRC* 8-10 roughness in the case of *band* = 0.0, 0.04, and 0.12, respectively.

b) Maximum entropy method (MEM)

FFT helps perform the spectral analysis much faster, but it is impossible for a performed *FFT* to escape the influence of truncation errors from random data. Burg (1967) suggested the estimated method of a spectrum from random data based on the concept that the spectrum is determined as the information entropy rises to its maximum. The information entropy of random time series data, $x(k\Delta t) = x_k$ $(k = 0, 1, \cdots, m)$, is defined by **Equation 3-16** as follows:

$$H = -\int p(x_0, x_1, \cdots, x_m)\log p\left(x_0, x_1, \cdots, x_m\right)dv \tag{3-16}$$

where p is the simultaneous probability distribution. When calculating the spectrum, p is presented by **Equation 3-17** based on the relationship between the spectrum and the auto-correlation, such as the Wiener-Khintchine theory, namely,

$$\int_{-f_N}^{f_N} P(f)e^{i2\pi fk\Delta t}df = C(k)$$
$$or \tag{3-17}$$
$$P(f) = \Delta t \sum_{n=-\infty}^{\infty} C(k)e^{-i2\pi fk\Delta t}$$

where f_N is the Nyquist frequency. Burg (1967) suggested that it was reasonable to estimate the auto-correlation function under the condition that the entropy had not increased, that is, the maximum entropy method (*MEM*),

$$\frac{\partial H}{\partial C(k)} = 0 \tag{3-18}$$

$$\int_{-f_N}^{f_N} \frac{e^{-2\pi fk\Delta t}}{P(f)} df = 0 \qquad (k \geq m+1) \quad . \tag{3-19}$$

Equation 3-19 shows that $1/P(f)$ can be an expanded limit series as follows:

$$1 / P(f) = (1 / \Delta t) \sum_{j=-m}^{m} b_j e^{i2\pi fj\Delta t} \quad . \tag{3-20}$$

And, the auto-correlation function is defined by **Equation 3-21**, namely,

$$C_k = \frac{1}{2\pi} \int_{-\pi}^{\pi} \frac{e^{2\pi fk\Delta t}}{\sum_{j=-m}^{m} b_j e^{i2\pi f_j \Delta t}} df \qquad (k = 0, 1, \cdots, N-1) \quad . \tag{3-21}$$

Since $P(f)$ is an even function, b_{-k} is equal to b_k. Therefore, the following resolution can be shown:

$$\sum_{j=-m}^{m} b_j e^{i2\pi f_j \Delta t} = \left| \sum_{k=0}^{N-1} \gamma_k e^{-2\pi f_k \Delta t} \right|^2 \quad . \tag{3-22}$$

If γ_k is a minimum phase, this resolution is unique. Then, in substituting **Equation 3-22** for **Equation 3-20**, the auto-correlation can be described by **Equation 3-23**, namely,

$$C_k = \frac{1}{2\pi} \int_{-\pi}^{\pi} \frac{e^{i2\pi fk\Delta t}}{\left| \sum_{s=0}^{N-1} \gamma_s e^{-2\pi fs\Delta t} \right|^2} df \qquad (k = 0, 1, \cdots, N-1) \quad . \tag{3-23}$$

In the next step, γ_k is estimated in **Equation 3-23** under the condition that C_k is known. **Equation 3-23** is multiplied by γ_t^* and the sum total is calculated, in other words,

$$\begin{aligned} \sum_{t=0}^{N-1} C_{t-k} \gamma_t^* &= \frac{1}{2\pi} \int_{-\pi}^{\pi} \frac{\sum_{t=0}^{N-1} \gamma_t^* e^{i2\pi f(t-k)\Delta t}}{\left| \sum_{s=0}^{N-1} \gamma_s e^{-2\pi fs\Delta t} \right|^2} df \\ &= \frac{1}{2\pi} \int_{-\pi}^{\pi} \frac{e^{-i2\pi fk\Delta t} \sum_{t=0}^{N-1} \gamma_t^* e^{i2\pi ft\Delta t}}{\left| \sum_{s=0}^{N-1} \gamma_s e^{-2\pi fs\Delta t} \right|^2} df \\ &= \frac{1}{2\pi} \int_{-\pi}^{\pi} \frac{e^{-i2\pi fk\Delta t} \sum_{t=0}^{N-1} \gamma_t^* e^{i2\pi ft\Delta t}}{\sum_{s=0}^{N-1} \gamma_s e^{-i2\pi fs\Delta t} \sum_{s=0}^{N-1} \gamma_s^* e^{i2\pi fs\Delta t}} df \end{aligned}$$

$$= \frac{1}{2\pi} \int_{-\pi}^{\pi} \frac{e^{-i2\pi fk\Delta t}}{\sum_{s=0}^{N-1} \gamma_s e^{-i2\pi fs\Delta t}} df \quad . \tag{3-24}$$

Since γ_S becomes the minimum value in **Equation 3-22**, the following relation can be shown:

$$1 / \sum_{s=0}^{N-1} \gamma_s e^{-i2\pi fst} = \sum_{n=0}^{\infty} \alpha_n e^{-i2\pi fn\Delta t} \quad . \tag{3-25}$$

Substituting **Equation 3-25** for **Equation 3-24** and integrating **Equation 3-24**, **Equation 3-26** can be shown as

$$\begin{aligned} \sum_{t=0}^{N-1} C_{t-k}\gamma_t^* &= \frac{1}{2\pi} \int_{-\pi}^{\pi} \frac{e^{-i2\pi fk\Delta t}}{\sum_{s=0}^{N-1} \gamma_s e^{-i2\pi fs\Delta t}} df \\ &= \frac{1}{2\pi} \int_{-\pi}^{\pi} \left(\sum_{n=0}^{\infty} \alpha_n e^{-i2\pi fn\Delta t}\right) e^{-i2\pi fk\Delta t} df \\ &= \frac{1}{2\pi} \int_{-\pi}^{\pi} \left(\sum_{n=0}^{\infty} \alpha_n\right) e^{-i2\pi f(k+n)\Delta t} df \\ &= \sum_{n=0}^{\infty} \alpha_n \delta(t + nt) \\ &= \alpha_n \delta_\tau \end{aligned} \tag{3-26}$$

where

$$\begin{aligned} &\delta_0 = 1, \quad \delta_\tau = 0 \ (\tau \neq 0) \\ &\alpha_0 = \sum_{m=1}^{N-1} C_m \gamma_m^* \end{aligned} \tag{3-27}$$

Introducing **Equation 3-26** to the matrix, **Equation 3-28** is shown as follows. It is generally called the Yule-Walker equation

$$\begin{bmatrix} C_0 & C_1 & \cdots & C_m \\ C_1 & C_0 & \cdots & C_{m-1} \\ \vdots & \vdots & \ddots & \vdots \\ C_m & C_{m-1} & \cdots & C_0 \end{bmatrix} \begin{bmatrix} 1 \\ \gamma_1 \\ \vdots \\ \gamma_m \end{bmatrix} = \begin{bmatrix} P_m \\ 0 \\ \vdots \\ 0 \end{bmatrix} \tag{3-28}$$

where γ_t is the prediction-error filter and P_m is the mean output from this filter. After calculating coefficient γ_k with **Equation 3-28**, the *MEM* spectrum can be determined from **Equations 3-20** and **3-22**, namely,

$$P(f) = 1 / \sum_{j=-m}^{m} b_j e^{-i2\pi fj\Delta t} = \Delta t \cdot \alpha_0 / \left| \sum_{k=0}^{N-1} \gamma_k e^{-i2\pi fk\Delta t} \right|^2 \quad . \tag{3-29}$$

There are two methods for solving **Equation 3-28**, namely, the Yule-Walker method and the Burg method. The Yule-Walker method is used when parameter C_k is known, while the Burg method is is used when parameter C_k is not known. In the Burg method, there are $m + 2$ numbers of unknown parameters, such as $\gamma_1, \gamma_2, \cdots, \gamma_m, C_m, and\ P_m$. Thus, other information will be needed to solve **Equation 3-28** since there are $m + 1$ numbers of equations in **Equation 3-28**. Under such this conditions, Burg suggested that the mean output, P_m, be reduced to a minimum, namely,

$$P_m = \left\{1/2(N-m)\right\} \sum_{i=1}^{N-m} \left\{ \left(x_i + \sum_{k=1}^{m} \gamma_{m,k} x_{i+k} \right)^2 + \left(x_{i+m} + \sum_{k=1}^{m} \gamma_{m,k} x_{i+m-k} \right)^2 \right\} \rightarrow \min . \tag{3-30}$$

In applying Levinson's algorithm, as shown in **Equation 3-31**, **Equation 3-30** is presented in **Equation 3-32** as

$$\begin{bmatrix} 1 \\ \gamma_{m,1} \\ \vdots \\ \gamma_{m,m-1} \\ \gamma_{m,m} \end{bmatrix} = \begin{bmatrix} 1 \\ \gamma_{m-1,1} \\ \vdots \\ \gamma_{m-1,m-1} \\ 0 \end{bmatrix} + \gamma_{m,m} \begin{bmatrix} 1 \\ \gamma_{m-1,m-1} \\ \vdots \\ \gamma_{m-1,1} \\ 1 \end{bmatrix} . \tag{3-31}$$

$$P_m = \left\{1/2(N-m)\right\} \sum_{i=1}^{N-m} \left\{ \left(b_{m,i} + \gamma_{m,m} b'_{m,i} \right)^2 + \left(b'_{m,i} + \gamma_{m,m} b_{m,i} \right)^2 \right\} \rightarrow \min . \tag{3-32}$$

Based on the condition that $\partial P_m / \partial \gamma_{m,m} = 0$, $\gamma_{m,m}$ is shown in **Equation 3-33** as follows:

$$\gamma_{m,m} = -2 \sum_{i=1}^{N-m} b_{m,i} b'_{m,i} / \sum_{i=1}^{N-m} \left(b_{m,i}^2 + b'^2_{m,i} \right) \tag{3-33}$$

where

$$\begin{aligned} b_{m,i} &= b_{m-1,i} + \gamma_{m-1,m-1} \cdot b'_{m-1,i} \\ b'_{m,i} &= b'_{m-1,i+1} + \gamma_{m-1,m-1} \cdot b_{m-1,i+1} \\ b_{0,i} &= b'_{0,i} = x_i,\ b_{1,i} = x_i,\ b'_{1,i} = x_{i+1} \end{aligned} \tag{3-34}$$

Using Levinson's algorithm, $\gamma_{m,k}$ and P_m are shown in **Equations 3-35** and **3-36**, respectively, as

$$\gamma_{m,k} = \gamma_{m-1,k} + \gamma_{m,m} \cdot \gamma_{m-1,m-k} \tag{3-35}$$

$$P_m = P_{m-1}(1 - \gamma_{m,m}^2) \tag{3-36}$$

Then, the power spectrum is shown in **Equation 3-37** through **Equation 3-29** as

$$P(f) = \Delta t \cdot P_m / \left| \sum_{k=0}^{m} \gamma_{m,k} e^{i2\pi fk\Delta t} \right|^2 . \tag{3-37}$$

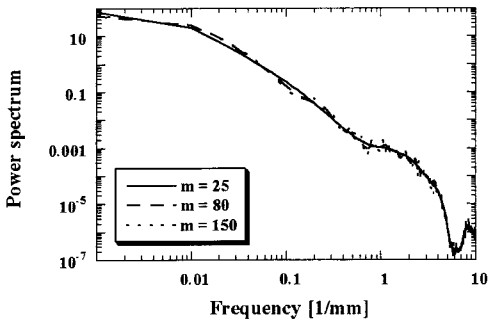

Figure 3.4 Power spectrum ~ Frequency relation for number of terms (m) in prediction-error function (in the case of *JRC* 8 - 10)

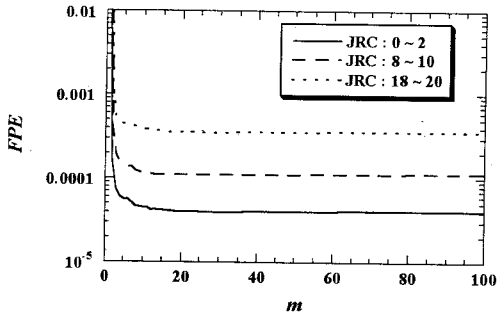

Figure 3.5 *FPE* ~ m relation

The advantages of *MEM* are that it is able to calculate the spectrum without the amount of data being restricted and it presents a high resolution of the spectrum (Hino, 1977a). On the other hand, the disadvantage of *MEM* is that it cannot reasonably show the standard determined number of limited terms, m, in the prediction-error filter (Hino, 1977b).

Figure 3.4 shows the results of the spectral analysis at *JRC* 8-10 using *MEM*. In this case, an analysis is done by changing the number of terms in the prediction-error filter, namely, m = 25, 50, 75, 80, 100, 150, and 200, respectively. In **Figure 3.4**, only the results for m = 25, 80, and 150 are shown. **Figure 3.5** then shows the relationship between the final prediction error (*FPE*) in the prediction-error filter and the number of terms, m, for *JRC* 0-2, 8-10, and 18-20, respectively. Akaike (1969a, b) defined *FPE* with the following equation:

$$(FEP)_m = S_m{}^2 \left\{ N + (m+1) \right\} / \left\{ N - (m+1) \right\} \tag{3-38}$$

where $S_m{}^2 = \sum_{in=m+1}^{N} \left(x_i + \gamma_{m,1} x_{i-1} + \gamma_{m,2} x_{i-2} + \cdots + \gamma_{m,m} x_{i-m} \right)^2 / (N-M)$. He suggested that the limited number of filter terms, m, was determined when *FPE* became minimum and the estimated range of m was presented by the following equation:

$$m < (2 \sim 3)\sqrt{N} \tag{3-39}$$

in which N represents the number of samples. As for the determination of the representative surface roughness, shown in **Figure 3.1**, 2048 points of data are handled and the range of m becomes $m < 90 \sim 136$. From **Figure 3.5**, the tendency exists for *FPE* to become constant around m = 20 in each type of *JRC*. According to **Figure 3.4**, the smooth shape of the spectrum can be found when m = 25 or 80. In the case of m = 150, however, which does not satisfy **Equation 3-39**, the shape of the spectrum is rough. Then, the stability of the spectral analysis is thought to be reduced. Based on the results in **Figures 3.4** and **3.5**, a spectrum analysis is carried out in this

research work with *MEM* under the condition that m is equal to 25. **Figure 3.6** shows the power spectra of *JRC* 0~2, 8~10, and 18~20, respectively, using an *MEM* analysis.

c) Comparison between FFT and MEM

As mentioned above, a spectral analysis of representative *JRC* applied to both *FFT* and *MEM* is performed. In the *FFT* spectrum, shown in **Figure 3.3**, the change in spectral shape depends upon the smoothing window. This change is more remarkable than the change in spectral shape which relies on the number of terms, m, in the prediction-error filter shown in **Figure 3.4**. In the case of the *MEM* analysis, the number of terms, m, can be determined by Akaike's concept (1969a, b). In the case of the *FFT* analysis, however, no standard for determining the band range for smoothing the spectrum has been established. In general, the method for determining the width of a band range is reasonable compared with some results by the human eye (Ohsaki, 1976c). In particular, *FFT* is sufficient for investigating only the frequency property of the wave. It is difficult, however, for an *FFT* analysis to determine the joint surface roughness in detail since the spectra of each representative *JRC* localize and concentrate under 1 *Hz* and the change in spectrum is not suitable for the quantitative determination of joint surface roughness using both the strength and the gradient of the power spectrum described in the following. The application of an *FFT* analysis limits the number of data to 2^N every time. In measuring the natural rock joint surface roughness, however, it is not necessary to measure the number of data at 2^N. In this case, after putting on 0-form data into the following part of the real data, the *FFT* analysis is performed. From **Figures 3.2** and **3.6**, the frequency properties of roughness are clustered, and the difference in spectra caused by the difference in roughness is very small. The joint surface roughness is sensitive, and the difference between real data and 0-form data and the physical meaning of 0-form data are unclear. Even if the joint surface roughness were measured accurately, it would probably not be reasonable to apply an artificial operation, such as putting on 0-form data into these roughness data so as to affect the influence of the artificial operation to spectral analysis. In performing the Fourier transform to roughness data, it is thought appropriate to apply a Fourier transform only to real data as much as possible. In consideration of these above points, an *MEM* analysis is conducted which yields a high-quality resolution and provides reliable results to the quantitative determination of joint surface roughness.

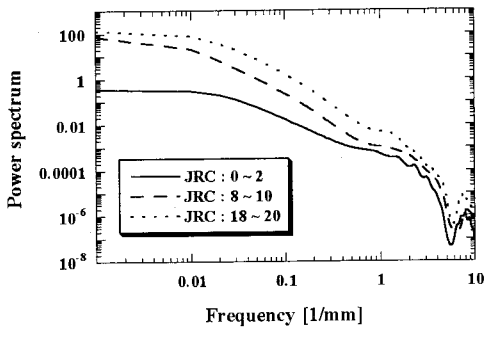

Figure 3.6 Power spectrum ~ Frequency relation by *MEM* for representative *JRC* ranges

3.2.3 Method of quantitative determination

a) Effective range of the spectrum

In typical results of the spectral analyses in **Figures 3.2** and **3.6**, the power spectrum in a lower frequency domain is larger than that in a higher frequency domain. As the frequency rises, the power spectrum gradually falls. This tendency can be found in each representative *JRC* in **Figure 3.1**.

The author considered which part of the power spectral distribution affected the shear behavior of the rock joint. In **Figures 3.2** and **3.6**, the maximum strength of the power spectrum is found to be in a lower frequency domain. In a domain of more than 1 *Hz*, the strength of the power spectrum appears to be less than 0.01% of the maximum. Based on the shear test results described in the following chapter, the peak shear strength can be found within a 0.5-*mm* shear displacement. That is, a 0.5-*mm* shear displacement is equal to 1% of the specimen length. A wave, whose frequency is more than 1 *Hz* (1/*mm*), is not affected by the shear behavior.

In general, when applying a Fourier transform to two types of waves which occur during the same time period but have different amplitudes, respectively, it is found that the strength of the spectra is proportional to the amplitude (Ohsaki, 1976d). The power spectrum, $P(f)$, and the Fourier amplitude spectrum, $B(f)$, are presented in the following proportional relation (Aizawa, 1992):

$$P(f) \propto |B(f)|^2 \quad . \tag{3-40}$$

It is assumed, therefore, that there is a proportional relationship between the amplitude and the power spectrum. Since the strength of a power spectrum with more than 1 *Hz* is less than 0.01% of the maximum, a wave with an amplitude of more than 1 *Hz* is less than 0.01 *cm* if the maximum strength of the power spectrum is 1, that is, the amplitude is 1 *cm*. Thus, the author defines the power spectral ratio, R_{ps}, representing the ratio of the maximum strength of the power spectrum, $P(f)_{max}$, to the strength of it at 1 *Hz*, $P(1)$, and the power spectrum ratio for all representative roughness values are shown in **Figure 3.7**.

$$R_{ps} = P(1) / P(f)_{\max} \quad . \tag{3-41}$$

From **Figure 3.7**, it is confirmed that in all *JRC*, the strength of the power spectrum at 1 *Hz* is less than 1/500 of the maximum strength. Therefore, it is thought that no wave of more than 1 *Hz* will affect the shear behavior and that waves of more than 1 *Hz* are eliminated when the roughness is determined.

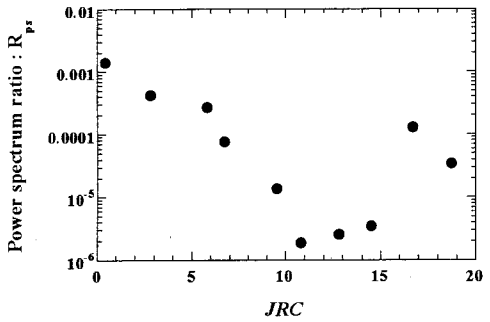

Figure 3.7 Power spectrum ratio (R_{ps}) ~ *JRC* relation by *MEM* (for $m = 25$)

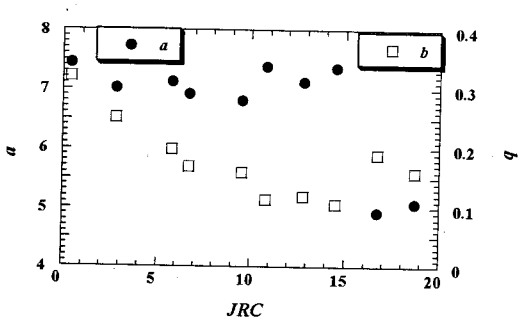

Figure 3.8 *a*- and *b*- values ~ *JRC* relation

b) Traditional methods for the quantitative determination of joint surface roughness

One type of quantitative determination for joint surface roughness is suggested. It states that the gradient of the power spectrum in the logarithmic space is calculated (Tanimoto, et al., 1991). The gradient of the power spectrum is calculated with a frequency domain of less than 1 *Hz* using the least-squares method. The approximate equation is shown as follows:

$$P = b \cdot f_r^{-a} \tag{3-42}$$

where P is the power spectrum [mm^2] and f_r is the space frequency [$1/mm$]. **Table 3.1** and **Figure 3.8** show *a*- and *b*-values for **Equation 3-42** for all representative *JRC* in the spectral analysis using *MEM* at $m = 25$. In comparing *MEM* with *FFT* at *band* = 0.0, 0.04, and 0.08, **Table 3.1** shows the *a*- and *b*-values calculated by *FFT*. As for the *FFT* analysis, for example, the *a*-value of *JRC* 4-6 at *band* = 0.0 is equal to that of *JRC* 0-2 at *band* = 0.04. Without the existence of a method to determine the band range of *FFT*, as mentioned above, it is impossible to determine one a-value against one *JRC*. Therefore, *FFT* is not suitable for the spectral analysis of joint surface roughness.

Table 3.1 *a* - and *b* - values for *JRC* profiles

JRC range	*JRC* value	*MEM* (m=25)		*FFT band*=0.0		*FFT band*=0.04		*FFT band*=0.08	
		a	*b*	*a*	*b*	*a*	*b*	*a*	*b*
0 - 2	0.4	7.4354	0.32071	8.1727	0.25847	7.4862	0.30828	7.3858	0.30570
2 - 4	2.8	7.0175	0.25175	8.0260	0.21858	7.0879	0.23599	6.9224	0.22971
4 - 6	5.8	7.1242	0.19882	7.4414	0.20834	7.0075	0.23431	6.8550	0.23717
6 - 8	6.7	6.9207	0.16992	6.9797	0.21332	6.8449	0.21480	6.7083	0.21824
8 - 10	9.5	6.8070	0.15923	7.2189	0.19388	6.7287	0.19517	6.5592	0.19091
10 - 12	10.8	7.3836	0.11383	7.3545	0.18976	7.0752	0.15481	6.7760	0.15083
12 - 14	12.8	7.1321	0.11972	7.1181	0.21020	6.8417	0.17789	6.6695	0.17379
14 - 16	14.5	7.3677	0.10643	7.7874	0.12363	7.1328	0.13876	6.7154	0.13702
16 - 18	16.7	4.9286	0.19034	4.5967	0.30464	4.4422	0.28283	4.3498	0.27778
18 - 20	18.7	5.0746	0.15924	5.1185	0.22897	4.7829	0.21128	4.6507	0.20902

According to **Figure 3.8**, with a *JRC* in the range of 0 to 16, the *a*-value remains constant and the *b*-value decreases. Then, the physical meanings of both *a*- and *b*-values are considered. Both parameters show the gradient of the spectral curve and the mean strength of the spectrum, respectively. That is, as the *a*-value is small, the power spectrum is distributed in a lower frequency domain, and as the *b*-value is large, the average of the power spectrum is too large. The fact that the power spectrum is large means that the unevenness of the roughness is strong and it is thought that the peak shear strength increases. When both *a*- and *b*-values are large, that is, the power spectrum has a wide distribution and its average strength is strong, the peak shear strength increases. On the other hand, when both *a*- and *b*-values are small, the peak shear strength decreases since the power spectrum has a narrow distribution and it is weak. In this way, when the joint surface roughness is determined, the *a*- and *b*-values present a close relation to each other and cannot be dealt with as independent parameters. However, both properties of frequency and unevenness must be totally considered for the quantitative determination of joint surface roughness.

One type of quantitative determination of rock joint surface roughness is the fractal dimension. Maetz and Franklin (1990) calculated the fractal dimensions for a representative *JRC* with the Yardstick method and compared them with the *JRC* values. They described the relationship between the *JRC* values and the fractal dimensions as having a linear approximation with a high correlation coefficient of 0.973. However, they showed that extremely little difference in fractal dimensions, such as a fractal range of 1.00 to 1.02, had been discussed in the estimation of joint surface roughness. In this case, the results are thought to depend on the resolution of both the input data and the analysis method. In general, when it is confirmed that power spectrum $P(f)$ is proportional to f^{-a}, the fractal dimension can be determined by **Equation 3-43** as follows:

$$D = \max\left(\frac{5-a}{2}, 1\right) \tag{3-43}$$

where D is the fractal dimension (Takayasu, 1987). Using this equation, the fractal dimensions for representative *JRC* are calculated with the results of the spectral analysis by *MEM* and all the fractal dimensions become 1. As for research on the estimation of rock joint surface roughness applied to the fractal analysis, works by Muralha and Charrua-Graca (1990), Barton and Larsen (1985), Turk, et al. (1987), Carr, et al. (1987), and Zipf and Bieniawski (1988) have been described. However, none of them is able to reasonably estimate the property of roughness from the following two points of view, namely, the difference in the estimated fractal dimension of the roughness is so extreme that it is impossible to measure the roughness which is not of high enough quality to resolve, and the physical meanings, such as the relation to mechanical properties of the fractal dimension, are not sufficiently clear.

c) Suggestion for the quantitative determination of joint surface roughness using M_S

Two new parameters, A_S and f_G, are suggested here in order to determine joint surface roughness in detail. One is the center of the frequency distribution and the other is parameter A_S, which is defined by the product of the strength of the power spectrum and the frequency resolution up to 1 *Hz*. These parameters are shown in the following equations:

$$A_s = \sum_{k=0}^{n} C_k \cdot \Delta f \tag{3-44}$$

$$f_G = \frac{\sum_{k=0}^{n} f \cdot C_k \cdot \Delta f}{A_s} \tag{3-45}$$

where C_k is the limited complex Fourier series, f is the space frequency [$1/mm$], Δf is the frequency resolution and n is represented as $n = 1 / \Delta f$.

f_G is located at the center of the frequency distributions, and if f_G increases, the power spectrum will have a wide distribution. On the other hand, if f_G decreases, it will have a narrow distribution. A_S can show the degree of unevenness for the roughness using **Equation 3-40**. That is, changes in the unevenness of the roughness are thought to affect the shear behavior and can be estimated by A_S. Fundamentally, as A_S increases, the peak shear strength also increases. **Table 3.2** presents A_S and f_G which have been calculated for ten types of representative *JRC*, as shown in **Figure 3.1**. **Figures 3.9** and **3.10** show the relationships between A_S and f_G and *JRC*, respectively. From **Figure 3.9**, it is found that A_S increases with a *JRC* in the range of 0 to 12. However, with a *JRC* in the range of 12 to 20, a good correlation cannot be found between A_S and *JRC*. On the other hand, as the *JRC* value increases, f_G decreases except with a *JRC* in the range of 8 to 16. Estimating the joint surface roughness with A_S and f_G is not enough to grasp the properties of the period and the asperity of the roughness at the same time. Thus, as an estimation of the combined properties of the period and the asperity of the joint surface roughness, the power spectral moment, an *Ms* value, is suggested. It is found by multiplying A_S and f_G. *Ms* is defined by the following equation:

$$M_s = f_G \cdot A_s \tag{3-46}$$

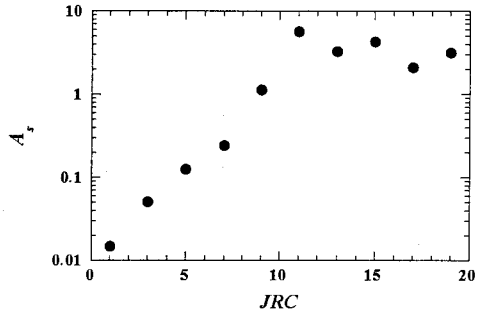

Figure 3.9 A_S ~ *JRC* relation

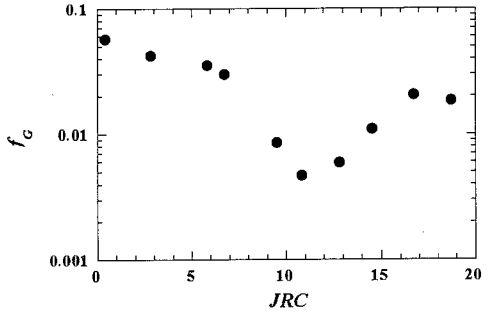

Figure 3.10 f_G ~ *JRC* relation

Table 3.2 A_S, f_G, and M_S-values for representative *JRC* profiles

JRC range	*JRC* value	A_S	f_G	M_S
0 - 2	0.4	0.01474	0.057630	0.0008493
2 - 4	2.8	0.05141	0.042020	0.0021600
4 - 6	5.8	0.12600	0.035240	0.0044410
6 - 8	6.7	0.24200	0.030190	0.0073170
8 - 10	9.5	1.1320	0.008573	0.0097020
10 - 12	10.8	5.6540	0.004673	0.026420
12 - 14	12.8	3.3020	0.005917	0.019530
14 - 16	14.5	4.2640	0.011020	0.047010
16 - 18	16.7	2.1060	0.020430	0.043020
18 - 20	18.7	3.1610	0.018440	0.058290

Table 3.2 and **Figure 3.11** show the relationship between *Ms* and *JRC*. It is thought that *Ms* can estimate both the period and the asperity of the joint surface roughness at the same time. In **Figure 3.11**, *Ms* increases as *JRC* increases. Based on **Figure 3.11**, the relationship between the *JRC* and the *Ms* values can be estimated as shown in **Equation 3-47**, namely,

$$JRC = \frac{\ln\left(\frac{M_s \cdot 10^3}{1.117}\right)}{0.23} \quad . \tag{3-47}$$

Using **Equation 3-47**, the *JRC* value has been calculated with the *Ms* value, and **Table 3.3** shows the results. In **Table 3.3**, it does not necessarily follow that the calculated *JRC* value is equal to Barton's *JRC* value, especially in the *JRC* range of 0-2, the calculated *JRC* value becomes negative. In fact, the coefficient of the correlation in **Equation 3-47** is 0.918, and there is not a high correlation. However, in consideration of the influence extracted from the representative *JRC* profiles in **Figure 3.1** and the background for determining *JRC* by Barton (1973), it is thought that *Ms* and **Equation 3-47** present a relatively good correlation for *JRC* in the forward analysis of rock joint surface roughness.

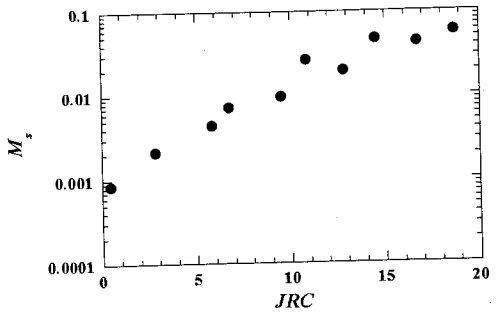

Figure 3.11 $M_S \sim JRC$ relation

Table 3.3 Comparison of calculated *JRC* and representative *JRC*

JRC range	*JRC* value	M_S	Calculated *JRC*
0 - 2	0.4	0.0008493	-1.19
2 - 4	2.8	0.0021600	2.87
4 - 6	5.8	0.0044410	6.00
6 - 8	6.7	0.0073170	8.17
8 - 10	9.5	0.0097020	9.40
10 - 12	10.8	0.026420	13.8
12 - 14	12.8	0.019530	12.4
14 - 16	14.5	0.047010	16.3
16 - 18	16.7	0.043020	15.9
18 - 20	18.7	0.058290	17.2

In considering the above-mentioned circumstances, the M_S value, defined by means of the power spectrum analyzed by *MEM*, is suggested for use in the estimation of rock joint surface roughness. This method is far better than other methods, from a resolution's point of view, and it is advantageous in that both the period and the asperity of the roughness can be grasped at the same time. Comparing *Ms* with *JRC*, the relationship between *Ms* and *JRC* can be obtained as shown in **Figure 3.1**. Therefore, knowledge of this relationship is very effective for grasping the joint surface roughness in detail.

3.3 Measurement and estimation of natural rock joint surface roughness and its estimation

3.3.1 Three-dimensional roughness profiler (*TOK-3DRP*)

Tanimoto, et al. (1990) developed a contact-type profiler as a roughness profiler for natural rock joints. Since it is a contact type of profiler, however, it measured extreme shearing off of the roughness. Therefore, it may not be able to (reasonably) measure the roughness exactly or to provide the amount of sheared roughness before or after performing the shear tests. Tanimoto and Kishida (1995) developed a three-dimensional non-contact roughness profiler (*TOK-3DRP*) and have used it to measure the joint surface roughness.

Photo 3.1 and **Figure 3.12** show the roughness profiler (*TOK-3DRP*). It consists of three parts, namely, the movable unit, the measuring unit, and the control unit. The measuring data are recorded in the computer through an amplifier.

a) The movable unit

With the movable unit, the *XY*-stage (LST-100XY(1) : Sigma Koki Co., Ltd.) is fixed on an anti-vibration pedestal made of cast iron. Since the movable adjuster sets the shear test's

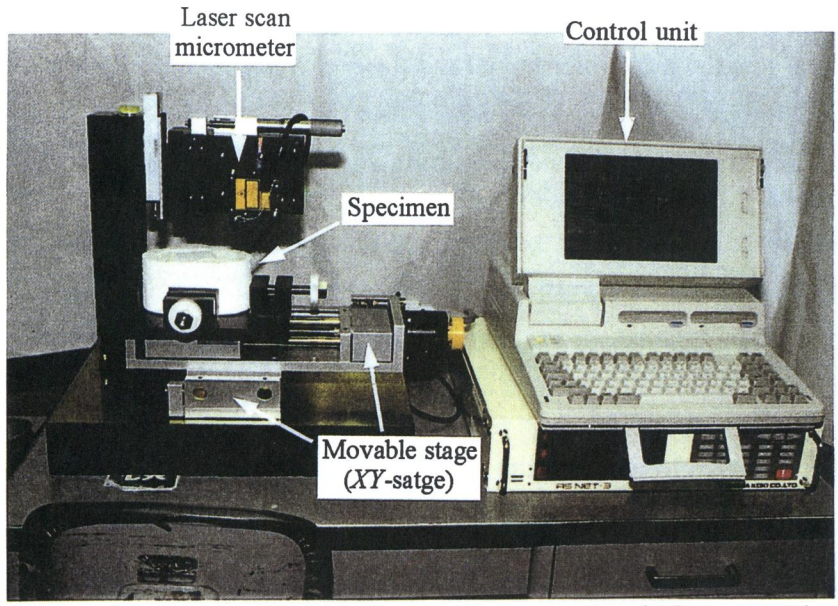

Photo 3.1 Apparatus of 3-D roughness profiler (TOK-3DRP)

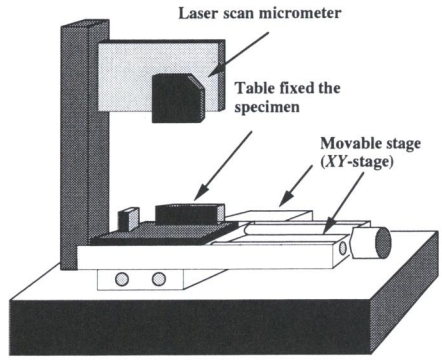

Figure 3.12 The roughness profiler (TOK-3DRP)

specimen up on a stage, the specimen can be fixed securely and reappearantly. The *XY*-stage consists of a movable guide, made of a linear ball bearing and a minute ball screw, which works when in motion. The guide is made of an aluminum alloy so as to be light in weight, but the structure is stiff enough. The movable mechanism is applied to a limit switch in order to prevent the movable guide from overrunning. The movable adjuster is designed for the exclusive use of the shear test's specimen, and it can be fixed to the specimen (through high reappearance) whose error is less than 1/1000 *mm*. In fact, since the movable adjuster has to work very effectively, changes in the roughness shape shown before and after the shear tests are discussed. As it is very easy to both set up the adjuster and remove it, the roughness of some types of specimens can be measured. Strokes in both *X* and *Y* directions are 100 *mm*.

b) The measuring unit

The measurement of the joint surface roughness is performed using a non-contact type of laser-scan micrometer (LB-045 : Keyence Co., Ltd.). This micrometer is fixed on an anti-vibration

pedestal with a bench, a guide, and a carrier. Since the stage can be adjusted and fixed on the micrometer with high accuracy, in both horizontal and vertical directions, the roughness can be measured. The focal length of the micrometer is 40 *mm* ± 5 *mm*, the minimum resolution of it is 4 *μm*, and the spot diameter is 0.2 *mm* ± 0.1 *mm*. Since the micrometer is fixed on the anti-vibration pedestal, no vibrations are noticed when measuring and no measurement errors are caused by such vibrations.

c) The control unit

As both the sampling interval and the number of scan lines are entered into the computer, data acquisition is fully automated. The control equipment used is AS-NET (Sigma Koki Co., Ltd.). Therefore, it is possible to move the *XY*-stage with an accuracy of 0.001 *mm*.

3.3.2 Measurement of natural rock joint surface roughness

In this research work, measurements of natural rock joint surface roughness are carried out through core samples. Fourteen kinds of specimens, including natural rock joints, are extracted through core samples recovered from Boreholes *A*, *B*, and *C* presented in Chapter 2 and shown in **Figure 3.13**(a). These specimens are used for direct shear tests and seismic propagating tests, as described in the following chapters. As for the rock types of the specimens, two are granite porphyry and twelve are rhyolite.

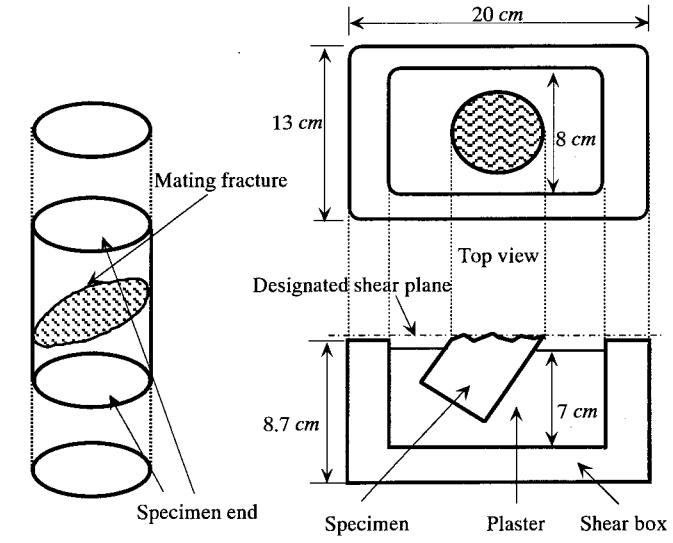

Figure 3.13 Setting of a natural joint into the shear box for the DTA-176 shear tester

The shape of the joint surface of each specimen is an oval, as shown in **Figure 3.13**(a). In the shear tests, two types of shear boxes are used. One is to set up an ordinary specimen, as shown in **Figure 3.13**(b), and the other is to extract a regular square section from the oval shape of the joint surface. The latter can be used easily to measure the roughness because of its regular square. On the other hand, since the former is oval, the condition of both the major and the minor axes must be considered. The specimen is set up such that the major axis is equal to the shear direction. First of all, the coordinates of both ends of the major axis are measured and the length of the major axis is calculated. In the next step, the number of measuring joints is entered into the computer. At the same time, the number of scan lines is parallel to the shear direction. As for the specimen with the oval shape, in this thesis, less than 49 scan lines and 512 points are measured along the major axis. Therefore, the measuring interval is constant for the same specimen. The number of measuring points varies according to the specimen and the scan line. The minimum number of measuring points for one scan line is 143. As for the specimens which have a regular square shape, on the other hand, they are measured at an interval of 0.5 *mm* in consideration of the spot diameter of the micrometer.

3.3.3 Results and analysis of natural rock joint surface roughness

Figure 3.14 shows a contour map of the natural rock joint surface roughness at Specimen No. *A*, while, **Figure 3.15** shows a bird's-eye view of the roughness. For each specimen, a different shape of roughness can be found. For each scan line, a spectral analysis by *MEM* has been carried out and the M_S value has been calculated, respectively. At the same time, the limited number of filter terms, m, has been set at 25 in consideration of the minimum number of measuring points on the shortest scan line. This number of terms satisfies **Equation 3-39**. In fact, *FPE* remains stable until there are 25 terms in each scan line.

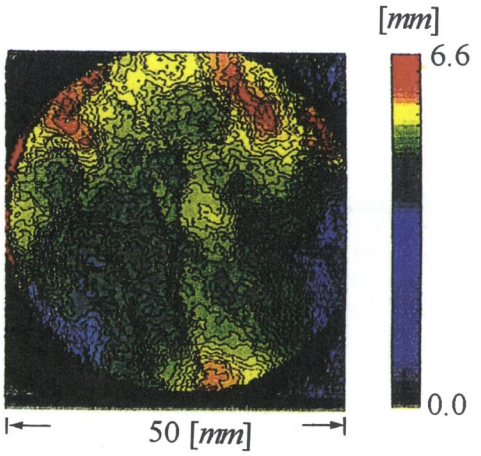

Figure 3.14 Contour map of natural rock joint surface roughness (Specimen No. *A*)

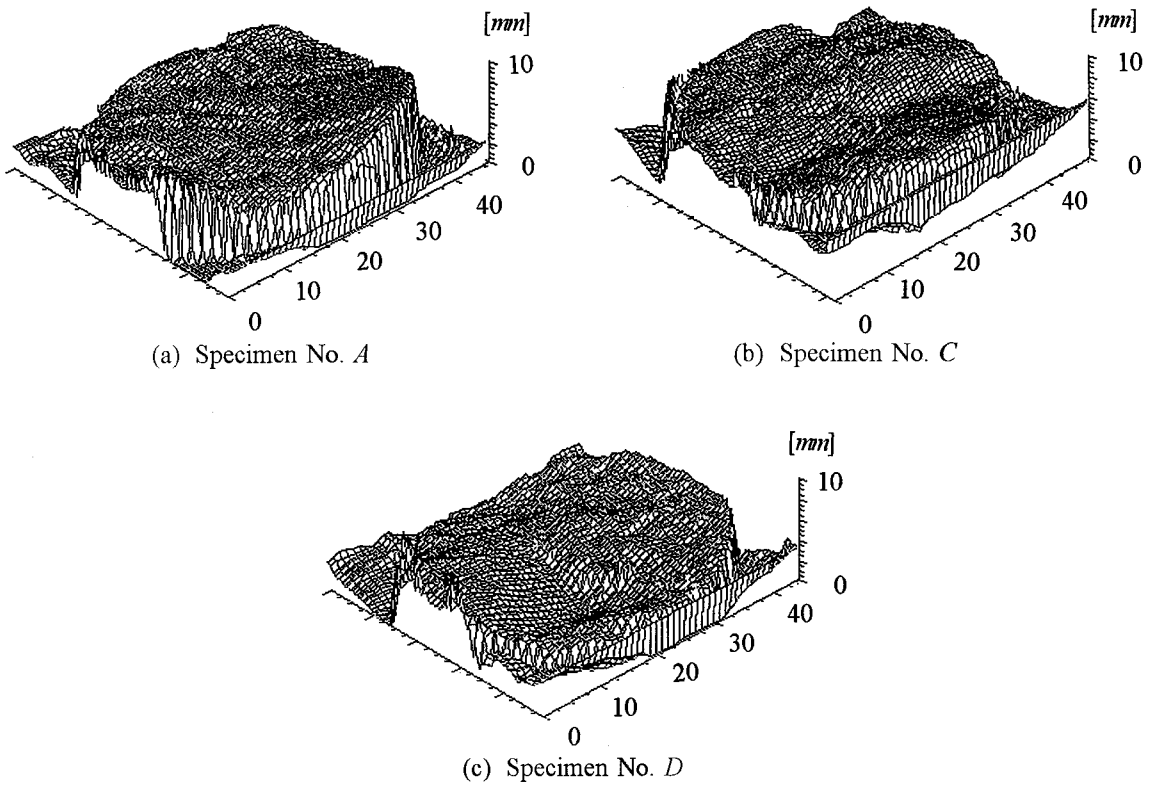

(a) Specimen No. *A*

(b) Specimen No. *C*

(c) Specimen No. *D*

Figure 3.15 Bird's-eye view of natural rock joint surface roughness

Since there are many scan lines for one specimen, many M_S values can be determined for each specimen. The following process is then defined so as to determine the representative M_S value for one specimen. First of all, each $M_{S,i}$ value is multiplied by each length, l_i, of the scan line, respectively, and its sum total, TM_S, is calculated with the following equation:

$$TM_s = \sum_{i=1}^{n} M_{s,i} \cdot l_i \tag{3-48}$$

where n is the number of scan lines. The representative M_S is defined by TM_S divided by TL, which is the total length of all the scan lines, in other words,

$$M_s = TM_s / TL \ . \tag{3-49}$$

Table 3.4 presents the M_S value for each specimen and the JRC value calculated by **Equation 3-47**.

3.4 Conclusion

In this chapter, the power spectral moment, M_S, has been defined through the results of a spectral analysis, and a quantitative determination of the natural rock joint surface roughness has been carried out. The conclusions are as follows:

Table 3.4 Measured M_S value of natural rock joint surface roughness

Specimen No.	M_S	*JRC*
A	9.121×10^{-3}	9.13
B	7.796×10^{-3}	8.45
C	1.112×10^{-2}	9.99
D	1.576×10^{-2}	11.51
E	2.791×10^{-2}	13.99
F	3.262×10^{-2}	14.67
1	1.533×10^{-2}	11.39
2	1.224×10^{-2}	10.41
3	2.021×10^{-2}	12.59
4	9.185×10^{-2}	20.92
5	8.730×10^{-2}	19.72
6	1.527×10^{-2}	11.32
7	2.436×10^{-2}	13.35

1) A spectral analysis has been performed on the representative *JRC*, suggested by Barton and Choubey (1977), and its power spectrum has been calculated. As for the spectral analysis of roughness, it has been confirmed that *MEM* has an advantage over *FFT*. With *MEM*, it is possible to calculate the spectrum of a high-quality resolution using a small amount of data; therefore, *MEM* can easily be applied to the measuring data of a specimen and reliable results can be obtained.
2) The M_S value has been defined in order to determine the roughness from the results of the spectral analysis. The M_S value presents the product of the center of the frequency distribution and the strength of the power spectrum in a range under 1 *Hz*. It is thought that the strength of the power spectrum represents the unevenness property of the roughness and the center of the frequency distribution represents the period property of it. Therefore, M_S has totally shown both unevenness and period properties of the roughness.
3) Barton's *JRC* has been determined using the M_S value. It has been confirmed that as the *JRC* value increases, the M_S value also increases. And, an equation describing the relationship between *JRC* and M_S has been introduced.
4) A roughness profiler has been developed to measure natural rock joint surface roughness accurately, and, the roughness has been measured by it. The M_S value, which represents the specimen, has been defined as the average M_S for each scan line in consideration of the weight value based on the scan length. Using the calculated M_S value, the *JRC* of the specimen can be estimated.

As mentioned above, the natural rock joint surface roughness has been determined quantitatively by the M_S value and the *JRC* has been calculated. It is necessary to confirm the relationship between the shear behavior and the M_S value, in particular, the relationship between

the peak shear strength from laboratory tests, M_S, and the peak shear strength estimated from Barton's empirical equation. They will be described in the following chapter.

REFERENCES

Aizawa, Y. (1992) : Chaos and 1/f fluctuation, *Mathematical Sciences*, Science Publisher, No. 349, pp. 8 - 16. (in Japanese)

Akaike, H. (1969a) : Fitting autoregressive models for prediction, *Ann. Inst. Statist. Math.*, Vol. 21, pp. 243 - 247.

Akaike, H. (1969b) : Power spectrum estimation through autoregressive model fitting, *Ann. Inst. Statist. Math.*, Vol. 21, pp. 407 - 419.

Barton, C. C. and Larsen, E. (1985) : Fractal geometry of two dimensional fracture networks at Yucca Mountain, Southwest Nevada, *Proc. of Int'l Symp. on Fundamentals of Rock Joints*, pp. 77 - 84.

Barton, N. (1973) : Review of a new shear-strength criterion for rock joints, *Engineering Geology*, Vol. 7, pp. 287 - 332.

Barton, N. and Choubey, V. (1977) : The shear strength of rock joints in theory and practice, *Rock Mechanics*, Vol. 10, pp. 1 - 54.

Blackman. R. B. and Tukey, J. W. (1958) : *The measurement of power spectra from the point of view of communication engineering*, Dover Publications, Inc..

Burg, J. P. (1967) : Maximum entropy spectral analysis, *Proc. of the 37th Annual International Meeting*, Soc. of Explor. Geophys..

Carr, J. R., et al. (1987) : Rock mass classification using fractal dimension, Proc. of 28th U. S. Rock Mech. Symp., pp. 73 - 80.

Cooley, J. W. and Tukey, J. W. (1965) : An algorithm for the machine calculation of complex Fourier series, Mathematics of Computation, Vol. 19, No. 90, pp. 297 - 301.

Goldstein, M., Goosev, B., Pyrogovsky, N., Tulinov, R. and Turovskaya, A. (1966) : Investigation of mechanical properties of cracked rock, *Proc. of 1st Congress of I.S.R.M.*, Lisbon, Vol. 1, pp. 521 - 524.

Goodman, R. E., Taylor, R. and Brekke, T. L. (1968) : A model for the mechanics of jointed rock, *Journal of SMFD*, A.S.C.E., Vol. 94, pp. 637 - 659.

Maetz, N. H. and Franklin, J. (1990) : Roughness scale effects and fractal dimension, *Scale Effects in Rock Masses*, Pinto da Cunha (ed.), Balkema, pp. 121 - 126.

Muralha, J. and Charrua-Graca, J. G. (1990) : An experience on the application of fractal theory to basic shear strength studies, *Rock Joints*, Barton and Stephansson (eds.), Balkema, pp. 667 - 671.

Hino. M. (1977a) : *Spectral analysis*, Asakura Publish Inc., pp. 91. (in Japanese)

Hino. M. (1977b) : *Spectral analysis*, Asakura Publish Inc., pp. 221 - 222. (in Japanese)

Ohsaki, Y. (1976a) : *Introduction to the spectral analysis for seismic waves*, Kajima Publish Inc., pp. 150 - 154. (in Japanese)

Ohsaki, Y. (1976b) : *Introduction to the spectral analysis for seismic waves*, Kajima Publish Inc., pp. 159 - 165. (in Japanese)

Ohsaki, Y. (1976c) : *Introduction to the spectral analysis for seismic waves*, Kajima Publish Inc., pp. 158. (in Japanese)

Ohsaki, Y. (1976d) : *Introduction to the spectral analysis for seismic waves*, Kajima Publish Inc., pp. 106 - 107. (in Japanese)

Patton, F. D. (1966) : Multiple modes of shear failure in rock, *Proc. of 1st Congress of I.S.R.M.*, Lisbon, Vol.1, pp. 509 - 513.

Takayasu, H. (1987) : *Fractal Science*, Asakura Publish Inc., pp. 240. (in Japanese)

Tanimoto, C., et al. (1990) : Roughness and shear behavior of rock joints, *Proceedings of the 8th Japan Symposium on Rock Mechanics*, ISRM-Japan, pp. 103 - 108. (in Japanese)

Tanimoto, C. and Kishida, K. (1995) : Quantitative determination of rock joint roughness by 3-D non-contact type profiler and the maximum entropy method, *Journal of Geotechnical Engineering*, J.C.S.E., No. 511/III-30, pp. 57 - 67.

Turk, N., et al. (1987) : Characterization of rock joint surface by fractal dimension, *Proc. of 28th U. S. Rock Mech. Symp.*, pp. 1223 - 1226.

Zipf, R. K. and Bieniawski, Z. T. (1988) : Microscopic studies of fractures generated under mixed mode loading, *Proc. of 29th U. S. Rock Mech. Symp.*, pp. 151 - 158.

Chapter 4

Experimental Study on the Shear Behavior of Rock Joints through Direct Shear Tests

4.1 Introduction

In general, the mechanical behavior of a jointed rock mass is strongly controlled by the rock joints and/or discontinuities. The mechanical behavior of rock joints is represented by both normal and shear behaviors. The shear behavior of rock joints is affected by several parameters, namely, joint surface roughness, the material properties of the intact rock, normal confining conditions, the weathering of the joint surfaces, the filling materials, etc.. Due to the combined effect of these parameters, it is not easy to precisely estimate the shear behavior of rock joints.

As mentioned in the previous chapter, Barton (1973) presented his empirical relationship among peak shear strength, joint surface roughness, the material properties of intact rock, and normal confining stress. Again, it is written as follows:

$$\tau_p = \sigma_n \cdot \tan\left\{ JRC \log\left(\frac{JCS}{\sigma_n}\right) + \phi_b \right\} \qquad (4\text{-}1)$$

where τ_p : peak shear strength
σ_n : effective normal stress
JRC : joint roughness coefficient
JCS : joint wall compressive strength
ϕ_b : basic friction angle (obtained from residual shear tests on flat unweathered rock surfaces).

In **Equation 4-1**, JRC is estimated by back analyzing the shear tests that have been performed. By conducting the shear tests, the peak shear strength and the effective normal stress can be obtained from the results. JCS is determined by a Schmidt hammer test. Then, JRC is calculated by applying these parameters to **Equation 4-1**.

On the other hand, Thapa et al. (1995 and 1996) explained how to estimate joint surface roughness from a borehole survey using the borehole scanner system (Tanimoto, et al., 1995) and image processing techniques. Based on the results, they then simulated the shear behavior through both a kinematic displacement dilation analysis and *DDA* (discontinuous deformation analysis). According to this method, if a relationship between the shear behavior of rock joints and several joint properties (joint surface roughness, the material properties of intact rock, normal

confining conditions, etc.) is established, the shear behavior of the rock joints survey can be determined from the borehole.

Direct shear tests are carried out on rock joints under various confining conditions, namely, a constant normal confining condition, a non-linear normal confining condition, and a constant loading angle condition. As for the constant loading angle test, it will be described in the following chapter since its results are used to discuss the determination of joint stiffness through borehole loading tests. In performing the shear tests, reproduced specimens as well as natural rock joints are used. The influence of the joint surface roughness on the shear behavior is considered. In addition, when making reproduced specimens, the combination ratio of water, cement, and sand is changed and the influence of the material strength is discussed. In this chapter, the shear behavior of rock joints is estimated through these laboratory shear tests. First of all, a comparison is made between the peak shear strength in laboratory tests and the estimated peak shear strength using Barton's equation (**Equation 4-1**). After discussing the validity of M_S, JRC, and Barton's empirical equation, as described in Chapter 3, an estimation of the natural rock joint surface roughness is suggested in consideration of the shear behavior. Then, some types of shear behavior are estimated, namely, the peak shear strength, the shear displacement, the shear-stress relation, and the displacement dilation, in consideration of joint surface roughness, the material strength of the intact rock, and the effective normal stress.

4.2 Direct shear tests in the laboratory

4.2.1 Direct shear tester

The direct shear tester of the rock joints (DAT-176, Seikensya), used to perform tests in this research work, was developed so as to investigate the shear behavior of rock joints (Tanimoto, et al., 1990 and 1991). A personal computer controls its performance test by test. **Photo 4.1** and **Figure 4.1** show the tester.

The horizontal-loading mechanism consists of electric- and mechanical-type motors and a load cell, whose maximum capacity is 2 *tf*. It works to measure the horizontal load. On the other hand, the vertical-loading mechanism consists of two interlocking systems, such as the constant-loading type powered by air pressure and the constant-displacement type powered by both electric and mechanical motors. The load cell, whose maximum capacity is 2 *tf*, also works to measure the vertical load.

The shear box is divided into upper and lower parts. The specimen can be fixed directly into the lower part. The roller bearing is installed in the upper part in this study so that the specimen can be moved in a vertical direction without the influence of friction. In measuring the

shear displacements, the displacements of both upper and lower parts are measured and the difference between the displacements, such as the relative displacement, represents the output data. The vertical displacement is measured at two points on the upper part of the shear box, and it is shown by the average of the two points.

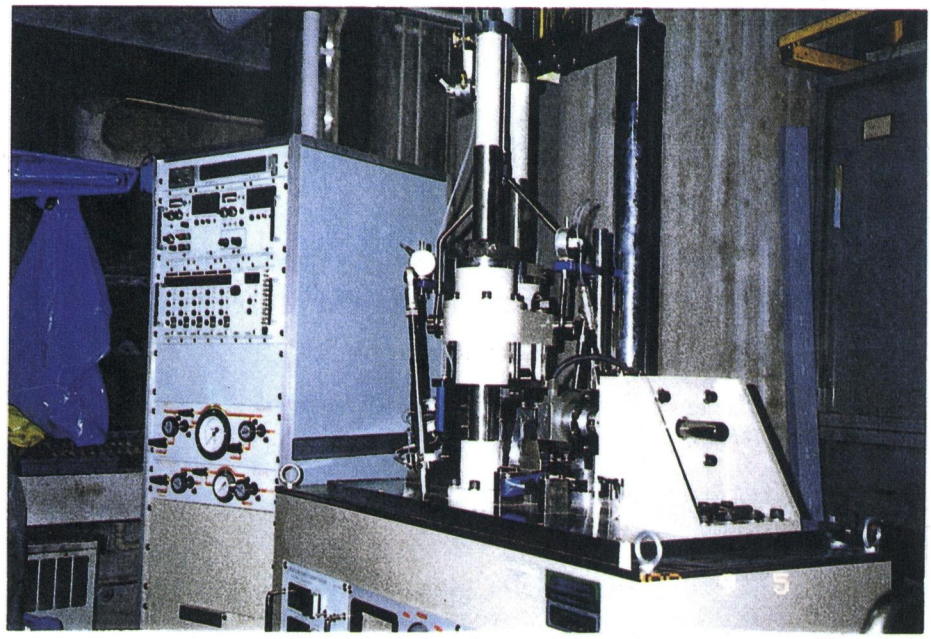

Photo 4.1 The direct shear tester of rock joints (DAT-176, Seikensya)

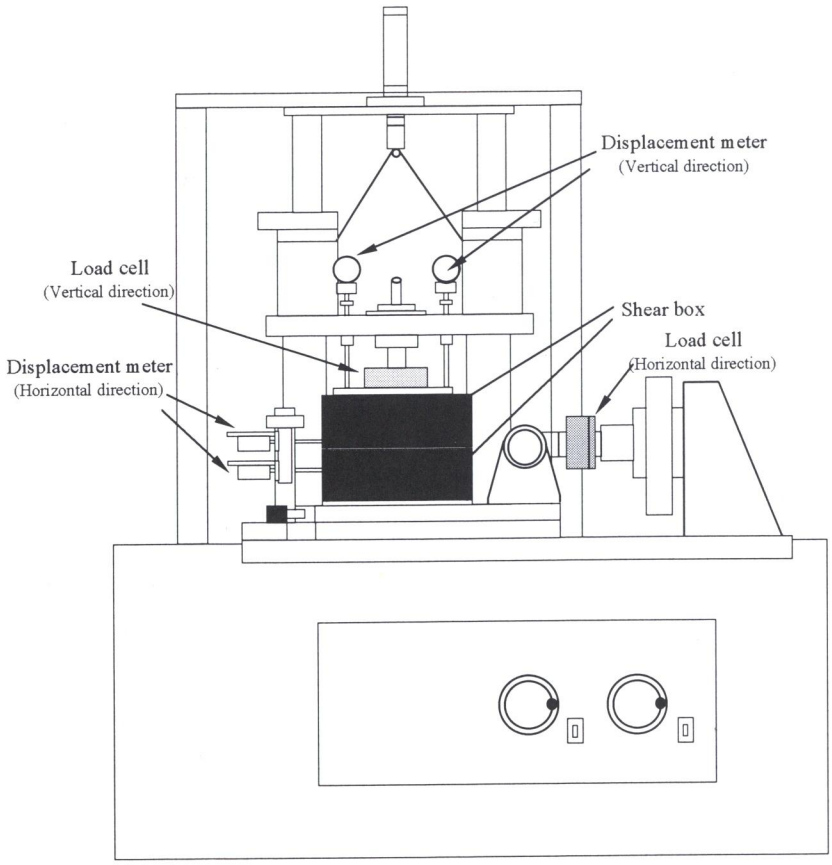

Figure 4.1 Rock joint direct shear tester (DAT-176, Seikensya)

4.2.2 Specimens

The specimens employed in the laboratory direct shear tests include natural joints taken from core samples (60 *mm* in diameter). After choosing seven kinds of natural joint surface roughness, impressions are made of them. Using the impressions, reproduced plaster specimens are then created. The impressions are made of Silicon rubber (TSE350, Toshiba Silicon). To make plaster specimens, two types of cement (Type A : Jet cement made by Sumitomo Cement Co. and Type B : Densit-binder made by Electric and Chemical Industry Co.) are used. By changing the combination ratio of cement, sand, and water, as shown in **Table 4.1**, three kinds of reproduced plaster specimens, which are representative of the different uniaxial compressive strengths, are made. When using the Jet cement, Keisa No. 6 aggregate sand is used. On the other hand, in the case of the Densit-binder cement, a combination of sand, namely, Keisa Nos. 3, 4, 5, and 6, is applied to make the plaster in combination ratios of 35.0%, 22.5%, 22.5%, and 20.0%. The basic friction angle of each material, shown in **Table 4.1**, was measured through direct shear tests on the specimen, which included a smooth joint, under various confining conditions, until the dilatancy was no longer found. Variations in surface roughness and material strength contained in the samples allowed us to carry out many types of direct shear tests. Thus, it is possible to discuss the results in view of the influence of joint surface roughness, the material strength of intact rock, and the effective normal stress.

Table 4.1 The combination ratio of cement, sand, water, and the uniaxial compressive strength and basic friction angles

Cement type	Cement : Sand : Water	σ_c (28th days)	ϕ_b
A	1 : 1: 0.375	52.0 *MPa*	38.0°
B	1 : 2 : 0.65	28.0 *MPa*	38.6°
C	1 : 1 : 0.2	100.0 *MPa*	11.3°

The measurement of joint surface roughness is performed using a non-contact type of laser-scan micrometer which is situated on a three-dimensional movable stage, a 3-D roughness profiler, as shown in **Figure 4.2** (TOK-3DRP) (Tanimoto & Kishida, 1994 & 1995). Data acquisition is fully automated by a computer and each joint surface roughness is measured at 0.5 *mm* intervals. A bird's-eye view of the measured joint surface roughness on both upper and lower sides of Specimen No. 5 is shown in **Figures 4.3**(a) and (b).

4.2.3 Shear loading conditions

In general, direct shear tests on rock joints are conducted under a constant normal confining condition. That is the reason why the control system is easy and the influence of some effective

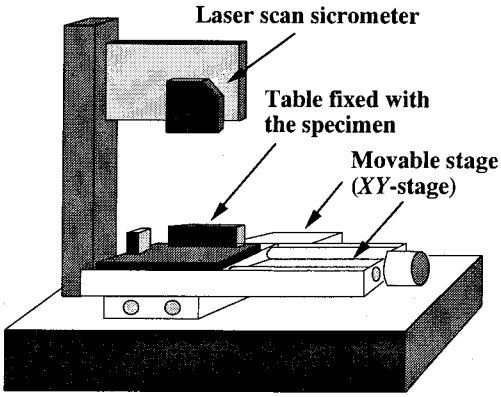

Figure 4.2 Roughness profiler (TOK-3DRP)

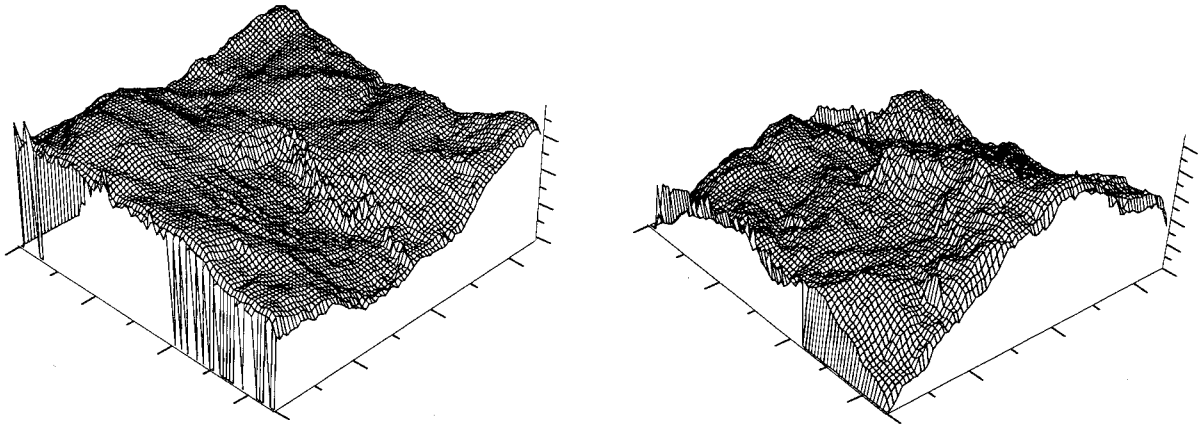

(a) Upper surface roughness (b) Lower surface roughness

Figure 4.3 Bird's-eye view of natural rock joint surface roughness

factors on the joint shear behavior can be understood without difficulty since the normal confining pressure, which is one of several effective factors, has already been grasped. As for the confining conditions of rock joints in the field, however, when the dilatancy is presented, it is thought that the confining pressure on the rock joints becomes variable due to the interlocking rock masses. In consideration of this matter, some researchers have carried out constant normal stiffness tests. In such tests, the normal confining pressure increases in proportion to the dilation of the rock joint. **Figures 4.4**(a), (b), (c), and (d) show the concept of each condition in the direct shear tests.

In this research work, direct shear tests are carried out not only under a constant normal confining condition, but also under a variable normal confining condition so as to grasp the properties of the shear behavior of the jointed rock masses.

Constant normal stiffness tests on the variable confining conditions are described as follows.

In past studies, since only an electric analog controller was provided for the control system of the direct shear tester in our laboratory, only tests under simple test conditions, such as

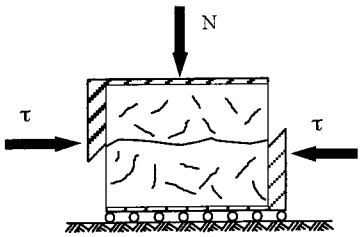

(a) The constant normal condition

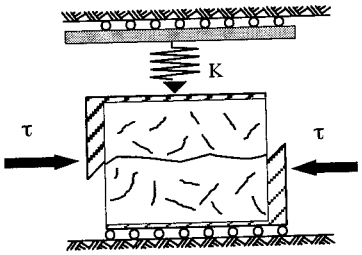

(b) The variable normal condition

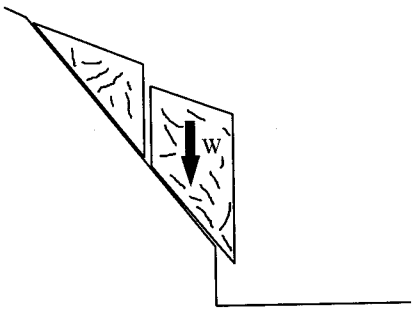

(c) The failure at the slope

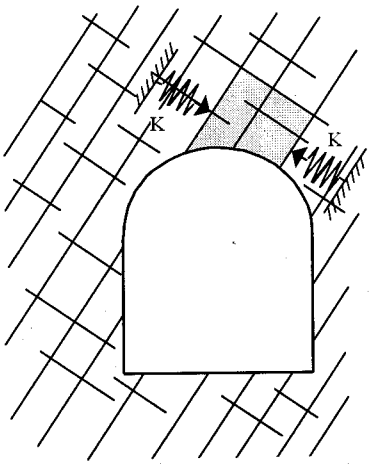

(d) The mechanical behavior of rock masses around an underground cavern

Figure 4.4 The concept of each direct shear test

constant normal confining and constant normal displacement, were carried out. However, since the control unit in the tester was introduced to the computer, direct shear tests can be performed in consideration of the in-situ confining conditions. **Figure 4.5** shows the control system of the direct shear tests.

The mechanical behavior of rock joints is presented as nonlinear. As for the relationship between normal stress (σn) and joint closure (ΔVj), the tangent gradient of the stress-displacement curve is gentle under the initial loading terms. But the gradient increases as the load increases. As for this mechanical behavior of rock joints, Bandis et al. (1983) suggested the hyperbolic approximate model as shown in the following equations:

$$\Delta V_j = \frac{\sigma_n \cdot V_m}{K_{ni} \cdot V_m + \sigma_n} \tag{4-2}$$

and

$$K_n = K_{ni}\left[1 - \frac{\sigma_n}{K_{ni} \cdot V_m + \sigma_n}\right]^{-2} \tag{4-3}$$

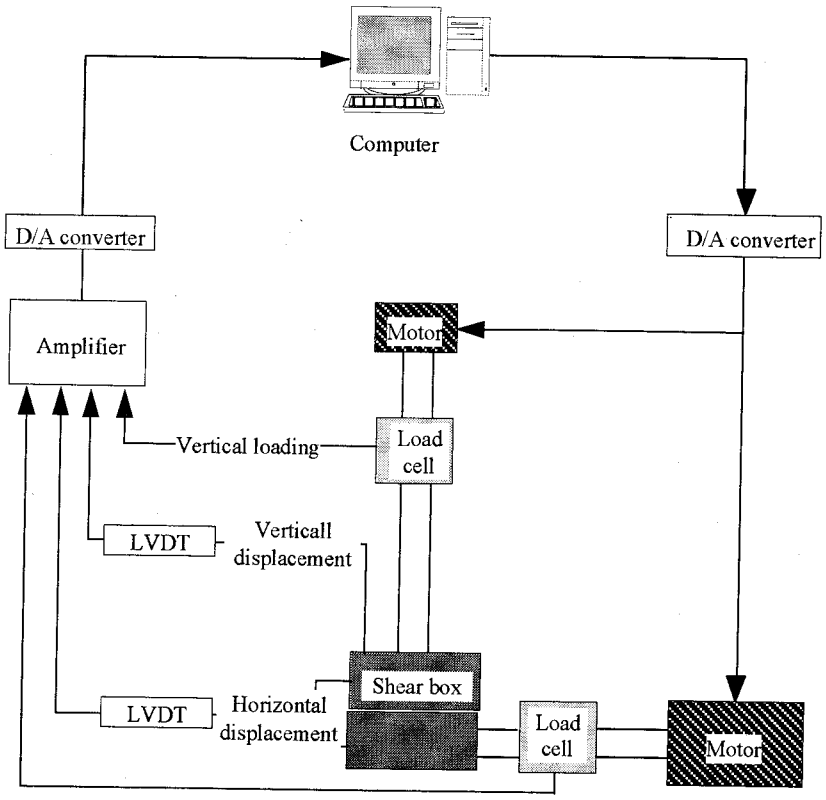

Figure 4.5 The control system of the direct shear tests

where ΔV_j is the joint closure under a given σ_n, V_m is the maximum closure, K_n is the normal stiffness of a joint, and K_{ni} is the initial normal stiffness. The values of K_{ni} and V_m uniquely define the hyperbolic stress ~ closure relation of a joint. The value of σ_n may be found from the derivative of **Equation 4-2**, namely,

$$\sigma_n = \frac{\Delta V_j \cdot V_m \cdot K_{ni}}{V_m - \Delta V_j} \quad . \tag{4-4}$$

In fact, since many joints can be found in in-situ rock masses, the mechanical behavior of jointed rock masses shows non-linearity. For example, for load~displacement curves obtained by borehole jacking and/or plate jacking in the field, the deformation coefficient increases along with increments in the displacement. **Figure 4.6** shows a sample of the load - displacement curve obtained through borehole jacking.

In this research, direct shear tests are carried out in consideration of in-situ confining conditions, so that for increments in joint dilation, the normal confining stress is increasingly non-linear. Based on the hyperbolic function shown in **Figure 4.7** and **Equation 4-4**, the control model has been determined as follows:

$$\sigma_n = \sigma_{ni} + \frac{K_{ni} \cdot \delta_{max} \cdot \delta}{\delta_{max} - \delta} \tag{4-5}$$

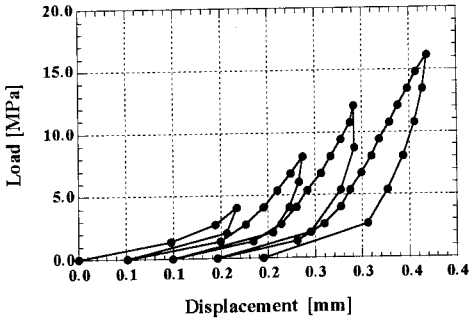

Figure 4.6 A sample of a load-displacement curve obtained through borehole jacking

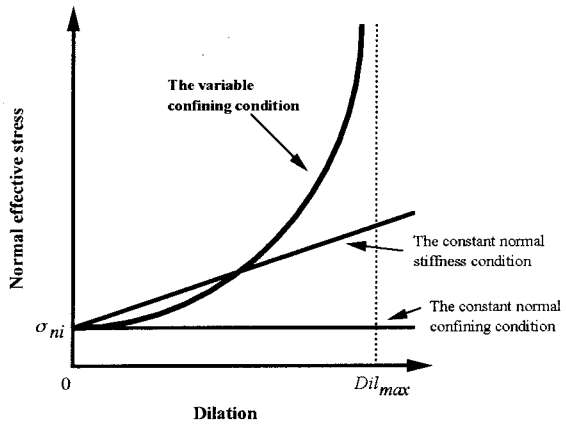

Figure 4.7 The loading system under the variable confining condition

where K_{ni} is the initial joint normal stiffness and δ_{max} is the maximum dilation. A shear test of this type is called a variable confining condition test.

4.2.4 Experiments

In this study, direct shear tests are conducted under the following conditions. As for the constant normal confining condition , direct shear tests on rock joints are carried out under a constant normal stress (σ_n = 0.032, 0.2, 0.4, and 0.8 *MPa*). Until reaching a shear displacement of 4 *mm* (1% of the specimen's length), the shear tests, which are carried out at a velocity of 0.2 *mm/min.*, are performed. Three types of specimens, described above, are applied. As for the varying confining conditions, on the other hand, one type of specimen, whose uniaxial compressive strength is 52.0 *MPa*, is applied. The initial normal stress, σ_{ni}, is 0.2 *MPa*, while the initial normal stiffness, K_{ni}, is 1.0 *MPa/mm*. The maximum dilation, δ_{max}, is fixed at 0.8, 1.0, and 1.5 *mm*, respectively. Then, the direct shear tests are performed.

4.3 Results of direct shear tests on rock joints

4.3.1 Constant normal confining condition

(a) The influence of normal stress

Figures 4.8(a), (b), and (c) show shear stress - shear displacement curves, stress ratio - shear displacement curves, and dilatancy curves for Specimen No. 6 whose uniaxial compressive strength is 100 *MPa*. Under conditions of identical roughness and material strength, increases in peak shear strength and residual strength can be associated with decreases in dilation due to increases in effective normal stress. In the range of a lower effective normal stress, the peak shear

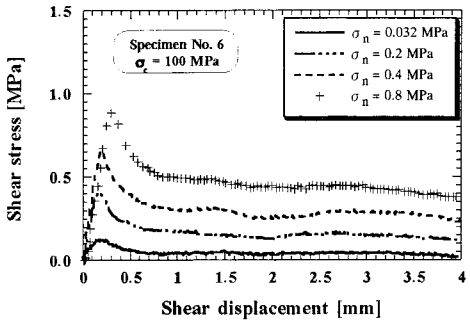

(a) Shear stress - shear displacement curves

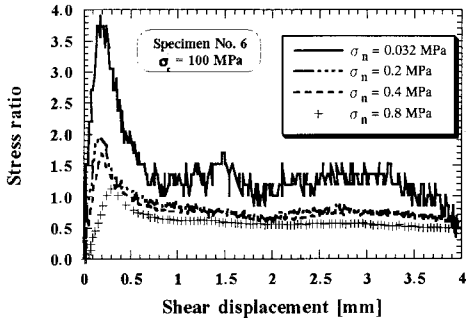

(b) Stress ratio - shear displacement curves

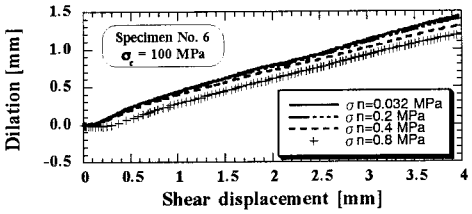

(c) Dilatancy curves

Figure 4.8 The results of shear tests under conditions of identical roughness and material strength (Specimen No. 6, $\sigma_C = 100\,MPa$)

displacement appears around 0.2 *mm*. On the other hand, the peak shear displacement moves toward 0.3 *mm* due to increases in effective normal stress. Considering the above-mentioned phenomena, increases in sheared-off asperities cause increases in both peak shear strength and displacement.

Figure 4.9 shows the relationship between the normal effective stress and the peak shear strength. For increments in normal effective stress, it is confirmed that the peak shear strength also increases in all specimens. However, there are varying degrees of increments for the peak shear strength of each specimen. The joint surface roughness is affected by this phenomena.

Coulomb's linear relation is basically fitted as follows:

$$\tau_p = c + \sigma_n \tan \phi \qquad (4\text{-}6)$$

to the normal effective stress - the peak shear strength relation, where c is the cohesion intercept and ϕ is the friction angle. In every specimen, cohesion intercept c can be found. In the case of the shear behavior of rock joints, c is thought to determine whether the upper roughness and the lower roughness match well or not under the initial condition, and c strongly affects the shear behavior of rock joints. However, it is difficult to present the influence of joint surface roughness using parameter c. Thus, the shear behavior has been discussed using the stress ratio which is the ratio of shear strength to normal effective stress. It is shown in **Figure 4.8**(b) as the parameter which presents the direction of the resultant force against the roughness.

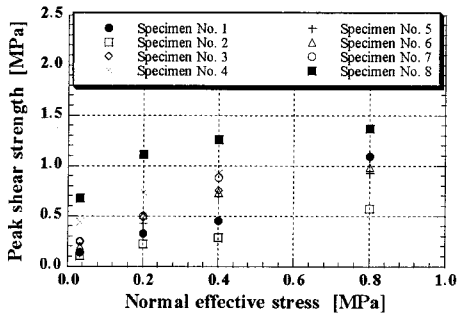

(a) Material strength σ_c = 100.0 *MPa*

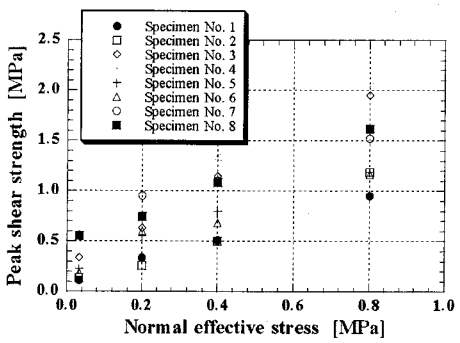

(b) Material strength σ_c = 52.0 *MPa*

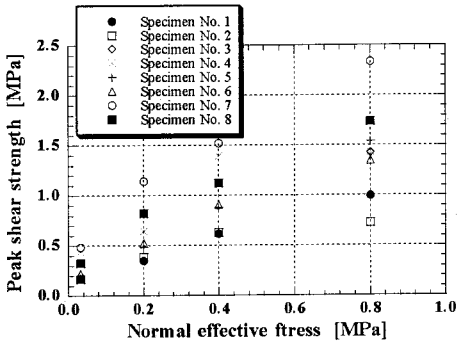

(c) Material strength σ_c = 28.0 *MPa*

Figure 4.9 The relationship between peak shear strength and normal effective stress

Figures 4.10(a), (b), and (c) show the relationship between the normal effective stress and the peak stress ratio for each specimen. From these figures, it is found that the stress ratio decreases with increments in the normal effective stress. If the joint surface were smooth, the stress ratio would be equal to tan ϕ_μ, which is the frictional sliding resistance, and it would not depend on the normal effective stress. Therefore, the variety of peak stress ratios is controlled by the influence resulting from whether the upper and the lower roughness match well or not. This factor is defined as the interlocking index, I_i, as presented in **Figure 4.11** and the following equation:

$$I_i = \frac{\tau_p}{\sigma_n} - \tan \phi_\mu \tag{4-7}$$

From **Figure 4.11**, it is found that the interlocking index decreases with increments in the normal effective stress. This is thought to be the reason why, as the resultant forces on the joints increase, the destruction and the deformation of the joint asperity increase and the interlocking of the surface roughness changes. As for the range in lower effective stress, the interlocking index shows a large value when the destruction of the joint asperity does not occur.

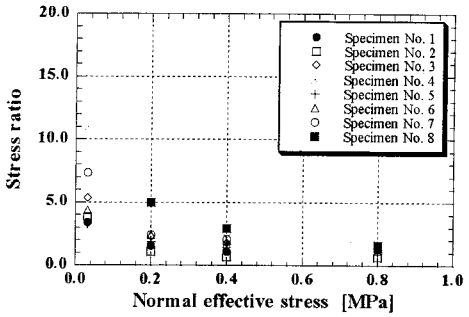

(a) Material strength $\sigma_c = 100.0\ MPa$

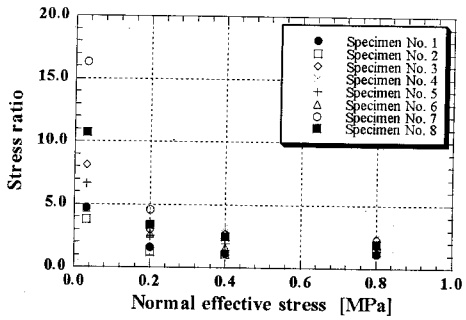

(b) Material strength $\sigma_c = 52.0\ MPa$

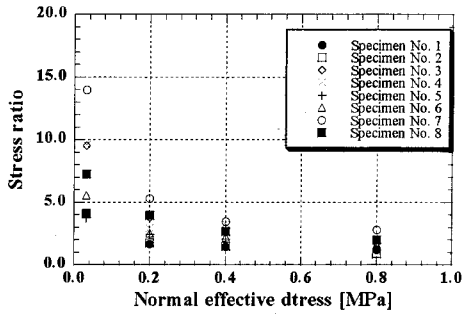

(c) Material strength $\sigma_c = 28.0\ MPa$

Figure 4.10 The relationship between stress ratio and normal effective stress

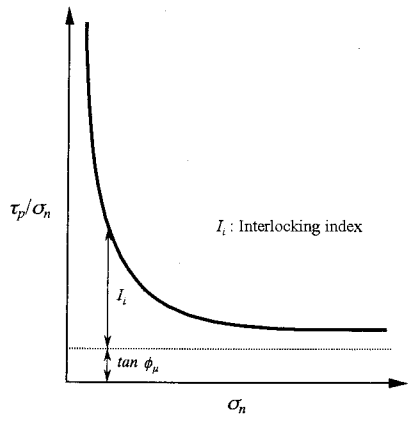

Figure 4.11 The concept of interlocking index, I_i

(b) The influence of joint surface roughness

Figures 4.12(a), (b), and (c) show shear stress - shear displacement curves, stress ratio - shear displacement curves, and dilatancy curves under constant conditions of both uniaxial compressive strength ($\sigma_c = 100\ MPa$) and effective normal stress ($\sigma_n = 0.8\ MPa$). Differences in joint surface roughness can be seen to cause changes in the peak shear strength, residual strength, dilatancy, and peak shear displacement. The influence of joint surface roughness on the shear behavior will be discussed in detail in the following sections.

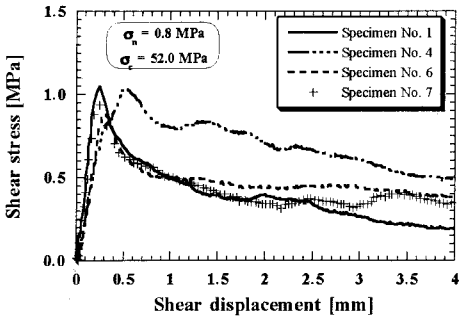

(a) Shear stress - shear displacement curves

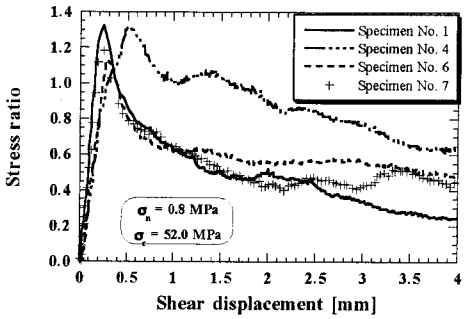

(b) Stress ratio - shear displacement curves

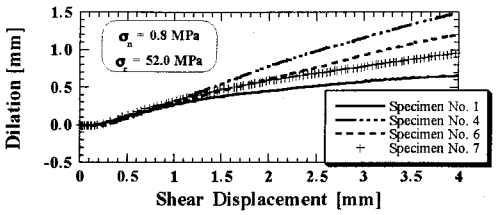

(c) Dilatancy curves

Figure 4.12 The results of the shear tests considering the differences in joint surface roughness ($\sigma_n = 0.8\,MPa$, $\sigma_c = 52.0\,MPa$)

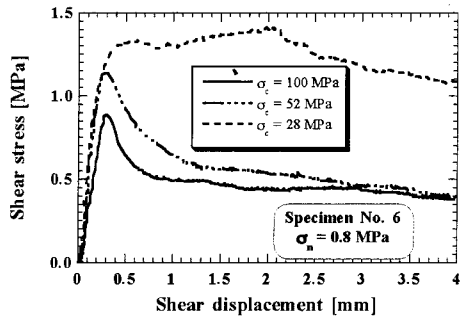

(a) Shear stress - shear displacement curves

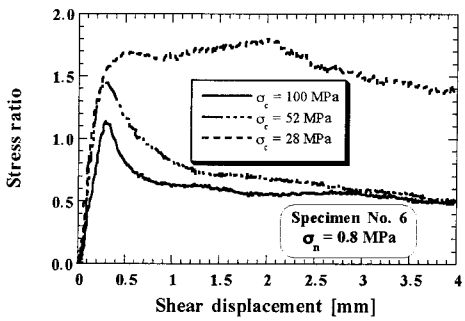

(b) Stress ratio - shear displacement curves

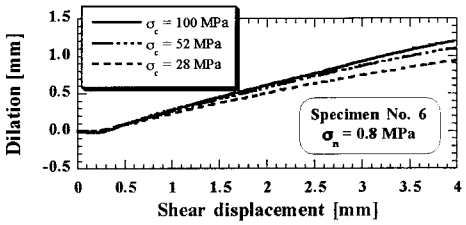

(c) Dilatancy curves

Figure 4.13 The results of the shear tests considering the differences of material strength (Specimen No. 6, $\sigma_n = 0.8\,MPa$)

(c) The influence of material strength

Differences in uniaxial compressive strength affect both the shear stress - shear displacement curves and the dilatancy curves, as shown in **Figure 4.13**. In the case of a hard material strength, the peak shear strength appears to be smaller and the dilatancy higher in

comparison to specimens in which the material strength is soft. In the case of identical joint surface roughness, that is, *JRC* is constant and the same effective normal stress exists, **Equation 4-1** predicts a large value for the peak shear strength as the material strength, that is, *JCS*, hardens. This is a different phenomenon from that shown in the results of **Figure 4.13**. The reason for this difference is thought to be as follows.

For a case in which the material strength is hard, a high value for the dilatancy angle can be found in **Figure 4.13**(c). In this case, the amount of asperities which are sheared off while performing the shear tests decreases and the dilation increases. As the dilation increases, the contact area of the upper and lower joint surfaces decreases and stress concentration occurs. Then, the asperities are sheared off under a lower stress condition. This means that the amount of roughness sheared off decreases and the peak shear strength also decreases with the same joint surface roughness and a harder material strength.

Figures 4.14(a), (b), (c), (d), (e), (f), (g), and (h) show the material strength and the I_i relation for each specimen. From these figures, I_i presents the same value for each normal effective stress and does not depend on the material strength. In a specimen which presents a high material strength, it is thought that the localization of the stress in the asperity occurs more than in a soft material strength specimen.

Before and after the shear tests, the shape of the joint surface roughness was measured with a 3-*D* roughness profiler. **Figures 4.15**(a) and (b) show the amount of sheared asperities. From these figures, it is clear that a very small and local area of joint surface affects the shear behavior. Comparing **Figures 4.15**(a) and (b), the difference in sheared-off asperities can be found under the same joint surface roughness and an almost equal ratio, namely, σ_c/σ_n. In the case of **Figure 4.15**, the material strength of (a) is harder than that of (b). In this way, it is thought that the material strength strongly affects the amount of sheared asperities.

(d) Stress ratio-shear displacement relation

As for the stress ratio - shear displacement relation shown in **Figures 4.8**(b), **4.12**(b), and **4.13**(b), the peak stress ratio decreases with increments in the normal effective stress (**Figure 4.10**). After presenting the peak stress ratio, the stress ratio ought to become the friction coefficient of the material. In this research work, however, the stress ratio is found to be higher than the friction coefficient at a 0.4 *mm* shear displacement. The reason will be described in the following.

From the dilatancy curves in **Figures 4.8**(c), **4.12**(c), and **4.13**(c), it is found that the dilation increased until the end of the shear tests. This means that the running up on asperities continued under the residual condition. The experimental evidence reported by Patton (1966) showed that the bilinear failure envelope fairly well described the shear strength for shearing along

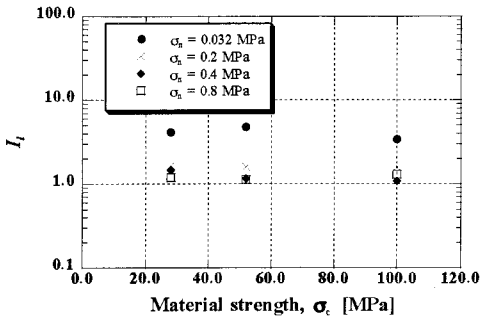

(a) Specimen No. 1

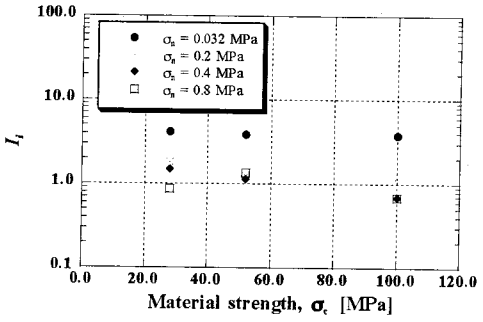

(b) Specimen No. 2

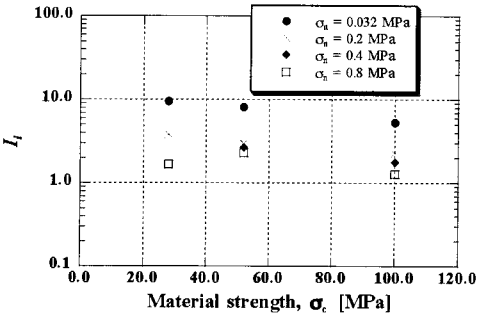

(c) Specimen No. 3

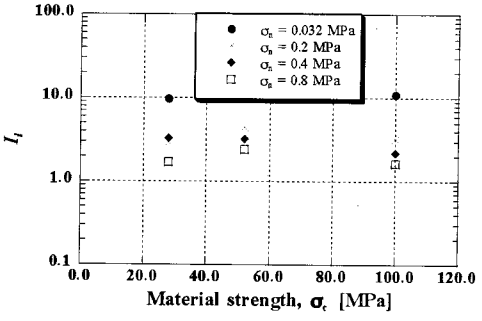

(d) Specimen No. 4

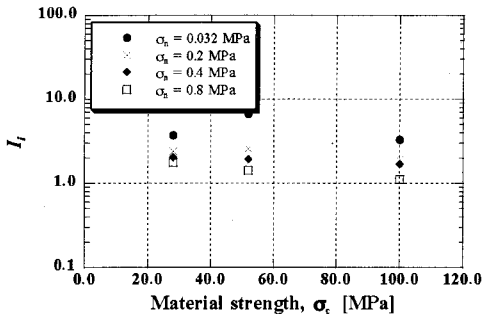

(e) Specimen No. 5

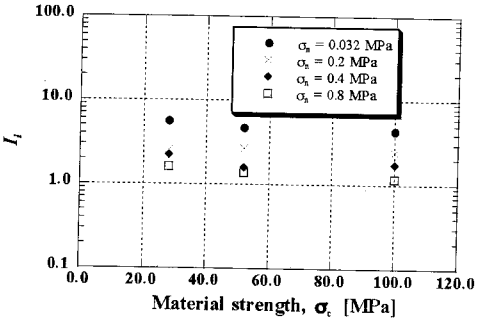

(f) Specimen No. 6

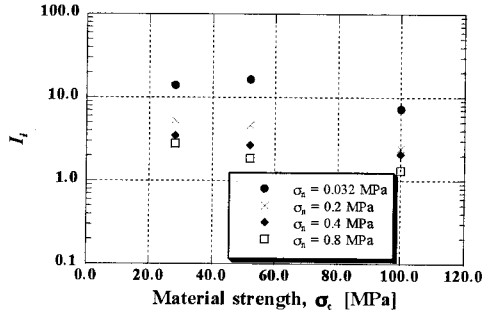

(g) Specimen No. 7

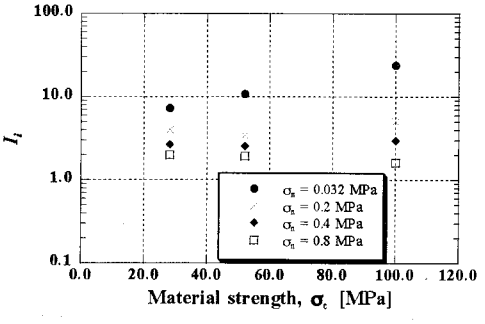

(h) Specimen No. 8

Figure 4.14 Interlocking index I_i ~ material strength relation

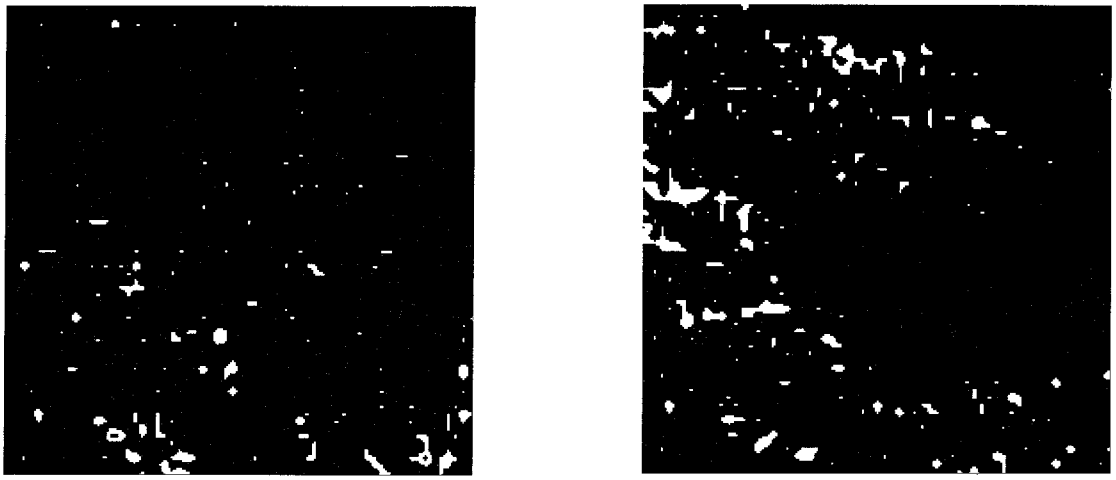

(a) Specimen No. 7, $\sigma_c / \sigma_n = 1{,}250$ (b) Specimen No. 7, $\sigma_c / \sigma_n = 1{,}300$

Figure 4.15 Change in asperities sheared off by performing shear tests
(Asperities are sheared off at the white parts)

the plane surface containing a number of regular and equal teeth. He presented the following equation:

$$\tau_p = \sigma_n \tan\left(\phi_\mu + i\right) \tag{4-8}$$

where ϕ_μ denotes the angle of frictional sliding resistance along the contact surface of the teeth and i is the angle of inclination of the teeth with respect to the general sliding surface. In this thesis, the angle of inclination in the initial phase of the dilatancy curve, d_n, is defined and calculated. Then, it is suggested that it is equivalent to angle i, as shown in **Equation 4-8**. The equivalent angle of frictional sliding resistance, ϕ_μ', is defined by **Equation 4-9**, namely,

$$\phi_\mu' = \tan^{-1}\left(\tau_p / \sigma_n\right) - d_n \tag{4-9}$$

Figures 4.16(a), (b), (c), and (d) show some samples of the changes in ϕ_μ' along the shear behavior. From these figures, it is found that fm' is almost equal to the angle of frictional sliding resistance in the material. Since fm' contains the component of interlocking roughness, it is easy to grasp the tendency for $\phi_\mu' > \phi_\mu$.

(e) Dilation and shear displacement relation

From **Figure 4.8**(c), it is seen that the dilation decreases with increments in normal effective stress. This means that for increments in normal effective stress, the amount of sheared asperities increases. And, in **Figure 4.13**(c), it is found that a large dilation increases the material

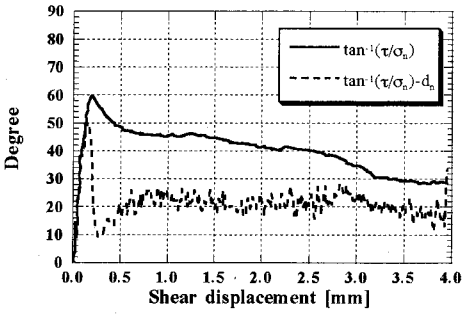

(a) Specimen No. 3, σ_c = 100.0 *MPa* σ_n = 0.4 *MPa*, ϕ_μ = 11.3 degrees

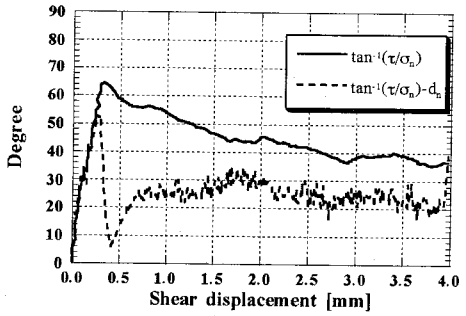

(b) Specimen No. 4, σ_c = 100.0 *MPa* σ_n = 0.4 *MPa*, ϕ_μ = 11.3 degrees

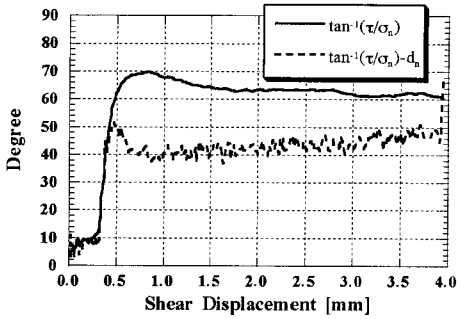

(c) Specimen No. 3, σ_c = 52.0 *MPa* σ_n = 0.4 *MPa*, ϕ_μ = 38.6 degrees

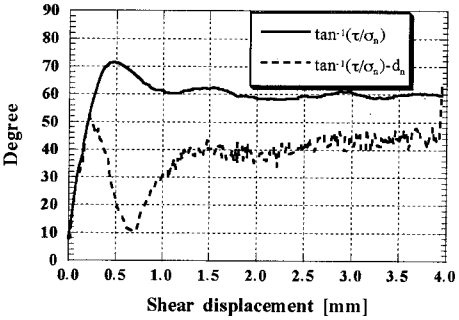

(d) Specimen No. 4, σ_c = 52.0 *MPa* σ_n = 0.4 *MPa*, ϕ_μ = 38.6 degrees

Figure 4.16 Some samples of changes in ϕ_μ'

strength. Concerning this type of case, the differences in material strength cause changes in the amount of sheared asperities and affect the dilatancy curves.

4.3.2 Variable normal confining condition

As for the direct shear tests conducted fairly well fairly well under the variable normal confining condition, the shear stress - shear displacement relation and the stress ratio - shear displacement relation are shown in **Figure 4.17**. **Figure 4.18** shows the normal effective stress - shear displacement relation and the dilatancy curves.

(a) The shear stress-shear displacement relation and the stress ratio-shear displacement relation

In the shear stress-shear displacement relation, the peak shear stress is not clearly shown. However, in the stress ratio-shear displacement relation, the peak can be found for each specimen and its value is almost equal to the peak stress ratio under the normal confining condition at σ_n = 0.2 *MPa*. In addition, the shear behavior after the peak stress ratio is similar to that in the results under the normal confining condition. It is thought that the shear displacement, in which the peak stress ratio appears, is an inflection point at which the factors controlling the shear behavior change from an interlocking roughness to a sliding along the joint surface.

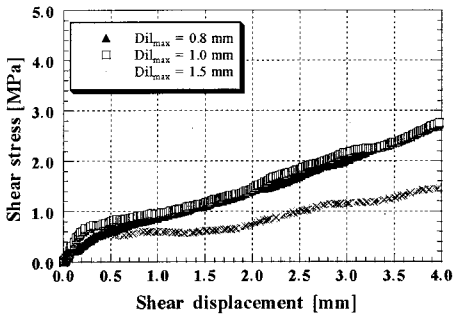

(a) The shear stress - shear displacment relation

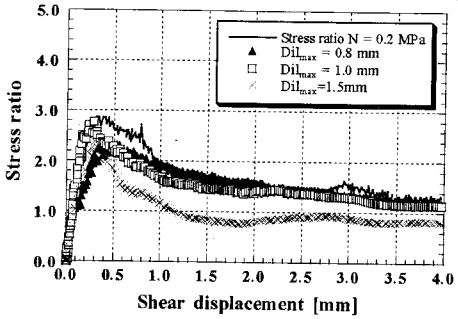

(b) The stress ratio - shear displacement relation

Figure 4.17 Results of the direct shear tests under the variable normal confining condition
(Specimen No. 5, σ_c = 52.0 *MPa*, K_{ni} = 1.0 *MPa/mm*)

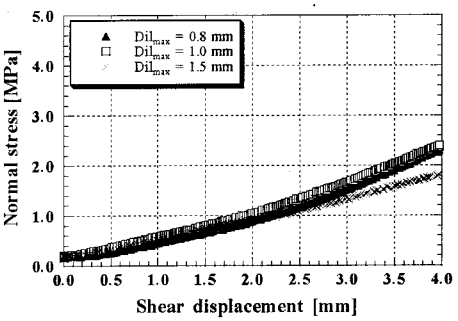

(a) The normal effective stress - shear displacment relation

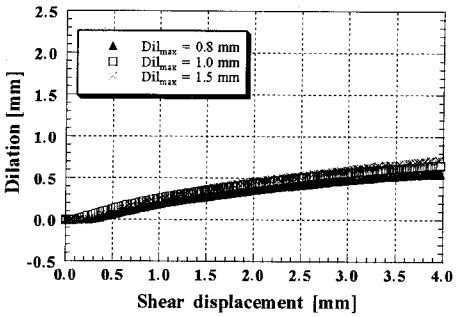

(b) Dilatancy curves

Figure 4.18 Results of the direct shear tests under the variable normal confining condition
(Specimen No. 5, σ_c = 52.0 *MPa*, K_{ni} = 1.0 *MPa/mm*)

(b) The normal effective stress-shear displacement relation

At the point where the peak stress ratio appears, the normal effective stress is constant since the dilation is small. As mentioned above, therefore, the peak stress ratio is equal to that under the constant normal confining condition. In the case of a comparison between the results under the constant normal confining condition and those under the variable confining condition, a clear difference in the peak stress ratio cannot be found even though the confining conditions are different. That is the reason why the normal effective stress is equal to both conditions, since it is thought that the initial confining stress is equal to the initial gradient of the tangent line in the stress ratio-dilation relation in the relationship between the dilation and the normal confining condition using this research work.

4.4 Discussion

4.4.1 Comparison of the experimental peak shear strength and the estimated peak shear strength through *JRC* values

In this section, an estimation of the peak shear strength is carried out, applying Barton's empirical equation (**Equation 4-1**, Barton, 1973), and a comparison is made with the experimental results.

As mentioned above, a method for measuring the profile of the joint surface roughness with a 3-*D* non-contact roughness profiler and determining the M_S value, which estimates joint surface roughness quantitatively with the spectral analysis, is presented. The M_S value for specimens which are used in the direct shear tests in this thesis were already shown in **Table 3.4**. In the empirical equation, **Equation 4-1**, Barton described the *JRC* value as a factor of joint surface roughness for the peak shear strength. In the original, *JRC* was calculated by a back analysis after performing the direct shear tests. However, the relationship between *JRC* and M_S was already determined, and the *JRC* for each specimen to the forward analysis was calculated before the direct shear tests were performed. **Equation 4-10** and **Table 4.2** again show the *JRC* - M_S relation and the estimated *JRC* value, respectively, as

$$JRC = \frac{\ln\left(\frac{M_s \cdot 10^3}{1.117}\right)}{0.23} \qquad (4\text{-}10)$$

Table 4.2 Measured M_S value of natural rock joint surface roughness

Specimen No.	M_S	*JRC*
1	1.533×10^{-2}	11.39
2	1.224×10^{-2}	10.41
3	2.021×10^{-2}	12.59
4	9.185×10^{-2}	20.92
5	8.730×10^{-2}	19.72
6	1.527×10^{-2}	11.32
7	2.436×10^{-2}	13.35

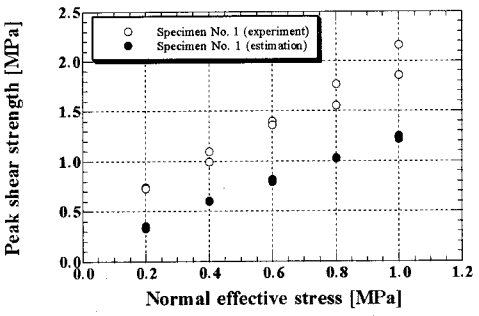

(a) Sepcimen No. 1

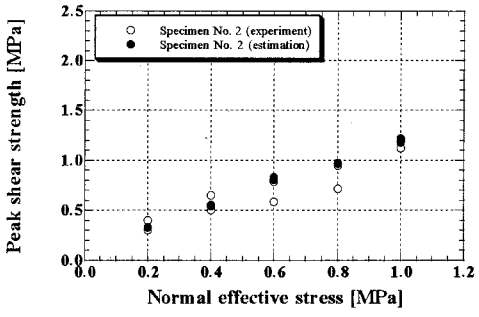

(b) Specimen No. 2

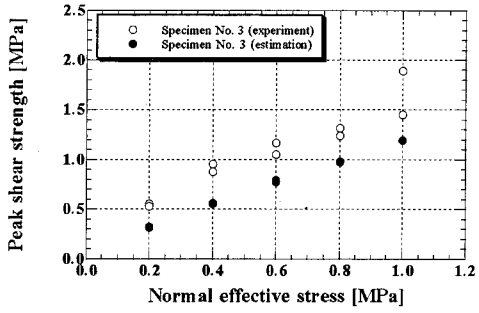

(c) Specimen No. 3

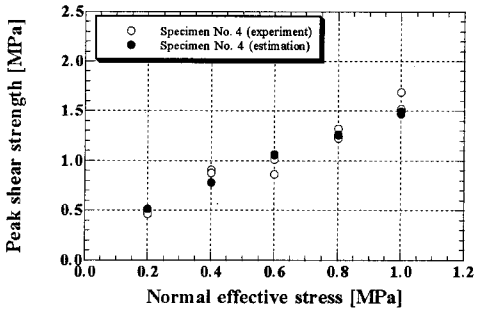

(d) Specimen No. 4

Figure 4.19 The comparison between estimated peak shear strength and that through the results of the direct shear tests (σ_c = 52.0 *MPa*, *JCS* = 13, ϕ_r = 38 degrees)

In this research work, the material strength of intact rock, σ_C, and the basic friction angle were already known before the direct shear tests were performed, since reproduced plaster specimens were used. The *JCS* presented in **Equation 4-1** shows the relation with the material strength, σ_C, as follows (Barton and Choubey, 1977) :

$$JCS = \frac{1}{4}\sigma_c \qquad (4\text{-}11)$$

Therefore, the peak shear strength can be estimated before the direct shear tests are performed. Assuming from **Table 4.1** that σ_C = 52.0 *MPa* and ϕ_b = 38.0 degrees, the peak shear strength is calculated. **Figure 4.19** shows a comparison between the estimated peak shear strength and that through the results of the direct shear tests in the relationship between the peak shear strength and the normal effective stress. For each specimen, the increment ratio of the estimated peak shear strength along the normal effective stress is equivalent to that of the experimental peak shear strength. In **Figures 4.19**(b) and (d), the estimated peak shear strength is equal to the experimental peak shear strength. However, in **Figures 4.19**(a) and (c), a good correspondence to the peak shear strength cannot be found. In this case, the estimated peak shear strength is less than the experimental one. It can be confirmed that, in spite of the difference in *JRC* values, the estimated peak shear strength is equivalent in each specimen.

As mentioned above, it is doubtful whether *JRC* itself can represent joint surface roughness. If the measuring system for the joint surface roughness profile were correct and the M_S value presented both the unevenness and the period property of the roughness at the same time, it would not be necessary to transfer M_S to *JRC*. It is thought that M_S is sufficient for estimating joint surface roughness. In fact, knowing how to use the typical roughness profile for *JRC*, shown in **Figure 3.1**, is difficult. Please note Barton's *JRC* concept again. *JRC* itself is calculated by a back analysis after performing the direct shear tests. *JRC* is estimated to contain the influence of the material strength, friction, and weathering. Therefore, *JRC* is not thought to be the estimated joint surface roughness profile itself. The results of **Figure 4.13**(a) show that the peak shear strength decreases with increments in the material strength for the same roughness profile and normal effective stress. In **Equation 4-1**, if the material strength, that is *JCS*, is increased under the same *JRC* and σ_n, the peak shear strength should also increase. The experimental results are quite to the contrary. From **Figure 4.15**, therefore, it is found that the sheared asperity is quite low. In the following sections, an estimation method for joint surface roughness will be suggested in consideration of the continuation and the width of the asperities and the estimation of the peak shear strength and the dilatancy curve.

4.4.2 Estimation of joint surface roughness in consideration of the shear behavior

From the profiling data on joint surface roughness, the geometrical shape of the roughness is estimated, as shown in **Figure 4.20**. In estimating the joint surface roughness, the continuation and the expanse of the asperities, which is viewed from the shear direction, are taken into account. At first, the asperity angles of adjacent profiling points are calculated. Considering the shear direction, the frequency distribution of positive asperity angles is shown in **Figure 4.21**. In truth, the number of asperities in a low angle range (less than 15 degrees) number more than 100. However, as compared with what follows, the range in frequency is fixed under 100, as shown in **Figure 4.21**. In the next step, the following method appears in ordered steps to consider both the continuation and the expanse of the surface roughness.

1) Make square meshes on a joint surface whose center of gravity is located at the middle point of each mesh, between two side by side profiling points, and take the weight value of 1 for the meshes possessing positive asperity angles and a weight value of 0 for the others.
2) If continuing with a weight value of 1 in a direction which lies at a right angle to the shear direction, a weight value of 1 is exchanged for the number of continuing meshes.
3) If continuing with the weight value in the shear direction, except for a weight value of 0, the weight value is added to the number of continuing meshes.
4) Multiply $1/\cos\theta$ by the weight value where θ is the asperity angle.

Figure 4.22 shows the frequency distribution of the asperity angles applied to the above-mentioned weight value. The range in frequency is equal to that shown in **Figure 4.21**. According to **Figure 4.15**, asperities which are sheared off represent a very small area of the joint surface

roughness. The sheared-off asperities are thought to be highly angled and are sheared off due to the shear behavior. Therefore, owing to the application of the function, as shown in **Equation 4-12**, frequency distributions which are emphasized by high asperity angles are improved, namely,

$$f(\theta) = 1 - \cos\left(90 \times \frac{\theta}{\theta_{\max}}\right) \tag{4-12}$$

where θ_{max} is the maximum asperity angle.

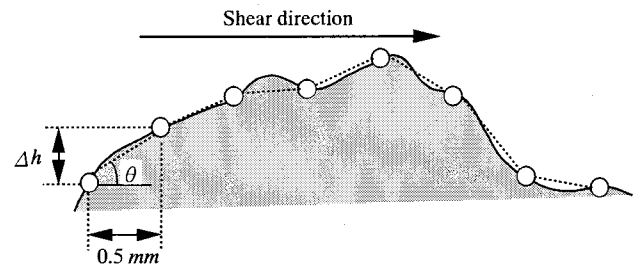

1. Calculating asperity angles of adjacent profiling points

Shear direction

0	1	1	1	0	0
0	0	0	0	0	0
0	1	1	1	0	0
1	1	1	1	0	0
0	0	0	1	0	0

2. Taking weight value 1 to meshes possessing positive asperity

Shear direction

0	1	1	1	0	0
0	0	0	0	0	0
0	2	2	3	0	0
1	2	2	3	0	0
0	0	0	3	0	0

3. If continuing the weight value 1 to the direction which lies at a right angle to the shear direction, the weight value 1 is exchanged for the number of continuing meshes

Shear direction

0	4	4	4	0	0
0	0	0	0	0	0
0	5	5	6	0	0
5	6	6	7	0	0
0	0	0	4	0	0

4. If continuing the weight value to the shear direction, except a weight value of 0, the weight value is added to the number of continuing meshes

5. Multiplying 1/cos θ to the weight value, where θ is the asperity angle

Figure 4.20 The concept of estimating the joint surface roughness

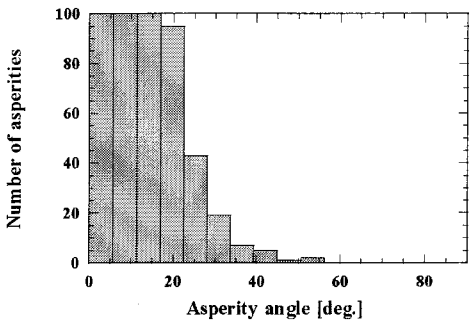

Figure 4.21 The frequency distribution of asperity angles

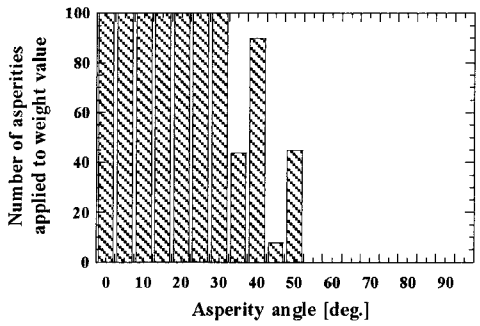

Figure 4.22 The frequency distribution of asperity angles considering each asperity's continuation and expanse

Sheared-off asperities are related not only to the asperity angles, but also to the material strength and the effective normal stress. Based on the knowledge obtained from the experimental results, in the case of a soft material strength of intact rock, many asperities are sheared off as the friction angles increase. Considering their influence, **Equation 4-12** is switched to **Equation 4-13** as follows:

$$f(\theta) = \sigma_n \left\{ 1 - \cos\left(90 \times \frac{\theta}{\theta_{\max}} \right) \right\}^{\log\left(\frac{\sigma_c^2}{\sigma_n}\right)} \quad . \tag{4-13}$$

The material strength has more influence than the effective normal stress on the sheared asperities. In **Equation 4-13**, the term of material strength is emphasized. The results of applying **Equation 4-13** to the frequency distribution of the asperity angles is shown in **Figure 4.23**. From **Figure 4.23**, the estimation parameter (*CRM*) which represents joint surface roughness is defined in **Equation 4-14** as follows:

$$CRM = \sum_{j=1}^{n} \theta_j \cdot f(\theta_j) / n \tag{4-14}$$

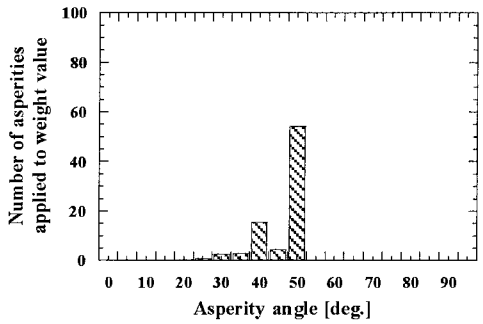

Figure 4.23 The frequency distribution of asperity angles applying **Equation 4.13**

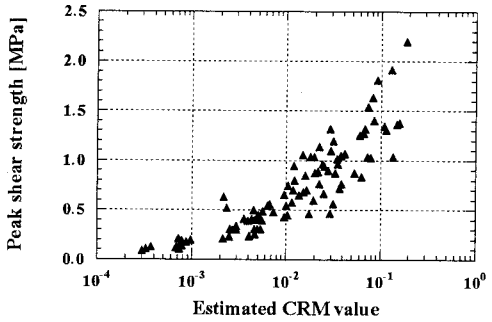

Figure 4.24 The relationship between the peak shear strength and *CRM* value

where n is the number of asperities. *CRM* is thought to represent the factor of joint surface roughness including the influence of the material strength and the effective normal stress.

4.4.3 Peak shear strength

Figure 4.24 shows the relationship between peak shear strength and *CRM*. Peak shear strength shows all the data obtained through several types of test conditions. The empirical relationship between peak shear strength and *CRM* is described by **Equation 4-15**, namely,

$$\tau_p = 1.85 + 0.579\log\left(CRM\right) \quad . \tag{4-15}$$

Equation 4-15 describes peak shear strength as a function of joint surface roughness, material strength, and effective normal stress. By measuring the shape of the roughness from a borehole survey, the peak shear strength can be determined using **Equation 4-15**.

4.4.4 Dilatancy curve

Figure 4.25 shows one example of the relationship between the gradient of the dilatancy curve (dv/du : v is dilation and u is shear displacement) and the shear displacement. The gradient of the dilatancy curve increases linearly before a peak point, and then it decreases linearly. As for this peak point, it is equal to the peak shear displacement for most samples. The dilatancy curve (v) is described with the function of shear displacement by **Equation 4-16** as follows:

$$v(u) = \int_0^u \frac{dv}{du} du \quad . \tag{4-16}$$

And the gradient of the dilatancy curve is written as follows:

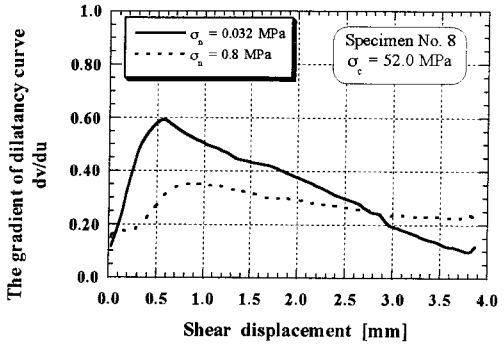

Figure 4.25 The gradient of the dilatancy ~ shear displacement relation

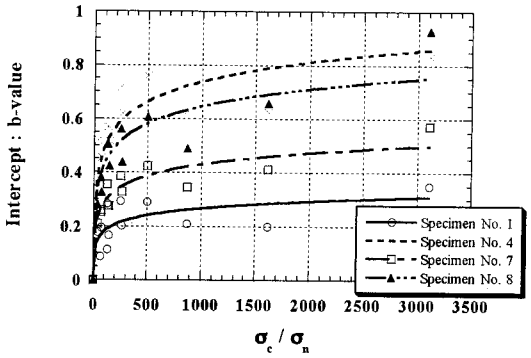

Figure 4.26 Intercept b-value ~ σ_c / σ_n relation

$$g(u) = \frac{dv}{du} = \begin{cases} m_1 u & (0 < u < u_p) \\ -m_2 u + b & (u_p \le u) \end{cases} \tag{4-17}$$

where u_p is the peak shear displacement. From this equation, if parameters m_2, b, and m_1 or u_p are determined, the dilatancy curve can be represented by **Equation 4-17**. In this thesis, therefore, parameters m_2 (inclination) and the b-value (intercept) can be investigated.

At first, the relationship between the intercept b-value and the ratio of uniaxial compressive strength (σ_c) / effective normal stress (σ_n) will be investigated. **Figure 4.26** shows this relation for each specimen, respectively. The relation for each specimen has a high correlation and can be represented by **Equation 4-18** as follows:

$$b = \alpha \cdot \log\left(\frac{\sigma_c}{\sigma_n}\right) . \tag{4-18}$$

In **Figure 4.26**, it can be found that the coefficient α-value described by **Equation 4-18** strongly relates to the specimen's property. In this case, the specimen's property is equal to the property of the joint surface roughness. Thus, the relationship between the α-value and the property of the joint surface roughness must be investigated for each of the specimens. Recall that the *CRM* described above in this thesis shows the property of joint surface roughness including the influence of the material strength and the effective normal stress. As compared with the α-value, however, the property of joint surface roughness alone is needed. Based on **Equation 4-12**, therefore, the estimated parameter of joint surface roughness is made itself.

$$SSA = \sum_{j=1}^{n} \theta_j \cdot \left\{ 1 - \cos\left(90 \times \frac{\theta}{\theta_{\max}} \right) \right\}^6 / n \tag{4-19}$$

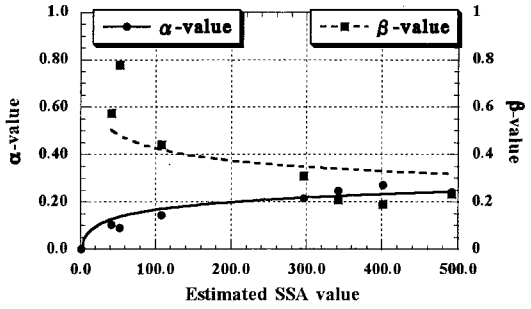

Figure 4.27 The relationship between *SSA*, α-value, and β-value

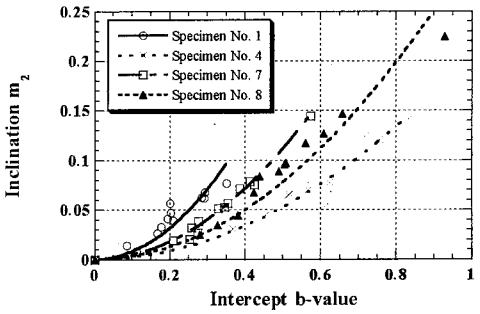

Figure 4.28 A comparison of intercept *b*-value and inclination m_2

The relationship among the α-value, the β-value, and *SSA* is shown in **Figure 4.27**. The relationship between the α-value and *SSA* can be written in **Equation 4-20** as follows:

$$\alpha = 0.018 \times SSA^{0.44} \quad . \tag{4-20}$$

This equation shows a good correlation and the *b*-value can be determined from the profiling data of joint surface roughness using **Equations 4-18** and **4-20**.

In the next step, m_2 will be considered. **Figure 4.28** shows the relationship between m_2 and the *b*-value for each specimen, respectively. This relation can be described by a 2nd order function as follows:

$$m_2 = \beta b^2 \quad . \tag{4-21}$$

This equation shows a high correlation for each specimen. In **Figure 4.28**, the coefficient β-value also has a good correlation for the specimen's property, that is, the property of the joint surface roughness. **Figure 4.27** shows the relationship between the β-value and *SSA* too. This relation is written in **Equation 4-22**, namely,

$$\beta = 4.57 \times SSA^{-0.5} \quad . \tag{4-22}$$

From the above-mentioned results, m_2 and the *b*-value can be determined by using the profiling data of joint surface roughness and by considering the conditions of the material strength and the effective normal stress. **Figure 4.29** shows the dilatancy curves calculated by the above method. In **Figure 4.29**, the dilatancy curves obtained in the shear tests are described as well.

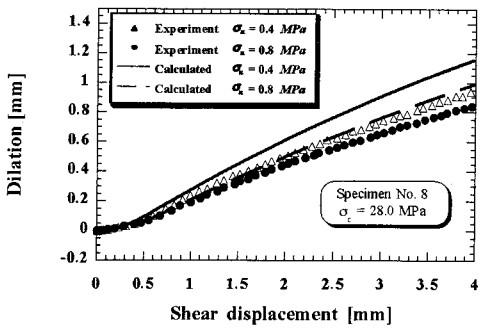

Figure 4.29 A comparison of calculated and tested dilatancy curves

4.5 Conclusion

In this chapter, direct shear tests have been carried out under both constant and variable confining conditions. As for the variable confining condition, it is known that the stress ratio-shear displacement relation is equivalent to that under a constant confining condition. Therefore, the shear behavior of rock joints under a low confining condition is controlled by the interlocking of the joint surface roughness and the sliding friction before and after the peak stress ratio appeared, respectively.

The *JRC* value has been estimated using the M_S value. *JRC* itself has been calculated by the back analysis in **Equation 4-1** and does not represent the factor of joint surface roughness. *JRC* is thought to represent the factor of joint surface roughness containing the influence of the material strength, the sliding friction, the normal effective stress, and weathering (or the nonoccurrence of it) in the direct shear tests.

From the experimental results, it has been shown that the shear behavior of rock joints can be affected by joint surface roughness, material strength, and effective normal stress. Under a condition with the same roughness form and material strength for both, increases in peak shear strength and residual strength and decreases in dilation can be observed due to increases in the effective normal stress. Considering the influence of the difference in joint surface roughness, changes in peak shear strength, residual strength, dilatancy, and peak shear displacement have been observed. The difference in material strength causes changes in the shear behavior. In particular, the peak shear strength decreases and dilatancy increases in comparison to specimens in which the material strength is soft.

Based on the results of direct shear tests, the parameter of joint surface roughness has been estimated in consideration of its form, the material strength, and the effective normal stress and it has determined the relationship among this parameter, the peak shear strength, and the dilatancy curves.

REFERENCES

Barton, N. (1973) : Review of a new shear-strength criterion for rock joints, *Engineering Geology*, Vol. 7, pp. 287 - 332.

Barton, N. and Choubey, V. (1977) : The shear strength of rock joints in theory and practice, *Rock Mechanics*, Vol. 10, pp. 1 - 54.

Bandis, S. C., Lumsden, A. C. and Barton, N. R. (1983) : Fundamentals of rock joint deformation, *Int. J. Rock Mech. Min. Sci. & Geomech. Abstr.*, Vol. 20, No. 6, Pergamon, pp. 249 - 268.

Patton, F. D. (1966) : Multiple Modes of Shear Failure in Rock, *Proc. of 1st Congress of ISRM in Lisbon*, Vol. 1, pp. 509 - 513.

Tanimoto, C., Morioka, H. and Kishida, K. (1990) : Roughness and shear behaviour of rock joints, *Proc. of the 8th Japan Symposium on Rock Mechanics*, ISRM-NG Japan, pp. 103 - 108. (in Japanese)

Tanimoto, C., Morioka, H., Kishida, K. and Umezawa, T. (1991) : Roughness and shear behaviour at rock joint under low confining pressure, *Proc. of the 23th Symposium of Rock Mechanics*, Committee of Rock Mechanics J.S.C.E., pp. 127 - 131. (in Japanese)

Tanimoto, C., Murai, S., Matsumoto, T., Kishida, K. and Ando, T. (1995) : Immediate image and its analysis of fractured/jointed rock mass through the borehole scanner, *Fractured and Jointed Rock Masses*, Myer, Cook, Goodman & Tsang (eds), Balkema, pp. 219 - 228.

Thapa, B. B., Goodman, R. E., Tanimoto, C. and Kishida, K. (1995) : Analysis of in-situ joint strength anisotropy and aperture, *Proc. of the 26th Symposium of Rock Mechanics*, Committee of Rock Mechanics J.S.C.E., pp. 549 - 553.

Thapa, B. B., Ke, T. C., Goodman, R. E., Tanimoto, C. and Kishida, K. (1996) : Numerically Simulation Direct Shear Testing of In-Situ Joint Roughness Profiles, *Int. J. Rock Mech. Min. Sci. & Geomech. Abstr.*, Vol. 33, No. 1, Pergamon, pp. 75 - 82.

Chapter 5

Laboratory Experiments on the Propagating Behavior of Seismic Waves through Several Kinds of Rock Joints under Uniaxial Conditions

5.1 Introduction

In the design and the construction of rock structures, such as tunnels, underground caverns, foundations, etc., seismic explorations are carried out in the preliminary surveys. Reflection seismology is often applied in civil engineering to clarify the geological structures. The following relations between seismic velocity and geological lithology have been described (Ikeda and Ohshima, 1975):

1) In general, the higher the velocity gets, the larger the uniaxial compressive strength becomes.
2) If rock weathers, the velocity decreases.
3) The velocity also decreases in crush zones and faults.
4) The velocity is slow in friable and porous rock.

With advances in computer and electronics technologies, the tomographic technique has been applied to the results of seismic data and visible objective areas have been represented by a seismic velocity distribution. In fact, this technique has been carried out very successfully and has been applied not only in the field of earth resources engineering, but also in the field of civil engineering (Sassa, 1990).

The tomographic technique has achieved tentative success. However, the results are thought to represent only the seismic velocity; they are not sufficient for estimating the geological structure in detail. In jointed rock masses, in particular, these results are not good enough to estimate rock joints which strongly affect the mechanical and the hydromechanical behaviors of jointed rock masses.

In the present thesis, both a velocity analysis and an amplitude attenuation analysis by seismic geotomography will be developed, and an estimation method for jointed rock masses will be established based on the results of the two analyses. When the geotomographic technique is applied in the civil engineering field, the idea of how the results of the technique can present the mechanical and the hydromechanical properties must be considered. This is essential for use of this technique in geotomography.

In general, the results obtained through a seismic velocity analysis are just an index, since the relationship among the seismic velocity, the joint distribution, and the mechanical properties

of the joints has not been substantially clarified. Tanimoto & Ikeda (1983) and Tanimoto, et al. (1994a) explained that when the magnitude of a joint aperture is less than 0.04 *mm* or the confining pressure at the joints varies in a range higher than 2 *MPa* in seismic propagating tests under a uniaxial confining condition using a specimen with a single joint, changes in velocity do not correspond to the influence of the existing joints. Changes in the amplitude of the propagating seismic waves, however, are able to reflect the effect of the joints, showing a clear reduction in the energy (amplitude) at the joints. The amplitude of the propagating seismic waves is more sensitive to reflecting joint conditions, namely, the contact area, the aperture, weathering (or the nonoccurrence of it), and joint surface roughness filling material. Based on these conclusions, the measurement of propagating seismic waves is performed in this thesis through joints under a uniaxial confining condition, and the relationship between the properties of the seismic propagating waves and the joint conditions (joint surface roughness, joint frequency, and filling material) are clarified. Based on knowledge obtained from the fundamental seismic experiments, it seems possible to give a detailed estimate of the seismic velocity distribution and the amplitude attenuation factor distribution through seismic geotomography and to obtain certain effective information which enables a discussion on jointed rock masses.

5.2 Preparation for the laboratory experiments

5.2.1 Specimens

Cylindrical specimens of intact rock, obtained from sites where seismic surveys were carried out, and plaster/cement cylinders of various lengths are used for the laboratory tests. The rock types used in this study are rhyolite, granite, and granite-prophyry. For the tests in which the specimens are subjected to normal loading, the samples are constructed by stacking individual cylinders of rock or plaster/cement to produce "jointed" samples with joints normal to the axial direction.

Several examples of the experimental set-up are shown in **Figure 5.1**.

In order to consider the influence of joint frequency, the experimental models are set up, as shown in **Figures 5.1**(a) ~ (c). These models exist in 2, 3, and 4 joints per same length of cylindrical specimens, respectively. All types of joints are smooth. Therefore, only the influence of the joint frequency on the propagating seismic wave can be considered. In **Figure 5.1**(d), a cylindrical specimen exists in a natural rock joint. In this model, the influence of the joint surface roughness on the seismic propagating wave will be considered. As for the measurement and the estimation of the joint surface roughness, the same method as described in Chapter 3 is used. The M_S value and the *JRC* of the specimens are presented in **Table 5.1**. In **Figure 5.1**(e), filter paper is used to produce the desired joint aperture and moisture content. A change in the number of

filter papers represents the filling material of the joint and the aperture. Next, the influence of these parameters on the propagating wave will be investigated. The upper and lower faces of the specimen and the artificial joint surface, shown in **Figures 5.1**(a) ~ (c) and (e), are made under the condition where the equilibrium degree is less than 0.01 *mm*. As for the contact of the artificial joint surface, the aperture is less than 0.01 *mm* and the entire surface area is contacted.

5.2.2 Measuring system for a seismic propagating wave

The measuring system for a seismic propagating wave is shown in **Figure 5.2**.

Table 5.1 Measured M_S value of natural joint surface roughness

Specimen No.	M_S	*JRC*
A	9.121×10^{-3}	9.13
B	7.796×10^{-3}	8.45
C	1.112×10^{-2}	9.99
D	1.567×10^{-2}	11.51
E	2.791×10^{-2}	13.99
F	3.262×10^{-2}	14.67

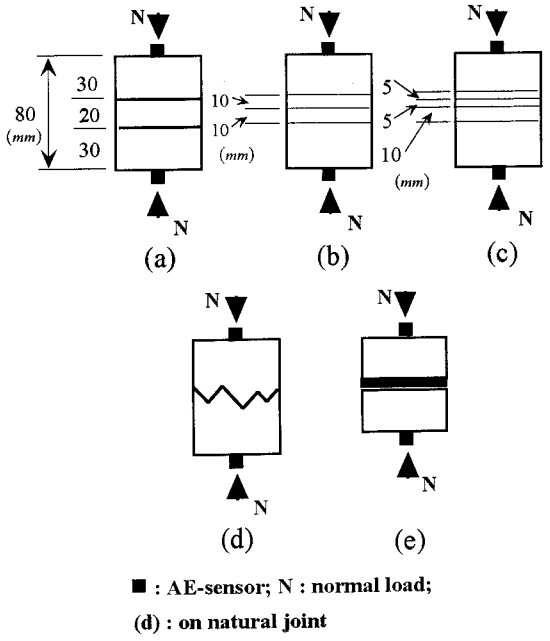

Figure 5.1 Experimental set-up of seismic behavior at joints

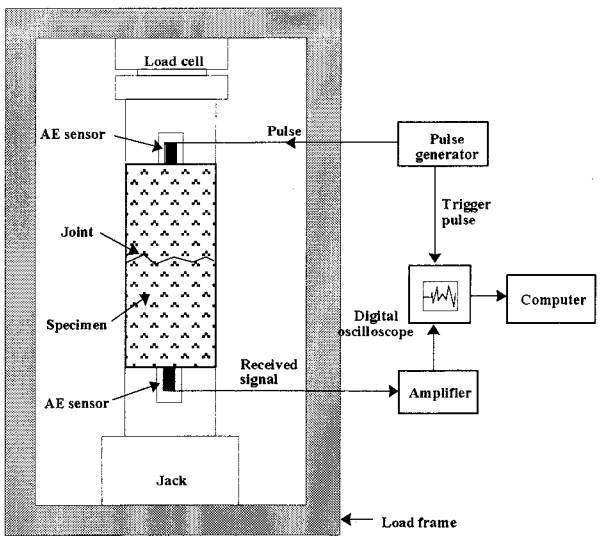

Figure 5.2 Schematic illustration of experimental set-up for seismic measurements

A seismic event (a single pulse for each event, amplitude : 4.8 *V*, frequency : 65 *kHz*) is generated by a pulse generator (Model 145 : WAVETEK), as shown in **Photo 5.1**. It is inputted into the specimen through an AE-sensor (AE900S-WB : NF Circuit Design Block Co. Ltd.), as shown in **Photo 5.2** and tightly fitted to the end of the specimen. An identical sensor is used to pick up signals at the opposite end of the specimen. Received signals are presented in an oscilloscope (Digital Storage Oscilloscope : NF Circuit Design Block Co. Ltd.) through the amplifier (9913 : NF Circuit Design Block Co. Ltd.) as shown in **Photo 5.1**. The signals are then forwarded from the oscilloscope to the computer, and the measurement of the traveltime and the amplitude of the first break can be performed.

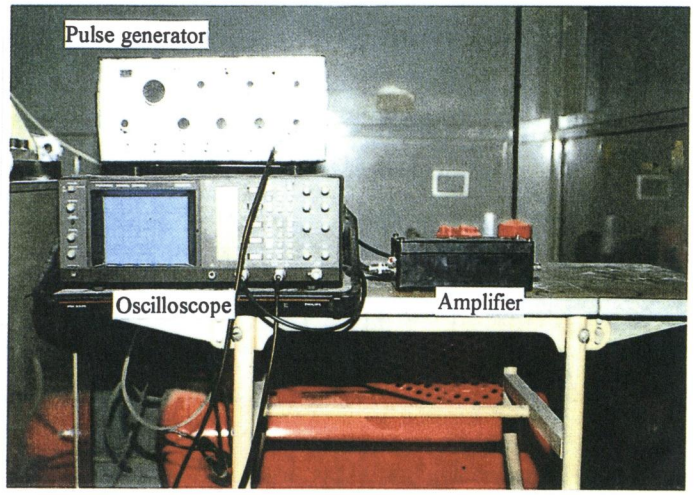

Photo 5.1 Pulse generator, oscilloscope, and amplifier

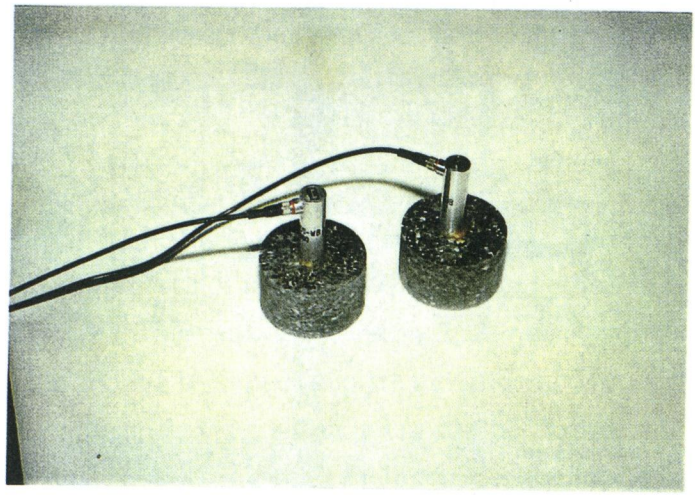

Photo 5.2 AE-sensor

The diameter and the length of the AE-sensor are 12 *mm* and 40 *mm*, respectively. The AE-sensor, which is a non-resonate type, is often used to perform spectral analyses. The frequency property is 100 *kHz* ~ 1 *MHz* and ± 10 *dB*, namely, it is wide and smooth. Electron wax (made by Sou Electric Industry) is used to connect the AE-sensor to the end of the specimen. In order to consider the influence of the propagating seismic wave due to the contact between the AE-sensor and the specimen, an experiment is conducted in which the received wave makes contact with and is then cyclically removed from the same specimen several times. In this way, it is confirmed that the same waveform is obtained every time. Therefore, it is considered that no influence to the seismic wave occurrs when the AE-sensor makes contact with the specimen.

5.3 Propagating behavior of a seismic wave in a cylindrical specimen

5.3.1 Preliminary experiment

In this section, before performing the seismic propagation experiment, the behavior of a propagating seismic wave through a cylinder specimen is investigated. Then, the concept of traveltime and the first break amplitude is shown in **Figure 5.3**. The waveform is recorded in the personal computer as digital data through the GPIB-board. The traveltime is determined to the point where the digital data fluctuates more than the threshold value. The first break amplitude is discussed using a non-dimensional parameter, as well as the amplitude ratio, which is described in the following.

Two cylindrical specimens (Specimens *A* and *B*) are made from plaster. The combined ratio of plaster is water : plaster of Paris = 6 : 5, and the uniaxial compressive strength is 13.3 *MPa*. By cutting the specimens gradually, as shown in **Figure 5.4**, the seismic propagating experiment is carried out. Specimen *A* is cut gradually toward the center from the girth at the middle point of the specimen length. On the other hand, Specimen *B* is cut gradually in the direction of the diameter from one end of the girth at the middle point along the length of the specimen. A rock saw is used to cut the specimens, and the rest of the diameter, the connected area, is measured by calipers. The cutoff aperture is about 2.0 *mm*. The length of the connecting part in the cutoff section is defined by parameter *de* (effective diameter). The measurement system is the same as that shown in **Figure 5.2**. The seismic wave is measured without being under a uniaxial confining condition. The waveform is identical to that in the main experiment.

As for Specimen *A*, a raypath can be specified and it seems to be a concentric circle. According to the relationship between the seismic velocity and the diameter of the concentric circle in the connected area, that is, effective diameter *de*, as shown in **Figure 5.5**, the seismic velocity does not change with decreases in the diameter of the concentric circle until 5 *mm*. Then, the shortest path of seismic propagation does not change in Specimen *A*.

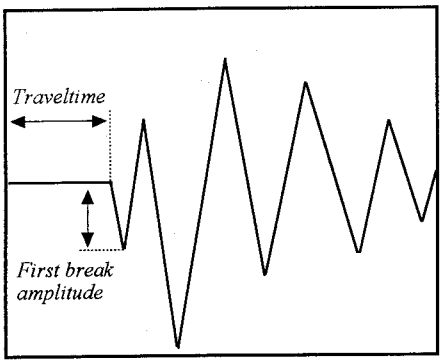

Figure 5.3 Read out traveltime and first break amplitude

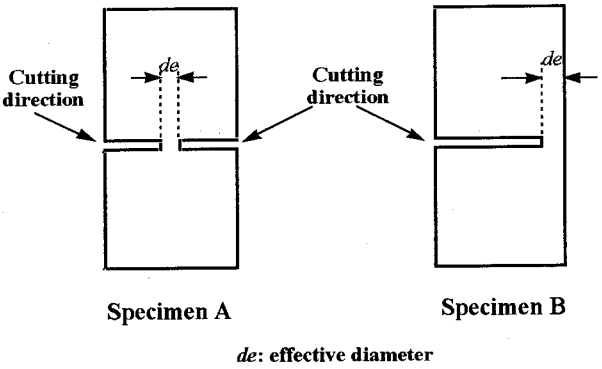

Figure 5.4 Schematic illustration of pre-experimental specimens for considering the seismic wave path at cylinders

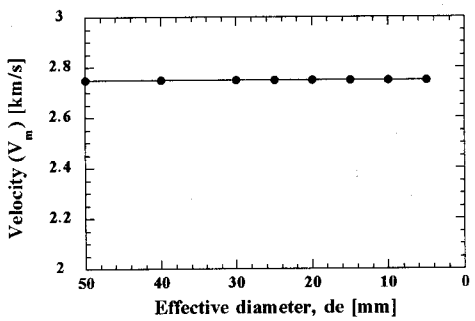

Figure 5.5 Velocity (V_m) v.s. effective diameter for Specimen *A*

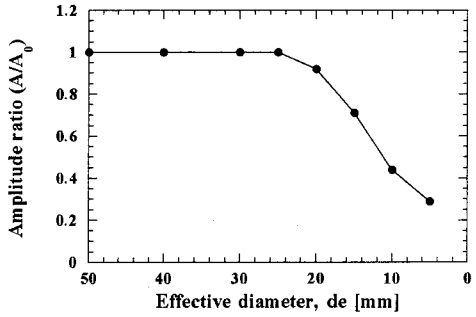

Figure 5.6 Amplitude ratio v.s. effective diameter for Specimen *A*

When considering the results of the first break amplitude, the first break amplitude ratio (*FBR*) is applied. It is defined as the ratio between the first break amplitude in an intact specimen, A_0, and the first break amplitude in each cutting stage, *A*. That is, *FBR* is defined in the following equation:

$$FBR = \frac{A}{A_0} \tag{5-1}$$

where A : the first break amplitude in each cutting stage

A_0 : the first break amplitude in the intact cylinder specimen.

According to the relationship between effective diameter *de* and the amplitude ratio, shown in **Figure 5.6**, the amplitude ratio begins to decrease when *de* drops to less than 20 *mm*.

In the next step, the results of the seismic propagating experiment for Specimen *B* are considered. According to the relationship between the seismic velocity and *de*, shown in **Figure 5.7**, the apparent velocity, V_m, can be found to decrease after the cutting length exceeds the center point of the cylinder specimen. In a case in which there is no cut in the specimen, the

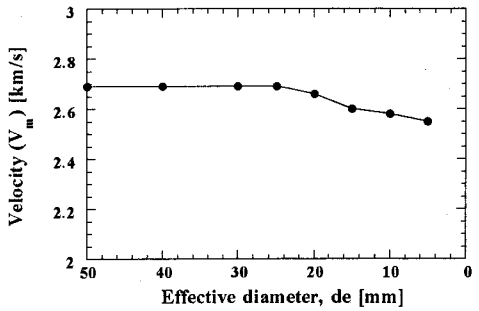

Figure 5.7 V_m v.s. effective diameter for Specimen *B*

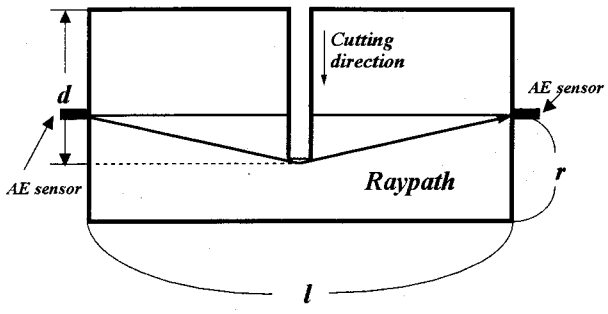

Figure 5.8 The concept of the raypath for Specimen *B*

apparent velocity is defined by the following equation since the raypath of the seismic wave is the shortest and is equal to the specimen's length:

$$V_m = \frac{l}{t} \tag{5-2}$$

where t : the observed traveltime

l : the specimen's length (100.0 *mm* in this experiment).

On the other hand, the shortest raypath of the seismic wave, l', changes when the cutting face exceeds the center line of Specimen *B*. **Figure 5.8** shows the concept of the shortest raypath after the cutting face exceeds the center line of Specimen *B*, and **Equation 5-3** presents the shortest raypath, l', namely,

$$l' = 2\sqrt{\left(\frac{l}{2}\right)^2 + (d-r)^2} \tag{5-3}$$

where l : the specimen's length

r : the radius of the cylinder specimen

d : the cutting length as shown in **Figure 5.8**.

Then, the real velocity of the seismic wave, V_r, can be calculated using the following equation:

$$V_r = \frac{l'}{t} \tag{5-4}$$

where t is the observed traveltime and l' is the shortest raypath. Then, by calculating the shortest raypath in each stage, l', the V_r vs. *de* relation can be presented in **Figure 5.9**. It is confirmed that V_r is constant against each *de*.

Figure 5.10 shows the results of the amplitude ratio for Specimen *B*. When the cutting length, *d*, exceeds 10 *mm*, as shown in **Figure 5.8**, the amplitude decreases. The results present the same tendency as that for Specimen *A*. Therefore, when the cutting length extends to the concentric circle of a specimen whose diameter is 20 *mm*, a change in the first break amplitude can be confirmed. Since the shortest raypath becomes long, the spherical divergence effect by the raypath length appears at the first break amplitude.

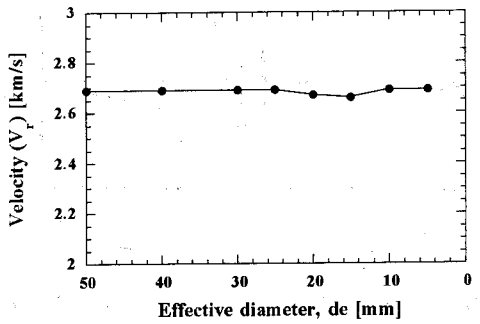

Figure 5.9 V_r v.s. effective diameter for Specimen *B*

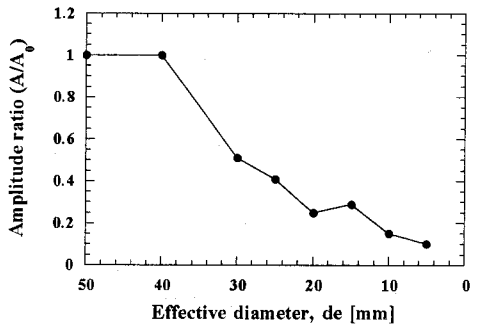

Figure 5.10 Amplitude ratio v.s. effective diameter for Specimen *B*

As mentioned above, in the seismic propagating experiments on the cylindrical specimens, it is confirmed that the seismic wave, which closely represents the seismic velocity and the first break amplitude, propagates through a limited range with a 10 *mm* radius from the center of the cylinder specimens. No influence from either the reflected wave from the side or the surface wave in the specimens against the first break amplitude is presented. In the seismic propagating experiment using rock joints, therefore, the traveltime and the first break amplitude of the seismic propagating wave can be measured and only the influence of the rock joints can be discussed without the influence of the boundary condition of the cylindrical specimens, the reflected wave from both sides, or the surfaces of the specimens. It is naturally that both the reflection and the interference must be considered if the size of the specimen changes.

5.3.2 The basic concept of the propagating seismic wave

In general, the seismic velocity of a primary wave (P-wave) is defined by the following equation using the modulus of elasticity of the conductor:

$$V_p = \sqrt{\frac{E}{\rho} \cdot \frac{1-\nu}{(1+\nu)\cdot(1-2\nu)}} \tag{5-5}$$

where E is the modulus of elasticity, ν is Poisson's ratio, and ρ is density (Sassa, et al., 1993). In the seismic propagating experiment on intact rock specimens under a uniaxial confining condition, changes in the properties along with changes in the stress levels cause the seismic velocity. On the other hand, in the case of jointed rock specimens, changes in the apparent velocity, V_m, are caused by the following two factors:

(i) With the same intact rock specimen, but a change in the confining stress condition, increments in the connectivity of the minerals and the closing of the micro-cracks cause changes in the properties of the intact rock.

(ii) Changes in the connecting points of the rock joints appear at some stress levels.

In the case of seismic propagation in jointed rock masses, the latter requires special mention. As noted above, in-situ rock masses contain joints and/or discontinuities and they control the mechanical behavior of the jointed rock masses. In general, when a block is put on a rough surface, the connecting surface area is nearly equal to 0 and the total connecting force supports more than three connecting points. As increments in the normal confining stress, elastic deformation, compression, and tension occur at the connecting points, the newly connected area expands (Goodman, 1976). In the same way, a joint, which does not contain filling material, does not close perfectly, and many points and areas at the joints are connected. With increments in the normal confining stress against the joint comes the expansion of the contact area. In this way, the contact condition of the joints is caused by the normal stress against the joints and the joint surface roughness. Therefore, in the case of seismic propagation, since the connecting points and the connected area are expanding with increments in the normal confining stress on the joints, changes in the seismic raypath occur and changes in the apparent velocity, V_m, are present. Until the yield point is reached, namely, the normal deformation of the joint is presented within the maximum joint closure (Goodman, 1976), the newly connected points appear as increments in the normal stress, the shortest raypath becomes short, and apparent velocity V_m increases.

Next, the amplitude of the seismic propagating wave will be considered. Changes in the amplitude are caused by certain factors. At first, in an ideal situation without the influence of the physical properties, a wave which presents the initial amplitude in a source point, A_0, basically measures amplitude A, at a receiving point located at a distance, r, from a source point. Amplitude A, is described in the following equation:

$$A = A_0 \frac{k}{r} \tag{5-6}$$

where k is the degree of the presented geometric spreading, r is the distance from a source point to a receiving point, A_0 is the amplitude of the source wave, and A is the observed amplitude. In the case of seismic propagation through rock production, considered to influence the internal visco-damping factor, **Equation 5-6** is described as follows:

$$A = A_0 \frac{k}{r} \exp\left(-\alpha r\right) \tag{5-7}$$

where α is the internal visco-damping factor (Sassa, 1993). However, since the seismic wave propagates through certain kinds of joint conditions, such as joint frequency, aperture, filling material conditions, and joint surface roughness, the propagating loss, reflection, refraction, and scatter of the seismic wave occur and its amplitude changes. Then, substituting these factors into **Equation 5-7**, the received amplitude is presented as follows:

$$A = A_0 \frac{k}{r} \exp\left(-\alpha r\right) \cdot F(n, b, \beta, f) \tag{5-8}$$

where F : the function describing the influence of rock joints

n : joint frequency
b : aperture
β : the internal visco-damping factor of filling materials
f : frequency of the propagating seismic wave.

If the influence of each parameter in function F on the changes in amplitude are determined, the seismic propagating behavior can be grasped in detail. And, with the developed geotomographic technique, in consideration of function F, it is thought that the properties of the joints can be determined from the results of geotomography.

For the case in which the seismic wave propagates through the joints which contain the filling material, changes in the first break amplitude generally cause a propagating loss because of the difference in acoustic impedance between intact rock and the filling material. However, in the case where a joint does not contain filling material, the propagating loss of the seismic wave may not occur unless changes in the properties of the intact rock, such as changes in the acoustic impedance, occur. In particular, in **Figures 5.1**(a) ~ (d), changes in the properties of the intact rock cannot be found and the joint surfaces have direct contact without any filling material. The changes in the first break amplitude cannot be explained from an acoustic impedance point of view. Changes in amplitude due to changes in the contact area at the joint cannot be explained from the concept of acoustic impedance.

Then, only for specimens which do not contain filling material in their joints, **Equation 5-8** changes to the following equation:

$$A = A_0 \frac{k}{r} \exp\left(-\alpha r\right) \cdot F'(P_c, p, s) \tag{5-9}$$

where P_C : uniaxial compressive stress
p : stress at contact points
s : contact area on the joint surface.

In this equation, the first break amplitude ratio defined in **Equation 5-1**, FBR, is presented as follows:

$$FBR = \frac{A}{A_0 \frac{k}{r} \exp\left(-\alpha r\right)} = F'(P_c, p, s) \tag{5-10}$$

Based on **Equations 5-8** ~ **5-10**, the experimental results will be discussed as described in the following section. These equations are applied in order to discuss the properties of the propagating seismic wave through a rock joint model, as shown in **Figure 5.1**, respectively. If the function, F or F', is clarified when applying these equations to the geotomographic technique, a geotomographic technique for grasping the rock joint conditions can be developed.

5.3.3 Numerical simulation of a seismic propagating wave through a rock joint

The modeling of a seismic wave shows how to propagate the seismic wave in an underground structure. It is classified into two methods, namely, the ray tracing and the wave equation modeling. The ray tracing method is used to determine the raypath in an objective area where the underground structure and the velocity distribution, using Snell's law and so on, are given. On the other hand, the wave equation method is used to understand the seismic disturbance. The solution for the wave equation can be found by the finite difference method, the Fourier transform, the finite element method, and the boundary element method. The finite difference method is more convenient for making the computer programs than the other methods. However, when applying the finite difference method to solve the wave equation, the convergence and the stability of the solution must be considered. In addition, with the finite difference method, a grid dispersion phenomenon often occurs. Grid dispersion means that if the number of grids against one wave length is small, the waveform will collapse while propagating. A small grid size can be used to avoid this difficulty. However, a small grid lengthens the calculation time. In the finite element method, nodes can be set to move freely, because they do not depend on the wave length. Consequently, the modeling of a seismic wave can be applied easily even for complex geological structures. Moreover, the finite element method deals with the 'artificial' reflection wave from the calculation boundary in a better way than the finite difference method. However, the calculation of the finite element method is totally complex. As for the modeling using the Fourier transform, faster and higher resolutions can be obtained than with the finite difference method (Murayama, et al., 1991). Comparing the Fourier transform with the finite difference approximation, the grid number per one wave length in the Fourier transform is shorter than that in the finite difference approximation and the calculation time required in the Fourier transform is less than that in the finite difference approximation at the same resolution level (Ashida, et al., 1991). Based on the theory of the continuous body, the displacement in a certain ground point can be described the source energy and the discontinuous displacement in the boundary surface. Therefore, the displacement can be also presented by the sum of the elemental integral of Green function and that of Green function for the stress. Using this consideration of the displacement, the matching of the boundary condition can be easily performed and the weight of each elemental integral can be calculated. This method is *BEM* (the boundary element method). Kawase (1988) actively applied *BEM* to the simulations of the earthquake problems.

In this section, a one-dimensional numerical simulation of the seismic propagating wave through a cylindrical specimen is conducted, and the relationship between the joint aperture and the frequency of the input wave is clarified. The numerical method used is the finite difference method, which applies the characteristic curve method (Tanaka, 1981), since the simulation is an easy one-dimensional types and the boundary condition is only considered for both end surfaces of the cylindrical specimen.

In a one-dimensional elastic body, stress σ presents a variable in each part, thus, force $(\partial\sigma / \partial x)\Delta x$ works in a micro area, Δx. The pressure wave and the particle velocity are presented by p and u, respectively. As the acceleration is presented by $\partial u / \partial t$, the movement equation is described as follows:

$$\rho\frac{\partial u}{\partial t} = \frac{\partial \sigma}{\partial x} \quad . \tag{5-11}$$

On the other hand, the stress - strain (σ - ε) relation is described as

$$\sigma = E\varepsilon \tag{5-12}$$

where E is the modulus of elasticity. Substituted into the displacement - strain (ξ - ε) relation, $\varepsilon = \partial\xi / \partial x$ and $u = \partial\xi / \partial t$, **Equation 5-12** is differentiated by parameter t and **Equation 5-13** can be obtained, namely,

$$\frac{\partial \sigma}{\partial t} = E\frac{\partial u}{\partial x} \quad . \tag{5-13}$$

Substituting **Equations 5-12** and **5-13** into the $p = -\sigma$ relation, the following differential equations can be obtained:

$$\rho\frac{\partial u}{\partial t} = -\frac{\partial p}{\partial x} \tag{5-14}$$

$$\frac{1}{E}\frac{\partial p}{\partial t} = -\frac{\partial u}{\partial x} \quad . \tag{5-15}$$

Equations 5-12 and **5-13** agree with the electric signal equation which presents the electric signal propagating through the resistless cable, namely,

$$L\frac{\partial I}{\partial t} = -\frac{\partial E}{\partial x} \tag{5-16}$$

$$C\frac{\partial E}{\partial t} = -\frac{\partial I}{\partial x} \tag{5-17}$$

where I is the electric current, E is the voltage, and L and C are the inductance and the capacitance per unit length, respectively. The characteristic of resistless cables is determined by two parameters, such as L and C. Instead of L and C, impedance Z and signal velocity c can be described as follows:

$$Z = \sqrt{\frac{L}{C}}\,,\; c = \frac{1}{\sqrt{LC}} \quad . \tag{5-18}$$

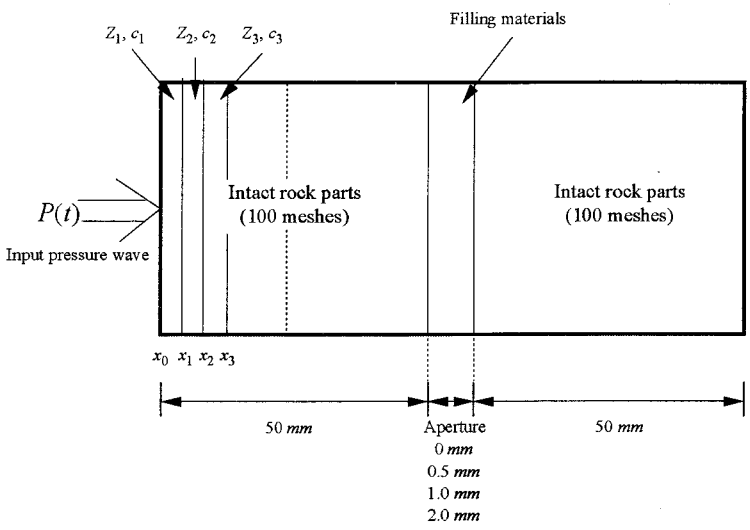

Figure 5.11 The numerical simulation model

For applying these equations to the elastic problem, the following equations can be obtained:

$$Z = \sqrt{k\rho}, \quad c = \sqrt{\frac{k}{\rho}} \quad . \tag{5-19}$$

The electric signal through resistless cables propagates in order to keep the constant waveform without the occurrence of attenuation along the way. Then, from this point of view, the one-dimensional elastic wave is equal to treat by the same way as electric signal.

When applying the pressure wave, $p(x_0, t)$, at the end of the long media toward the x direction ($x = x_0$), as shown in **Figure 5.11**, the purpose is to calculate $p(x,t)$ and $u(x,t)$ at each point. Before performing the numerical simulation, the characters of the multiple-layers media are given. And, at the end of the numerical model, pressure wave is obtained. The initial condition is presented as $p = 0$ and $u = 0$. The numerical simulation is basically equal to the differential equations, namely, **Equations 5-14** and **5-15**. Substituting Z and c, **Equations 5-14** and **5-15** transform into the following simultaneous equations:

$$\begin{aligned} Z\frac{\partial u}{\partial t} + c\frac{\partial p}{\partial x} &= 0 \\ \frac{\partial p}{\partial t} + Zc\frac{\partial u}{\partial x} &= 0 \end{aligned} \tag{5-20}$$

To order to apply the characteristic curve method, **Equation 5-20** becomes simplified, namely, the characteristic curves are described as

$$x / c - t = \alpha \tag{5-21}$$

$$x / c + t = \beta \tag{5-22}$$

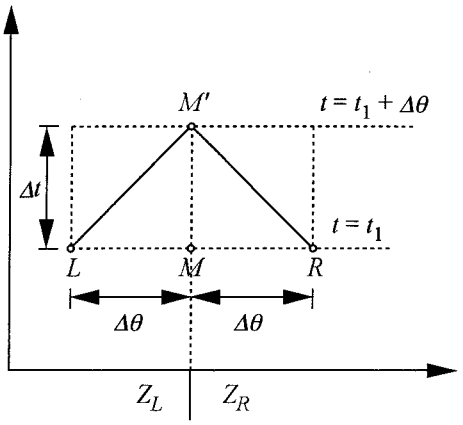

Figure 5.12 Computation by the finite difference method

where α and β are paramters. Substituted into these equations, **Equation 5-20** transforms as follows:

$$p + Zu = const. \tag{5-23}$$

$$p - Zu = const. \tag{5-24}$$

Equations 5-21 and **5-22** present the forward and the backward propagating waves, respectively.

In the multiple layers, the penetration and the reflection of the seismic wave repeat. If the loci of the seismic wave are represented by the distance (x) - time (t) domain, the gradients of the loci are different for each layer because of the difference in the propagating wave velocity, C_i. Instead of x, the other parameter is then defined as

$$\theta = x / c_i \tag{5-25}$$

in which θ shows the traveltime for each layer. In the θ - t plane, the gradients of the loci are constant ($\pm$ 1) without a difference in the layers.

The finite meshes, whose size is $\Delta\theta$, are considered when the differential equation is solved. This size ($\Delta\theta$) does not relate to a numerical error. **Figure 5.12** shows the calculated flow from $t = t_1$ to $t = t_1+\Delta t$ in the θ - t plane. Then, if Δt is equal to $\Delta\theta$, LM' and RM' which are presented in **Figure 5.12** will then agree with the characteristic curves of the forward and the backward propagating waves, respectively. Therefore, **Equations 5-23** and **5-24** are described by the following equations:

$$p_{M'} + Z_L u_{M'} = p_L + Z_L u_L \tag{5-26}$$

$$p_{M'} - Z_R u_{M'} = p_R - Z_R u_R \,. \tag{5-27}$$

Table 5.2 Parameters of the numerical simulation

	Intact rock	Joint filling material
Propagating wave velocity	4.0 [*km/sec.*]	1.0 [*km/sec.*]
Density	2.5	1.5
Impedance	10.0	1.5

In **Figure 5.12**, point M corresponds to the boundary point of the multiple layers, and different impedances at the left side (Z_L) and the right side (Z_R) are presented. The simultaneous equations, **Equations 5-26** and **5-27** are solved for $p_{M'}$ and $u_{M'}$, in other words,

$$p_{M'} = \frac{(p_L + Z_L u_L) - (p_R - Z_R u_R)}{Z_L + Z_R} \tag{5-28}$$

$$u_{M'} = \frac{Z_R(p_L + Z_L u_L) + Z_L(p_R - Z_R u_R)}{Z_L + Z_R} \tag{5-29}$$

Then, since p and u at points L and R ($t = t_1$) are known, p and u at point M' ($t = t_2$) can be determined.

Table 5.2 presents the parameters which is used to the numerical simulation in this research work. The model for the simulation is shown in **Figure 5.11**. One mesh size, $\Delta\theta$ is 0.125 (μsec). Then, since the velocity is 4 *km/sec*, 1 *mm* corresponds to two meshes in the intact rock part, and 1 *mm* in the joint part agrees with eight meshes due to the velocity of 1 *km/sec*. **Equation 5-30** shows the condition of both the stability and the convergence of the solution to a differential equation, namely,

$$0 < \frac{c \cdot \Delta\theta}{\Delta x} \leq 1 \tag{5-30}$$

In the simulation, this condition can be satisfied. However, the grid dispersion is not found in all cases. The joint aperture changes by 0.0, 0.5, 1.0, and 2.0 *mm*, respectively, and the frequency of the input wave changes each 10 *kHz* in the range of 10 *kHz* to 200 *kHz*.

The relationship between the first break amplitude and the frequency is shown in **Figure 5.13**, in which the first break amplitude is defined in **Figure 5.3**. In the case of a non-joint model, the first break amplitude is constant for each frequency. In other cases, however, the first break amplitude decreases with increments in the input wave's frequency. **Figure 5.14** shows the relation between the amplitude ratio and the frequency. The amplitude ratio is defined by the first break amplitude in each case divided by the non-joint model's first break amplitude. **Figure 5.14** shows the same tendency as **Figure 5.13**.

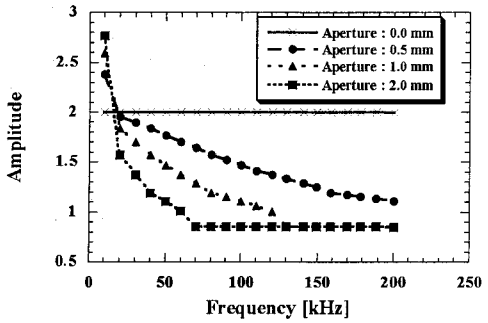

Figure 5.13 Relationship between amplitude and frequency through the numerical simulation

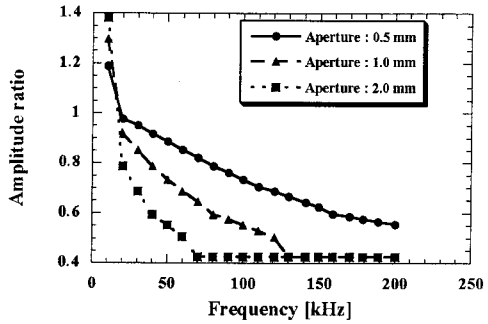

Figure 5.14 Relationship between amplitude ratio and frequency through the numerical simulation

When the seismic wave propagates from one media to another, the penetrated ratio, γ_{12}, is defined in **Equation 5-31** using the impedances, Z_1 and Z_2, as follows:

$$\gamma_{12} = \frac{2Z_1}{Z_1 + Z_2} \quad . \tag{5-31}$$

Propagating forward and backward from one media to another , which is similar to this simulation model, the penetrated ratio, γ, is defined as follows:

$$\gamma = \gamma_{12} \times \gamma_{21} = \frac{2Z_1}{Z_1 + Z_2} \times \frac{2Z_2}{Z_2 + Z_1} \quad . \tag{5-32}$$

From **Table 5.2**, substituting **Equation 5-30** into the rock part impedance, Z_1, and the joint part impedance, Z_2, the penetrated ratio in this simulation is equal to 0.45. In the case of both 1.0 and 2.0 *mm* joint apertures, the amplitude ratio is found to become 0.43, a range of more than 70 or 130 *kHz* in **Figure 5.14**. These results agree with the theoretical penetrated ratio. Break, in lower frequency domains (10 ~ 50 *kHz*) with a 0.5 *mm* joint aperture model, the amplitude ratio does not become 0.43. The multiple reflection occurs in the joint part due to aperture size and frequency. Therefore, in a lower frequency domain, the joint aperture size can be determined from the difference in amplitude ratios.

From these numerical simulations, the amplitude ratio can present the influence of joint apertures sensitively and effectively. In particular, if the frequency of the input wave is considered, the variation in apertures can be estimated in detail.

5.4 Experimental results for the propagating seismic wave through rock joints

As shown in **Figure 5.1**, the seismic propagating experiments are performed under a uniaxial confining condition on some experimental models. Recovered core samples are used for the cylindrical specimens. The specimens are rhyolite. Their uniaxial compressive strength and their seismic velocity at the intact part are 200 *MPa* and 5.81 ~ 5.93 *km/sec.*, respectively. Before describing the experimental results, the relationship between the experimental models and the in-situ rock mass is discussed.

As for **Figures 5.1**(a) ~ (c), the influence of the joint frequency presented in **Equation 5-8**, n, can be discussed since joint surface roughness does not appear (Case 1). In **Figure 5.1**(d), the variation in joint surface roughness, the contact area, and the contact pressure at the joints can be discussed (Case 2). Since the model in **Figure 5.1**(e) shows the variation in apertures and filling material, parameter b in **Equation 5-8** can be discussed (Case 3).

5.4.1 Experimental results of Case 1

Through laboratory experiments, the remarkable distinction between velocity (V_p) and amplitude (A) (or amplitude ratio A/A_0, where A_0 is an amplitude obtained through intact rock) is observed in normal loadings, as shown in **Figures 5.15 to 5.20**.

Figure 5.15 shows the seismic propagating velocity measured in the models in **Figures 5.1**(a) ~ (c). No variation in seismic velocity can be confirmed for the variation in joint frequency, n, in the condition of a smooth joint surface and a uniaxial confining condition of more than 0.5 *MPa*. That is, V_p converges at a constant level regardless of the joint frequency. As mentioned above, the variation in apparent velocity, which changes either the intact rock property or the contact conditions at the joint, does not apply to these models. The contact condition on the smooth joint surface roughness is stable, and the $V_p \sim P_C \sim n$ relation does not make noticeable sense. P_C is the uniaxial load. On the other hand, in a confining condition range of less than 0.5 *MPa*, the seismic velocity drops for each joint frequency. This is the reason why, under a lower confining condition, the contact condition on the joint smooth surface is unstable. And, preexisting fissures and micro-cracks are opened since the stress condition becomes lower than the in-situ initial stress condition. Then, after most of the fissures have closed with increments in the uniaxial load, further compression produces bulk rock compression, consisting of pore deformation and grain compression at an approximately linear rate, and the seismic velocity converges at a constant level regardless of the smooth joint frequency. Therefore, until the initial stress condition, **Figure 5.15** shows that the seismic velocity increases.

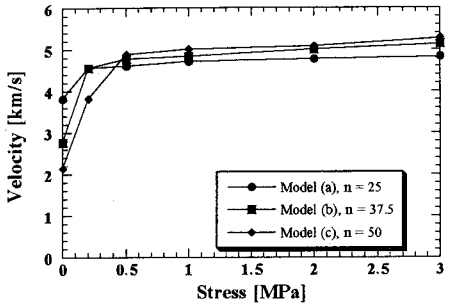

Figure 5.15 Velocity of joint frequency under normal loading
(n = 25, 37.5, and 50 [1/m])

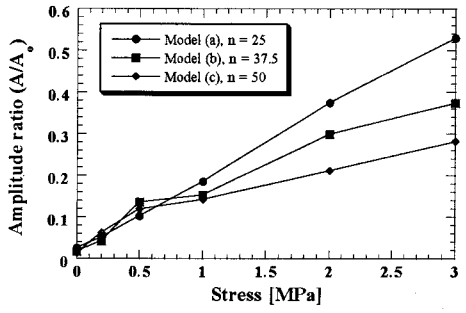

Figure 5.16 Amplitude ratio of joint frequency under normal loading
(n = 25, 37.5, and 50 [1/m])

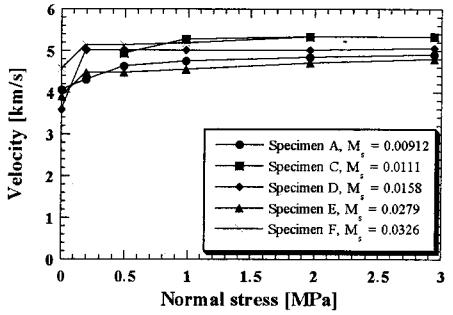

Figure 5.17 Velocity v.s. normal stress for the variation in joint surface roughness
(M_S = 9.12, 11.1, 15.8, 27.9, and 32.6 x 10^{-3})

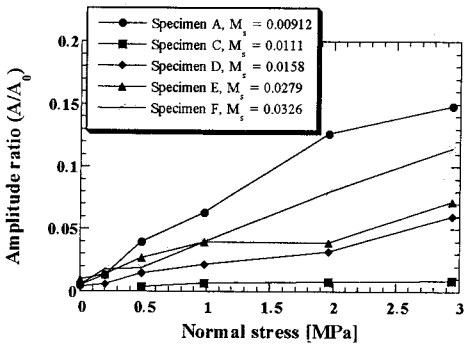

Figure 5.18 Amplitude v.s. normal stress for the variation in joint surface roughness
(M_S = 9.12, 11.1, 15.8, 27.9, and 32.6 x 10^{-3})

Figure 5.16 shows the $A/A_0 \sim P_C \sim n$ relation. The amplitude ratio, A/A_0, increases depending on the joint frequency, n, as the confining pressure, P_C, rises. In particular, under a uniaxial load of more than 0.5 MPa, A/A_0 clearly estimates the variation in joint frequency. Therefore, with increments in joint frequency n, A/A_0 decreases.

As mentioned above, it is confirmed that amplitude ratio A/A_0, such as the first break amplitude, is more sensitive under a constant confining condition than the seismic velocity in order to estimate the variation in joint frequency. On the other hand, the $V_P \sim P_C \sim n$ relation does not make noticeable sense.

5.4.2 Experimental results of Case 2

To speak of the joint surface roughness (M_S) ~ P_C relation shown in **Figures 5.17** and **5.18**, using the model in **Figure 5.1**(d), a common tendency which was obtained in **Figures 5.15** and **5.16** is recognized. V_P converges at a constant level regardless of the joint surface roughness. Then, the variation in joint surface roughness is not clearly reflected in the $V_P \sim P_C$ relation. On the other hand, the amplitude ratio can be confirmed to reflect the variation in joint surface

roughness. Therefore, the first break amplitude is more advantageous than the seismic velocity for estimating the variation in joint surface roughness.

To speak of the $M_S \sim A/A_0$ relation shown in **Figure 5.18**, it should be noted that the amplitude ratio decreases as the roughness increases, except for Specimen *A*. Then, it is thought that the variation in the first break amplitude can estimate the variation in joint surface roughness in detail. Since it is impossible to contact rock joints perfectly in a specimen consisting of natural joint surface roughness, the first break amplitude through the natural joint surface roughness is determined by parameters, namely, s (contact area on rock joints) and p (contact pressure on rock joints) which are presented by the function, F, in **Equations 5-9** and **5-10**. From these experimental results, it is confirmed that there is a tendency for the first break amplitude to become smaller as M_S grows smaller, that is, the joint surface roughness becomes smooth. Therefore, in order to estimate the joint surface roughness quantitatively through the propagating behavior of a seismic wave, the relationship between the property of the seismic wave and certain kinds of parameters must be considered, namely, the contact area and the contact pressure on the rock joint aperture estimated from the shape of the rock joint surface (Iwano and Einstein, 1993), and the maximum joint closure, based on the estimation of joint surface roughness described in Chapter 3.

A strain gage is attached to both upper and lower parts of an intact rock and the total displacement of the specimen is measured by the displacement meter. Then, changes in aperture are calculated using these data. **Figures 5.19** and **5.20** show the velocity ~ aperture relation and the amplitude ~ aperture relation. From these results, it is clear that the velocity does not show any change, but the amplitude suggests significant variations in the aperture ~ roughness ~ confining pressure relations under normal stress levels.

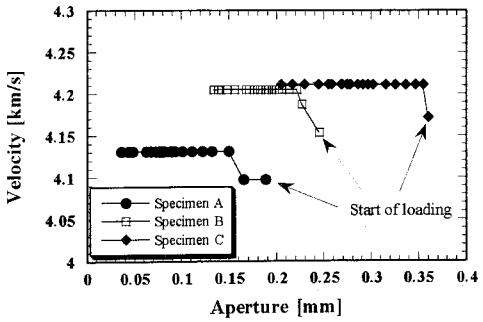

Figure 5.19 The relationship between velocity and aperture under normal loading
(M_S = 9.12, 7.79, and 11.1 x 10^{-3} for Specimens *A*, *B*, and *C*)

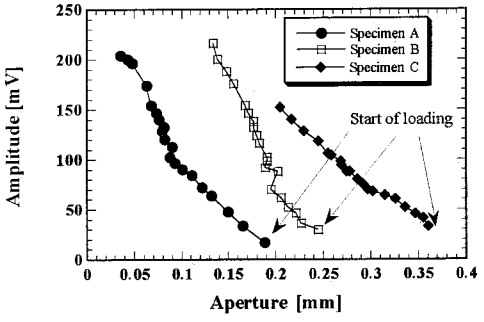

Figure 5.20 The relationship between amplitude and aperture under normal loading
(M_S = 9.12, 7.79, and 11.1 x 10^{-3} for Specimens *A*, *B*, and *C*)

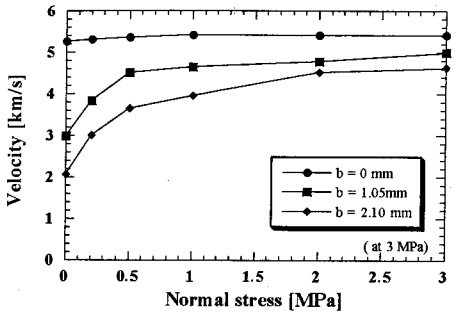

Figure 5.21 Velocity of the variation in aperture under normal loading (b = 0, 1.05, and 2.10 *mm* at 3 *MPa*)

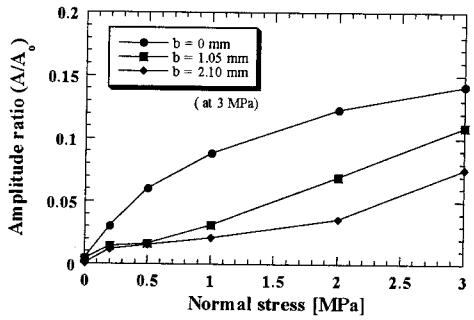

Figure 5.22 Amplitude ratio of the variation in aperture under normal loading (b = 0, 1.05, and 2.10 *mm* at 3 *MPa*)

5.4.3 Experimental results of Case 3

Figures 5.21 and **5.22** show the $V_p \sim P_c \sim b$ relation and the $A/A_0 \sim P_c \sim b$ relation measured from the model in **Figure 5.1**(e), respectively. The thickness of the filling material at a 3 *MPa* normal confining condition is b. Then, b is equal to the joint aperture.

From the results of the seismic velocity in **Figure 5.21**, the apparent seismic velocity decreases as the number of filter papers increases, that is, the aperture becomes wider with each normal confining condition. In this experiment, the apparent seismic velocity, V_m, is defined as follows:

$$V_m = \frac{l+b}{t} = \frac{l+b}{\frac{l}{V}+\frac{b}{v}} \tag{5-33}$$

where t : observed traveltime
V : seismic velocity of intact rock
v : seismic velocity of filling material
l : length of intact rock
b : thickness of filling material.

In this equation, the apparent seismic velocity is affected by both the seismic velocity and the thickness of the filling material. **Figure 5.21** shows that the apparent seismic velocity can be confirmed to decrease with an approximately constant ratio as the number of filter papers increases.

As for the amplitude ratio, A/A_0, it also becomes smaller as the number of filter papers increases, as shown in **Figure 5.22**. It is confirmed that the first break amplitude grows smaller with increments of b, which represent the aperture and/or the thickness of the filling material in **Equation 5-8**.

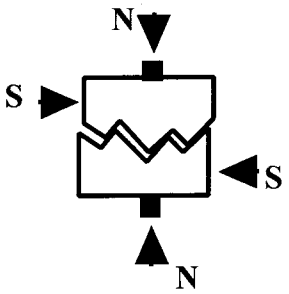

Figure 5.23 Experimental set-up of the seismic propagating experiment under shear loading

When the aperture is wider than 1 *mm*, both the velocity and the amplitude correspond with changes in contact (confining) pressure, as shown in **Figures 5.21** and **5.22**. However, the amplitude still has a higher capability of sensing the reduction in confining pressure. It is very useful to discussions on the effects of support elements in tunneling or large underground excavation works.

5.4.4 Experimental results under a shear loading condition

In order to investigate the seismic propagating behavior under a shear loading condition, laboratory experiments are carried out using the experimental set-up shown in **Figure 5.23**. The observing system of the seismic wave corresponds to that under a normal loading experiment. The experiments are done with a roughness of 11.1 x 10^{-3} in M_S (9.99 in *JRC*) under three different confining pressures, namely, 0.2, 0.4, and 0.6 *MPa*. Through laboratory experiments, a remarkable distinction between the seismic velocity (V_p) and the first break amplitude (A) in the shear loading is observed, as shown in **Figures 5.24** ~ **5.27**. The same tendency is recognized as in the case of normal loading.

The shear displacement along the joint is of great concern, because it causes a comparatively aggressive reduction in shear resistance against excavations and it is not easy to find. As shown in **Figures 5.24** and **5.25**, only the amplitude may suggest a magnitude of shear displacement in the primary stage which is subjected to a rather high change in amplitude for a low range in displacement such as 1 *mm* or so. Loosening is related to this low range in shear displacement. Also, from the same point of view, changes in the aperture of the joint should be detected adequately in the excavation work. From the results shown in **Figures 5.26** and **5.27**, it is clear that the velocity does not show any change, but the amplitude suggests a significant variation in the dilation ~ roughness ~ confining pressure relations under shear stress levels.

Thus, the sensitivity of the amplitude is much higher than that of the velocity. It is greater than was primarily expected. Tanimoto, et al. (1994b) confirmed the same tendency in the laboratory tests applied to various roughness levels for a range in *JRC* of 6 to 20. It is clearly concluded that changes in the joint aperture can be detected in terms of the amplitude of the traveling *P*-wave in cases of both normal and shear loadings. Therefore, seismic attenuation

geotomography (*SAT*) is more sensitive than seismic velocity geotomography (*SVT*) in the investigation of rock joints. This is why the application of *SAT* is strongly promoted in the following chapter.

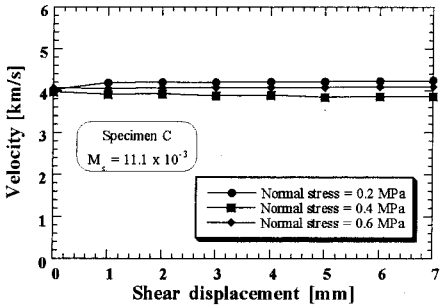

Figure 5.24 The velocity ~ shear displacement relation under shear loading (M_S = 1.11 x 10^{-2}, P_c = 0.2, 0.4, and 0.6 *MPa*)

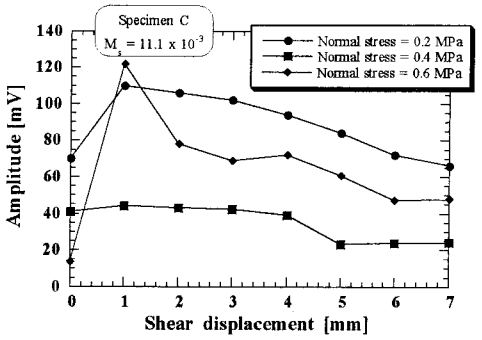

Figure 5.25 The amplitude ~ shear displacement relation under shear loading (M_S = 1.11 x 10^{-2}, P_c = 0.2, 0.4, and 0.6 *MPa*)

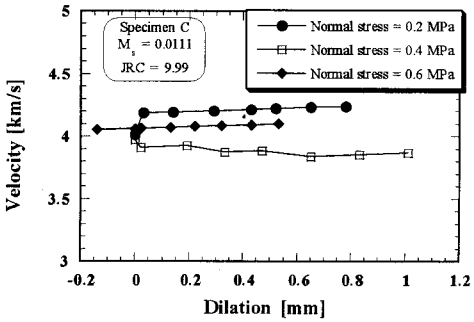

Figure 5.26 The relationship between velocity and dilation under shear loading (M_S = 1.11 x 10^{-2}, P_c = 0.2, 0.4, and 0.6 *MPa*)

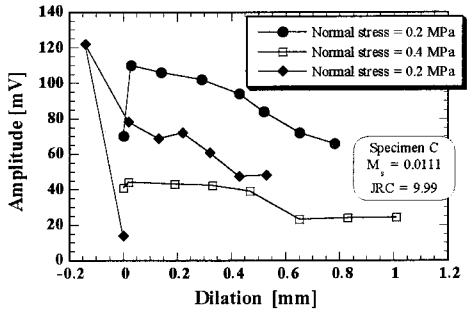

Figure 5.27 The relationship between amplitude and dilation under shear loading (M_S = 1.11 x 10^{-2}, P_c = 0.2, 0.4, and 0.6 *MPa*)

5.5 Conclusion

In the present chapter, several specimens consisting of certain kinds of joint conditions have been used for seismic propagating experiments under normal and shear loading conditions. Just how the seismic propagating behavior has affected the joint conditions has been considered.

Based on experimental results, knowledge such as the following can be presented:

(1) Using specimens which consist of smooth artificial joints, the seismic velocity does not change with variations in joint frequency. However, the first break amplitude shows remarkable sense.

(2) Performing the seismic propagating experiments on five kinds of natural joint surface roughness, variations in seismic velocity cannot be found, but the first break amplitude can be found to show a remarkable distinction against the joint surface roughness. Thus, a good correlation between joint surface roughness and the first break amplitude can be confirmed.

(3) In the case of a model which includes filling material, both the seismic velocity and the first break amplitude decrease with increments in the thickness of the filling material.

(4) Under a shear loading condition, variations in the first break amplitude are more sensitive than those of the seismic velocity. In particular, variations in joint surface roughness and changes in aperture and/or dilation are clearly presented by the first break amplitude.

As mentioned above, the first break amplitude is more useful than the seismic velocity for discussing the effects of joint frequency and joint surface roughness. However, both the seismic velocity and the first break amplitude are useful for estimating the filling material. And, the first amplitude is useful for presenting variations in the dilation and the aperture under shear loading, that is, for discussing the effects of support elements in tunneling or large underground excavation works.

Applying these remarkable conclusions to a discussion on the results of field investigations, rock structures can be estimated at an objective area in detail using both seismic velocity and the seismic attenuation geotomography. In the following chapter, the analyzing method for the seismic geotomographic technique will be described, and the analyzed results based on knowledge from fundamental laboratory experiments presented in the present chapter will be discussed.

REFERENCES

Ashida, Y., Murayama, Y. and Sassa, K. (1991) : Simulation of seismic disturbances by using of the Fourier Transform - Model studies and considerations -, *BUTSURI-TANSA*, Vol. 44, No. 3, pp. 113 - 125. (in Japanese)

Goodman, R. E. (1976) : *Methods of Geological Engineering in Discontinuous Rocks*, West Publishing Company, pp. 170 - 173.

Ikeda, K. and Ohshima, H. (1975) : *Introduction to civil engineering geology*, Civil Engineering Publisher, pp. 82 - 83. (in Japanese)

Iwano, M. and Einstein, H. H. (1993) : Stochastic analysis of surface roughness, aperture and flow in a single fracture, *Eurock' 93*, Ribeiro e Sousa & Grossmann (eds.), pp. 135 - 141.

Kasaes, H. (1988) : Time-domain response of a semi-circular canyon for incident *SV*, *P*, and Rayleigh waves calculated by the discrete wavenumber boundary element method, *Bull. Seismic Soc. Am.*, 78, pp. 1415 - 1437.

Murayama, Y., Ashida, Y. and Sassa, K. (1991) : Simulation of seismic disturbances by using of the Fourier Transform - Theory and calculation method -, *BUTSURI-TANSA*, Vol. 44, No. 1, pp. 18 - 26. (in Japanese)

Sassa, K. (1990) : Applications of geotomography to rock engineering, *Proceeding of SEGJ International Symposium on Geotomography*, pp. 21 - 28.

Sassa, K., Ashida, Y. and Sugano, T. (1993) : *Geophysical Exploration*, Morikita Publisher Inc., pp. 13 - 15. (in Japanese)

Tanaka, K. (1981) : Reduction of seismic vibration of blasting by the technique of multiple shot (II) - Simulation of vibration of elastic multiple layer, *Journal of the Industrial Explosives Society, Japan*, Vol. 42, No. 4, pp. 233 - 238. (in Japanese)

Tanimoto, C and Ikeda, K. (1983) : Acoustic and mechanical properties of jointed rock, *Proc. of 5th ISRM Congress*, Balkema, pp. A15 - 18.

Tanimoto, C., Kishida, K., Odawara, Y., Nakanishi, Y., Yoshizu, Y. and Kunii, K. (1994 a) : Fundamental study on seismic geotomography in consideration of amplitude attenuation at discontinuities, *Proc. of the 9th Japan Symp. on Rock Mechanics*, ISRM-Japan, pp. 325 - 330. (in Japanese)

Tanimoto, C., Kishida, K., Yoshizu, Y. and Kunii, K. (1994 b) : Seismic Attenuation Geotomographic Technique in Designing a Large Underground Cavern, *Proc. of the 1994 ISRM International Symposium, Integral Approach to Applied Rock Mechanics*, Vol. 1, M. Van Sint Jan (ed), pp. 195 - 206.

Chapter 6

Development of the Seismic Geotomographic Technique and its Application to Jointed Rock Masses

6.1 Introduction

The geotomographic technique has been employed in various fields to improve its ability to map sections of the earth's interior. The capabilities of the tomographic technique applied to the fields of geophysics, petroleum exploration, and rock engineering are different from the medical ones. In other words, while it is rather easy to find abnormalities in a human body surrounded entirely on a 360-degree angle and knowledge of the inner structure obtained through plenty of past surgical experience, interpretations of underground geo-structures are subject to being made with a very limited amount of known factors. Thus, rock engineers should create their own methods, from data acquisition to the final interpretation, depending on their objectives.

Geotomography is a kind of remote sensing technique which enables us to visualize the inner structure and/or the distribution of the physical properties of an objective body (rock and/or soil) in a certain cross section in terms of the movements of elastic and electromagnetic waves, electric currents, and water pressure pulses to be generated around the objective space or area. The tomographies for obtaining the two-dimensional distribution of propagation velocity and the attenuation of elastic waves (called 'seismic velocity' and 'seismic attenuation' tomographies, respectively) and electrical resistivity are well applied in the field of rock engineering (Ishii, 1990; Sassa, 1990; Tanimoto and Shibata, 1992).

Although the propagation velocity of a seismic wave is an overall index, the mechanical properties of rock, including discontinuities, have not yet been clarified. This means that even if a highly sophisticated seismic geotomography has been developed for jointed rocks without accurate knowledge of the joint parameters, such as joint orientation, joint (fracture) frequency, apertures, filling material, weathering effects, water table, moisture content, etc., the distribution of wave velocities remains an index which is available only for the same type of rock mass; no significant mechanical properties of the rock mass are shown (Tanimoto and Ikeda, 1983; Tanimoto and Kishida, 1994).

From an engineer's point of view, seismic velocity geotomography as well as seismic attenuation geotomography have been developed to pursue further details on the respective joints than the available seismic geotomography which gives no consideration to an accurate joint distribution. As for seismic velocity geotomography, the capability of its analysis, especially

with respect to such boundary conditions as the locations of the source and the receiver points, the relationship between raypaths, and the inclination of the lower velocity zone, will be discussed. Several fundamental models are illustrated in terms of the numerical simulation. At present, the immediate targets of both seismic velocity and attenuation geotomographies are rock hydraulics and safety inspections of rock structures. This is because changes in the attenuation characteristics are more detectable those that in velocity for magnitudes of water saturation and fracturing. Judging from the reality obtained through continuous observation, the application of attenuation geotomography provides more reliable information on fracturing for the case described in the present chapter.

6.2 Algorithm of seismic geotomography

6.2.1 Concept of seismic geotomography

Geotomography enables us to visualize the inner structure and/or the distribution of the physical properties of an objective body (rock and/or soil) in a certain cross section in terms of the movements of elastic and electromagnetic waves, electric currents, and water pressure pulses to be generated around an objective space or area. The prefix 'tomo' comes from the Greek language and means 'the cut' or 'the cross section', that is, tomography is a technique for making images of a cross section (Saito, 1991). In general, tomography is associated with *X*-ray *CAT* scans (in Japan the term "*CT* scans" is used) in the medical field (**Figure 6.1**). This type of imaging medical examination has been developing since Dr. Röntgen discovered *X*-rays in 1885. With the remarkable progress of computer technology, *X*-ray *CAT* scans were invented in 1972. From a medical point of view, the invention of *X*-ray *CAT* is equal in importance to the discovery of *X*-rays. In the past quarter century, medical imaging examinations have made rapid improvements with great advances in the semiconductor and electronics. Not only *X*-ray *CAT* scans, but also *MRI*s, γ-cameras, Specs, and Pets have been developed, and they are capable of detecting cancer and/or polyps which are less than 1 *cm* in size and stopping blood vessels which are less than 1 *mm* in size.

In the same way, geotomography can create underground images. Using propagating methods, geotomography has been classified into seismic geotomography, electromagnetic wave geotomography, electric resistivity geotomography, and so on. Both seismic and electromagnetic wave geotomographies are applied to the phenomenon of wave emotion, but electric resistivity geotomography is applied to the theory of electric potential. The former presents the properties (velocity and the damping factor, etc.) along the ray paths. The latter presents the relative distribution of electric resistivity in the investigated field (Shima, 1989).

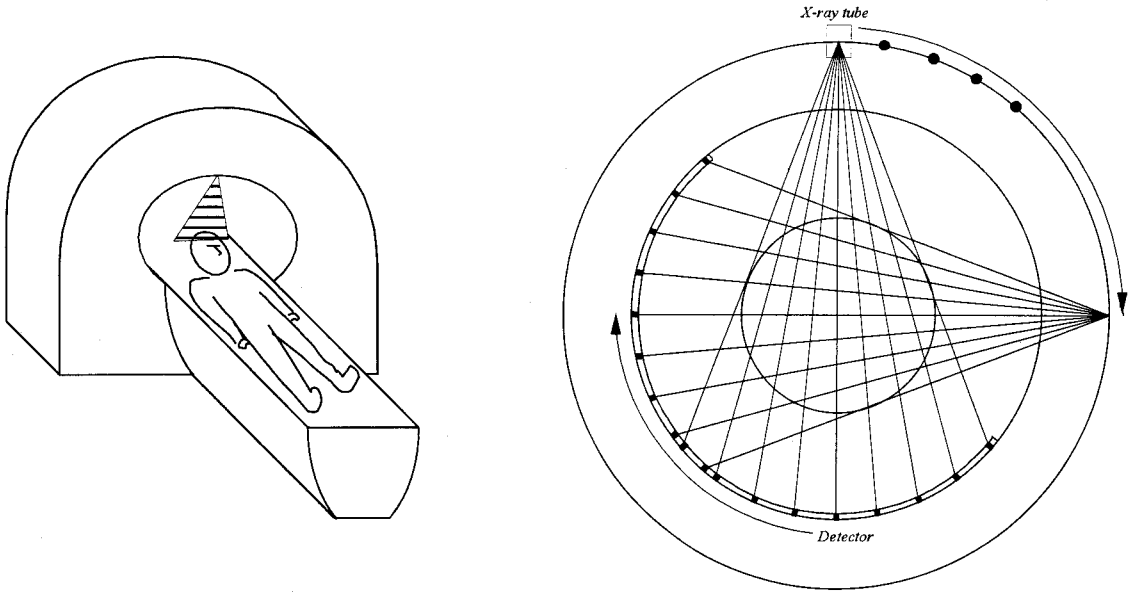

(a) *X*-ray computer tomography (b) Rotate/Rotate-type *X*-ray computer tomography

Figure 6.1 The concept of *X*-ray computer tomography

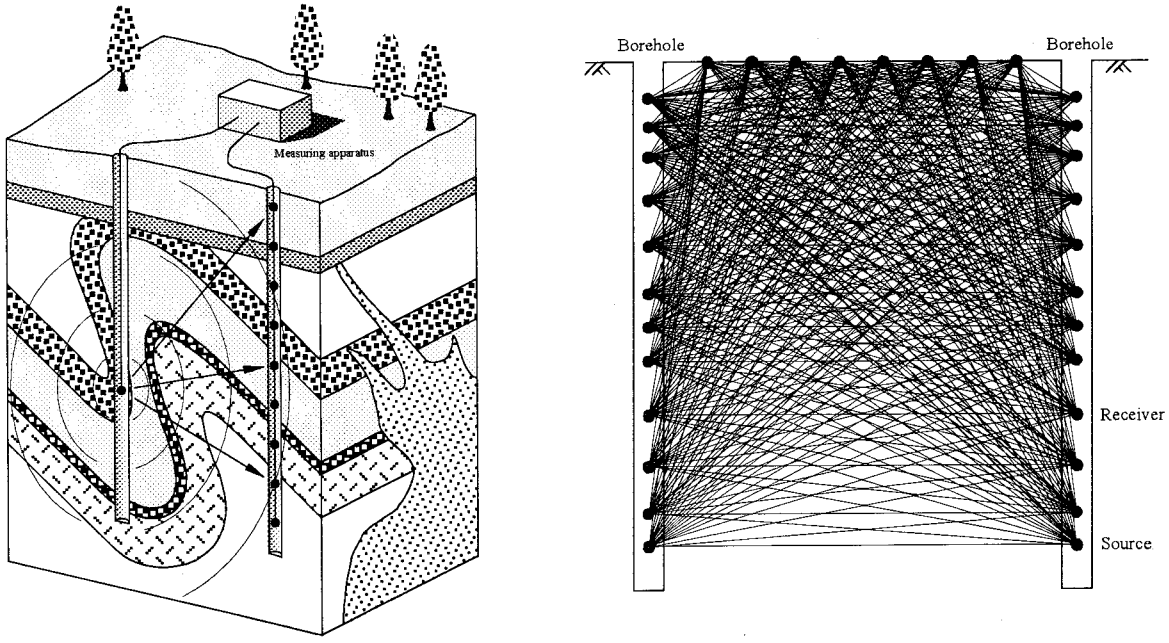

(a) Image of geotomography (b) The seismic geotomography
(borehole - borehole or borehole - surface)

Figure 6.2 The concept of seismic geotomography

Seismic geotomography sets up both the source and the receiver points around an objective area, as shown in **Figure 6.2**. It presents the distribution of velocity and the damping factor at an objective area using the traveltime and the amplitude. In the investigated method and analysis, seismic geotomography is different from the exploration of either refraction or reflection waves. That is, since seismic waves begin and are received at many points, a large amount of data can be

obtained. And, combined with an inversion analysis, the results become very highly accurate. The basic concept of seismic geotomography corresponds to that of *X*-ray *CAT*. However, there are some differences between seismic geotomography and *X*-ray *CAT* as follows:

1) *X*-ray *CAT* scans can easily present the distribution of the absorbed coefficients of a human body through the strength of propagating *X*-rays, since a straight raypath can be assumed. In seismic geotomography, however, seismic waves cannot propagate in a straight line. They become refracted due to the complex underground structures. Therefore, it is important to determine the raypaths of the seismic waves in a seismic geotomographic analysis.
2) It is easy to assume a straight ray path in the analysis of an *X*-ray *CAT* scan. However, the analysis of seismic geotomography is performed by a back analysis with an iterative calculation because of the estimation of the raypath. Therefore, *X*-ray *CAT* scan results can be found immediately, whereas seismic geotomography requires too much time before the results are finally found.
3) In the case of an *X*-ray *CAT* scan, the source and the receiver points can be set up around an objective area, that is, a human body, as shown in **Figure 6.1**(b), and an *X*-ray path around 360 degrees can be measured toward the human body. Therefore, we can obtain many projection data through numereous ray paths. On the other hand, it is impossible with seismic geotomography to set up source and receiver points such as with the *X*-ray *CAT* scan (**Figure 6.1**(b)) because of geometrical and operating limitations.
4) As for the human body, personal differences in the structure of internal organs seldom or never appear. We know the location of every internal organ. However, this cannot be said of seismic geotomography. The geology presents its own particulars at each point. Thus, it is difficult to discuss the results of seismic geotomography.

The theory of tomography is based on the projection slice theorem. **Figure 6.3** shows the objective function, $f(x, y)$, and the waveform of the projection, $P_\phi(\xi)$. The objective function presents the distribution of physical features. In the case of seismic velocity geotomography, slowness, S, is defined by the reciprocal of the propagating velocity. The waveform of the projection, $P_\phi(\xi)$, is defined by **Equation 6-1**, wherein the η-axis is in the projection direction, the ξ-axis is the orthogonal axis against the η-axis, and the angle, ϕ, forms the cross between the x-axis and the ξ-axis, as shown in **Figure 6.3**. In other words,

$$\begin{aligned} P_\phi(\xi) &= \int_{ray} f(x,y)d\eta \\ &= \int_{?}^{?} f(\xi\cos\phi - \eta\sin\phi,\ \xi\cos\phi + \eta\sin\phi)d\eta \end{aligned} \tag{6-1}$$

In the above equation, the Fourier transform is carried out along the ξ-axis direction.

$$\hat{P}_\phi(k_\xi) = \iint_{-\infty}^{\infty} f(\xi\cos\phi - \eta\sin\phi,\ \xi\cos\phi + \eta\sin\phi)\cdot\exp\left(-ik\xi\right)d\xi d\eta \tag{6-2}$$

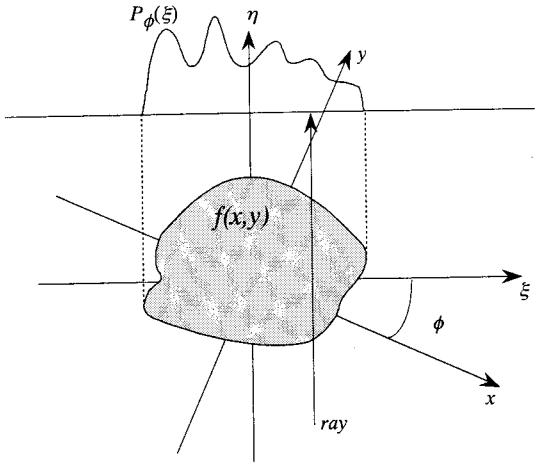

Figure 6.3 The basic concept of the projection slice theorem

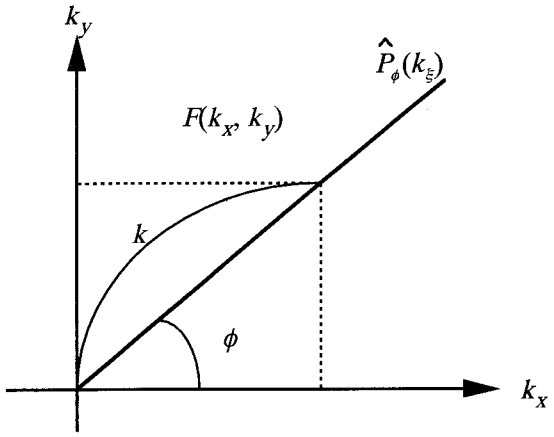

Figure 6.4 The geometrical relationship between $P_\phi(k\xi)$ and $F(k_x, k_y)$ in the frequency domain

The relationship between x, y and η, ξ shows the following equation:

$$\begin{pmatrix} \xi \\ \eta \end{pmatrix} = \begin{pmatrix} \cos\phi & \sin\phi \\ -\sin\phi & \cos\phi \end{pmatrix} \begin{pmatrix} x \\ y \end{pmatrix} . \tag{6-3}$$

Using **Equation 6-3**, the integral transform from η, ξ to x, y is carried out. Since the determinant of the Jacobian matrix is equal to unity, the integral equation of **Equation 6-2** can be transformed to

$$\hat{P}_\phi(k_\xi) = \int\int_{-\infty}^{\infty} f(x,y) \cdot \exp\left\{-ik\xi\left(x\cos\phi + y\sin\phi\right)\right\} dxdy . \tag{6-4}$$

Then, the two-dimensional Fourier transform, $F(k_x, k_y)$, of the objective function, $f(x, y)$, is presented as follows:

$$F(k_x, k_y) = \int\int_{-\infty}^{\infty} f(x,y) \cdot \exp\left\{-i\left(k_x x + k_y y\right)\right\} dxdy . \tag{6-5}$$

From **Equations 6-4** and **6-5**, the following relation can be obtained:

$$\hat{P}_\phi(k_\xi) = F\left(k_\xi\cos\phi, k_\xi\sin\phi\right) . \tag{6-6}$$

Equation 6-6 is the projection slice theorem. In **Figure 6.4**, the Fourier transform of the projection waveform along the ξ direction corresponds to the value of the objective function, $f(x, y)$, along the ϕ direction line which is applied to the two-dimensional Fourier transform. Therefore, $\hat{P}_\phi(k_\xi)$ is calculated with a change in f from 0 to 180 and is plotted on the k_x - k_y plane. When the two-dimensional Fourier inverse transform of $\hat{P}_\phi(k_\xi)$ is carried out, the original objective function can be re-constructed. This is the basic theory of tomography. In the case of *X*-ray *CAT*, the objective function is the damping ratio of the *X*-ray.

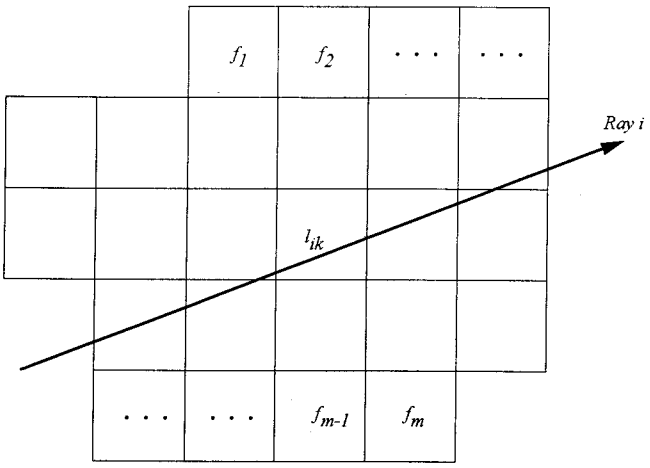

Figure 6.5 Division of cells and the objective function

As mentioned above, slowness, which is the reciprocal of the seismic velocity through the underground, is the objective function in seismic geotomography. Since neither sources nor receivers can be set up anywhere against an objective area, it is impossible to calculate $\hat{P}_{\phi}(k_{\xi})$ with a change in ϕ from 0 to 180, as shown in **Figure 6.4**. And, since the seismic wave is refractive through underground structures, the raypath is not straight and it is impossible to apply the Fourier transform to the seismic geotomography. If ϕ changes from 0 to 180 in the cross-hole geotomography, an unlimited borehole drill must be made.

6.2.2 Algorithm of the seismic velocity geotomographic technique (*SVT*)

When a seismic survey is carried out in the field, traveltime between two points (the shot and the receiver points) is gained. Based on many sets of traveltimes along the various raypaths which densely propagate through an objective medium (rock mass), the seismic velocity geotomographic technique (*SVT*) shows the distribution of velocities in a project profile. In *SVT*, the concept of slowness is conveniently employed instead of velocity. Slowness is defined by the reciprocal of velocity. In *SVT*, slowness is the objective function. In **Figure 6.5**, if an objective area is divided throughout M number of cells, each cell is taken to an objective function, S_k. Therefore, **Equation 6-1** can be approximately shown in a discrete form, using l_{ik}, which presents the length when the i-th ray crosses the k-th cell, namely,

$$P_i = \sum_{k=1}^{M} \left(S_k \cdot l_{ik} \right) \quad . \tag{6-7}$$

Based on **Figure 6.6**, it is then explained concretely. **Figure 6.6**(a) shows an objective area between boreholes. In one borehole, the sources are set up; in the other, receivers are set up. The objective area is divided up by a certain number of cells, as shown in **Figure 6.6**(b). Starting from

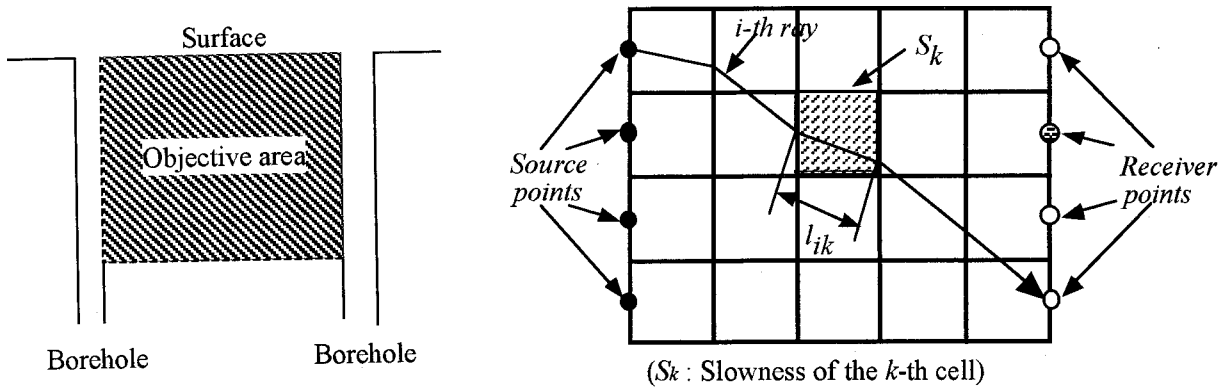

(a) The objective area

(b) Calculation of traveltime for each raypath

Figure 6.6 The objective area and the cell division

the source point the seismic wave propagates through the rock mass and measures each receiver point. Then, the fundamental equation is given by **Equation 6-8**, namely,

$$t_i = \int_{l_i} S(x, y)dl \tag{6-8}$$

where t_i is the arrival time of the first break at the i-th ray, l_i denotes an integrated length along the i-th raypath, and $S(x, y)$ is a slowness field. According to the rectangular cell discretization shown in **Figure 6.6**(b), the traveltime along the i -th ray is represented in the form of

$$t_i = \sum_k l_{ik} \cdot S_k \tag{6-9}$$

where l_{ik} is a segmented length in the k -th cell and S_k is the slowness of the k -th cell.

The system of the tomographic analysis for the field data in this thesis is shown in **Figure 6.7** (Tanimoto & Kishida, 1994 and Tanimoto, et al., 1994). The algorithm of *SVT* is discussed in the slowness ~ traveltime domain. It consists of the alternative feedback between two steps, namely, ray-tracing (Step A) and the reconstruction of slowness (Step B).

Step A, ray-tracing, can be done by obtaining the path length matrix, $[l_{ik}]$ or $[\boldsymbol{L}]$, under the assumption of known parameters, namely, T_i and S_k. For the initiation of Step A, observed first arrival times $\{T^*\}$ and uniformly distributed slowness field $[S^{(0)}]$ are given, and traveltimes at respective grid points (corners of cells) are calculated by solving the eikonal equation as shown by

$$\left(\frac{\partial T}{\partial x}\right)^2 + \left(\frac{\partial T}{\partial z}\right)^2 = S^2(x,z) \tag{6-10}$$

where $T(x,z)$ is the traveltime field for the seismic energy propagating from a source point through a medium with a slowness distribution of $S(x,z)$. The solution to the eikonal equation gives the

traveltimes throughout the model. Vidale (1988) presented a method using the finite difference. In many cases, however, the direct application of finite difference to the eikonal equation is subjected to an ill-condition due to the irregularity of the path length matrix. Hence, new techniques for the finite difference solution were presented along the expanding wavefronts, such as van Trier & Symes (1991) and Qin et al. (1992). Tanimoto and Kishida (1994) developed a combined method of finite difference and Huygens' principle proposed by Itoh et al. (1983), Saito (1989), Moser (1991) etc., and it can solve the eikonal equation quite successfully.

Once traveltime distribution $[T]$ is known, the length of l_{ik}, which is included in the k-th cell, can be obtained by interpolation with the finite difference, corresponding to a given slowness, $S_k^{(0)}$. A figure at the shoulder (0) means the initial value of slowness in Step A for the first cycle. Hence, the path length matrix, $[\boldsymbol{L}]$, becomes known as $[\boldsymbol{L}]^{(1)}$. Namely, ray tracing for the first cycle is tentatively determined. Next, by making the ray path lengths known, respective traveltime residuals for all ray paths, ΔT_i, are calculated as follows:

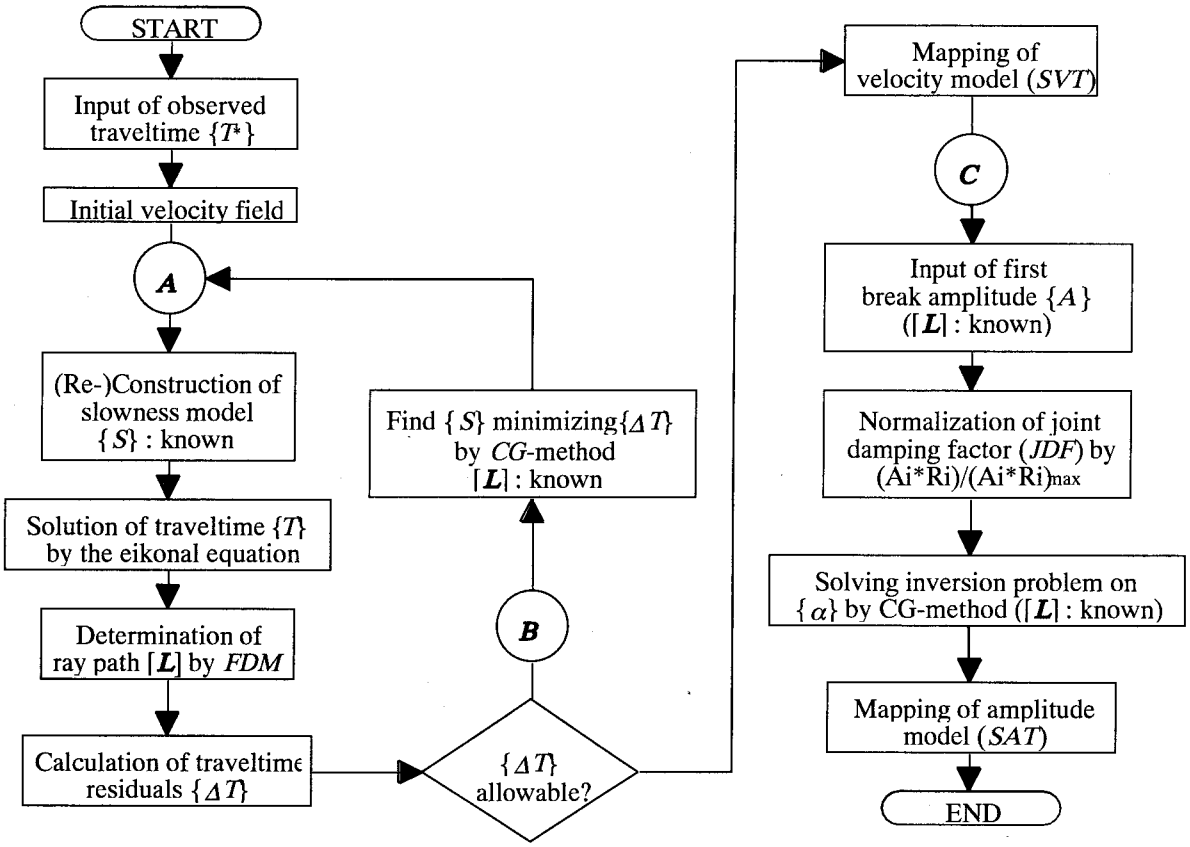

Remarks {S} : slowness vector, [L] : ray path matrix, {T} : calculated traveltime vector, {T^*} : observed traveltime vector (known), {ΔT} : traveltime residual vector, {α} : joint damping factor vector, *FDM* : finite difference method, *CG* : conjugate gradient, A : start of ray tracing, B : start of reconstruction of slowness, C : start of *SAT*

Figure 6.7 Flow chart for seismic velocity geotomography (*SVT*) and seismic amplitude geotomography (*SAT*)

$$\begin{aligned} \Delta T_i^{(1)} &= T_i^* - T_i^{(1)} \\ &= T_i^* - \sum_k l_{ik}^{(1)} \cdot S_k^{(0)} \end{aligned} \tag{6-11}$$

where T_i^* and $T_i^{(1)}$ are observed and calculated traveltimes of first arrivals for the i-th ray in the first cycle, respectively. Then, making slowness field S_k unknown in Step B, while observed traveltime T_i^* and raypaths l_{ik} are known, slowness field $S_j^{(0)}$, which minimizes the absolute value of the traveltime residuals, $\{\Delta T\}^{(1)}$, is solved with regard to all raypaths by means of various methods such as singular value decomposition (*SVD*), the white noise method, the conjugate gradient method (*CG* method) (Scales, 1987), etc. This procedure is a type of inversion problem seeking a least square solution. The *CG* method is used in this computation. Thus, the new slowness field has been obtained in the first cycle through two steps, A and B.

The newly obtained $[\boldsymbol{S}]^{(1)}$ is given back to Step A for the second cycle, and path length matrix $[\boldsymbol{L}]$ is recalculated as $[\boldsymbol{L}]^{(2)}$. Through the same iteration procedure, the slowness field is updated cycle by cycle.

When $\{\Delta T\}^{(q)}$ in the q-th cycle becomes smaller than the designated allowance for the traveltime residual (limit of negligible error), the iteration is complete. Consequently, the velocity distribution is constructed by that of slowness and is illustrated in the form of tomography.

6.2.3 Algorithm of the seismic amplitude (attenuation) geotomographic technique (*SAT*)

The seismic amplitude (attenuation) geotomographic technique (*SAT*) is created on the basis of the *SVT* results, that is, the raypaths. An iteration such as between Steps A and B in *SVT* is not necessary any more. The *SAT* method was proposed by Tanimoto and Kishida (1994) and is shown below.

Let us consider an observed wave which penetrates through a certain medium of l in thickness and α in damping factor. When a medium is homogeneous and continuous, the relation of the amplitude between the projected and the received waves is generally represented in the form of

$$A = \frac{k}{l} A_0 \cdot exp\,(-\alpha l) \tag{6-12}$$

where A_0 and A are the amplitudes of the projected and the received waves, respectively, as shown in **Figure 6.8**, and k is a constant given due to a diffusion condition ($k = 1$, $(\sqrt{\pi})^{-1}$, and $(2\sqrt{\pi})^{-1}$ for planar, cylindrical, and spherical waves, respectively). **Equation 6-12** includes two causes influencing changes in amplitude, namely, geometrical (raypath length) and viscous

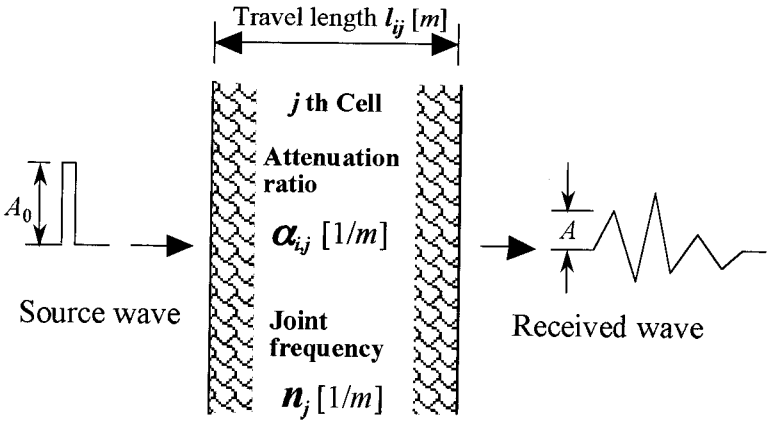

Figure 6.8 The concept of a seismic attenuation model for a jointed rock with joint frequency n (n : the number of joints per meter)

(damping) factors. Waves expressed in the discrete model are given by **Equation 6-13**, in other words,

$$A_i = \frac{k}{L_i} A_0 \cdot exp\left(-\sum_j \alpha_j l_{ij}\right) \tag{6-13}$$

where A_i, L_i, α_j, and l_{ij} are the observed amplitudes of the i-th ray, the summed length along the i-th ray, the damping factor of the j-th cell, and the segmented path length of the i-th ray in the j-th cell, respectively.

As the raypaths were already known through the *SVT* analysis, **Equation 6-13** is changed to

$$A_i \cdot L_i = k\, A_0 \cdot exp\left(-\sum_j \alpha_j l_{ij}\right) \tag{6-14}$$

where k and A_0 are constant regardless of the raypaths and the cells. Then, by taking the ratio of **Equation 6-14** to the maximum value of the product of $A_i{*}L_i$, $(A_i{*}L_i)_{max}$, **Equation 6-15** is given as

$$\frac{A_i \cdot L_i}{(A_i \cdot L_i)_{max}} = exp\left\{-\sum_j \left(\alpha_j l_{ij} - \alpha_j l_{mj}\right)\right\} \tag{6-15}$$

where l_{mj} is a segmented path length along the ray which shows the maximum value for $A_i{*}L_i$. **Equation 6-15** is expressed in logarithmic form, namely,

$$ln\,\frac{A_i L_i}{(A_i L_i)_{max}} = -\sum_j \left(l_{ij} - l_{mj}\right)\alpha_j \tag{6-16}$$

The left side of **Equation 6-16** becomes a constant, e_i, and the value of $(l_{ij}\text{-}l_{mj})$ is known. The calculation of damping factor distribution α_j is attributed to the same problem as that in Step *B* of the *SVT*. No iteration procedure is necessary.

It should be noted that the distribution of the damping (or attenuation) factor obtained by **Equation 6-16** does not include any influence given by the attenuation due to travel length, namely, it is determined independently of the travel length. This means that values for α_j of respective cells express the relative magnitude of the propagating energy attenuation to a common amount (a reference scale) of $(A_i{*}L_i)_{\max}$, corresponding to the magnitudes of joint frequencies and joint apertures. The inner (viscous) damping effect in a rock substance is eliminated, and now the damping factor matrix $[\alpha]$ corresponds only to the rock joints. Hereafter, therefore, it is called the joint damping factor (*JDF*). A value of α_j, whose unit is $[1/m]$, may grow larger than 1.0 in some cases. The larger the α-value (*JDF*) becomes, the more attenuation takes place at the discontinuities in the rock mass.

6.3 Numerical simulations for the seismic velocity geotomographic technique (*SVT*)

6.3.1 Purpose of the numerical simulations

The reliability of *SVT* is the key to a successful *SAT*. The influence of the boundary condition and the capability of reconstructing an objective image are studied through several numerical models.

As an example, the locations of the source and the receiver points are shown in **Figure 6.9**. Arrangements I (**Figure 6.9**(a)), II (**Figure 6.9**(b)), and III (**Figure 6.9**(c)) are all-around sensing (360-degree scanning as in medical cases), ground surface - two vertical drillholes, and two vertical holes (conventional cross-borehole scanning), respectively. In medical cases, the all-around sensing of a human body can be performed. In geotomography, however, all-around sensing cannot be applied. Arrangement II or III is generally applied to measure the seismic prospecting. In this section, the precision of the reappearance image will be discussed through several numerical simulations.

6.3.2 Influence of the inclinations of a low velocity zone

(a) Numerical models

First of all, the following numerical simulations are carried out in order to discuss the influence of the inclinations of a lower velocity zone making reconstruction images. Assuming an

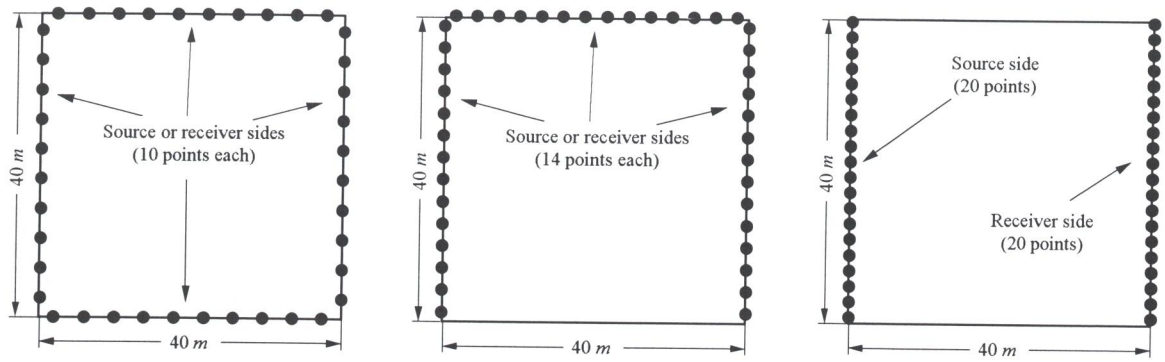

Figure 6.9 Arrangement of wave sources and receivers

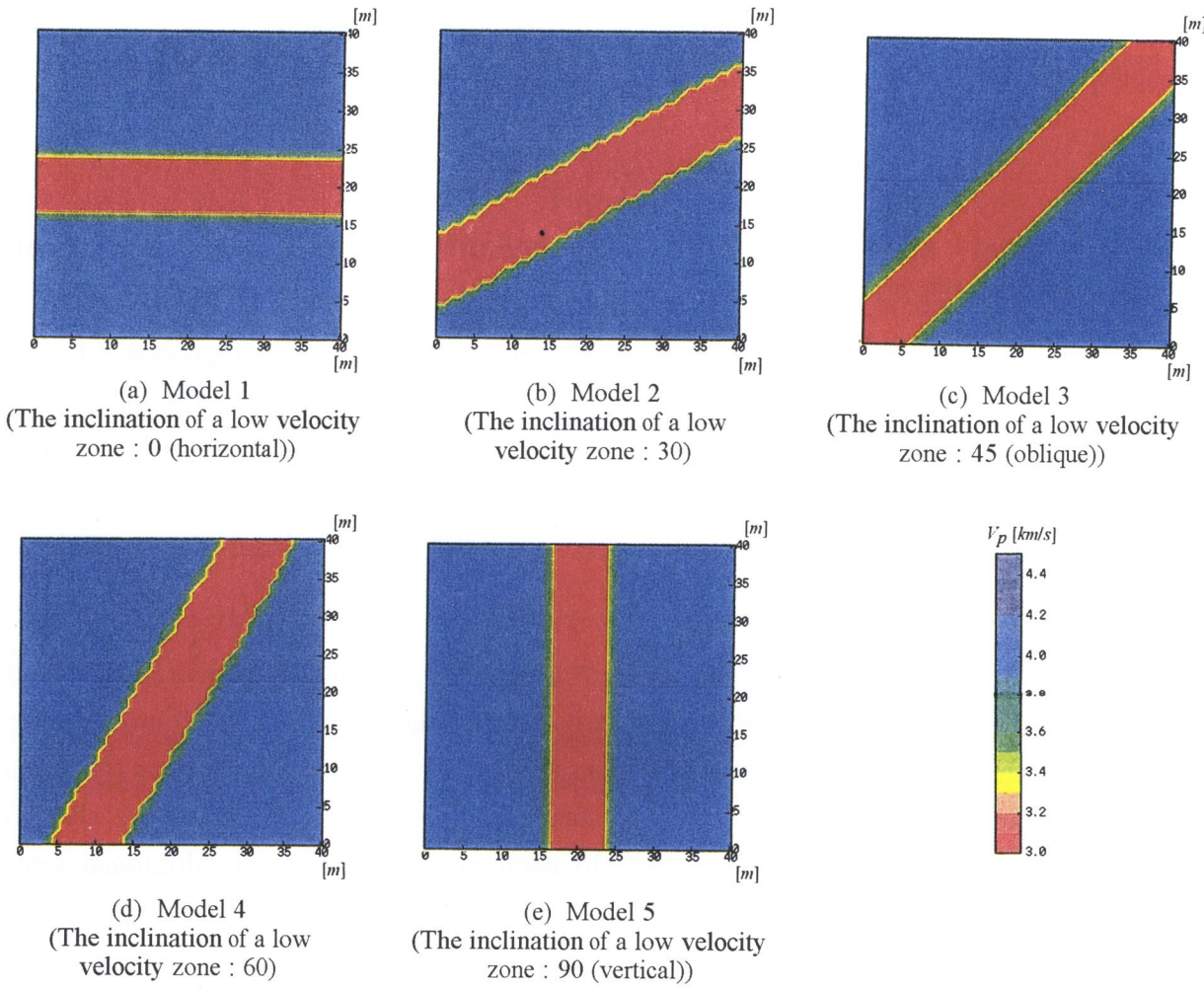

Figure 6.10 Numerical experiment models

area, 40 *m* by 40 *m*, and structures for which a low velocity zone, 10 *m* in width, is sandwiched, as shown in **Figures 6.10**(a) - (e), the capability of the reconstruction of the distribution of given velocities will be discussed. The inclination of the low velocity zone is 0 (horizontally), 30, 45 (obliquely), 60, and 90 (vertical) degrees, respectively. The velocity of the low velocity zone is assumed to be 3 *km/sec*, while the other area's velocity is 4 *km/sec*. Without stopping to

calculate, both sides of the low velocity zone are assumed to be 3.5 *km/sec* due to radical changes in velocity. The locations of the source and the receiver points are shown in **Figures 6.9**(a) - (c).

In accordance with the procedure shown in **Figure 6.7**, velocity models were reconstructed. The cycles of iteration for the routines of Steps *A* and *B*, were 10, and the traveltime error was designated at less than 1%. The number of cells covering the objective area is 32 by 32.

(b) Results applied to Arrangement I

As for the three numerical models whose respective inclinations of the low velocity zone are vertical, oblique, and horizontal, a numerical simulation has been performed and applied to Arrangement I. **Figure 6.11** shows the results. Arrangement I shows a good agreement with the originally assumed velocity models in all cases. *SVT* can work well. As we have already seen, however, we cannot help applying the geotomographic technique to the open-boundary condition, because the all-around scanning (360 degrees), namely, the closed boundary condition, is very hard to apply to geo-space. As for the discussion on the inclinations of the low velocity zone, therefore, Arrangements II and III will have been applied as follows.

(c) Results applied to Arrangement II

Figure 6.12 shows the results of the numerical simulation applying Arrangement II. Arrangement II shows close agreements with the originally assumed velocity models. No influence of the inclination of the lower velocity zone exists. However, some false images can be found on one side where no source or receiver points are located. The area where the false images can be found presents a lower density of raypaths than the other. In the iteration of Steps *A* and *B* for the area in which the raypath densities are low, s shown in **Figure 6.7**, it may be judged that the seismic wave cannot propagate, namely, a low velocity zone exists. It must be understood that a deflection of the raypaths can affect the results of *SVT*.

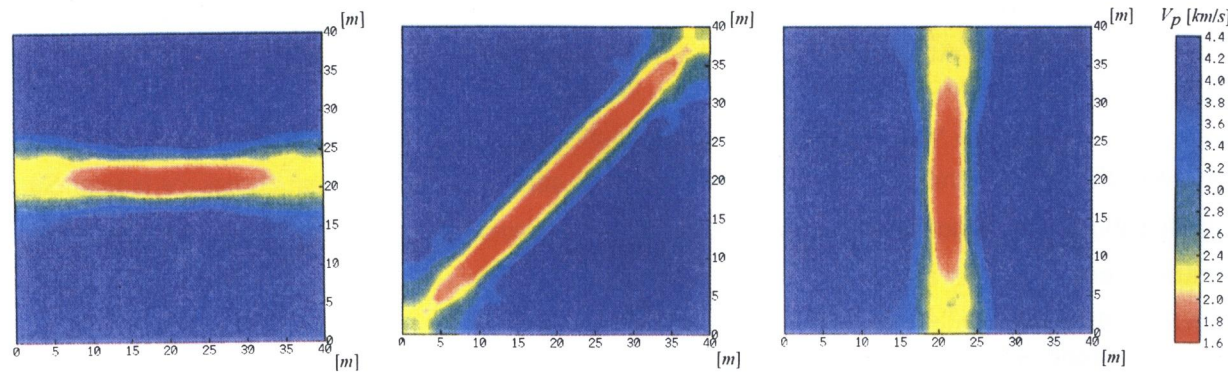

(a) Model 1
(The inclination of a low velocity zone : 0 (horizontal))

(b) Model 3
(The inclination of a low velocity zone : 45 (oblique))

(c) Model 5
(The inclination of a low velocity zone : 90 (vertical))

Figure 6.11 Reconstructed velocity models applying Arrangement I

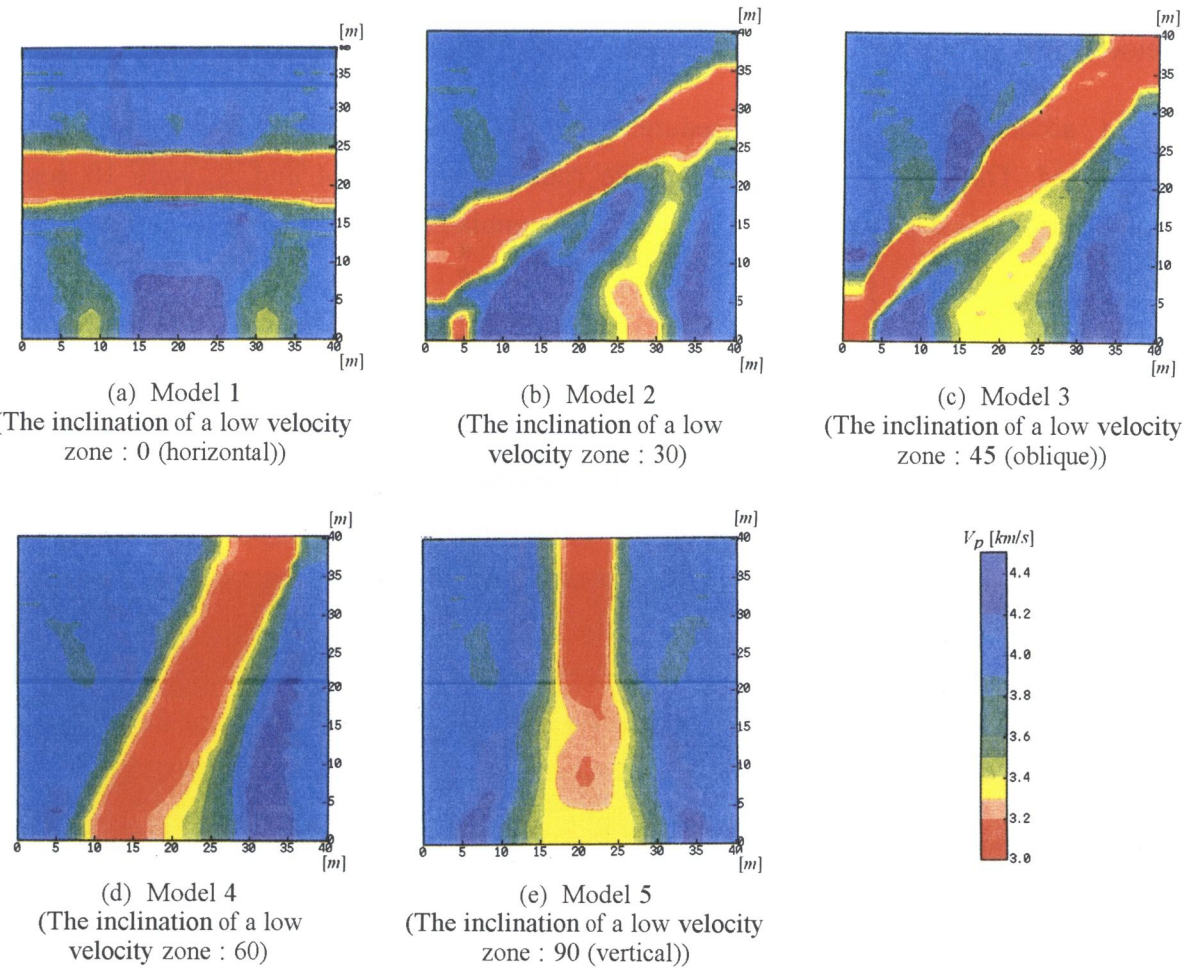

(a) Model 1
(The inclination of a low velocity zone : 0 (horizontal))

(b) Model 2
(The inclination of a low velocity zone : 30)

(c) Model 3
(The inclination of a low velocity zone : 45 (oblique))

(d) Model 4
(The inclination of a low velocity zone : 60)

(e) Model 5
(The inclination of a low velocity zone : 90 (vertical))

Figure 6.12 Reconstructed velocity models applying Arrangement II

(d) Results applied to Arrangement III

The results of the numerical simulation applying Arrangement III are shown in **Figure 6.13**. In the range of the inclination angle of a low velocity zone from horizontal to oblique, the reconstructed velocity models show good agreements with the original models. *SVT* can work well. However, with inclination angles of 60 and 90 degrees, the original images cannot be reconstructed. As for Arrangement III, it is a mistake to make a reconstructed image of the vertical low velocity zone.

On the other hand, the reconstructed velocity models cannot show ghosts or noise. Since the distribution of the raypath densities in Arrangement III is more uniform than that in Arrangement II, ghosts and noise, which occur due to the bias of the raypath densities, cannot appear in the reconstructed images.

As mentioned above, Arrangement III takes advantage of the distribution of raypath densities and there is no worry of numerical ghosts or noise. However, care must be taken in the consideration of the vertical low velocity zone.

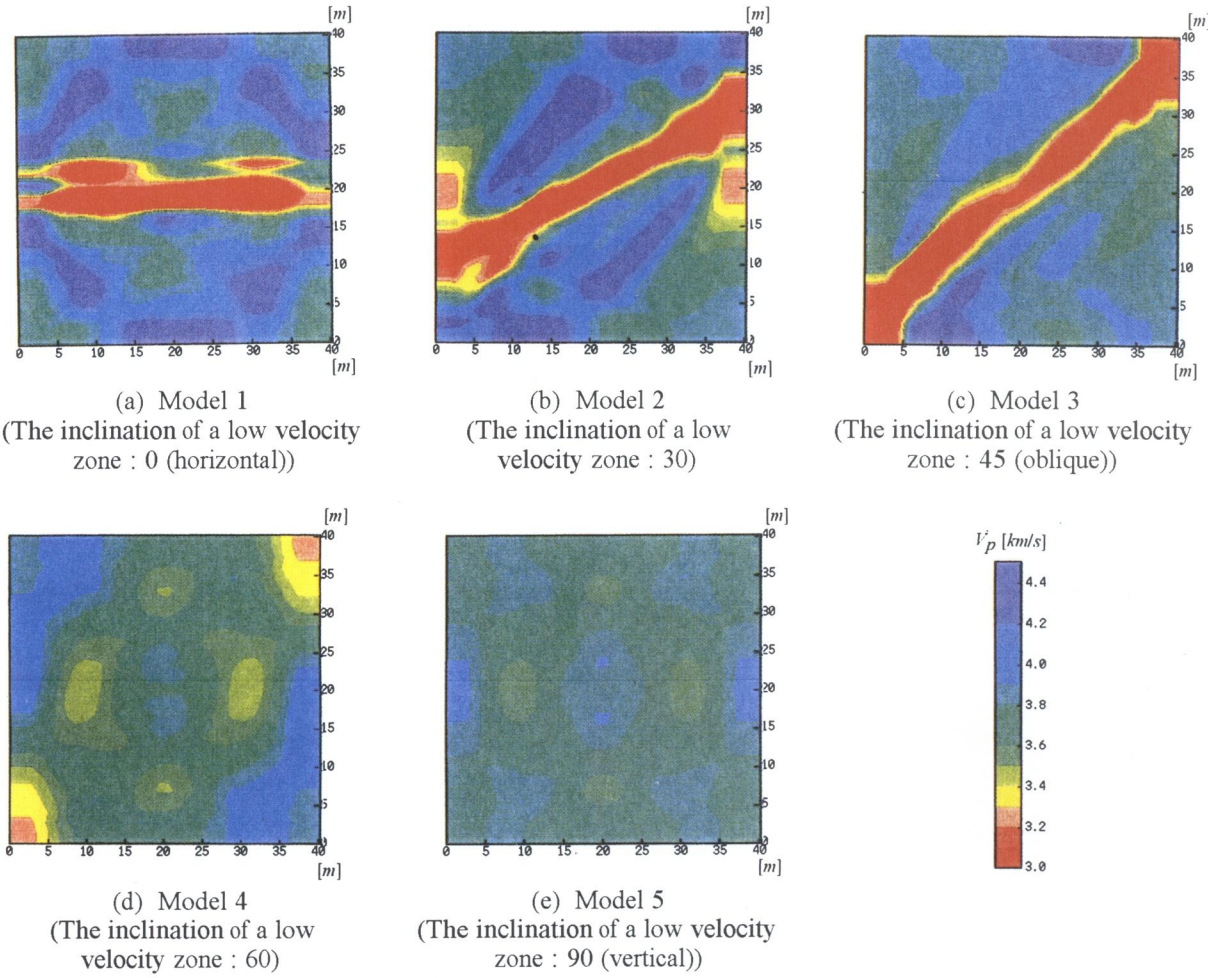

(a) Model 1 (The inclination of a low velocity zone : 0 (horizontal))

(b) Model 2 (The inclination of a low velocity zone : 30)

(c) Model 3 (The inclination of a low velocity zone : 45 (oblique))

(d) Model 4 (The inclination of a low velocity zone : 60)

(e) Model 5 (The inclination of a low velocity zone : 90 (vertical))

Figure 6.13 Reconstructed velocity models applying Arrangement III

6.3.3 Influence of the width of a low velocity zone

As compared with the difference in width of a low velocity zone, numerical simulations are conducted using the velocity models shown in **Figure 6.14.** Since the width of the present low velocity zone is 3 *m*, results are compared with **Figures 6.12** and **6.13**, which show the results of a low velocity zone 10 *m* in width. Then, the influence of the width of the low velocity zone is discussed. The numerical conditions, namely, the inclinations of the low velocity zone, the number of iteration cycles, and the number of cells, are equivalent to those in Section 6.3.2. The locations of the source and the receiver points are applied to Arrangements II and III. The results corresponding to Arrangements II and III are shown in **Figures 6.15** and **6.16**, respectively.

When making a reconstruction image, the influence of the inclination of a low velocity zone, 3 *m* in width, agrees with that of the models 10 *m* in width. It is seen that the quality of the reconstructed image obviously deteriorates as the width of the low velocity zone grows narrow. This tendency is clearly found in the case of models whose inclination angles of the low velocity zone are 60 and 90 degrees. With these inclination angles, the reconstruction of a low velocity

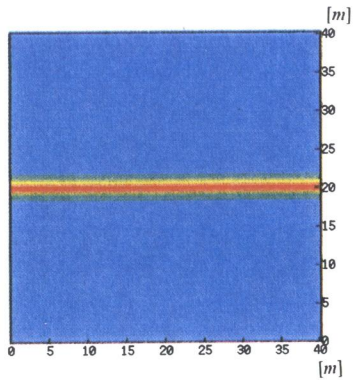

(a) Model 1
(The inclination of a low velocity zone : 0 (horizontal))

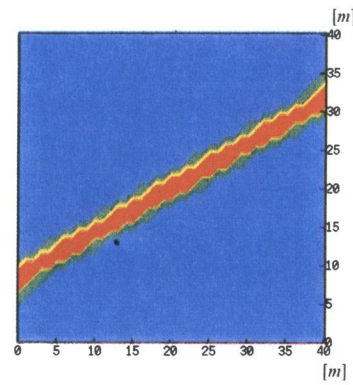

(b) Model 2
(The inclination of a low velocity zone : 30)

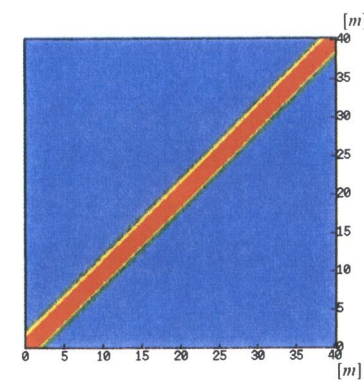

(c) Model 3
(The inclination of a low velocity zone : 45 (oblique))

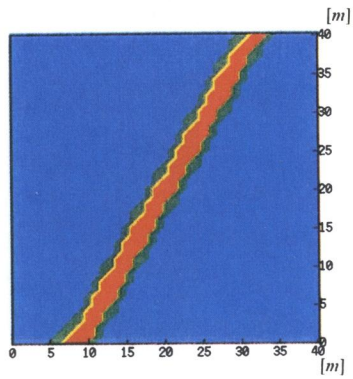

(d) Model 4
(The inclination of a low velocity zone : 60)

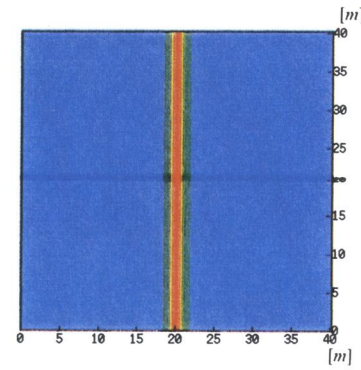

(e) Model 5
(The inclination of a low velocity zone : 90 (vertical))

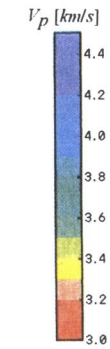

Figure 6.14 Numerical experiment models (the width of the low velocity zone is 3 *m*)

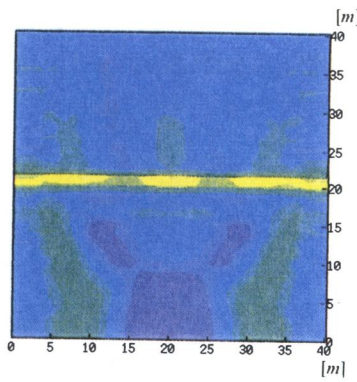

(a) Model 1
(The inclination of a low velocity zone : 0 (horizontal))

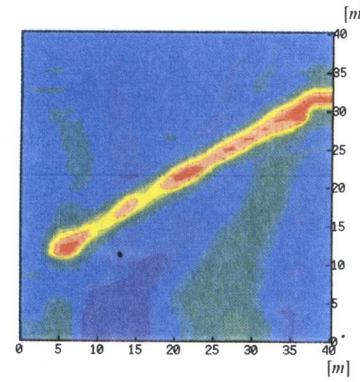

(b) Model 2
(The inclination of a low velocity zone : 30)

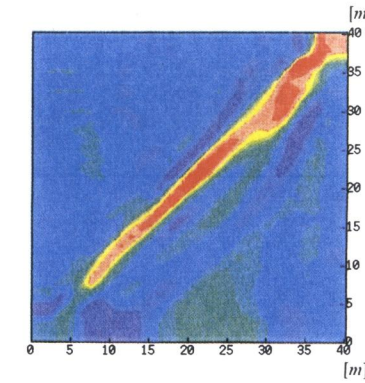

(c) Model 3
(The inclination of a low velocity zone : 45 (oblique))

Figure 6.15 Reconstructed velocity models applying Arrangement II
(the width of the low velocity zone is 3 *m*)

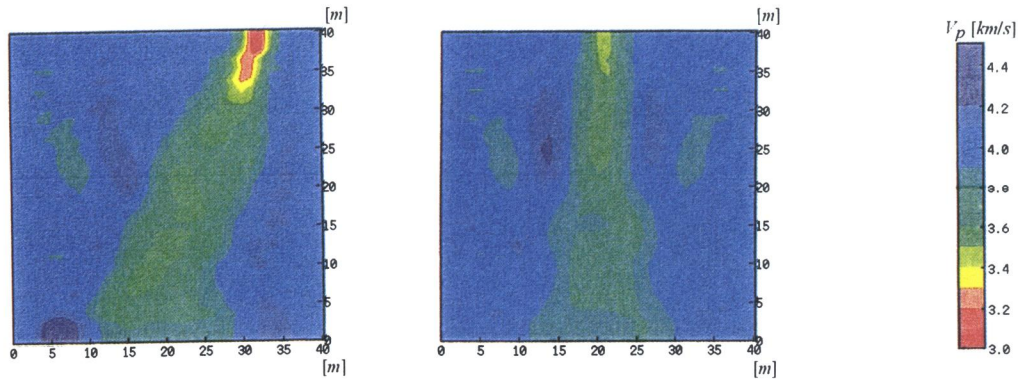

(d) Model 4
(The inclination of a low velocity zone : 60)

(e) Model 5
(The inclination of a low velocity zone : 90 (vertical))

Figure 6.15 Reconstructed velocity models applying Arrangement II
(the width of the low velocity zone is 3 *m*)

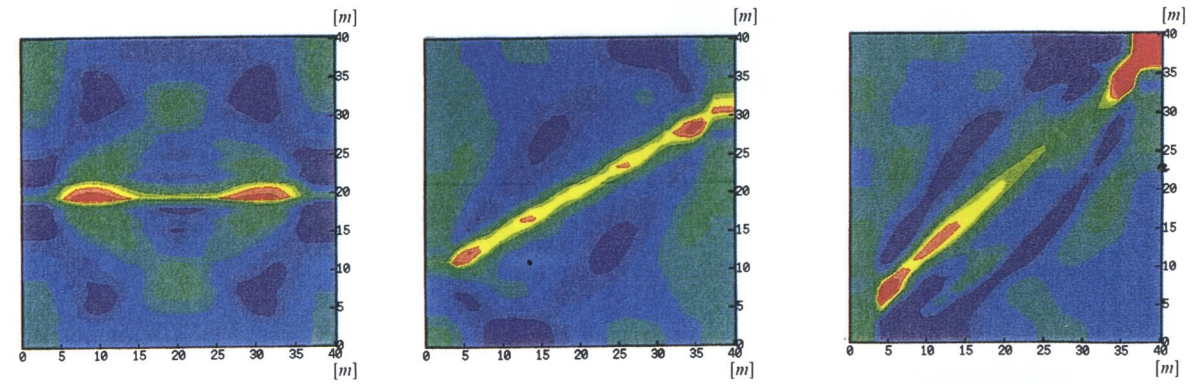

(a) Model 1
(The inclination of a low velocity zone : 0 (horizontal))

(b) Model 2
(The inclination of a low velocity zone : 30)

(c) Model 3
(The inclination of a low velocity zone : 45 (oblique))

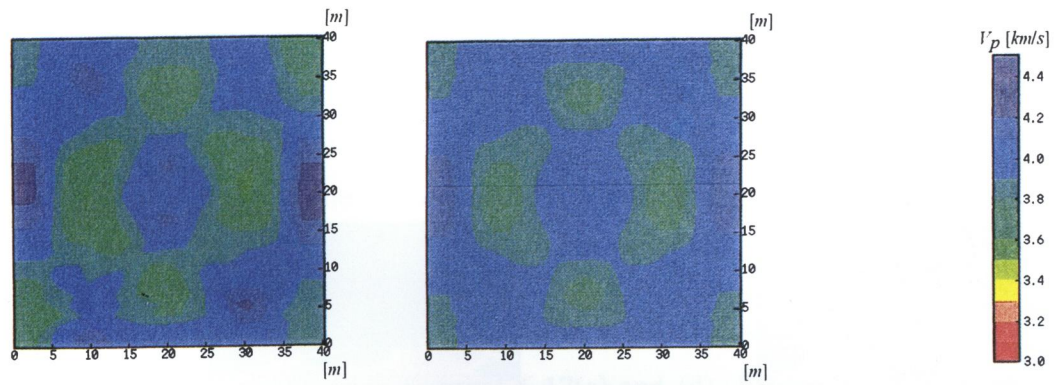

(d) Model 4
(The inclination of a low velocity zone : 60)

(e) Model 5
(The inclination of a low velocity zone : 90 (vertical))

Figure 6.16 Reconstructed velocity models applying Arrangement III
(the width of the low velocity zone is 3 *m*)

zone model, 10 *m* in width, is not yet been confirmed by applying Arrangement III. Only when applying Arrangement II, could the reconstruction be confirmed. However, as the width of the low velocity zone becomes 3 *m*, the inclination of the zone can be estimated, but the quality of

the low velocity zone is deteriorating at Arrangement II. For the other inclination angles, a ghost can be found in the low velocity zone models 3 *m* in width.

In spite of the locations of the source and the receiver points, the reconstruction of the models deteriorates to an extreme degree as the width of the objective zone grows narrow.

6.3.4 Influence of the interval between the source and the receiver points

In this thesis, the field measurements of the propagating seismic wave, described in the following, are carried out using two boreholes, that is, Arrangement III. Using Arrangement III, the influence of the interval between the source and the receiver points will be discussed.

The intervals between the source and the receiver points are set up at 1 *m*, 2 *m*, and 4 *m*. Therefore, the number of ray paths is 1681, 441, and 121, respectively. The same models which have been used in other numerical simulations are analyzed. The number of numerical cells is determined to be half the number of ray paths so as to prevent a break in the calculations.

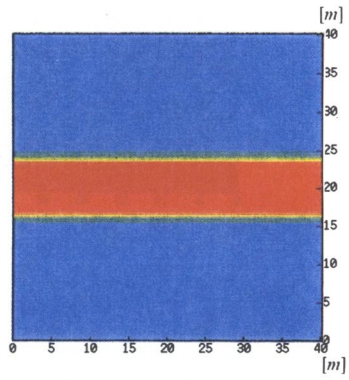

(a) The original velocity model

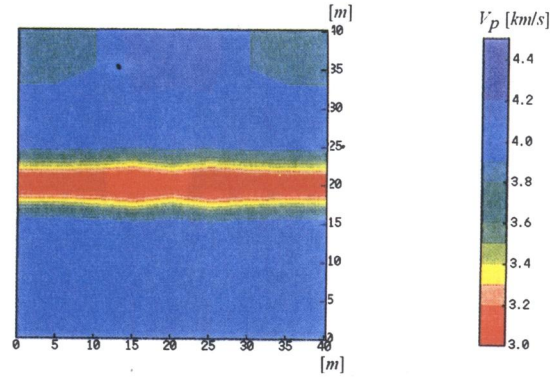

(b) The numerical results
(The interval between the source and the receiver points is 4 *m*; the number of raypaths is 121; the numerical meshes are 9 x 9.)

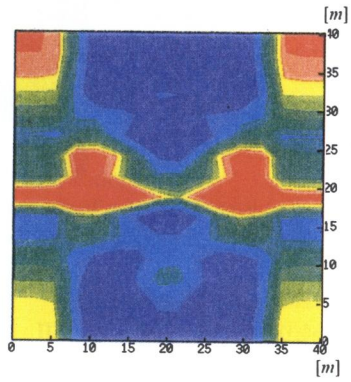

(c) The numerical results
(The interval between the source and the receiver points is 2 *m*; the number of raypaths is 441; the numerical meshes are 16 x 16.)

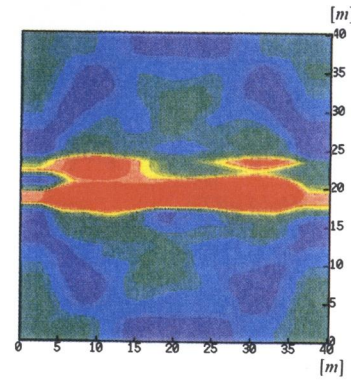

(d) The numerical results
(The interval between the source and the receiver points is 1 *m*; the number of raypaths is 1681; the numerical meshes are 30 x 30.)

Figure 6.17 Reconstructed velocity models
(The inclination and width of the low velocity zone are 0 (horizontal) and 10 *m*.)

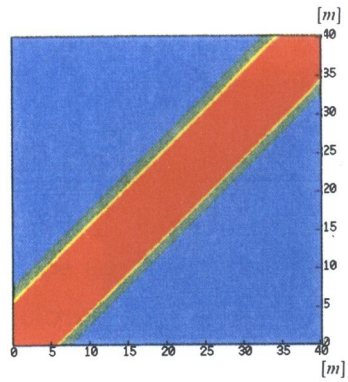

(a) The original velocity model

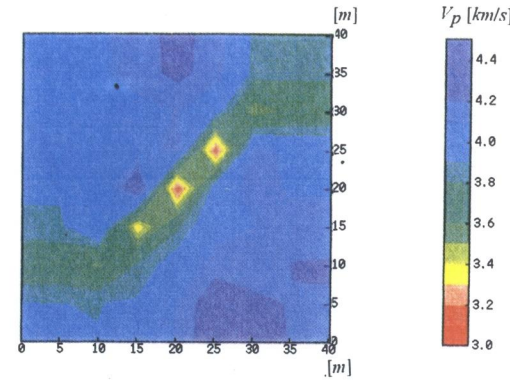

(b) The numerical results
(The interval between the source and the receiver points is 4 *m*; the number of raypaths is 121; the numerical meshes are 9 x 9.)

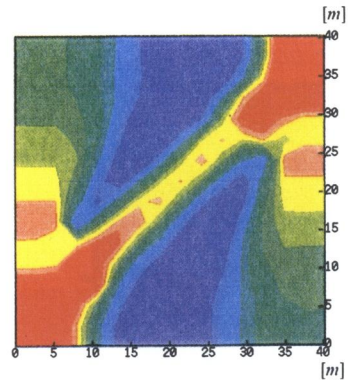

(c) The numerical results
(The interval between the source and the receiver points is 2 *m*; the number of raypaths is 441; the numerical meshes are 16 x 16.)

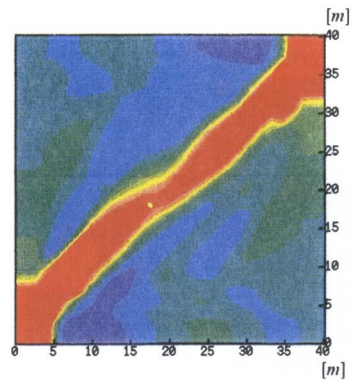

(d) The numerical results
(The interval between the source and the receiver points is 1 *m*; the number of raypaths is 1681; the numerical meshes are 30 x 30.)

Figure 6.18 Reconstructed velocity models
(The inclination and width of the low velocity zone are 45 (oblique) and 10 *m*.)

Figure 6.17 shows the results of the numerical simulations. The original model whose width and inclination of the low velocity zone are 10 *m* and 0 degree (horizontal), respectively, is shown in **Figure 6.17**(a). The case of a 4-*m* interval between the source and the receiver points, as shown in **Figure 6.17**(b), presents a better agreement with the original velocity models than other cases. As for other results (**Figures 6.17**(c) & (d)), a horizontal low velocity zone can be confirmed in the middle part of the model. In each corner of the model, however, a low velocity area has appeared. In comparing **Figures 6.17**(c) and (d), **Figure 6.17**(d) clearly shows better result than **Figure 6.17**(c). As the interval decreases, namely, the raypath density on the numerical area increases, the reconstructed result brings about an improvement.

Next, a numerical simulation is carried out for a model whose width and inclination for the low velocity zone are 10 *m* and 45 degrees, respectively. The original model is shown in **Figure 6.18**(a). As for the inclination and the velocity value of the low velocity zone, the results of the 1-*m* interval analysis, shown in **Figure 6.18**(d) present a better agreement with the original model than the others. It seems that it is sufficient for predicting the low velocity zone. On the other

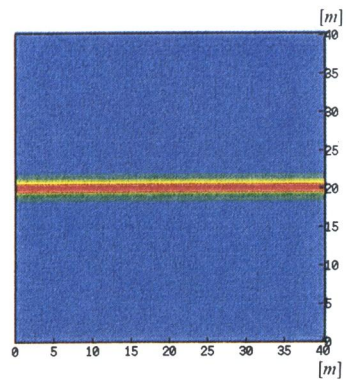

(a) The original velocity model

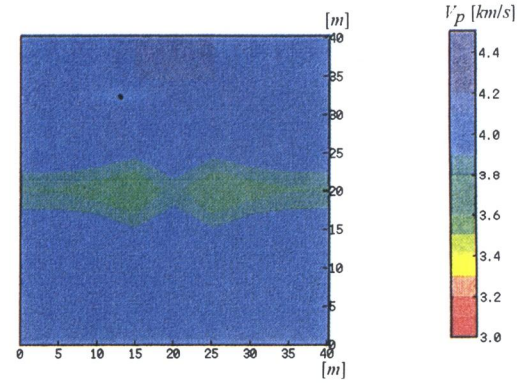

(b) The numerical results
(The interval between the source and the receiver points is 4 *m*; the number of raypaths is 121; the numerical meshes are 9 x 9.)

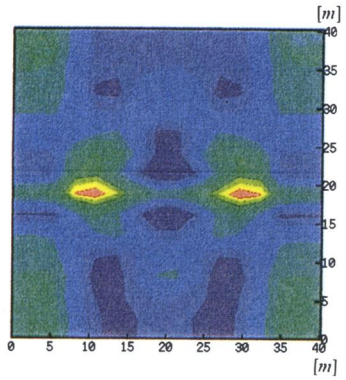

(c) The numerical results
(The interval between the source and the receiver points is 2 *m*; the number of raypaths is 441; the numerical meshes are 16 x 16.)

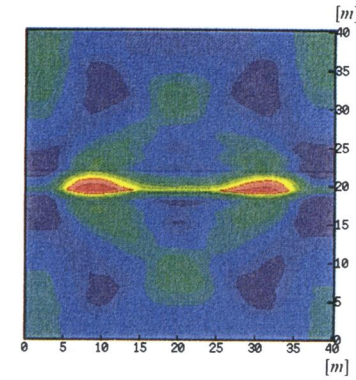

(d) The numerical results
(The interval between the source and the receiver points is 1 *m*; the number of raypaths is 1681; the numerical meshes are 30 x 30.)

Figure 6.19 Reconstructed velocity models
(The inclination and width of the low velocity zone are 0 (horizontal) and 3 *m*.)

hand, in the case of the 2-*m* interval analysis, shown in **Figure 6.18**(c), it is found that a low velocity area along the boreholes appears, but the inclination of the low velocity zone can be confirmed at 45 degrees. The low velocity zone itself can be reconstructed. However, in the case of the 4-*m* interval analysis, **Figure 6.18**(b) could hardly present the original model.

As mentioned above, in the 10-*m* wide low velocity zone, the influence of the interval between the source and the receiver points is discussed. Except for **Figure 6.17**(b), which makes the interval small, the reconstructed model can be obtained in detail. Since the number of raypaths and numerical cells can be increased, the result of the reconstructed model makes progress. Naturally enough, with as much measuring data for the raypath as possible, it is better for a high-precision analysis to be performed.

Next, a numerical simulation for a model which includes the 3-*m* wide low velocity zone is carried out and the influence of the source and the receiver intervals will be discussed.

At first, a numerical simulation of a model which has a horizontal and 3-*m* wide low velocity zone is conducted, as shown in **Figure 6.19**(a). The results are shown in **Figures 6.19**(b), (c), and (d). In the case of the 4-*m* interval analysis, a ghost can hardly be found and the results clearly show the reconstruction of the model. However, the velocity value of the low velocity zone itself cannot be reconstructed sufficiently. As the source and the receiver intervals grow small, the low velocity zone appears. However, as compared with the results of the 10-*m* wide low velocity zone model, shown in **Figure 6.17**, the reappearance of the low velocity zone becomes poor.

For the case in which the model's width and inclination are 3 *m* and 45 degrees, respectively, a numerical simulation has been performed. **Figure 6.20** presents the original model and the results. Only in the case of a 1-*m* interval analysis, whose results are shown in **Figure 6.20**(d), the numerical simulation can be estimated as presenting a low velocity zone with a 45-degree angle inclination. Other analyses, as shown in **Figures 6.20**(b) and (c), can hardly distinguish the low velocity zone from the ghost.

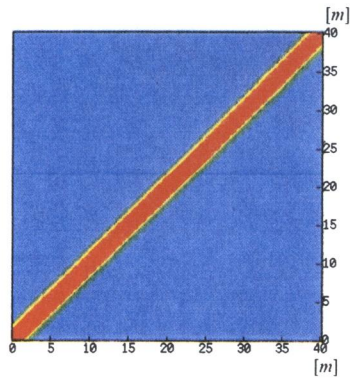

(a) The original velocity model

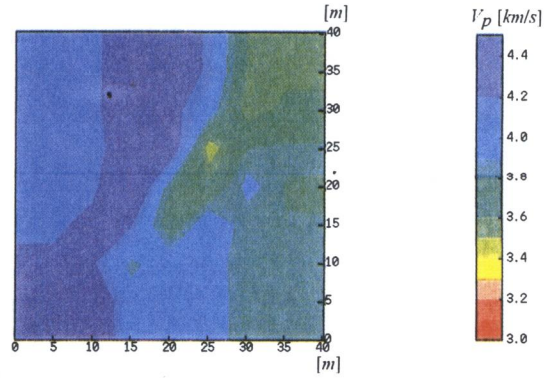

(b) The numerical results
(The interval between the source and the receiver points is 4 *m*; the number of raypaths is 121; the numerical meshes are 9 x 9.)

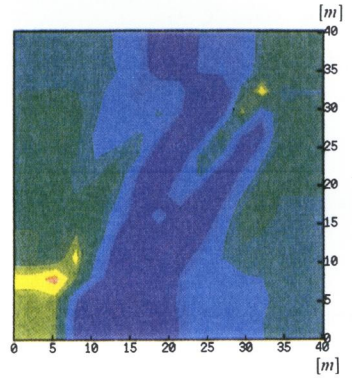

(c) The numerical results
(The interval between the source and the receiver points is 2 *m*; the number of raypaths is 441; the numerical meshes are 16 x 16.)

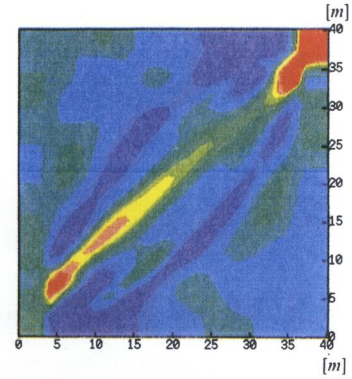

(d) The numerical results
(The interval between the source and the receiver points is 1 *m*; the number of raypaths is 1681; the numerical meshes are 30 x 30.)

Figure 6.20 Reconstructed velocity models
(The inclination and the width of the low velocity zone are 45 (oblique) and 3 *m*.)

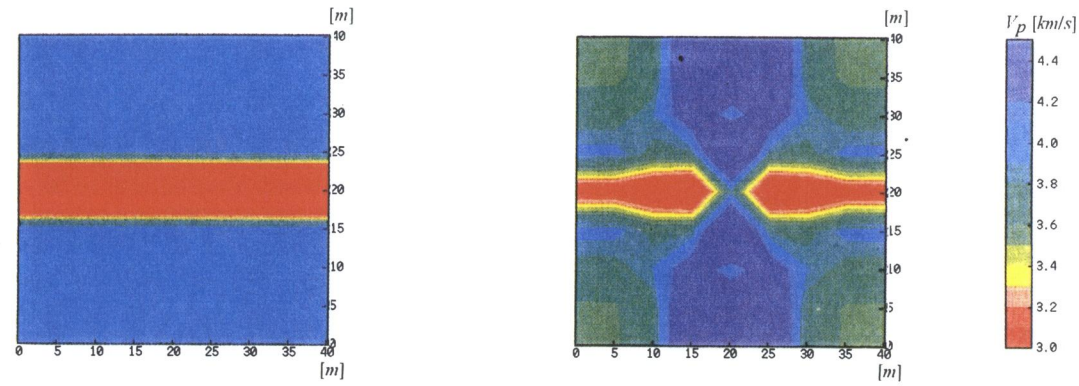

(a) The original velocity model

(b) The numerical results
(The number of raypaths is 121;
the numerical meshes are 9 x 9.)

(c) The numerical results
(The number of raypaths is 441;
the numerical meshes are 16 x 16.)

(d) The numerical results
(The number of raypaths is 1681;
the numerical meshes are 30 x 30.)

Figure 6.21 Reconstructed velocity models in consideration of mesh size
(The interval between the source and the receiver points is 1 *m*, and
the inclination and the width of the low velocity zone are 0 (horizontal) and 10 *m*.)

As mentioned above, when the interval is wider than the objective matter, the reappearance of the objective matter is deteriorating. It is difficult to reconstruct an objective area whose size is smaller than the interval. And, when the interval between the source and the receiver points decreases, improvements in the reappearance of the 3-*m* wide model are more remarkable than those of the 10-*m* wide model.

6.3.5 Influence of the number of numerical cells

A numerical simulation is carried out in consideration of the size and the number of numerical cells, and the influence of the number of numerical cells will be discussed. Therefore, with a fixed interval between the source and the receiver points at 1 *m*, the number of numerical cells is varied and the numerical simulation is performed. A scanning pattern is applied to Arrangement III and the number of cells is set at 9 x 9, 16 x 16, and 30 x 30, respectively. The original model presents a low velocity zone whose width is 10 *m*. The inclination of the low

velocity zone is discussed with two kinds of angles, namely, 0 (horizontal) and 45 degrees. **Figures 6.21** and **6.22** show the results.

For each inclination angle of a low velocity zone, the reconstructed model changes and the appearance deteriorates as the number of cells decreases even if the number of raypaths is equivalent in each simulation. Based on **Figures 6.21** and **6.22**, it is confirmed that the varied number of cells has a tremendous effect on the numerical results.

In an analysis of geotomography, it is impossible to set up the number of cells for unknown factors which exceeds the number of ray paths. Even if the traveltime is measured for many raypaths, it is difficult to perform a high-precision analysis under a limited number of cells. In order to perform a high-precision analysis, therefore, the number of cells must be set up as much within the permitted range of the calculation as possible.

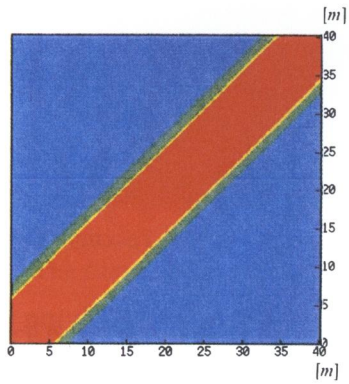

(a) The original velocity model

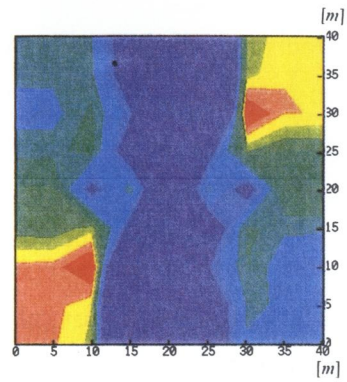

(b) The numerical results
(The number of raypaths is 121;
the numerical meshes are 9 x 9.)

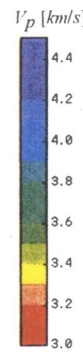

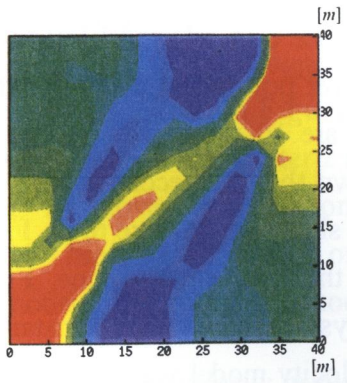

(c) The numerical results
(The number of raypaths is 441;
the numerical meshes are 16 x 16.)

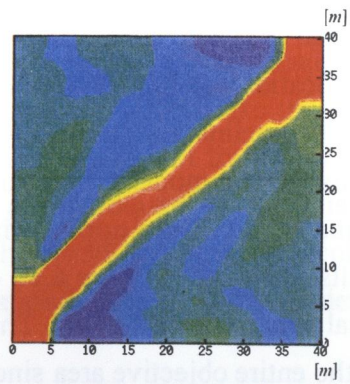

(d) The numerical results
(The number of raypaths is 1681;
the numerical meshes are 30 x 30.)

Figure 6.22 Reconstructed velocity models in consideration of mesh size
(The interval between the source and the receiver points is 1 *m*, and
the inclination and the width of the low velocity zone are 45 (oblique) and 10 *m*.)

6.3.6 Attempts to improve the seismic velocity geotomographic technique by applying other field measurement results

According to numerical simulations, a low velocity zone which runs approximately parallel to the borehole cannot be reconstructed when applying Arrangement III (two-borehole scanning). However, this problem must be prevented and better results must be shown in the analysis of geotomography. Otherwise, effective information which is useful to the construction in the civil engineering cannot be obtained. Arrangement III is often applied when measurements are taken in the field. Then, so as to attempt to improve the appearance of a low velocity zone whose inclination is rapid against a borehole, the following methods, which are used for other field investigations, are applied to the numerical simulation and the validity of those methods is discussed.

(a) Improving the initial velocity model

In seismic velocity geotomography, first of all, the initial velocity model must be set up. Then, the calculation is started. As shown in **Figure 6.7**, Steps *A* and *B* are repeated many times until the difference in traveltime between the measurements and the calculation becomes allowable. The velocity model improves with each iteration. Therefore, the initial velocity model affects the convergence of the difference in traveltime and the quality of the reconstructed model.

In general, the average velocity for calculating all measured traveltimes, applying the straight raypath, is used for the initial velocity. And, the initial velocity model is uniform. This is equal to both the in-situ analysis and the numerical simulation. Then, other information is applied for the making of the initial velocity model and whether the appearance has made progress or not is discussed in using the obtained initial velocity model.

In the numerical simulation, the velocity distribution of the original model is applied to the initial model. The locations of both the source and the receiver points are used for Arrangement III. The width and the inclination of the low velocity zone are 10 *m* and 90 degrees (vertical), respectively. In this original model, it has already been shown that the reconstructed model was not obtained adequately enough to apply Arrangement III, as shown in **Figure 6.13**. **Figure 6.23** presents the results. Although **Figure 6.13** does not show the low velocity zone, **Figure 6.23** shows the vertical low velocity zone. The current analysis showed the constant velocity distribution over the entire objective area since the initial velocity model was uniform. However, the reconstruction is considered to have made progress, even though the location of the reconstructed low velocity zone is a little different. It is confirmed that the initial velocity model strongly affects the results of the seismic velocity geotomography, and provided with information obtained from field investigations on the initial velocity model, confidence in the numerical results grows higher.

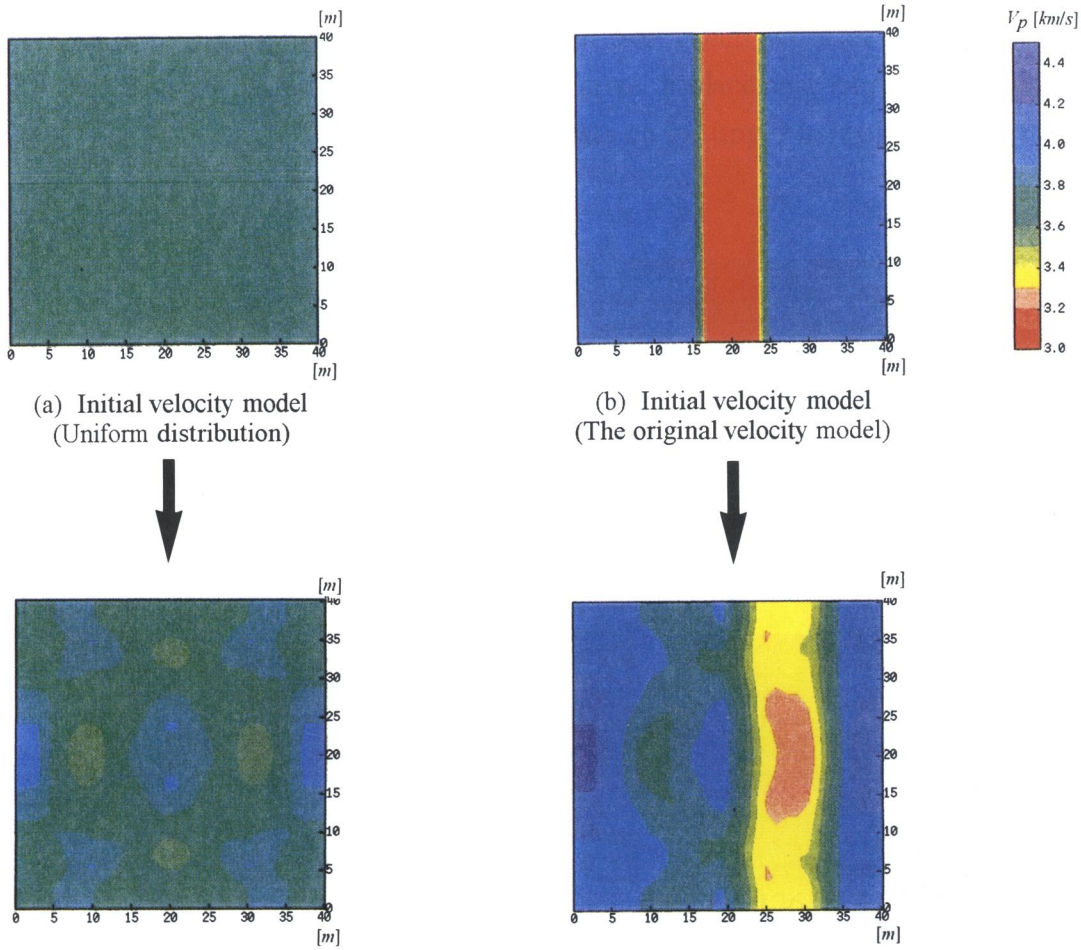

(a) Initial velocity model (Uniform distribution)

(b) Initial velocity model (The original velocity model)

(c) The numerical results through (a)

(d) The numerical results through (b)

Figure 6.23 Reconstructed velocity models in consideration of the initial velocity model
(The locations of the source and the receiver points are Arrangement Ⅲ, and the inclination and the width of the low velocity zone are 90 (vertical) and 10 *m*.)

There is a problem, however, of how to provide some information to the initial velocity model in the in-situ analysis of the seismic velocity geotomography. In order to solve the problem in this thesis, it is suggested that the initial velocity model is made to apply the joint frequency map, as shown in **Figure 6.23**. The problem of how to make the joint frequency map was already explained in Chapter 2 and the distribution of the joint frequency at an objective area is known. Moreover, the relationship between joint frequency and seismic velocity was presented by Ikeda (1979). Based on this relation, the seismic velocity is calculated and the initial velocity model is made. This method and its application will be described in detail as follows.

(b) Fixing the seismic velocity in some cells

Applying certain information to the initial velocity field, the precision of the geotomographic calculation makes progress and it is confirmed that some information from other field measurements can be applied effectively. However, this is only a discussion on numerical simulations. As for in-situ analyses, it is difficult to obtain an accurate initial velocity field at an all-objective area. If the velocity distribution can be determined for an objective area from other

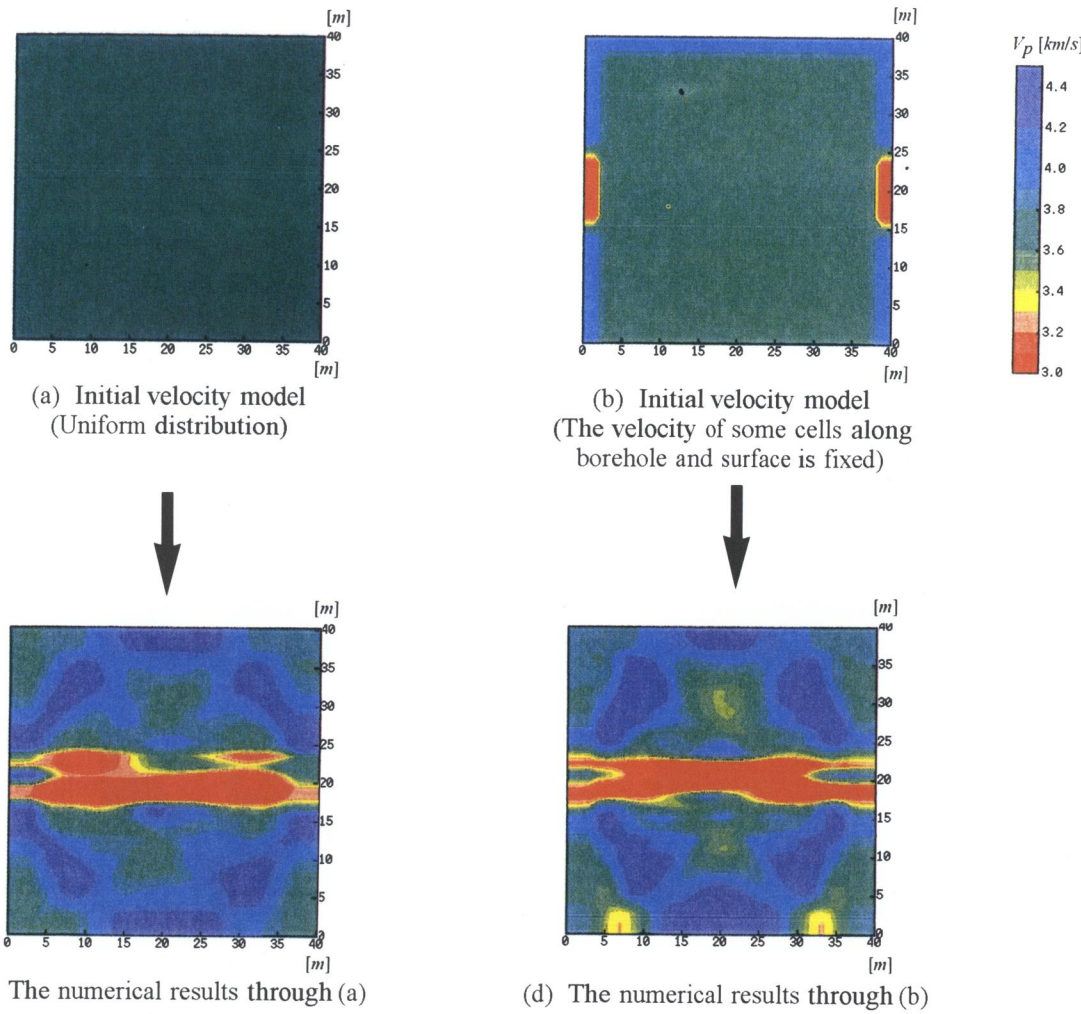

(a) Initial velocity model (Uniform distribution)

(b) Initial velocity model (The velocity of some cells along borehole and surface is fixed)

(c) The numerical results through (a)

(d) The numerical results through (b)

Figure 6.24 Reconstructed velocity models in consideration of the initial velocity model (The locations of the source and the receiver points are Arrangement Ⅲ, and the inclination and the width of the low velocity zone are 0 (horizontal) and 10 *m*.)

surveys, it is necessary to apply the geotomography to clarify the distribution of the seismic velocity.

In the field, an accurate velocity distribution can be obtained at the ground surface and around the borehole from the *P*-*S* logging. Then, as the seismic velocity is fixed on some numerical cells where it can actually be measured in the field, that is, the location around the borehole, the iterative calculation of geotomography is performed. In order to confirm how progress can be made on the precision, numerical simulations are carried out. **Figures 6.24** and **6.25** show the numerical results. **Figure 6.24** shows a case in which the low velocity zone is horizontal, and **Figure 6.25** shows a case in which the low velocity zone is vertical.

In the case of a horizontal low velocity zone, no difference can be found between **Figure 6.24** and the usual results. However, in the case of a vertical low velocity zone, a difference can be found in **Figure 6.25**. As in a usual analysis, the results show a uniform velocity distribution. On the contrary, when some velocity-fixed cells are introduced, the low velocity zone can be found in the center of the objective area. However, since the velocity-fixed cells are only located

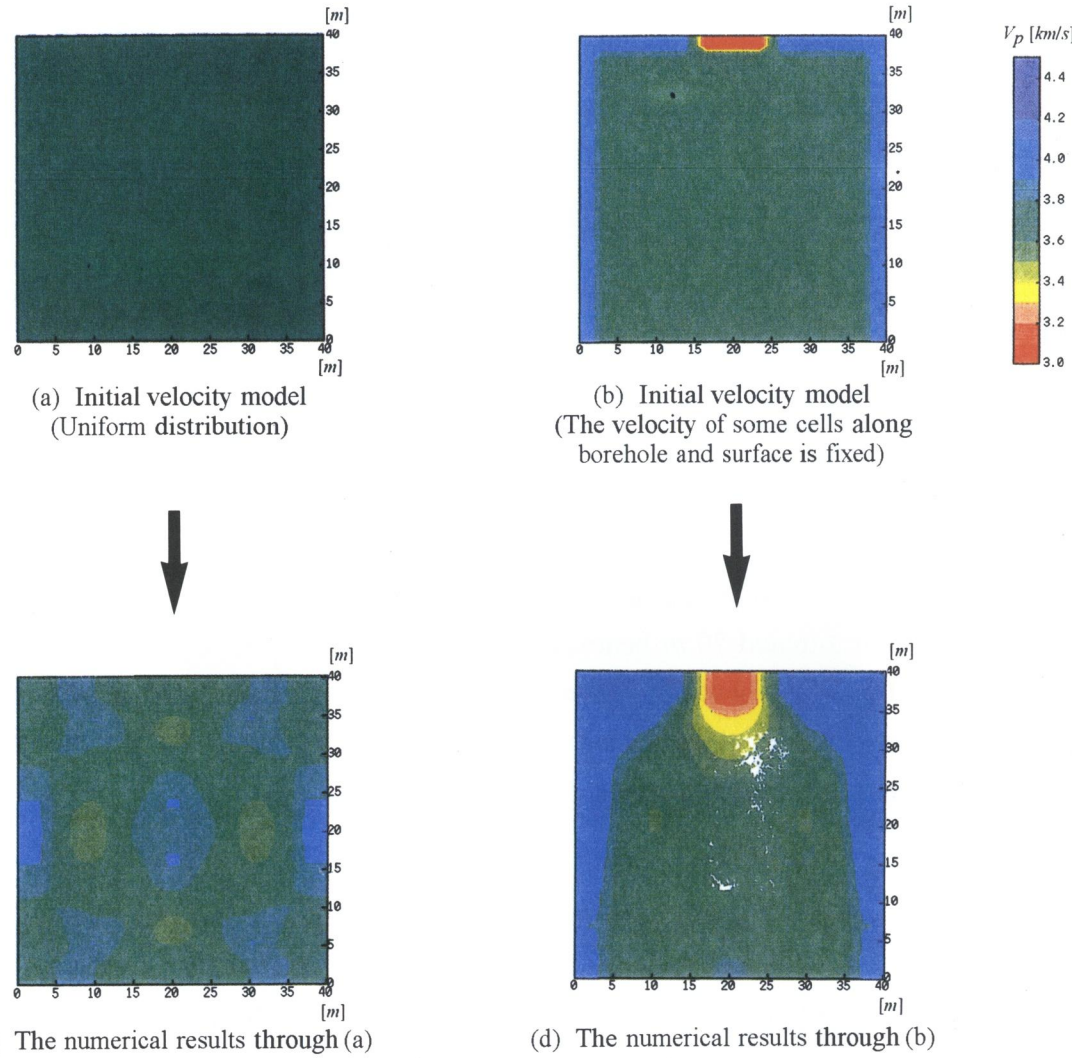

(a) Initial velocity model (Uniform distribution)

(b) Initial velocity model (The velocity of some cells along borehole and surface is fixed)

(c) The numerical results through (a)

(d) The numerical results through (b)

Figure 6.25 Reconstructed velocity models in consideration of the initial velocity model (The locations of the source and the receiver points are Arrangement III, and the inclination and the width of the low velocity zone are 90 (vertical) and 10 *m*.)

on the upper and both (right and left) sides of the numerical area, the velocity distributions in the lower area are still uniform as in a usual analysis. Compared with the usual analytical results, it is thought that progress has been made in the precision of geotomographic analyses.

When applying the initial velocity, the validity of the estimated velocity and the influence it has on the numerical results must be discussed in consideration of other field measurements. However, when some numerical cells are fixed using the actual measurement data, it seems that more advantages are needed to improve the numerical precision. This will be discussed in the field analysis.

6.4 Application of the geotomographic technique in the field

In this section, the application of seismic geotomography in the field will be described and the validity of seismic geotomography will be discussed. Then, a new concept for the classification of jointed rock masses will be suggested.

6.4.1 Outline of the field and the measurements

The same field which was described in Chapter 2 has been used for a seismic exploration, and its results have been applied to the geotomography.

A feasibility study for a new underground powerhouse, to be constructed in the vicinity of an existing hydro-electric power plant, is being carried out in the central part of Honshu Island. The objective site is situated 70 *m* beneath a steep valley which has been subjected to the late Cretaceous Cauldron Movement. The basement rock consists of granite porphyry, rhyolite, and slate. These types of rock contain many joints which dip at steep angles and have comparatively high joint frequencies and wide apertures.

Four boreholes, 70 *m* in depth, are prepared for the investigation by the geotomographic technique shown in **Figure 6.26** (the same as **Figure 2.3**). The number of source and receiver points is 70 for each, and the points are installed at 1-*m* intervals, respectively. This means that the number of meshes (or cells) for the geotomographic discrete model is 70 x 70 and that 4,900 raypaths are analyzed. The energy source at each shot point is the detonation of two pieces of instantaneous EB-caps, and the data logger and the receivers employed in the survey are McSeis-16000 (OYO made) and Hydro-phones (ITI made), as shown in **Photo 6.1** and **Photo 6.2**, respectively. The sampling interval and the amount of different data for one wave are 0.04 *msec* and 2048, respectively.

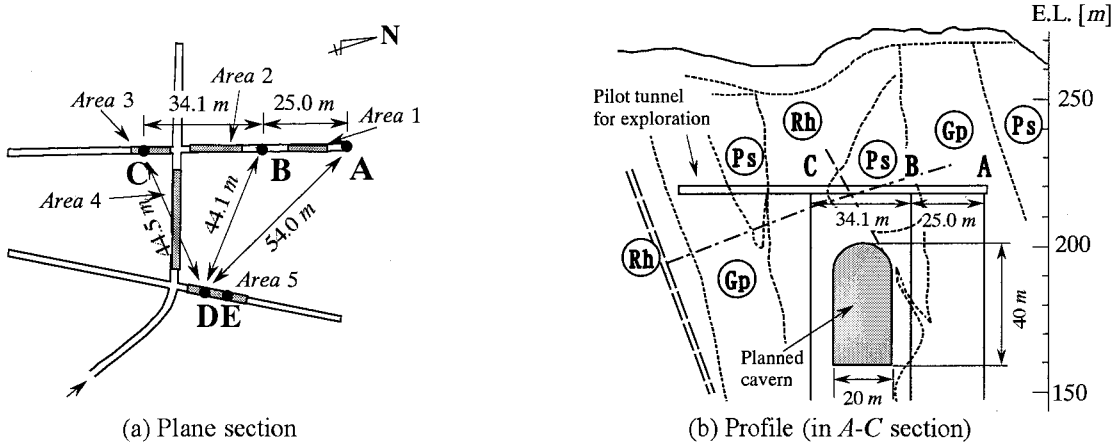

(a) Plane section
(*A*, *B*, *C*, *D*, & *E* : boreholes, *Area* : joint mapping area)

(b) Profile (in *A*-*C* section)
(Ps : slate, Gp : granite prophyry, Rh : rhyolite, *A*, *B*, & *C* : boreholes)

Figure 6.26 Locations of the boreholes and the geology map

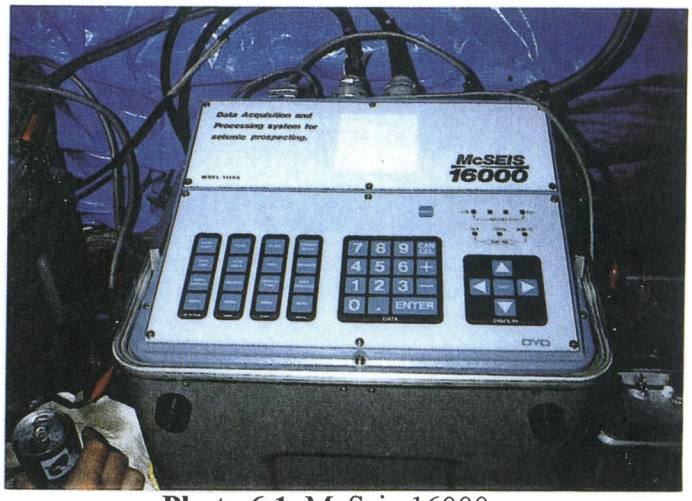

Photo 6.1 McSeis-16000

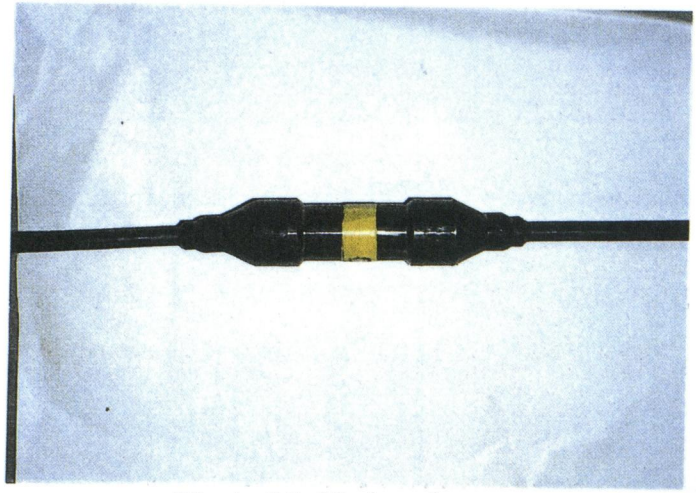

Photo 6.2 Hydro-phone

6.4.2 Results of the seismic velocity geotomographic technique (*SVT*)

Figure 6.27 shows the results of the seismic velocity geotomography in the cross section between Boreholes *A* and *C*. As compared with the distribution of geology, the seismic velocity does not presented a good agreement with the geology. In order to compare seismic velocity with joint frequency, Ikeda's equation (Ikeda, 1979) will be applied. and the relation between the seismic velocity and joint frequency will be discussed.

Based on the empirical results which were obtained by field measurements at more than 100 points, Ikeda described the following equation (1979):

$$n = \frac{5}{k^2} - 4 \qquad (6\text{-}17)$$

where n is the joint frequency [$1/m$] and k is the joint index. Then, k was defined as follows:

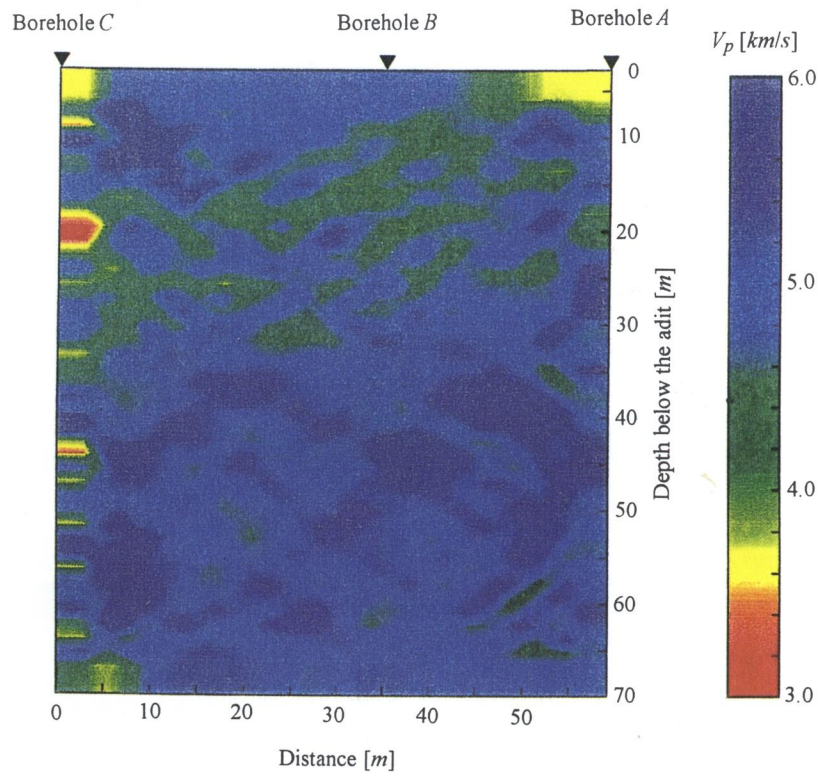

Figure 6.27 Velocity distribution map for Section *A*-*C*

$$k = \frac{V_{pf}}{V_{pc}} \tag{6-18}$$

where V_{pf} is the in-situ seismic *P*-wave velocity and V_{pc} is the seismic *P*-wave velocity of the core sample, that is, the seismic velocity of the intact rock. In performing laboratory tests for the propagating seismic wave through the intact core sample, the seismic velocity of the intact rock is already known. The average is 5.8 *km/sec*, and substituting its value and the seismic velocity through **Figure 6.27** into **Equations 6-16** and **6-17**, the distribution of joint frequencies between Boreholes *A* and *C* can be determined. The results are shown in **Figure 6.28**. On the other hand, the distribution of joint frequencies along the borehole is obtained through the borehole wall survey shown in **Figure 6.29**.

The area presenting a higher joint frequency along Boreholes *A* and *C* shows a good agreement with **Figure 6.28**, since it is made based on the borehole survey data from *A* and *C*. However, **Figure 6.28** shows a lower joint frequency at a deeper area, although a higher joint frequency can be found at the same area from the borehole survey results at Borehole *B*. Next, this will be compared with the joint frequency map shown in **Figure 6.32**. Naturally enough, **Figure 6.32** shows a good correlation to **Figure 6.29**, since the joint frequency map was provided from the information on the borehole wall survey.

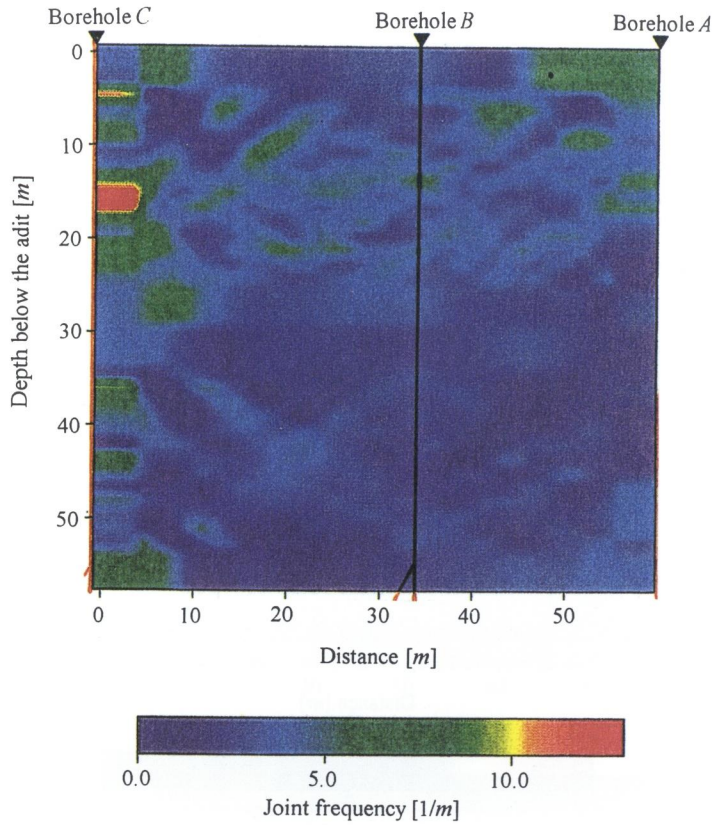

Figure 6.28 Joint frequency map through velocity distribution

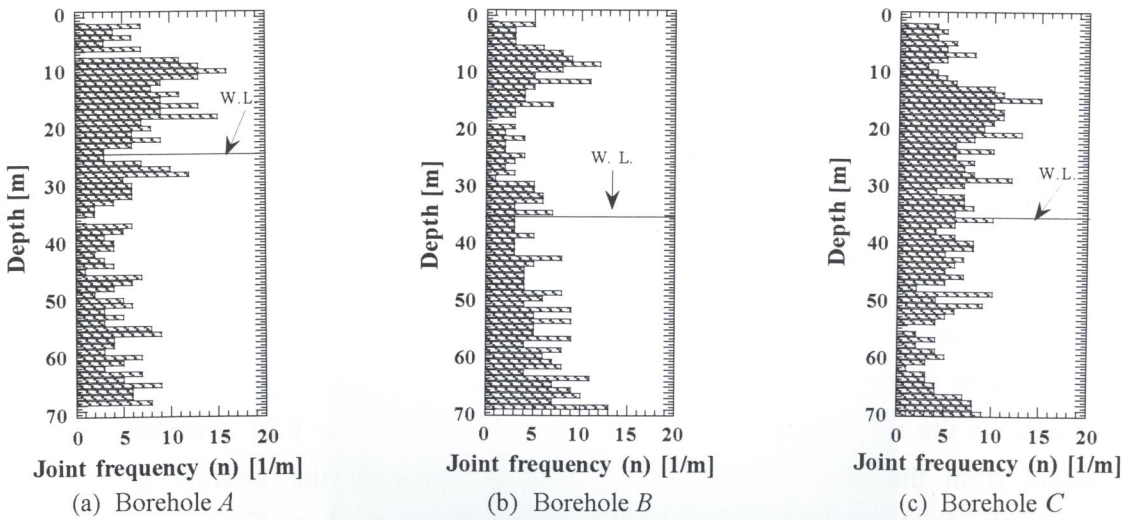

Figure 6.29 Distributions of joint frequencies along boreholes (by 1-*D* survey)

As for the joint frequency map, its reliability along the boreholes is higher based on actual measurements. On the other hand, the geotomographic analysis presents the velocity distribution at an objective area, wide and on the average. Based on the numerical simulation described above, progress has been made in the quality of the geotomographic analysis in its application to the information which is already known. Then, introducing the joint frequency map so as to apply the already known information, we have tried to carry out a geotomographic analysis. An ordinary analysis of geotomography is used for the uniformed initial velocity field. Then, the

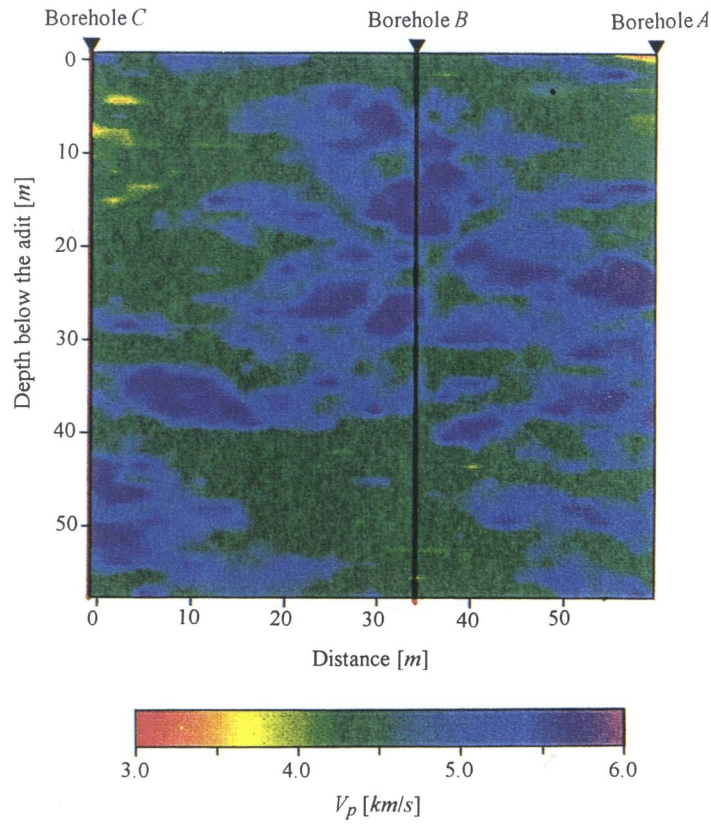

Figure 6.30 Initial velocity distribution through joint frequency map

joint frequency is converted into the seismic velocity through **Equations 6-17** and **6-18**, and the distribution of the seismic velocity is estimated as shown in **Figure 6.30**. Using **Figure 6.30** as the initial velocity field, the seismic geotomographic analysis is performed and its results are shown in **Figure 6.31**.

When comparing **Figure 6.31** with the usual results, as shown in **Figure 6.27**, a clear difference is not seen and a change generally does not occur. As for the area around Borehole *B* and the lower area of the objective field, **Figure 6.31** shows a good agreement with the actual measurements of the borehole wall joint survey although **Figure 6.27** presents a difference measurement from the joint distribution. Therefore, applying the seismic geotomographic technique to the joint frequency map improves the initial velocity field and upgrades the reliability of the seismic geotomography.

As the initial velocity field is estimated by the joint frequency map and is applied to the geotomographic analysis, it is confirmed that the reliability of the geotomographic analysis has made progress. However, the results are very likely to control the estimation of the joint frequency map. Then, another improved method is applied to the geotomographic analysis. The joint distribution around the boreholes shows the actual measurements, and the estimated seismic velocity around the borehole is reliable. Then, the numerical cells around the boreholes put on the estimated seismic velocity and their velocity values are fixed until the iterative analysis is complete. The results are shown in **Figure 6.32**. As compared with the other results, **Figure**

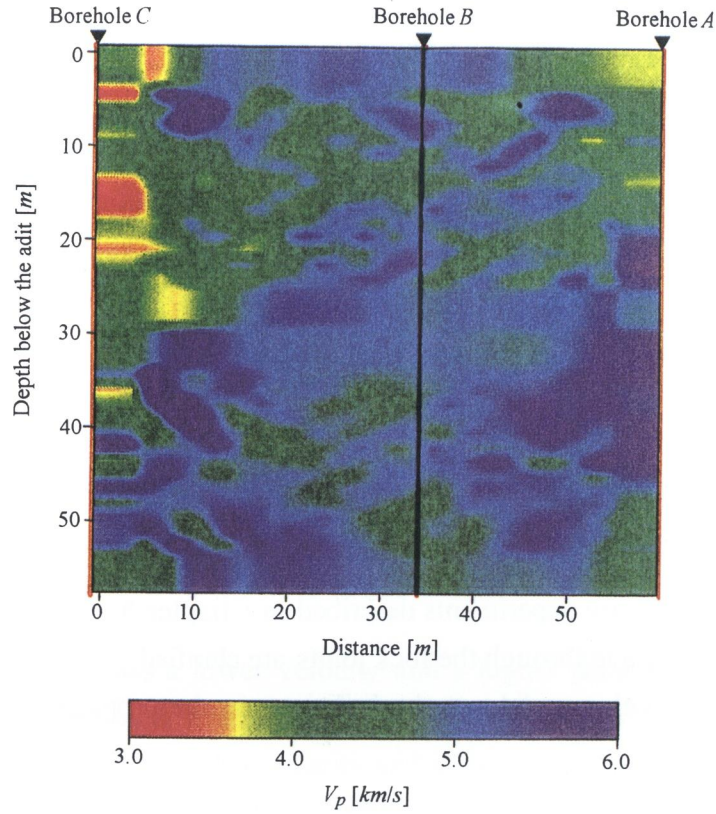

Figure 6.31 Velocity distribution map for Section *A*-*C* using initial model as shown in **Figure 6.30**

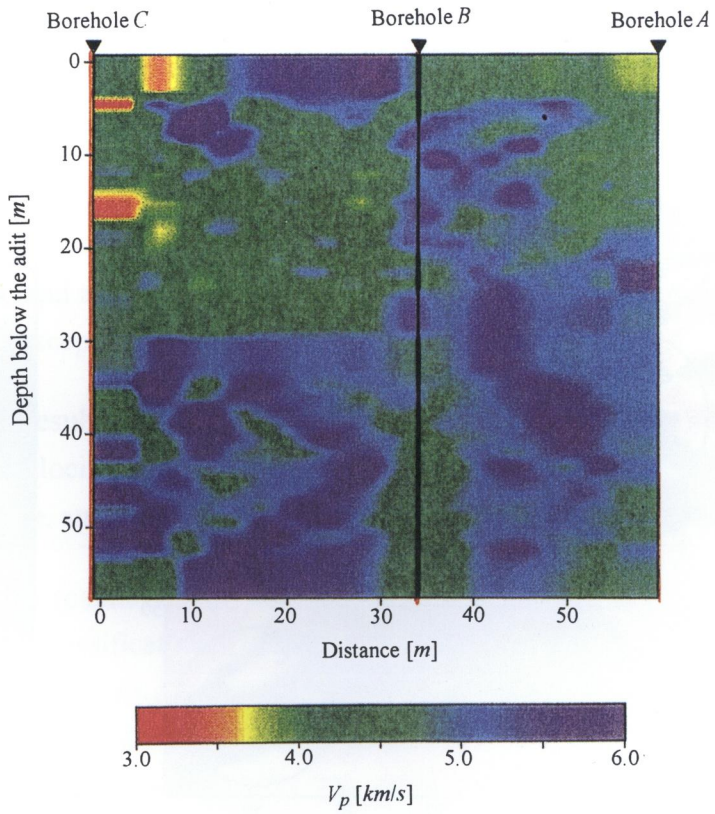

Figure 6.32 Velocity distribution map for Section *A*-*C* is a case in which the velocity of some cells is fixed

6.32 reflects the influence of the joint distribution around the boreholes. As for the actual measurements, this method has made progress in terms of the reliability of the geotomographic analysis.

6.4.3 Results of the seismic amplitude geotomographic technique (*SAT*) and a proposal for the classification of jointed rock masses through the results of seismic geotomography and a joint frequency map

Using **Equation 6-16**, an analysis of the seismic amplitude geotomographic technique (*SAT*) on the section between Boreholes *A* and *C* is carried out. **Figure 6.33** shows the attenuation factor distribution maps for Section *A-C*. The raypaths are applied to the results so as to solve **Figure 6.31**.

Based on the laboratory experiments described in Chapter 5, the following conclusions for the propagating seismic wave through the rock joints are clarified.

i) The seismic velocity did not show changes in the propagation of closely connected joints.

ii) The amplitude damping factor reflected both closely connected joints and the joints of wide apertures.

Applying such knowledge to a discussion on both *SVT* and *SAT* results, the following suggestions can be presented.

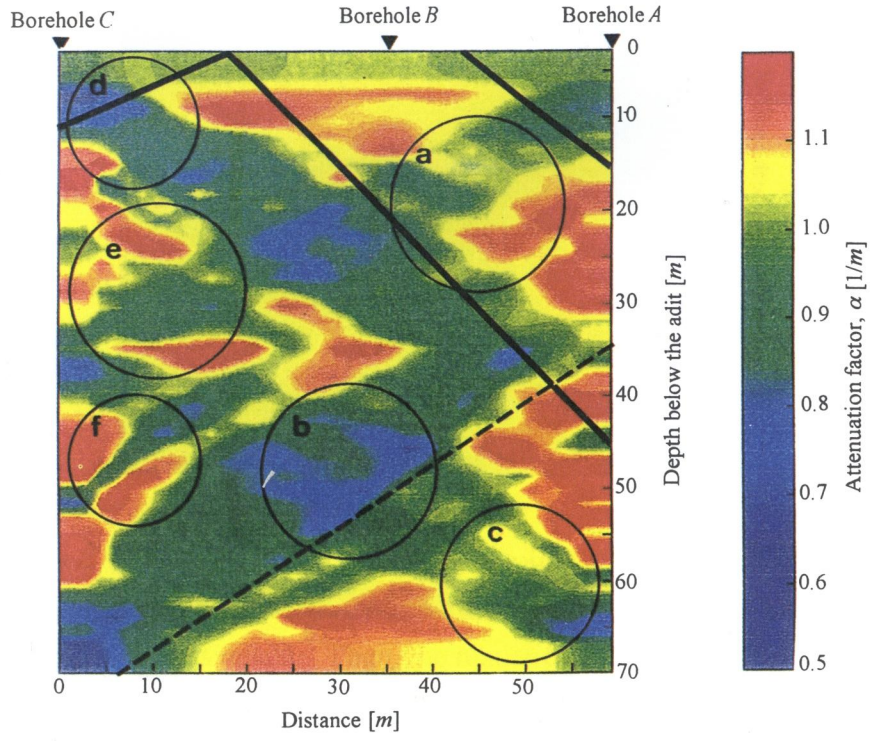

Figure 6.33 Attenuation ratio distribution map for Section *A-C*

Table 6.1 Rock classification based on three different maps

Classification	*SVT* (V_p [km/s])	*SAT* (α [1/m])	n [1/m]
good (*H*)	over 5.0	below 0.7	below 5
medium (*M*)	4.0 - 5.0	0.7 - 0.9	5 -10
poor (*L*)	below 4.0	over 0.9	over 10
Zone-*a*	4.0 - 4.5 (*M*)	0.9 - 1.2 (*L*)	15 -20 (*L*)
Zone-*b*	5.5 - 6.0 (*H*)	0.6 - 0.8 (*M*)	3 - 5 (*H*)
Zone-*c*	4.5 - 5.0 (*M*)	0.8 - 1.0 (*M*)	5 - 8 (*M*)
Zone-*d*	4.0 - 5.5 (*M*)	0.5 - 0.7 (*H*)	4 - 7 (*H*~M)
Zone-*e*	3.5 - 4.5 (*L*)	0.9 - 1.2 (*L*)	15 - 20 (*L*)
Zone-*f*	5.0 - 5.5 (*H*)	0.9 - 1.2 (*L*)	8 - 12 (*L*)

i) A zone which shows a lower velocity and a higher damping factor for each result consists of many joints which have wide apertures and filling material.

ii) A zone which shows a higher velocity and a higher damping factor consists of joints which are packed closely together.

In order to propose a classification for jointed rock masses, the following is discussed. Adding a joint frequency map (n) (**Figure 2.32**) to these two tomographic maps, the appearance of various rock are compared conditions on the respective maps which are classified into three classes. They are i) good (*H*), ii) medium (*M*), and iii) poor (*L*) classes. **Table 6.1** shows the results of the rock classification concerning the six zones shown in **Figure 6.33**.

In comparing the three different maps, Zones *c* and *e* show a good agreement with each other regarding Classes *M* and *L*. Zones *b* and *d* show an agreement between the *SVT* and the joint frequency maps, and also there is a remarkably good agreement between the *SAT* and the joint frequency maps, except in the case of Zone *b*.

Judging from the results of the comparison among *SVT*, *SAT*, and the joint frequency maps, the magnitude of the velocity does not always correspond with such rock joint conditions as joint frequency, aperture, and so on, which control the mechanical behavior of rock masses.

The sensitivity to (capability of detecting) joint orientation is discussed, as well as the agreements on the rock classification. The clearly identified small faults (through the geologist's visual investigation in the pilot) are illustrated with solid lines in **Figure 6.33**. The broken line shows the orientation of the fault which is assumed to exist 10-15 *m* behind Section *A-C* from the observation through borehole scanning (*BSS*). The propagating behavior of the projected waves is very spatial, and it is highly recommended that a seismic survey should be carried out in a three-dimensional manner as much as possible.

6.5 Conclusion

According to certain types of numerical simulations, the following conclusions can be obtained for the geotomographic analysis.

First of all, as for the location of the source and the receiver points, naturally enough, Arrangement I, namely, all-around sensing (360-degree scanning like in medical cases), has the advantage over other arrangements. However, it is impossible to apply Arrangement I in the civil engineering field. On the other hand, Arrangement II, that is, the ground surface and two scanning boreholes, shows results in a good agreement with the original model and without the effect of the inclination of a low velocity zone. Since the density of the ray paths presents an unbalance in the objective area, however, a numerical ghost appears and it is difficult to judge the existence or non-existence of a ghost in the practical results. As for Arrangement III, two vertical scanning boreholes (for conventional cross-borehole scanning), the distribution of the raypaths in an objective area presents a good balance. However, the low velocity zone running parallel to the boreholes cannot be created for the reconstructed model. It is concluded that scanning only between boreholes does not provide reliable images. Thus, scanning in three directions, such as in Arrangement II, should be employed in addition to the fact that the scanning area should be at least twice as large as the objective area, that is, the depth of the boreholes in the case of Arrangement II should be two or more times deeper than 40 *m*. This is due to the excessive difference in the raypath densities propagating through the respective cells. The distribution of rays (traveling waves) must be as uniform as possible.

As for the locations of the source and the receiver points, the reappearance of the reconstructed model makes progress since the interval between the source and the receiver points decreases, namely, the density of the raypaths increases. However, if the target is smaller than the interval, the target cannot be shown in the reconstructed model and the high-precision reconstructed model cannot be obtained. In addition, in order to perform a high-precision analysis in geotomography, as many cells as possible must be set up, according to the limits, to prevent a break in the calculations.

It is shown that the seismic geotomographic technique, based on the attenuation behavior of traveling waves, can provide more detailed information concerning rock joints by giving consideration to both laboratory experiments and applications in the field.

The following conclusions can be made :

1) When the number of joints with smooth fracture planes and thin apertures increases, the amplitude distribution technique (*SAT*) corresponds much better than the velocity distribution technique (*SVT*).

2) Concerning variations in joint roughness and changes in normal and shear stresses, *SAT* is more sensitive than *SVT*.
3) When filling materials and thick apertures exist in joints, both *SAT* and *SVT* show a good correspondence.
4) By employing the joint frequency mapping through *BSS* (the borehole scanner system), the geotomographic technique (consisting of *SVT* and *SAT*) may be suggested and may distinguish the following cases from each other :
   - the existence of weak zones and joints with fillings in the case of low velocity and high attenuation, and
   - the distribution of tightly jointed fractures in the case of high velocity and high attenuation.

REFERENCES

Ikeda, K. (1979) : The Property and the Strength of Fissured Rock Masses, *Journal of the Japan Society of Engineering Geology*, Vol. 20, No. 4, pp. 20 - 32.

Ishii, Y. (1990) : Usefulness and Problems of Geotomography, *Proceedings of SEGJ International Symposium on Geotomography*, SEGJ, pp. 1 - 18.

Itoh, K., et al. (1983) : A model for approximate computation of first arrival traveltimes in seismic refraction modeling, *Proc. of 1983 Spring Meeting SEG Japan*, pp. 11 - 12 (in Japanese).

Moser, T. J. (1991) : Shortest path calculation of seismic rays, *Geophysics*, Vol. 56, pp. 59 - 67.

Qin, F., et al. (1992) : Finite-difference solution of the eikonal equation along expanding wavefronts, *Geophysics*, Vol. 57, No. 3, pp. 478 - 487.

Saito, H. (1989) : Traveltimes and ray paths of first arrival seismic waves: Computation method based on Huygens' principle, extended abstract, *59th Annual Int'l SEG Meeting*, pp. 244 - 247.

Saito, M. (1991) : Fundamental Theory of Geotomography, *Journal of Geology and Investigation*, Vol. 2, pp. 8 - 12. (in Japanese)

Sassa, K. (1990) : Applications of geotomography to rock engineering, *Proceedings of SEGJ International Symposium on Geotomography*, SEGJ, pp. 21 - 28.

Scales, J. A. (1987) : Tomographic inversion via the conjugate gradient method, *Geophysics*, Vol. 53, No. 2, pp. 179 - 185.

Shima, H. (1989) : Resistivity Tomography - Basic concepts and its application, BUTSURI-TANSA, Vol. 42, No. 6, pp. 442 - 457. (in Japanese)

Tanimoto, C. and Ikeda, K. (1983) : Acoustic and mechanical properties of jointed rock, *Proc. of 5th ISRM Congress*, Balkema, pp. A15 - 18.

Tanimoto, C. and Kishida, K. (1994) : Seismic geotomography : Amplitude versus velocity in consideration of joint aperture and spacing, *Rock Mechanics*, Nelson & Laubach (eds), Balkema, pp. 147 - 155.

Tanimoto, C., Kishida, K., Yoshizu, Y. and Kunii, K. (1994) : Seismic attenuation geotomographic technique in designing a large underground cavern, *Integral approach to applied rock mechanics* (*Proceedings of the 1994 ISRM International Symposium*), M. Van Sint Jan (ed.), Vol.1, pp. 195 - 206.

Tanimoto, C. and Shibata, T. (1992) : Deep Underground Construction and Geomechanics, *Proceeding of U.S. - Korea - Japan Trilateral Seminar*, Honolulu, pp. 439 - 454.

van Trier, J. and Symes, W. W. (1991) : Upwind finite-difference calculation of traveltimes, *Geophysics*, Vol. 56, No. 6, pp. 812 - 821.

Vidale, J. (1988) : Finite-difference calculation of traveltimes, *Bull. Seis. Soc. Am.*, Vol. 78, No. 6, pp. 2062 - 2076.

Chapter 7

The Property of Deformation of Jointed Rock Masses and the Determination of Joint Stiffness through Borehole Loading Tests

7.1 Introduction

In the design and the construction of rock structures, it is very essential to understand the realistic deformability of rock masses. It is not sufficient to characterize rock deformability by the elastic constants alone, for many rocks are inelastic. Elasticity refers to the property of the reversibility of deformation in response to load. Many fresh, hard rocks are elastic when considered as laboratory specimens. On the field scale, however where rocks can be expected to contain fissures, fractures, bedding planes, contacts, zones of altered rock, and clay with plastic properties, most rocks do not exhibit perfect elasticity. The extent of the irrecoverability of strain in response to load cycles is as important to the design as the slope of the load/deformation curve.

The most widely used testing procedures for deformability measurements are laboratory compression and bending tests, wave velocity measurements in the laboratory and in the field, field loading tests using flat jacks or plate-bearing apparatus, and borehole expansion tests. The borehole expansion tests are classified into two types. One is a dilatometer test in which expanding rubber sleeves provide uniform inner pressure around the entire circumference of the borehole wall, and the other is a borehole jack test in which the loads are applied unidirectionally across the diameter.

Goodman (1980) suggested a concept for the "modulus of permanent deformation (M)", whose definition is shown in **Figure 7.1**. Borehole jack tests are carried out in three drillholes, all 70 *m* in length, and the relationship among the elastic modulus of the intact rock, the deformation coefficient of the rock mass, joint stiffness, and the modulus of permanent deformation are clarified. In particular, the physical meaning of permanent deformation which is presented through cyclic loading-unloading is considered. Then, based on the discontinuity information at the loading point, a concept for the determination of joint stiffness is suggested. Laboratory tests which consider the loading mechanism of the borehole jack test are carried out, and the validity of the joint stiffness determined through the borehole jack tests is investigated.

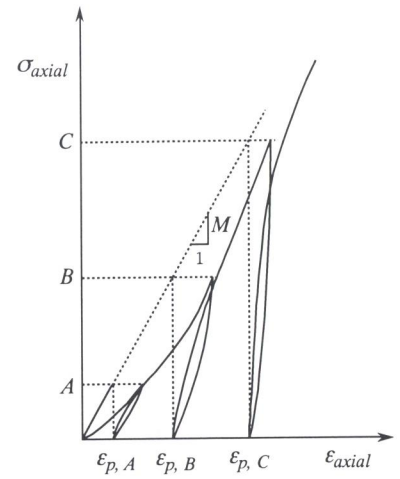

Figure 7.1 Determination of the modulus of permanent deformation, *M* (Goodman, 1980)

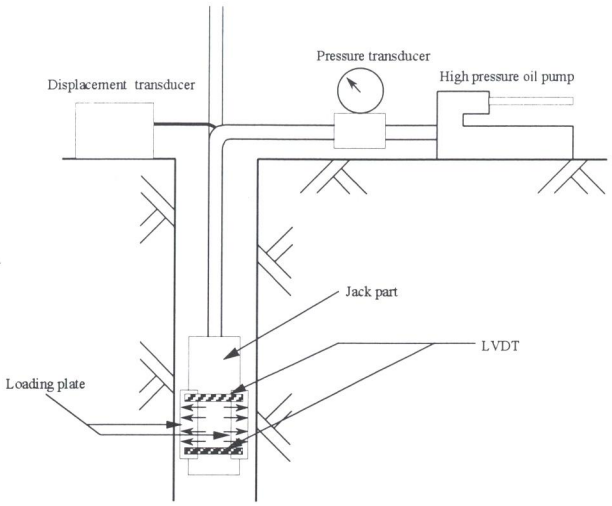

Figure 7.2 Apparatus of the Goodman jack

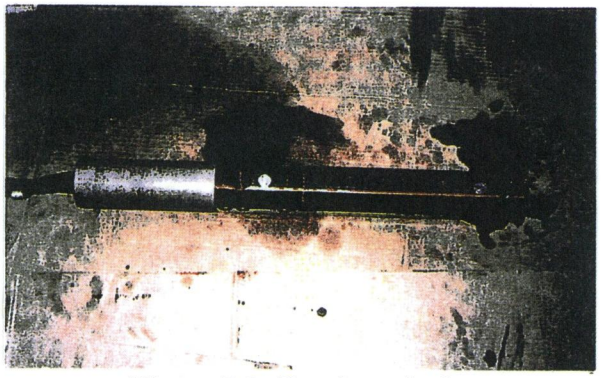

Photo 7.1 Goodman jack

7.2 Goodman-type borehole jack tests

7.2.1 Borehole jack tests

Borehole jack tests are carried out using a Goodman jack (Model-52101, SINCO) in order to consider the deformation of rock masses as the loading direction. Since the loading plate of a Goodman jack is made of stainless steel, it is very stiff and solid. And, as the loading capacity is very high (a maximum capacity of 70 *MPa*), it can be applied to both soft and hard rock. The loading can be performed to pump up the oil, and the load can be indicated to the pressure transducer on the ground. The displacement can be measured by two linear-displacement transducers (*LVDT*) which fit into both ends of the loading plate and can be indicated to the displacement instrument on the ground. The precision of the *LVDT* is 1/100 *mm*. The area of the jack face is 30 *mm* (in width) by 300 *mm* (in length). **Figure 7.2** and **Photo 7.1** show the outline of the Goodman jack.

In order to estimate the various mechanical parameters of each loading level and to consider the non-elastic behavior, loading and unloading up to four loading levels are carried out. Four boreholes (Boreholes *A*, *B*, *C*, and *E*), 70 *m* in depth, are made in the location where the construction of an underground cavern is planned, as shown in **Figure 2.3**, and were provided for use in the tests at 63 selected depths. So as to clarify the relationship between the property of the deformation of the jointed rock mass and the loading direction, that is, the relationship between the orientation of the joints and the loading direction, the borehole jack tests are carried out in two or three different directions at a selected depth. When discussing the relationship between the property of deformation and the orientation of the joints, the Goodman-type jack has an effective advantage since the loading direction is clear. Therefore, the borehole jack tests are carried out in a total of 126 loading directions.

Prior to the borehole jack tests, the insides of the boreholes are scanned by the borehole scanner system (*BSS*), and joints crossing the borehole are investigated in as precise an undisturbed state as possible. The *BSS*, which was described in Chapter 2, is unique and is characterized by its principle and its performance capabilities such as direct digital data acquisition, continuous imagery through a rotating scanner, its incredibly high observation speed (72 *m* per hour), image quality (0.1 *mm* resolution), and so on (Tanimoto, et al., 1992). The observed numbers of joints and joint frequencies are shown in **Table 7.1**, and the average frequency of the joints is 5.9 joints per meter, corresponding to the classification of 'moderately fissured' (Class $C_H \sim C_L$ ranked by CRIEP-Japan). Based on the careful observation of a complete image through *BSS*, 63 points are selected as the objective loading points from the points of view of a variety of joint orientations, apertures, spacing, filling, etc..

7.2.2 Results of the borehole jack test

Several examples of load - displacement curves are shown in **Figure 7.3**. Respective pairs of (a) and (b), at a depth of 52.30 *m*, and (c) and (d), at a depth of 53.60 *m* at Borehole *A*, are obtained for different loading directions forming 45 degrees. The former is done from the average state of joints, while the latter is done from the state of a comparatively wide aperture. The dotted lines show inelastic deformations, and the magnitudes of deformation are as different from each other as the concept shown in **Figure 7.1**. Actually, with a different loading direction, it is confirmed that the obtained load - displacement curves and the magnitude of permanent deformation are different at the same depth. **Figure 7.4** shows some examples of joints monitored at loading points, as presented in **Figure 7.3**. **Figure 7.4**, which comes from the *BSS* borehole wall survey, shows the three-dimensional display of joints at the loading points and presents the different joint distributions at each loading point.

Since the localized part of the borehole wall is presented to the deformation as loading by borehole loading tests, joints strongly affect the deformation at the loading points. From **Figures**

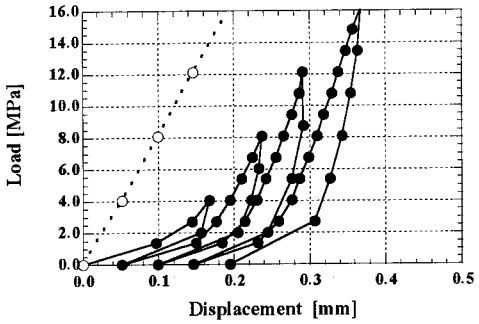

(a) Depth : 52.30 *m*, Loading direction : N115W

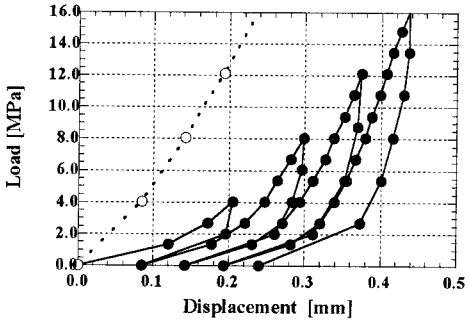

(b) Depth : 52.30 *m*, Loading direction : N70W

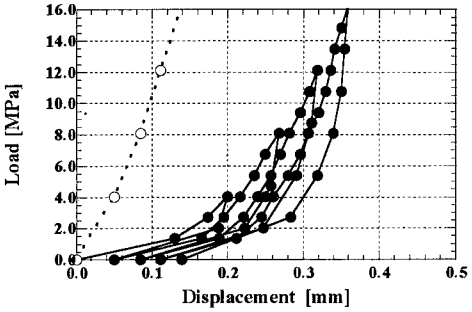

(c) Depth : 53.60 *m*, Loading direction : N90E

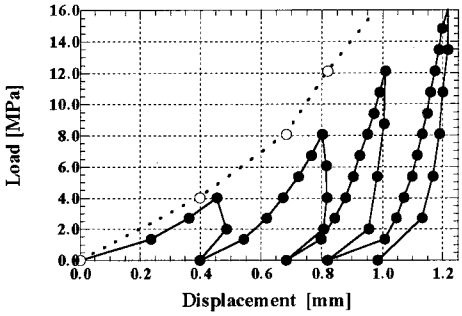

(d) Depth : 53.60 *m*, Loading direction : N135E

Figure 7.3 Examples of the load - displacement curves through the borehole loading tests

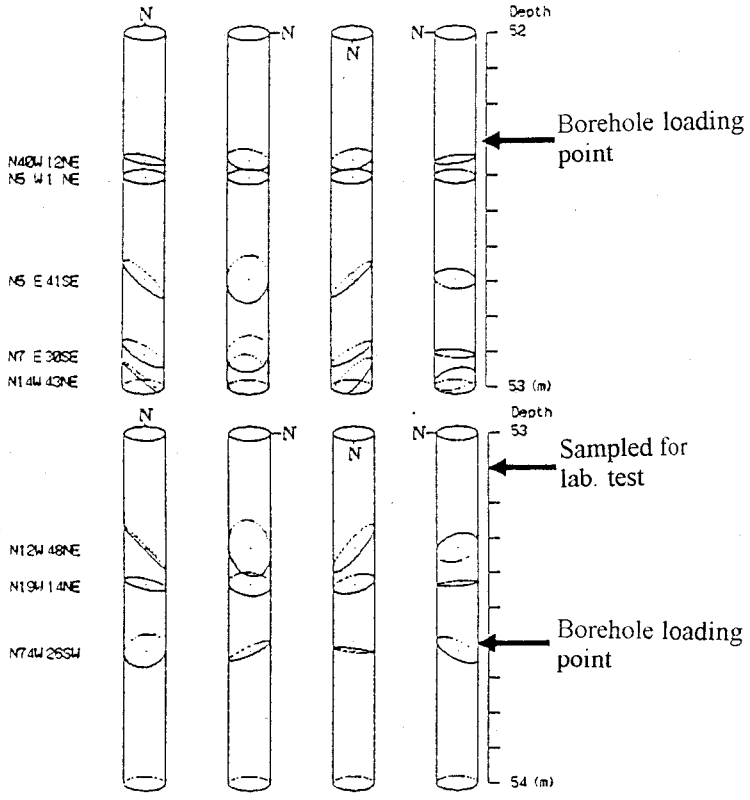

Figure 7.4 Three-dimensional continuous image of joints

Table 7.1 The number of joints and joint frequencies

	Borehole *A*	Borehole *B*	Borehole *C*	Borehole *E*
The number of joints through *BSS*	403	357	439	477
Joint frequency [1/*m*]	5.76	5.10	6.27	6.81

Table 7.2 Parameter specimens and test results

Specimen no.	Pick-up point		Diameter [*cm*]	Length [*cm*]	Weight [*g*]	Unit weight [g/cm^3]	Uniaxial compressive strength [*MPa*]	Elastic modulus [*MPa*]	Poisson's ratio	Control
	Borehole no.	Depth [*m*]								
6	*A*	20.10	4.99	10.00	513.4	2.63	$2.07x10^2$	$7.03x10^4$	0.210	A. D.
8	*A*	9.50	5.00	10.00	515.8	2.63	$1.51x10^2$	$5.80x10^4$	0.200	A. D.
9	*A*	41.55	5.00	9.99	515.3	2.63		$5.80x10^4$	0.250	C. L.
10-1	*A*	47.75	5.00	10.00	513.1	2.61		$8.12x10^4$	0.200	C. L.
10-2	*A*	47.85	4.99	8.61	442.2	2.63		$8.19x10^4$	0.210	C. L.
12	*A*	53.10	5.00	10.00	513.3	2.62		$7.02x10^4$	0.160	C. L.
18	*B*	26.55	4.99	10.00	517.8	2.65		$8.83x10^4$	0.210	C. L.
21	*B*	45.30	5.00	10.00	518.0	2.64	$2.03x10^2$	$7.80x10^4$	0.245	A. D.
23	*B*	61.10	5.00	10.01	515.6	2.62	$2.05x10^2$	$7.18x10^4$	0.270	A. D.
31	*C*	41.45	4.99	10.00	515.9	2.63		$8.12x10^4$	0.225	D. D.
34	*C*	47.65	4.99	9.99	521.7	2.67	$2.54x10^2$	$8.55x10^4$	0.245	D. D.
37	*C*	57.80	4.99	10.00	516.5	2.64		$8.63x10^4$	0.215	C. L.

A.D. : Axial displacement control
D.D. : Lateral displacement control
C.L. : Cyclic and constant loading control

7.3 and **7.4**, the deformation and the permanent deformation are different. Moreover, at the same loading point, the deformation and the permanent deformation are obtained differently as each load has an effect in a different direction.

7.2.3 Stiff loading tests in the laboratory

In order to obtain Poisson's ratio to estimate the mechanical parameters through borehole loading tests and to compare the mechanical behavior of intact rock with that of a jointed rock mass, uniaxial compression tests are carried out. In these tests, the specimens, in which no joints can be found, are taken from recovered borehole core samples. The ends of the intact rock specimens are finished with an allowance of 0.01 *mm* or smaller. **Photo 7.2** shows the set-up of the specimen. A stiffness loading test machine made by MTS is used, and the data logger (TDS-301, Tokyo Sokki Institute, Ltd.) measures certain types of strain. The strain gauge (PC-10-11, Tokyo Sokki Institute, Ltd.) is glued to the specimen using glue (CN glue, Tokyo Sokki Institute, Ltd.).

There are two purposes for this test, namely, the estimation of such mechanical parameters as Poisson's ratio, the uniaxial compressive strength, and the elastic modulus, and the estimation of the mechanical behavior of intact rock. Therefore, tests on certain specimens are performed under axial displacement control (0.04 ~ 0.004 *mm/min.*), under lateral displacement control, such as dilatancy control (0.01 ~ 0.005 *mm/min.*), and under cyclic and constant loads which are equal to those of the borehole loading tests. The purpose of the latter is to clarify the mechanical behavior.

Table 7.2 shows parameter specimens and test results. The uniaxial compressive strength is as different as the control systems. As for the axial strain (displacement) control and the constant axial loading control, the yield point is passed all at once since the amount of displacement is constant or increasing around the yield point. On the other hand, as the load is controlled in detail around the yield point in the lateral displacement control, the uniaxial compressive strength appears to be higher. In spite of differences in the loading control, the elastic modulus and Poisson's ratio are almost constant for each specimen.

Figure 7.5 shows the stress - strain relation of Specimen No. 12, sampled from a depth of 53.10 *m* in Borehole *B*, as shown in **Figure 7.4**. The stress - strain relation is linear and a slight hysteresis is observed under cyclic loading. This cyclic loading is equal to that of the borehole loading test in the field. This hysteresis is different, however, from that observed in the load - displacement relation through the borehole loading tests and is negligible in consideration of the main objective of this thesis.

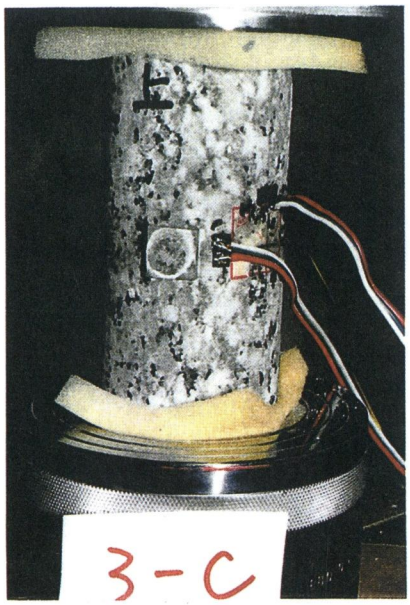

Photo 7.2 Set-up of the specimen for the uniaxial compression test

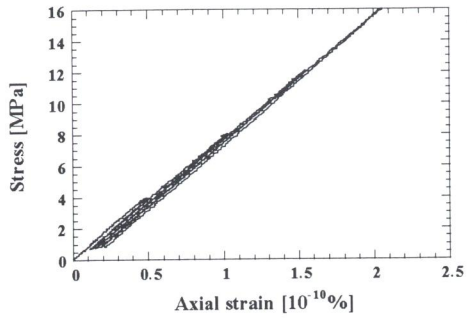

Figure 7.5 The stress - strain relation of intact rock under cyclic loading

7.3 Discussion on the results of the borehole loading tests

7.3.1 Elastic modulus and deformation coefficient through the borehole loading tests

In general, deformation coefficient D is determined by an enveloping line to the hysterestic curves, and elastic coefficient E (of the rock mass) is found by a tangential gradient at the maximum load in a load - displacement curve (JSCE, 1983). Following the JSCE designation and using Goodman's elastic equation (Goodman, et al., 1968), the deformation and the elastic coefficients obtained in **Figure 7.3** are as shown in **Table 7.3**. Goodman's elastic equation is assumed on the plane strain condition under a two-dimensional isotropic elastic body and the boundary stress distribution around the borehole. Then, it is presented as follows:

Table 7.3 Deformation coefficient (D) and elastic modulus (E) determined by the empirical method in **Figure 7.3**

Borehole	Depth [m]	Loading direction	D [MPa]	E [MPa]
A	52.30	$N115W$	2.13×10^3	4.69×10^3
A	52.30	$N70W$	2.04×10^3	4.86×10^3
A	53.60	$N90E$	3.10×10^3	7.38×10^3
A	53.60	$N135E$	6.89×10^2	3.23×10^3

$$D \text{ or } E = \frac{d}{2} \cdot \psi(\beta, \upsilon) \cdot \frac{\Delta P}{\Delta u} \tag{7-1}$$

where d is the diameter of the borehole, β is the curvature of the loading plate, υ is Poisson's ratio, ψ is the function determined by β and υ, and ΔP and Δu are the increment ratios of load and displacement, respectively (Goodman, et al., 1968). In this thesis, u and β are 0.25 and 27.5, respectively. The values for the elastic coefficient are far different from those of the intact rock (7.02×10^4 *MPa*). The values for D and E are conveniently employed in deformation and stress analyses, respectively, but their physical meanings are unclear. It is also pointed out that the determination of the elastic coefficient (E) by the tangent may include human error caused by an individual's visual observation and/or loading patterns. In this sense, determination by a secant is more meaningful than one by a tangent.

Figure 7.6 shows the dependency of the deformation coefficient on the applied load. Respective coefficients corresponding to load increments are plotted. According to **Figure 7.6**, the deformation coefficient increases up to a certain load pressure (4 - 5 *MPa*), and then maintains a constant value at a level higher than the above-mentioned pressure. Conventionally, many engineers employ this constant value for the deformability of a rock mass. When the mechanical behavior of loosened rock is considered, the dependency of the deformability on a low confining pressure in a covering rock should be noted. On the other hand, the deformation coefficient does not become constant at the higher loading level in **Figures 7.6**(c) and (d), since the joint at the loading point is strongly affected by the property of deformation of the jointed rock mass.

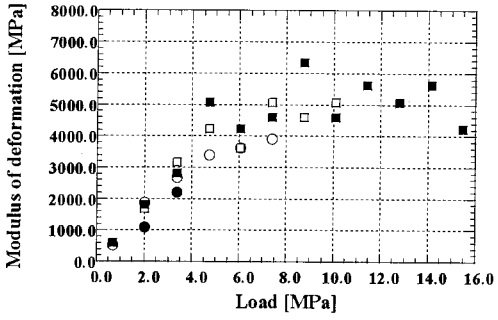

(a) Depth : 52.30 *m*, Loading direction : N115W

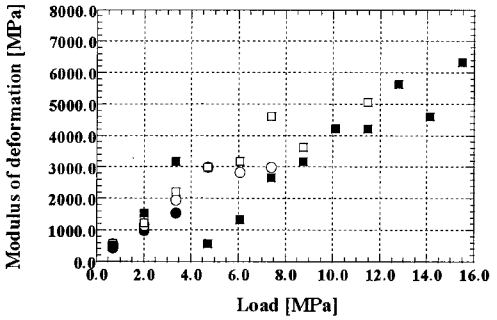

(b) Depth : 52.30 *m*, Loading direction : N70W

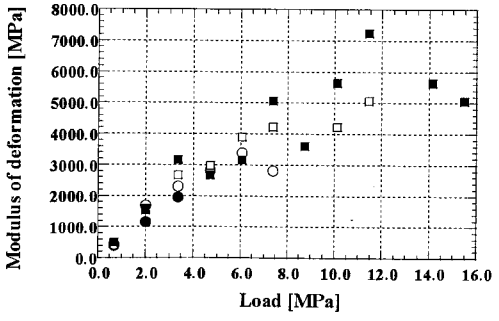

(c) Depth : 53.60 *m*, Loading direction : N90E

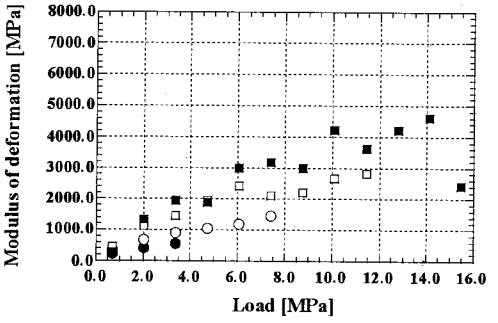

(d) Depth : 53.60 *m*, Loading direction : N135E

Figure 7.6 Load dependency of deformation coefficient D

Then, the physical meanings of the deformation of the jointed rock mass must be considered under several pressure levels, especially permanent deformation M.

7.3.2 Modulus of permanent deformation through the borehole loading tests

When the magnitude of the load returns to zero under cyclic loading, a nonrecoverable or permanent deformation is more or less recognized. Goodman (1980) defined 'modulus of permanent deformation M' as the ratio of stress magnitude to permanent deformation, as shown in **Figure 7.1**. Namely, it is the coefficient indicating a relation between maximum load and inelastic deformation in respective cyclic loading.

The modulus of permanent deformation in the plate bearing test was defined by Goodman (1980) as follows:

$$M = Ca(1 - \upsilon^2) \cdot \frac{\Delta P}{\omega - \omega_{elas}} \tag{7-2}$$

where C is the parameter determined by the boundary condition, a is the radius of the bearing plate, υ is Poisson's ratio, ω is the displacement, and ω_{elas} is the displacement at reloading. When a borehole jack is employed, the modulus of permanent deformation, M, is given by **Equation 7-3** based on Goodman's elastic equation as described in **Equation 7-1**, namely,

$$M = \frac{d}{2} \cdot \psi(\beta, \upsilon) \cdot \frac{\Delta P}{\Delta u - u_p} \tag{7-3}$$

where d is the diameter of the drillhole, P is the increment of the load, u is the displacement caused by P, u_p is the residual (permanent) displacement caused by P, and $\psi(\beta, \upsilon)$ is the constant given by Poisson's ratio of the rock and the curvature of the loaded surface (Tanimoto et al., 1991). **Equation 7-3** is transformed by the Goodman's elastic equation.

According to **Equation 7-3**, values for M in the load - displacement curves shown in **Figures 7.3** and **7.4** are obtained as shown in **Table 7.4**. **Table 7.4** also shows values for M in the uniaxial compression tests shown in **Figure 7.5**. In the uniaxial compression tests in the laboratory, the specimen with no joints (intact rock) shows a much higher value for M than in other field data. Even in the load - displacement curve for intact rock, a slight hysteresis can be observed when cyclic loading is applied. This is because cycles of loading and unloading produce 'hysteresis loops' as energy is consumed by sliding on cracks and fissures inside the rock volume. This hysteresis is negligible because of too high a value for M, such as 10^6 to 10^7 *MPa*, for a displacement which is given by the inverse of M is as small as 10^{-4} to 10^{-5} of the value for jointed rock. From the fundamental tests on the modeled rock mass, mentioned in the previous section, it is concluded that the higher the joint frequency becomes the greater the hysteresis becomes. And, the higher the confining pressure is, the smaller the hysteresis becomes. This means that most or

Table 7.4 Obtained permanent deformation coefficient M

Borehole	Depth [m]	Loading direction	Permanent deformation coefficient M [MPa]			
			M1	M2	M3	M4
A	52.30	*N115W*	2.91×10^3	3.21×10^3	3.21×10^3	3.08×10^3
A	52.30	*N90W*	1.77×10^3	2.65×10^3	2.96×10^3	3.20×10^3
A	53.10	uniaxial	6.27×10^5	1.13×10^6	1.29×10^7	1.55×10^7
A	53.60	*N90E*	3.02×10^3	4.31×10^3	5.81×10^3	5.39×10^3
A	53.60	*N135E*	3.78×10^2	5.30×10^2	1.11×10^3	9.21×10^3

all of the permanent deformation (in an engineering sense) by borehole jacking is governed by joints in a rock mass. For example, **Figures 7.3**(c) and (d) correspond to wide apertures, and the difference in M is remarkably directional. Knowledge of the relative positioning between the loading direction and the orientation of the joint plane is extremely essential to the understanding of the load - displacement curve through the borehole jack tests.

Fundamental laboratory tests on the joint models are carried out in order to investigate the relationship between the characteristics of a joint and its deformability. A biaxial loading cell with a steel cylinder, 60 *cm* in diameter, 40 *cm* high, and 2.5 *cm* thick, is prepared. After setting the joint model assemblage into the cell, four flat jacks, 40 *cm* square, are installed onto the four sides, and the space between the assemblage and the cell is filled in tightly with stiff cement mortar, as shown in **Figure 7.7**. The joint model is formed by assembling many cubes and rectangular prisms made of plaster. The mixing ratio is 3 to 2 for plaster to water, and the physical properties of the plaster block are 5.27×10^3 *MPa* and 0.20 for Young's modulus E_0 and Poisson's ratio υ, respectively. These values are constant during the test period (Tanimoto, et al., 1988). Model No. 1 is prepared for a continuous rock without any joints, while Model Nos. 2 to 5 are prepared for jointed rock masses and are designed so as to correspond with joint frequencies n (number of joints per meter) of 7.5, 15, 25, and 35, respectively. Joint frequency n can be defined by dividing the total length of the joints (in meters) with respect to a horizontal plane by the objective area (in square meters). This has an equal dimension to the 'number of joints per meter' along an objective line.

Arbitrary combinations of confining pressures (or contact pressures at joints) can be applied to the models by controlling the surrounding flat jacks. The loading pattern which is employed in the laboratory tests is a step-wisely repeated loading, and the peak load of each loading process is divided into four and increased step by step with increments of a quarter of the peak load. The magnitudes of the peak load are 1.0 to 4.0 *MPa*, corresponding to the same levels of confining pressure of 1.0 to 4.0 *MPa*, respectively.

Figure 7.8 illustrates the relationship between joint frequency (n) and the 'deformability ratio' (D/E_0), namely, the ratio of the average D for a jointed mass versus that of a solid body (intact rock) with no joints (E_0). It is easy to recognize that the deformation coefficient D is

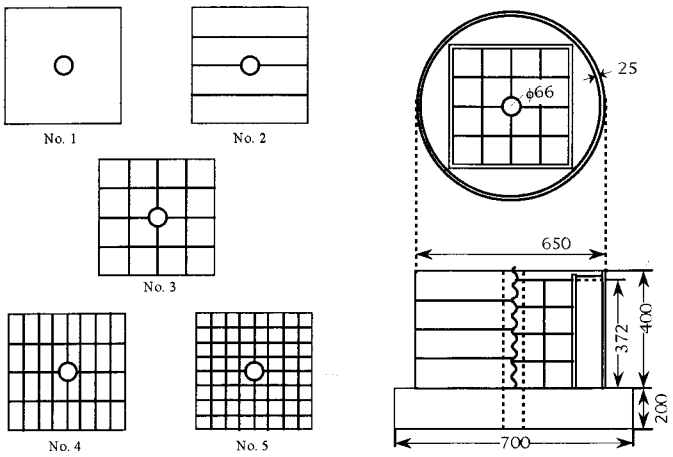

Figure 7.7 Modeled rock mass and loading cell

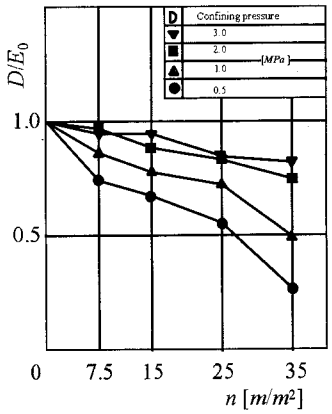

Figure 7.8 D/E_0 vs. joint frequency

greatly affected by the degree of joint frequency. And, the higher a joint frequency is, the more remarkable the reduction in the deformation coefficient becomes under a lower confining pressure. This suggests that the shear resistance (strength) of the jointed rock depends highly on the magnitude of the confining pressure when the confining pressure is low, such as 1 to 2 *MPa*. This matter relates to the mechanical behavior of loosened rock near free faces to be exposed by excavation.

Figure 7.9 presents the load - volumetric displacement relation under a confining pressure of 0.5 *MPa* for Model Nos. 1, 3, and 4, as shown in **Figure 7.7**. **Figure 7.9** also presents the relation under a confining pressure of 3.0 *MPa* for Model No. 3. From these results, a clear hysteresis can be observed for many joint frequency models and a slight hysteresis can be observed in the case of a higher confining pressure. Based on this knowledge, it is thought that the permanent deformation of a jointed rock mass is strongly controlled by the deformation of the joints. The permanent deformation of a jointed rock mass, or that presented in **Figure 7.9**, is more difficult than that of intact rock under uniaxial compression, as shown in **Figure 7.5**. Actually, a different magnitude for the permanent deformation can be observed at the same loading point in the borehole loading tests, if the loading direction changes. In particular, in comparison to **Figures 7.3**(c) and (d), different magnitudes of the permanent deformation can be clearly found. This is the reason why a joint aperture at the loading point is widely observed through the borehole wall survey. And, the relative relation between the loading direction and the location of the joint is closely affected by the permanent deformation. Therefore, the deformation of a jointed rock mass obtained through borehole loading tests can consist of both elastic deformation and permanent deformation which occur on a joint.

Then, the physical meanings and the mechanism of the permanent deformation are considered. Cyclic loading tests under a uniaxial compressive condition are carried out using a cylindrical specimen which includes a single joint. The specimen is made of plaster, although it includes a natural rock joint. This joint is located in the middle of the specimen and is almost parallel to both end planes of the specimen. The strain gauge is stuck on both intact rock parts

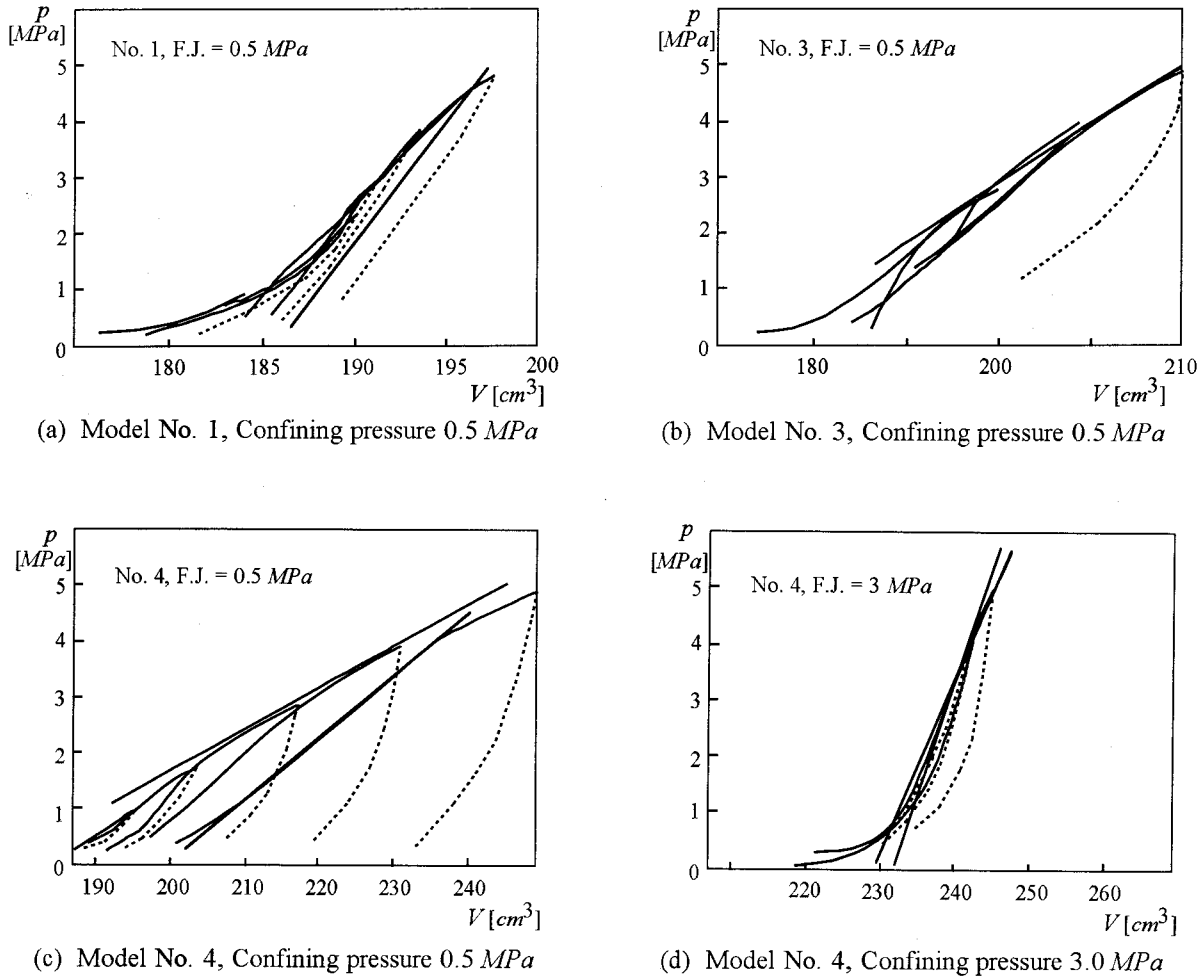

(a) Model No. 1, Confining pressure 0.5 *MPa*

(b) Model No. 3, Confining pressure 0.5 *MPa*

(c) Model No. 4, Confining pressure 0.5 *MPa*

(d) Model No. 4, Confining pressure 3.0 *MPa*

Figure 7.9 Load - volumetric displacement relation

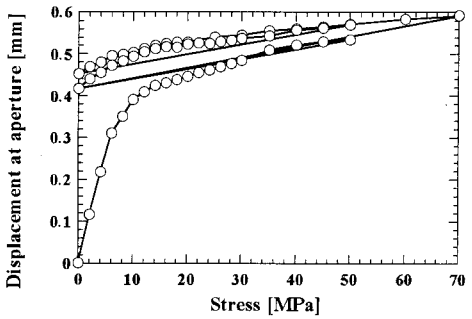

Figure 7.10 Stress - aperture displacement relation under the cyclic uniaxial compression tests on a rock joint

and the total displacement of the specimen is measured by a contact-type displacement transducer. Therefore, the normal displacement for the joint is determined by deducting the displacement of the intact rock from the total displacement of the specimen. A sample of the stress - displacement at the aperture curve is shown in **Figure 7.10**. In the initial cyclic loading, a permanent deformation in the normal direction at the joint can be observed. In the second and third cyclic loadings, the permanent deformation can not be clearly observed. On the other hand, using a specimen which has the same shape as the natural joint surface roughness in the uniaxal

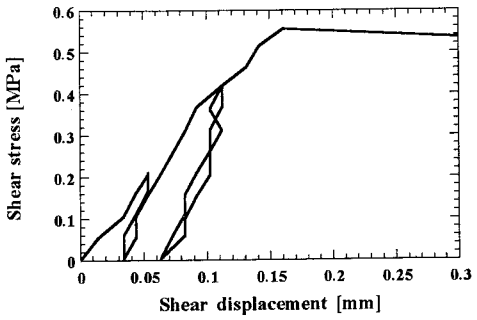

Figure 7.11 Shear stress - shear displacement relation under the cyclic direct shear tests on a rock joint

cyclic loading tests, the cyclic direct shear tests on the rock joint are carried out. The shear stress - shear displacement curve is shown in **Figure 7.11**. An almost constant magnitude of permanent deformation can be found in every cyclic shear loading. As mentioned above, the permanent deformation of a joint is more strongly affected by the shear behavior of a rock joint than by the normal behavior of it. As described in Chapter 4, the shear behavior of a rock joint is strongly affected by the natural joint surface roughness. In the cyclic shear tests, it is thought that the permanent deformation is caused by the overclimbing of the asperity of the joint.

7.3.3 Deformation of a jointed rock mass

As described in Section 7.3.2, it is confirmed through the borehole loading test that the deformation of a jointed rock mass consists of elastic deformation and permanent deformation, and that the permanent deformation occurs to the deformation of the rock joint, especially the shear behavior of the rock joint.

Next, the elastic deformation of a jointed rock mass will be considered. The elastic modulus which is given by the entire gradient of a load - displacement curve around a higher loading level is apart from it throughout the uniaxial compression tests, as shown in **Figure 7.5**. And, with the same rock type and the same loading point, the elastic deformation differs with changes in the loading direction. Therefore, the elastic deformation of a jointed rock mass consists of the elastic deformation of both the intact rock and the rock joint.

As mentioned above, it is known through the borehole loading tests that the deformation of a jointed rock mass consists of elastic deformation and non-elastic deformation; this relation can be described by **Equation 7-4**, namely,

$$u_{total} = u_e + u_p \tag{7-4}$$

where u_{total} is the total displacement of the jointed rock mass and u_e and u_p are elastic and non-elastic components of the displacement, respectively. Then, using deformation coefficient D, elastic modulus E, and permanent deformation coefficient M, **Equation 7-4** is transformed by **Equation 7-5** or **Equation 7-6**, namely,

$$\frac{P}{D} = \frac{P}{E} + \frac{P}{M} \tag{7-5}$$

or

$$\frac{1}{D} = \frac{1}{E} + \frac{1}{M} \tag{7-6}$$

E is not equal to the elastic modulus of the intact rock. D is defined as the gradient of an enveloping straight line onto the hysteresis of several cyclic loading - unloading curves with different peak stress levels, and E is defined as the gradient of a reloading or unloading curve. D and E are conveniently employed in the design of a rock structure, but the relationship between them is discussed only as a kind of empirical rule, but not well explained in a quantitative form. The introduction of Goodman's "permanent deformation coefficient (M)" gives a solution to the mathematical expression.

It has already been explained in this thesis that the non-elastic deformation of a jointed rock mass occurs to the joint itself, since the intact part of the jointed rock mass is very stiff. Therefore, the elastic deformation of a jointed rock mass actually consists of that of both the intact rock and the rock joint. Thus, the following relation can be obtained:

$$\frac{1}{E_{mass}} = \frac{1}{E_{intact}} + \frac{1}{E_{joint}} \tag{7-7}$$

in which E_{mass}, E_{intact}, and E_{joint} are the elastic moduli of the jointed rock mass, the intact rock and the rock joint, respectively. In this research work, since the borehole loading tests are carried out in two loading directions at the same loading point, two types of E_{mass} can be determined for the same loading point. And, E_{intact} can be determined through laboratory tests using intact rock. Therefore, if the relationship between the loading direction and some parameters of the rock joint can be clarified, the mechanical parameter of the joint, namely, joint stiffness, can be found through **Equation 7-7**.

7.4 Determination of joint stiffness through the borehole loading tests

7.4.1 Joint stiffness

In the elastic body, Kishida (1992) and Ando (1995) described the following equation which presents the displacement at a point along the loading axis during the borehole loading tests, namely,

$$f(x) = \alpha x^{-1} \tag{7-8}$$

where x is the distance from the center of the borehole, α is a coefficient determined by the displacement of the loading plate, and $f(x)$ is a function of the displacement. Then, if the stress and/or the load is constant over a very slight range in the elastic body, the following relation can be described:

$$\begin{aligned} P &= E_{intact} \frac{f(x+dx) - f(x)}{dx} \\ &= E_{intact} \frac{\frac{\partial f(x)}{\partial x} dx}{dx} \\ &= E_{intact} \frac{\partial f(x)}{\partial x} \\ &= E_{intact} \cdot \alpha x^{-2} \end{aligned} \tag{7-9}$$

E_{intact} is supposed to be constant over the effective area of the borehole loading tests. P is the stress and/or the load in a point along the loading direction. P is different from P_0 which is the load applied to the loading plate. In the borehole loading tests, the expansion of the load and/or the stress onto the rock around the borehole is supposed to agree with Goodman's concept as described by **Equation 7-1** (1968). Then, substituting Goodman's function, for **Equation 7-9**, $\psi(\beta, \upsilon)$ **Equation 7-10** can be obtained and coefficient parameter α can be determined by **Equation 7-11**, namely,

$$\begin{aligned} P(r) &= \psi(\beta, \upsilon) \cdot P_0 \\ &= E_{intact} \cdot \alpha r^{-2} \end{aligned} \tag{7-10}$$

$$\alpha = \frac{\psi(\beta, \upsilon) \cdot P_0 \cdot r^2}{E_{intact}} \tag{7-11}$$

where r is the radius of the borehole. Therefore, the stress (the load) and the displacement at a disposal point of the rock mass along the loading direction can be presented by **Equations 7-12** and **7-13** after performing the borehole loading tests.

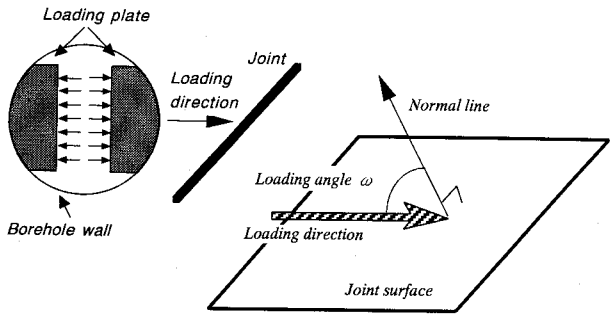

Figure 7.12 The concept of a loading angle in the borehole jacking

$$P(x) = \frac{\psi(\beta, \upsilon) \cdot P_0 \cdot r^2}{x^2} \tag{7-12}$$

$$f(x) = \frac{\psi(\beta, \upsilon) \cdot P_0 \cdot r^2}{E_{intact} \cdot x} \tag{7-13}$$

Based on **Equation 7-13**, the displacement of the intact rock at the borehole wall can be shown in the following equation:

$$\begin{aligned} u_{intact} &= f(r) \\ &= \frac{\psi(\beta, \upsilon) \cdot P_0 \cdot r}{E_{intact}} \end{aligned} \tag{7-14}$$

Next, the displacement of a rock joint will be considered. It is assumed that the rock joint, when it is located near the loading point, yields to the displacement so as to apply it to the stress along the loading direction. In the numerical analysis of the elastic body, the function of the stress around the borehole is presented by the distance along the loading direction (Kishida, 1992, Ando, 1995). Considering the distance from the rock joint to the loading point along the loading direction, the stress and/or the load applied to the rock joint can be estimated. Therefore, the displacement of the rock joint can be calculated in order to determine the nearest rock joint from the loading point and to measure its orientation. Before presenting the displacement of the rock joint, the modulus of the deformation of the rock joint and the loading mechanism on the rock joint are discussed. In this thesis, the loading angle on the rock joint is defined by a normal line of rock joints and a loading direction. The model, which presents the displacement applying joint stiffness along the loading direction, $K(\omega)$, is assumed. This concept is shown in **Figure 7.12**. The concept of joint stiffness $K(\omega)$ is an overall parameter including normal stiffness K_n and shear stiffness K_s.

Figure 7.13 shows the relation between the borehole and the rock joint and three kinds of rectangular coordinate systems, as defined in the following:

x_i coordinate system : x_1 is north - south, x_2 is east - west, and x_3 is in a vertical direction

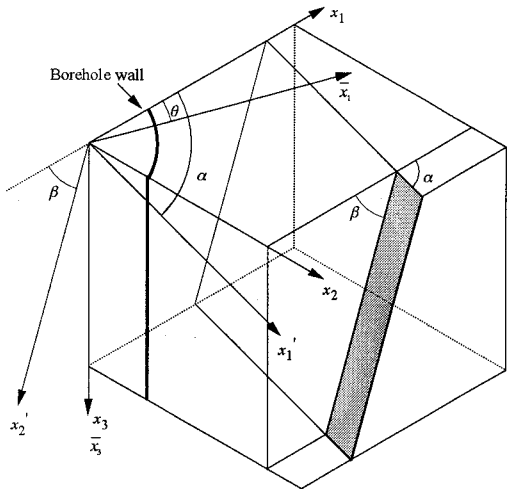

Figure 7.13 Joint orientation and loading direction

$\bar{x}_i$ coordinate system : x_i coordinate system is rotated on an x_3 axis turning q clockwise, and the loading direction is in agreement with $\bar{x}_1$

x_i' coordinate system : x_i coordinate system is rotated by turning the strike angle, a, and the dip direction, b, and the x_3' axis is in agreement with a normal line of rock joints.

If the load in the borehole loading tests is applied under a uniaxial compressive condition, the stress tensor in the $\bar{x}_i$ coordinate system can be described as follows:.

$$\bar{\sigma} = \begin{bmatrix} p & 0 & 0 \\ 0 & 0 & 0 \\ 0 & 0 & 0 \end{bmatrix} . \tag{7-15}$$

The transformed tensor from the $\bar{x}_i$ coordinate system to the x_i coordinate system is defined by **Equation 7.16**, namely,

$$Q = \begin{bmatrix} \cos\theta & -\sin\theta & 0 \\ \sin\theta & \cos\theta & 0 \\ 0 & 0 & 1 \end{bmatrix} . \tag{7-16}$$

Using the transformed tensor, Q, the stress tensor in a rock mass can be presented in the x_i coordinate system.

$$\begin{aligned} \sigma &= Q \cdot \bar{\sigma} \cdot Q^T \\ &= \begin{bmatrix} p\cos^2\theta & p\sin\theta\cos\theta & 0 \\ p\sin\theta\cos\theta & p\sin^2\theta & 0 \\ 0 & 0 & 0 \end{bmatrix} \end{aligned} \tag{7-17}$$

Next, the transformed tensor from the x_i coordinate system to the x_i' coordinate system is defined by the following equation:

$$
\begin{aligned}
S &= \begin{bmatrix} 1 & 0 & 0 \\ 0 & \cos\beta & \sin\beta \\ 0 & -\sin\beta & \cos\beta \end{bmatrix} \cdot \begin{bmatrix} \cos\alpha & \sin\alpha & 0 \\ -\sin\alpha & \cos\alpha & 0 \\ 0 & 0 & 1 \end{bmatrix} \\
&= \begin{bmatrix} \cos\alpha & \sin\alpha & 0 \\ -\sin\alpha\cdot\cos\beta & \cos\alpha\cdot\cos\beta & \sin\beta \\ \sin\alpha\cdot\sin\beta & \cos\alpha\cdot\sin\beta & \cos\beta \end{bmatrix} \\
&= [S_{ij}]
\end{aligned} \tag{7-18}
$$

The normal vector of the rock joint is presented by **Equation 7-19**.

$$
\begin{aligned}
\vec{n} &= S^T \begin{bmatrix} 0 \\ 0 \\ 1 \end{bmatrix} \\
&= \begin{bmatrix} \sin\alpha\cdot\sin\beta \\ -\cos\alpha\cdot\sin\beta \\ \cos\beta \end{bmatrix} \\
&= \begin{bmatrix} S_{31} \\ S_{32} \\ S_{33} \end{bmatrix}
\end{aligned} \tag{7-19}
$$

Using **Equations 7-17** and **7-19**, therefore, the stress vector on the rock joint, $\vec{T}$, is presented by **Equation 7-20**.

$$
\begin{aligned}
\vec{T} &= \sigma\cdot\vec{n} \\
&= \begin{bmatrix} pS_{31}\cos^2\theta + pS_{32}\sin\theta\cdot\cos\theta \\ pS_{31}\sin\theta\cdot\cos\theta + pS_{32}\sin^2\theta \\ 0 \end{bmatrix}
\end{aligned} \tag{7-20}
$$

Then, vector $\vec{T}$ is transformed in the x_i' coordinate system, in other words,

$$
\begin{aligned}
\vec{T}' &= S\cdot\vec{T} \\
&= \begin{bmatrix} p(S_{11}\cos\theta + S_{12}\sin\theta)(S_{31}\cos\theta + pS_{32}\sin\theta) \\ p(S_{21}\cos\theta + S_{22}\sin\theta)(S_{31}\cos\theta + pS_{32}\sin\theta) \\ p(S_{31}\cos\theta + S_{32}\sin\theta)^2 \end{bmatrix} \\
&= \begin{bmatrix} T_1' \\ T_2' \\ T_3' \end{bmatrix}
\end{aligned} \tag{7-21}
$$

By use of joint stiffness $K(\omega)$, the relative displacement on the rock joint, u', can be described by the following equation:

$$u' = \begin{bmatrix} u_1' \\ u_2' \\ u_3' \end{bmatrix} = \frac{\vec{T}'}{K(\omega)} \quad (7\text{-}22)$$

The relative displacement on the $\bar{x}_i$ coordinate system is transformed as follows:

$$\bar{u} = Q^T \cdot S^T \cdot u' \quad (7\text{-}23)$$

Substituting **Equation 7-23** for **7-22**, the relative displacement can be presented using the joint stiffness.

$$\bar{u} = \frac{p}{K(\omega)} \begin{bmatrix} S_{31}\cos\theta + S_{32}\sin\theta \\ 0 \\ 0 \end{bmatrix} \quad (7\text{-}24)$$

The loading angle, ω, between a normal line of rock joints and a loading direction is therefore defined by **Equation 7-25**, namely,

$$\omega = \arccos\left(S_{31}\cos\theta + S_{32}\sin\theta\right) . \quad (7\text{-}25)$$

The elastic displacement of rock joints is considered once again. Using **Equation 7-10** and joint stiffness $K(\omega)$, the elastic displacement of the rock joint can be described as follows:

$$\begin{aligned} u_{joint} &= \frac{P\left(\frac{h}{\cos\omega}\right)}{K(\omega)} \\ &= \frac{\frac{\psi(\beta, \upsilon)\cdot P_0 \cdot r^2}{\left(\frac{h}{\cos\omega}\right)^2}}{K(\omega)} \\ &= \frac{\psi(\beta, \upsilon)\cdot P_0 \cdot r^2 \cdot \cos^2\omega}{h^2 \cdot K(\omega)} \end{aligned} \quad (7\text{-}26)$$

where r is the radius of the borehole and h is the minimum distance from the loading point to the rock joint. Based on **Equations 7-7**, **7-14**, and **7-26**, therefore, the elastic modulus of the jointed rock mass can be presented by **Equation 7-27**, namely,

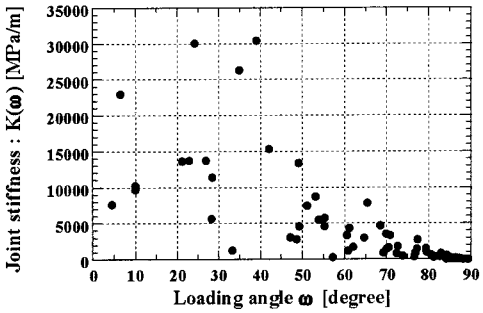

Figure 7.14 The relationship between joint stiffness $K(\omega)$ and loading angle ω through the borehole loading tests

$$E_{mass} = 2r\psi(\beta, \upsilon)\frac{P_0}{2u_{intact} + u_{joint}}$$

$$= 2r\psi(\beta, \upsilon)\frac{P_0}{2\dfrac{P_0 r\psi(\beta, \upsilon)}{E_0} + \dfrac{\psi(\beta, \upsilon)\cdot P_0 \cdot r^2 \cdot \cos^2\omega}{h^2 \cdot K(\omega)}}$$

$$= \frac{1}{\dfrac{1}{E_0} + \dfrac{r \cdot \cos^2\omega}{2h^2 \cdot K(\omega)}}$$

That is,

$$E_{mass} = \left[\frac{1}{E_0} + \frac{r \cdot \cos^2\omega}{2h^2 \cdot K(\omega)}\right]^{-1} \quad (7\text{-}27)$$

Figure 7.14 shows the relationship between joint stiffness $K(\omega)$ and loading angle ω through the results of the borehole loading tests. As mentioned above, the joint stiffness can be determined through the results of the borehole loading tests. So as to estimate the mechanical properties of rock joints using $K(\omega)$ and ω, however, these relations have to be clarified. Then, in order to clarify the mechanical properties of the rock joint, a laboratory test, which considers the loading angle of the rock joint, will be performed.

7.4.2 Rock joint loading tests at a constant loading angle in the laboratory

To grasp the property of deformation of the rock joint, laboratory tests are carried out and the relationship between the loading angle and the joint stiffness along the loading direction is discussed.

Specimens employed in thess laboratory tests include natural joints taken from core samples (60 *mm* in *diameter*). After choosing five types of natural joint surface roughness, impressions are made of them. This is the same method as that described in Chapter 4. Using the

impressions, reproduced plaster specimens are made. The impressions are made of Silicon rubber (TSE350, Toshiba Silicon Co. Ltd.). To make plaster specimens, Jet cement (Sumitomo Cement Co.) is used. The combination ratio of cement, sand, and water is 1 : 1 : 0.375. The compressive strength of the specimen is almost constant at 52.0 *MPa* with more than fourteen days passing after making them.

As shown in **Figure 4.1**, the rock joint loading tests at a constant loading angle are carried out using a rock joint direct shear tester (Seikensya). Since an intelligent-type control system was developed using a personal computer, the tests are performed for the purpose of controlling both the loading and the displacement directions on the rock joint. They seem to present the mechanism of the borehole loading in the constant displacement-type borehole loading tests.

Aimed at the loading mechanism of the borehole loading, the behavior of the rock joint and the observed data will be discussed. **Figure 7.12** assumes the performance of the borehole loading tests on a rock joint. The loading angle from the normal line of the rock joint is presented in **Figure 7.12**. In the constant displacement-type borehole loading tests, the load is worked along the loading direction, that is, the loading plate is moved along one direction by force, and in reaching the loading level, the displacement along the direction is observed. At that time, the displacement along the loading direction appears forcibly on the rock joint, and it is thought that the mechanical behavior of the rock joint is controlled by the load. In order for the loading condition of the rock joint to appear in the laboratory, the following control is carried out:

i) To set up loading angle ω, deformation u_r on the rock joint is forced to occur along the loading direction.

ii) Both normal and shear forces, P_n and P_s, respectively, are measured, and the resultant forces are calculated.

iii) Until the loading direction's component P_r of the resultant force reaches a setting level, the deformation of the rock joint is maintained.

Figure 7.15 shows the concept of this control system. By performing this control system in a laboratory, it is thought that the loading condition of the rock joint, applied for the borehole loading tests reappears. And, in the case of setting up a loading angle of $\omega = 0$, the shear behavior of the rock joint occurs and is equivalent to that in the uniaxial compressive tests controlled by the load. It is not suitable, therefore, to call it a shear test. The test using the above-mentioned control system is called a rock joint loading test under a constant loading angle.

In actuality, six types of loading angles, namely, $\omega = 0$, 15, 30, 45, 60, and 75 were divided into four loading levels, namely, 2.5, 5.0, 7.5, and 10.0 *MPa*, and tests were carried out. The loading velocity was set at 1.0 *MPa/min.*. Some samples of the results are shown in **Figures 7.16**(a), (b), (c), and (d). The results are similar to those of the borehole loading tests. From these results, the joint stiffness of the loading direction, $K(\omega)$, can be determined.

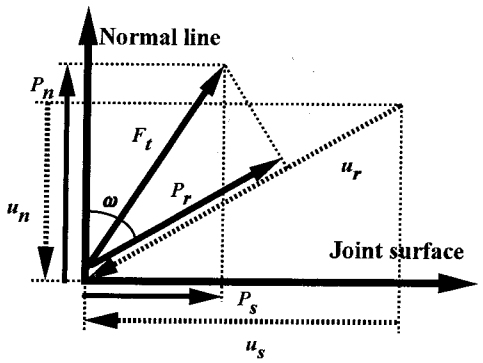

Figure 7.15 The concept of joint stiffness $K(\omega)$

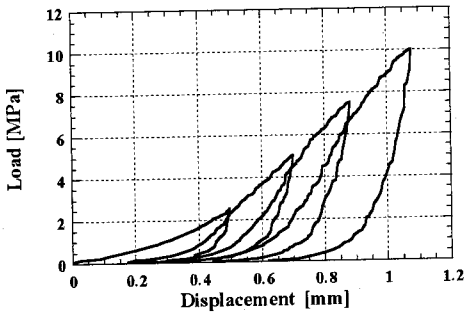

(a) Sample 1, Loading angle = 75

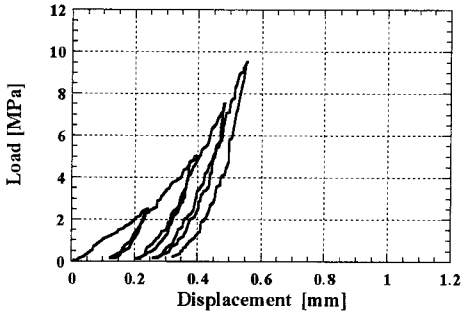

(b) Sample 2, Loading angle = 60

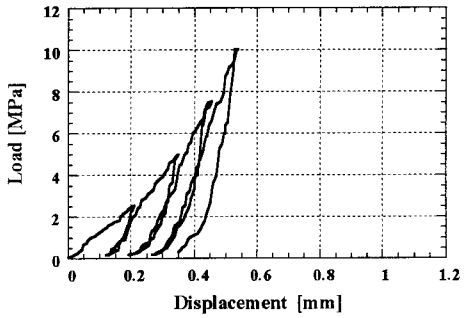

(c) Sample 3, Loading angle = 45

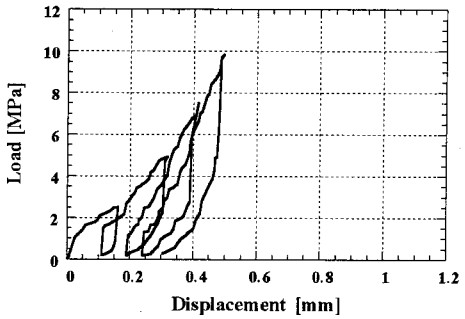

(d) Sample 4, Loading angle = 30

Figure 7.16 Examples of load - displacement curves through the rock joint loading tests on constant loading angles

7.4.3 Discussion

In the same way as the joint stiffness is estimated through the in-situ borehole loading tests, the joint stiffness will be determined through the results of laboratory tests, and a discussion will be conducted.

In the case of field measurements, the combined deformation from the intact rock and the rock joint is measured. On the other hand, only the deformation of the rock joint is assumed in the laboratory. Moreover, the area of the rock joint affected by the shear behavior is smaller in

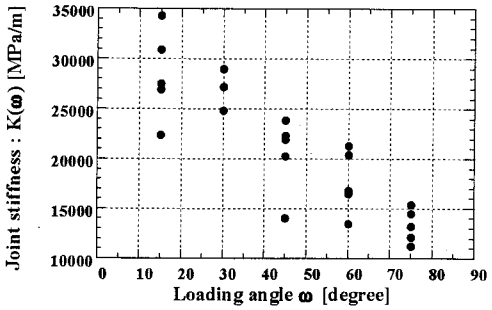

Figure 7.17 The relationship between joint stiffness $K(\omega)$ and loading angle ω through the rock joint loading tests with a constant loading angle

the laboratory than in the field, and it is thought that the scale effect produces some influence. It is not suitable, therefore, to compare the joint stiffness through laboratory tests with that through tests in the field. However, it is necessary to compare the tendency of these values so as to verify the method for estimating the joint stiffness.

Figure 7.17 shows the relationship between joint stiffness $K(\omega)$ and loading angle ω through laboratory tests. As for the tendency of the data plotting points, this figure is in agreement with **Figure 7.14**. It is shown that the laboratory tests represent the loading mechanism of the borehole loading tests in the field. Therefore, it is effective to introduce the concept of joint stiffness along loading direction $K(\omega)$, and the deformation of the rock joint can be estimated through borehole loading tests.

In the next step, the relationship between $K(\omega)$ and normal and shear stiffness, K_n and K_S, respectively, will be discussed. In **Figure 7.12**, the displacement vector of rock joint $\vec{u}_r$ can be divided into normal and shear components, u_n and u_S, respectively, using loading angle ω and scalar size u_r of the displacement vector $\vec{u}_r$, namely,

$$\vec{u}_r = u_r \begin{pmatrix} \sin\omega \\ \cos\omega \end{pmatrix} = \begin{pmatrix} u_s \\ u_n \end{pmatrix} . \tag{7-28}$$

From each displacement component, shear load P_S and normal load P_n can be measured. The following relation exists between the displacement and the loads:

$$P_s = K_s \times u_s \tag{7-29}$$

$$P_n = K_n \times u_n \tag{7-30}$$

Therefore, force $\vec{P}_r$, which is actually working on the rock joint, can be described as follows:

$$\begin{aligned}\vec{P}_t &= \begin{pmatrix} P_s \\ P_n \end{pmatrix} \\ &= \begin{pmatrix} K_s \cdot u_s \\ K_n \cdot u_n \end{pmatrix} \\ &= \begin{pmatrix} K_s \\ K_n \end{pmatrix} \cdot \vec{u}_r \end{aligned} \quad . \tag{7-31}$$

Then, since observed load P_r is a loading direction's component of $\vec{P}_t$, the following relation can be described using **Equations 7-28** and **7-31**:

$$\begin{aligned} P_r &= \frac{\vec{P}_t \cdot \vec{u}_r}{\left|\vec{u}_r\right|} \\ &= \frac{d_r^2\left(K_n \cdot \cos^2\omega + K_s \cdot \sin^2\omega\right)}{d_r} \\ &= d_r \cdot \left(K_n \cdot \cos^2\omega + K_s \cdot \sin^2\omega\right) \end{aligned} \quad . \tag{7-32}$$

Using **Equation 7-32**, the joint stiffness of the loading direction can therefore be described as follows:

$$K(\omega) = \frac{P_r}{d_r} = K_n \cdot \cos^2\omega + K_s \cdot \sin^2\omega \quad . \tag{7-33}$$

If both normal and shear stiffness are assumed as constants, the results of the rock joint loading tests at a constant loading angle can be described by **Equation 7-33**. Using **Equation 7-33**, the average values for the normal and the shear stiffness can be estimated from the results. In this research work, normal stiffness K_n is obtained by 4.1×10^4 *MPa/m* and shear stiffness K_S is obtained by 4.5×10^3 *MPa/m* from laboratory tests, respectively.

7.5 Conclusion

The deformation of rock masses is influenced by joint orientation, spacing, apertures, roughness, filling materials, etc.. Even if one rock type (intact rock) is the same as another, the deformability is quite different. The introduction of permanent deformation coefficient M helps to better explain the practical deformation behavior of rock masses. The rock classification based on M will be significant.

In particular, the factors appearing in the permanent deformation have been considered. Through the results of laboratory tests, the permanent deformation in jointed rock masses occurs to the shear behavior of the rock joints. Therefore, the mechanical properties of the rock joints must be considered, along with the permanent deformation. In addition, in order to estimate the permanent deformation, it is important to grasp the joint conditions of the objective area.

Applying **Equation 7-33** to the results of the borehole loading tests in the field, the average values of the normal stiffness $K_n = 1.7 \times 10^4$ *MPa/m* and shear stiffness $K_S = 3.0 \times 10^2$ *MPa/m* have been obtained. The normal stiffness is also in agreement with the results of the laboratory tests. It has been confirmed that rock joint loading tests at a constant angle have correctly presented the loading condition in the borehole loading tests. As for the normal deformation of the rock joint, it is appropriate to estimate the normal stiffness using the concept of this thesis. With the shear stiffness, however, one order of difference between the results in the field and those in the laboratory has been confirmed. It is thought that the difference occurs due to the scale effect. As for the shear behavior of the rock joint, the scale effect must be considered. Finally, it is important to determine the effective areas of the rock joints when discussing the shear behavior through the results of the borehole loading tests.

REFERENCES

Ando, N. (1995) : Study on the properties of the deformation of in-situ rock masses in consideration of joint stiffness, *M.C. Thesis at Kyoto University*. (in Japanese)

Goodman, R. E. (1980) : *Introduction to Rock Mechanics*, John Wiley & Sons, pp. 170 - 200.

Goodman, R. E., Van, T. K., Heuze, F. W. (1968) : The measurement of rock deformability in boreholes, Proceedings of 10th U.S. Symposium on Rock Mechanics, pp. 525 - 555.

Japan Society of Civil Engineers (1983) : *A guideline for testing methods of deformability and shear strength of in-situ rock masses*, pp. 10 - 12. (in Japanese)

Kishida, K. (1992) : Estimation of jointed rock masses through seismic geotomography and the borehole jacking test, *M.C. Thesis at Kyoto University*. (in Japanese)

Tanimoto, C., et al. (1988) : Numerical interpretation of borehole jack test in consideration of joint stiffness, *Proceedings of the 6th International Conference on Numerical Methods in Geomechanics*, Innsbruck, Balkema, pp. 863 - 870.

Tanimoto, C., Kishida, K. and Okamura, M. (1991) : Determination of joint stiffness through borehole jack test, *Proceedings of the 26th Japan National Conference on Soil Mechanics and Foundation Engineering*, pp. 1147 - 1150. (in Japanese)

Tanimoto, C., Murai, S., Matsumoto, T., Kishida, K. and Ando, T. (1992) : Immediate image and its analysis of fractured/jointed rock mass through the borehole scanner, *Fractured and Jointed Rock Masses*, Myer, Tsang, Cook & Goodman (eds), Balkema, published in 1995, pp. 219 - 228.

Chapter 8

Conclusion

Discontinuity characteristics and mechanical properties of jointed rock masses have been described in this thesis. The goals of this research have been to estimate the distribution of discontinuities and/or joints in the field and to determine the mechanical properties of the rock joints from field measurements and laboratory tests. In order to clarify these objectives, joint mapping, a borehole survey, seismic exploration, and borehole loading tests have been carried out in the field. In addition, certain laboratory tests, namely, the determination of joint surface roughness, direct shear tests on rock joints, and seismic propagating tests, have been conducted to interpret the results of the field measurements. The results obtained in each chapter are described below.

In **Chapter 2**, "Joint Survey and Joint Analysis", a geological survey and a joint investigation were carried out and the joint data were analyzed. Then, the joint aperture, the joint frequency, and the orientation of the joints, such as the dip and the dip direction, were estimated, and a discontinuity model for a jointed rock mass and a semi-continuity model were made based on the joint frequency.

In the investigation of discontinuities and/or joints, borehole wall sensing was performed by *BSS* and the character of the discontinuities was grasped in detail. *BSS* was confirmed to have an advantage regarding images and analyses over other investigating methods. In particular, in comparing the number of joints and *RQD* obtained from the *BSS* images with those obtained through the investigation of recovered core samples, the values were found to be different for the same borehole. Since the core samples were broken, it is thought that the *BSS* images presented a more practical picture of the in-situ rock mass than the core samples. From the *BSS* images, the orientation, the aperture, and the joint surface roughness were estimated.

Based on the orientation data, an orientation analysis was carried out and joint sets were extracted. Using the extracted results, it was possible to perform a discontinuity simulation, such as *DEM*, to represent the joint orientation. In the extraction of joint sets, however, only the number of joints was considered. It is thought that only considering the number of joints is not sufficient for estimating the mechanical and the hydromechanical properties of a jointed rock mass. In this research, therefore, *R.I.*, which presents the relative importance of a joint set, was proposed. This parameter was believed to have been influenced by the number of joints, the extension (an area), and the apertures. Based on the idea that a joint, which consists of a wide aperture and covers a large area, strongly affects both the mechanical and the hydromechanical behaviors more than others, *R.I.* was able to estimate both properties in detail. In particular, it was confirmed that a joint set presents a large number for *R.I.*, although it has shown more small

numbers of joints than other joint sets. It is thought that an insufficient amount of consideration was given to the extension of joints since only the borehole survey data was analyzed in this thesis. However, the apertures of most joints in a joint set were found to be wide, although the number of joints was few. The joint analysis estimated the intensive orientation, only giving consideration to the same number of joints as usual. However, *R.I.* supplemented the joint analysis with other factors, such as the apertures and the extension of joints, and joint sets were obtained in consideration of both mechanical and hydromechanical properties. Regarding the above-mentioned reasons, it is thought that *R.I.* presented essential information on jointed rock masses.

As for the semi-continuity model for a jointed rock mass, a joint frequency map was proposed. While making the joint frequency map, the composition of the geology and a comparison of the orientation of major faults with that of the joints were considered. Then, the model was created in consideration of the geological structure. As for the extension of joints, consideration for the index of the joint apertures was given. This consideration is based on the concept that joints with wide apertures present high continuity. The joint frequency map can be applied to some numerical models.

In **Chapter 3**, "Quantitative Determination of Rock Joint Surface Roughness", the power spectral moment, M_S, was defined through the results of a spectral analysis and the quantitative determination of the natural rock joint surface roughness was carried out.

A spectral analysis was performed on the representative *JRC*, suggested by Barton and Choubey (1977), and its power spectrum was calculated. As for the spectral analysis of roughness, it was confirmed that *MEM* has an advantage over *FFT*. With *MEM*, it is possible to calculate the spectrum of a high-quality resolution using a small amount of data; therefore, *MEM* can easily be applied to the measuring data of a specimen and reliable results can be obtained.

The M_S value was defined in order to determine the roughness from the results of the spectral analysis. The M_S value presented the product of the center of the frequency distribution and the strength of the power spectrum in a range under 1 *Hz*. It is thought that the strength of the power spectrum represents the unevenness property of the roughness and the center of the frequency distribution represents the period property of it. Therefore, M_S showed both unevenness and period properties of the roughness.

Barton's *JRC* was determined using the M_S value. It was confirmed that as the *JRC* value increases, the M_S value also increases. And, an equation describing the relationship between *JRC* and M_S was introduced.

A roughness profiler was developed to measure the natural rock joint surface roughness accurately, and the roughness was measured by it. The M_S value, which represents the specimen,

was defined as the average M_S for each scan line in consideration of the weight value based on the scan length. Using the calculated M_S value, the *JRC* of the specimen can be estimated.

As mentioned above, the natural rock joint surface roughness was determined quantitatively by the M_S value, and the *JRC* was calculated. It is necessary to confirm the relationship between the shear behavior and the M_S value, in particular, the relationship between the peak shear strength from laboratory tests, M_S, and the peak shear strength estimated from Barton's empirical equation.

In **Chapter 4**, "Experimental Study on the Shear Behavior of Rock Joints through Direct Shear Tests", direct shear tests were carried out under both constant and variable confining conditions. As for the variable confining condition, it is known that the stress ratio-shear displacement relation is equivalent to that under a constant confining condition. Therefore, the shear behavior of rock joints under a low confining condition is controlled by the interlocking of the joint surface roughness and the sliding friction before and after the peak stress ratio appeared, respectively.

The *JRC* value was estimated using the M_S value. *JRC* itself is calculated by the back analysis in Barton's empirical equation as follows:

$$\tau_p = \sigma_n \cdot \tan\left\{ JRC \log\left(\frac{JCS}{\sigma_n}\right) + \phi_b \right\} \tag{8-1}$$

and does not represent the factor of joint surface roughness. *JRC* is thought to represent the factor of joint surface roughness containing the influence of the material strength, the sliding friction, the normal effective stress, and weathering (or the nonoccurrence of it) in the direct shear tests.

From the experimental results, it was shown that the shear behavior of rock joints can be affected by joint surface roughness, material strength, and effective normal stress. Under a conditions with the same roughness form and material strength for both, increases in peak shear strength and residual strength and decreases in dilation were observed due to increases in the effective normal stress. Considering the influence of the difference in joint surface roughness, changes in peak shear strength, residual strength, dilatancy, and peak shear displacement were seen. The difference in material strength caused changes in the shear behavior. In particular, the peak shear strength decreased and the dilatancy increased in comparison to specimens in which the material strength is soft.

Based on the results of direct shear tests, the parameter of the joint surface roughness was estimated in consideration of its form, material strength, and effective normal stress and can determined the relationship among this parameter, the peak shear strength, and the dilatancy curves.

In **Chapter 5**, "Laboratory Experiments on the Propagating Behavior of Seismic Waves through Several Kinds of Rock Joint under Uniaxial Conditions", several specimens consisting of certain kinds of joint conditions were used for seismic propagating experiments under normal and shear loading conditions. Just how the seismic propagating behavior has affected joint conditions was considered.

Using specimens which consist of smooth artificial joints, the seismic velocity did not change with variations in joint frequency. However, the first break amplitude showed remarkable sense.

In performing the seismic propagating experiments with five kinds of natural joint surface roughness, variations in seismic velocity could not be found. However, the first break amplitude was found to show a remarkable distinction against the joint surface roughness. Thus, a good correlation between joint surface roughness and the first break amplitude was confirmed.

In the case of a model which includes filling material, both the seismic velocity and the first break amplitude decreasd with increments in the thickness of the filling material.

Under a shear loading condition, variations in the first break amplitude were more sensitive than those of the seismic velocity. In particular, variations in joint surface roughness and changes in aperture and/or dilation were clearly presented by the first break amplitude.

As mentioned above, the first break amplitude was more useful than the seismic velocity for discussing the effects of joint frequency and joint surface roughness. However, both the seismic velocity and the first break amplitude are useful for estimating the filling material. And, the first break amplitude is useful for presenting variations in the dilation and the aperture under the shear loading, that is, for discussing the effects of support elements in tunneling or large underground excavation works. Applying these remarkable conclusions to a discussion on the results of field investigations, rock structures can be estimated in detail over an objective area using both seismic velocity and seismic attenuation geotomography.

In **Chapter 6**, "Development of the Seismic Geotomographic Technique and its Application in Jointed Rock Masses", seismic geotomography was developed and a certain numerical simulation and analyses of field data were conducted.

First of all, as for the locations of the source and the receiver points, naturally enough, Arrangement I, namely, all-around sensing (360-degree scanning like in medical cases), had the advantage over the other arrangements. However, it is impossible to apply Arrangement I to the civil engineering field. On the other hand, Arrangement II, that is, the ground surface and two scanning boreholes, yielded results which show a good agreement with the original model without the effect of the inclination of a low velocity zone. Since the density of the raypaths presented an unbalance in the objective area, however, a numerical false appeared and it was difficult to judge

the existence or the non-existence of a false in the practical results. As for Arrangement III, two vertical scanning boreholes (for conventional cross-borehole scanning), the distribution of the raypaths in an objective area presented a good balance. However, the low velocity zone running parallel to the boreholes could not be created for the reconstructed model. It was concluded that scanning only between boreholes does not provide reliable images. Thus, scanning in three directions, such as in Arrangement II, should be employed in addition to the fact that the scanning area should be at least twice as large as the objective area. In other words, the depth of the boreholes in the case of Arrangement II should be two or more times deeper than 40 *m*. This is due to the excessive difference in raypath densities propagating through the respective cells. The distribution of rays (traveling waves) must be as uniform as possible.

As for the locations of the source and the receiver points, the reappearance of the reconstructed model made progress since the interval between the source and the receiver points decreased, namely, the density of the raypaths increased. However, if the target was smaller than the interval, the target could not be shown in the reconstructed model and the high-precision reconstructed model could not be obtained. In addition, in order to perform a high-precision analysis in geotomography, as many cells as possible must be set up, according to the limits, to prevent a break in the calculations.

It was shown that the seismic geotomographic technique, based on the attenuation behavior of traveling waves, was able to provide more detailed information concerning rock joints by giving consideration to both laboratory experiments and applications in the field. The following conclusions can be made :

1) When the number of joints with smooth fracture planes and thin apertures increases, the amplitude distribution technique (*SAT*) corresponds much better than the velocity distribution technique (*SVT*).
2) Concerning variations in joint roughness and changes in normal and shear stresses, *SAT* is more sensitive than *SVT*.
3) When filling materials and thick apertures exist at joints, both *SAT* and *SVT* show a good correspondence.
4) By employing joint frequency mapping through the borehole scanner system (*BSS*), the geotomographic technique (consisting of *SVT* and *SAT*) may suggest and distinguish the following cases from each other :
   - the existence of weak zones and joints with fillings in the case of a low velocity and a high attenuation, and
   - the distribution of tightly jointed fractures in the case of a high velocity and a high attenuation.

In **Chapter** 7, "The Property of Deformation of Jointed Rock Masses and the Determination of Joint Stiffness through Borehole Loading Test", borehole loading tests were

carried out in the field and the determination of joint stiffness through the results of the borehole loading tests was discussed.

The deformation of rock masses is influenced by joint orientation, spacing, apertures, roughness, filling materials, etc.. Even if one rock type (intact rock) is the same as another, the deformability is quite different. The introduction of permanent deformation coefficient M helps to better explain the practical deformation behavior of rock masses. The rock classification based on M will be significant.

In particular, the factors appearing in the permanent deformation were considered. Through the results of laboratory tests, the permanent deformation in jointed rock masses was seen to occur to the shear behavior of the rock joints. Therefore, the mechanical properties of the rock joints must be considered, along with the permanent deformation. Also, in order to estimate the permanent deformation, it is important to grasp the joint conditions of the objective area.

Applying **Equation 7-33** to the results of the borehole loading tests in the field, the average values of the normal stiffness $K_n = 1.7 \times 10^4$ *MPa/m* and the shear stiffness $K_S = 3.0 \times 10^2$ *MPa/m* were obtained. The normal stiffness was also in agreement with the results of the laboratory tests. It was confirmed that rock joint loading tests at a constant angle correctly presented the loading conditions of the borehole loading tests. As for the normal deformation of the rock joint, it is appropriate to estimate the normal stiffness using the concept of this thesis. With the shear stiffness, however, one order of difference between the results in the field and those in the laboratory was confirmed. It is thought that the difference occurs due to the scale effect. As for the shear behavior of the rock joint, the scale effect must be considered. Finally, it is important to determine the effective areas of rock joints when discussing the shear behavior through the results of borehole loading tests.

Figure 8.1 shows the relationship between conclusions in each chapter. In this figure, the goal of this research work is to estimate the constitutive model of the jointed rock masses. This thesis could not sufficiently present the constitutive model of the jointed rock masses. However, it is thought that the determination of the mechanical properties of jointed rock masses, which is important to discuss the modeling, could be presented.

Issues concerning the mechanical behavior of jointed rock masses are found to be strongly affected by joints and/or discontinuities. In the construction and the design of rock structures on jointed rock masses, both the distribution and the mechanical properties of the rock joints must be clarified. Then, effective knowledge obtained through field measurements and laboratory tests is important to the construction and the design of the rock structures. In this thesis, it is thought that these points were clarified.

REFERENCES

Barton, N. and Choubey, V. (1977) : The shear strength of rock joints in theory and practice, *Rock Mechanics*, Vol. 10, pp. 1 - 54.

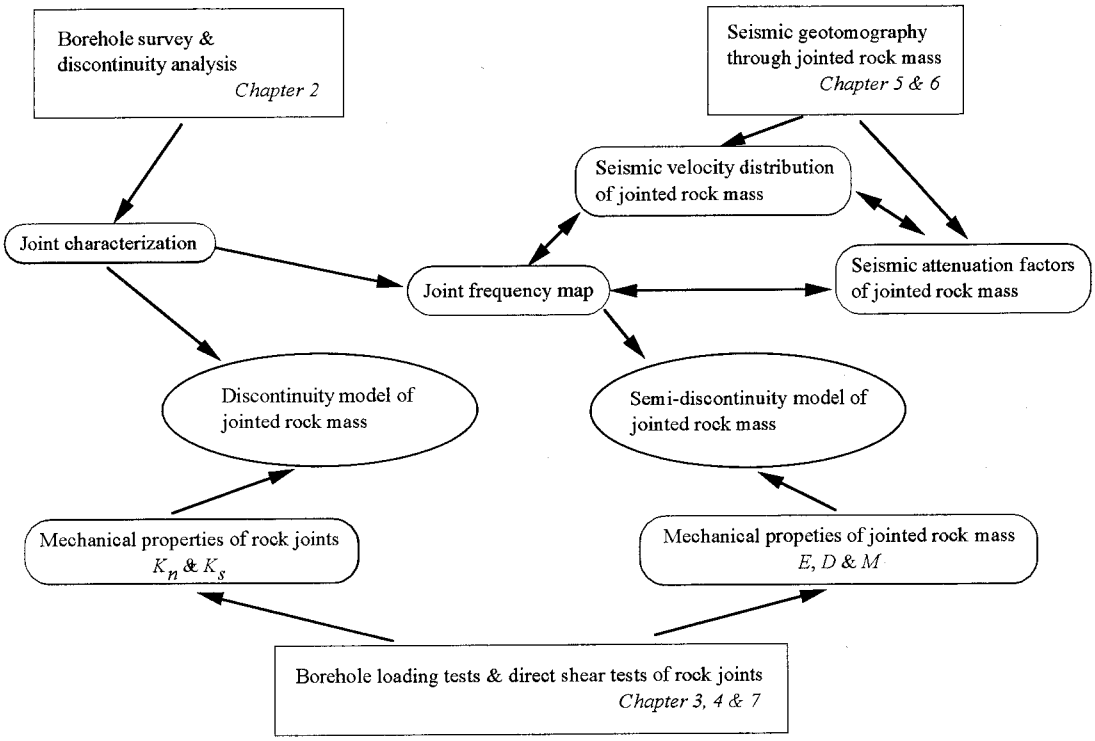

Figure 8.1 Schematic view of conclusion of this thesis